Proteolytic Antibodies – Myth or Reality?

Attempts to isolate proteolytic antibodies via **P**roteolytic **A**ntigen **C**leavage-**M**ediated **A**mplificatio**N** (PACMAN)

Inaugural-Dissertation

zur Erlangung des Doktorgrades der Mathematisch-Naturwissenschaftlichen Fakultät der Heinrich-Heine-Universität Düsseldorf

vorgelegt von

Jan Filip Tristan Hasecke

aus Köln

Düsseldorf, August 2023

aus dem Institut für Physikalische Biologie
der Heinrich-Heine-Universität Düsseldorf

Gedruckt mit der Genehmigung der
Mathematisch-Naturwissenschaftlichen Fakultät der
Heinrich-Heine-Universität Düsseldorf

Berichterstatter:

1. Jun.-Prof. Dr. Wolfgang Hoyer

2. Prof. Dr. Dieter Willbold

Tag der mündlichen Prüfung: 22.03.2024

“An expert is a person who has made all the mistakes that can be made in a very narrow field.”

Niels Bohr

Abstract

This thesis encompasses two key topics. As the prime topic, I present the development of a novel method called Proteolytic Antigen Cleavage-Mediated AmplificatioN (PACMAN) which aims to enable the isolation of proteolytic antibodies from combinatorial libraries. Proteolytic antibodies differ from conventional antibodies as they possess the unique ability to not only recognize and bind their antigen, but also enzymatically cleave it. However, this adds to the challenge that proteolytic antibodies fail to be effectively captured via well-known display methods, such as phage display, as the antibodies hydrolyze their antigen upon binding, leading to dissociation of the binding complex. To address this challenge, I invented the PACMAN method. It aims to allow the isolation of antigen-specific proteolytic antibodies from combinatorial libraries by *in vitro* expression of microbead-bound DNA of individual library members in picoliter-sized water-in-oil emulsions and subsequent detection and recovery of microbeads carrying DNA of active library members via fluorescence-activated cell sorting (FACS) using the successful cleavage of a simultaneously microbead-bound dual fluorescent labeled antigen-substrate as a reporter. In this thesis, the principle of PACMAN was successfully validated by recovery of DNA encoding Tobacco-Etch-Virus protease from a dilute mixture with excess irrelevant DNA.

The second focus of this thesis is an investigation into the formation and pathophysiological implications of amyloid-β oligomers (AβO) in Alzheimer's disease. The 'dimAβ' model, which forms metastable AβO, was leveraged to selectively examine the influence of AβO on fibril aggregation, AβO biogenesis and their impact on neuronal processes. It was demonstrated that AβO form independent from fibril formation and actively hinder the proliferation of amyloid fibrils. Furthermore, a potential *in vivo* pathway for AβO generation was discovered. A slightly acidic pH of 4.5–5.5, which is physiologically present in endolysosomal vesicles, accelerated AβO formation by $Aβ_{42}$ approximately ∼8,000-fold. Under these conditions, the critical $Aβ_{42}$ concentration necessary for AβO formation was decreased to ∼3 µM, which was shown to be present in endolysosomal vesicles. These findings indicate that the endolysosomal system might be an important site for toxic AβO generation *in vivo*. Lastly,

the specific impact of AβOs on primary mouse neurons was examined. The results revealed that AβO prominently bind to dendritic spines while neurons exposed to AβO stimuli exhibited decreased spontaneous Ca^{2+}-oscillations and translocation of the microtubule-associated protein tau from their axons to their somatodendritic compartments. This translocation of tau is known as a critical event implicated in the pathogenesis of Alzheimer's disease.

In conclusion, this thesis presents the development of the PACMAN method, along with an in-depth investigation into AβO and their role in Alzheimer's disease. The PACMAN method offers a promising approach for the isolation of proteolytic antibodies from combinatorial libraries against amyloid targets, while the insights gained into AβO formation and their impact on fibril aggregation and neuronal processes contribute to a deeper understanding of the underlying pathology of Alzheimer's disease.

Zusammenfassung

Diese Arbeit umfasst zwei Hauptthemen. Im Hauptteil präsentiere ich die Entwicklung einer neuartigen Methode namens Proteolytic Antigen Cleavage-Mediated AmplificatioN (PACMAN), welche die Isolierung proteolytischer Antikörper aus kombinatorischen Bibliotheken ermöglichen soll. Proteolytische Antikörper unterscheiden sich von herkömmlichen Antikörpern darin, dass sie die einzigartige Fähigkeit besitzen, ihr Antigen nicht nur zu erkennen und zu binden, sondern es auch enzymatisch zu spalten. Dies stellt jedoch eine Herausforderung für die Selektion dar, da proteolytische Antikörper über altbekannte Display-Methoden wie dem Phagen-Display nicht einfach erfasst werden können, da die Antikörper ihr Antigen nach initialer Bindung hydrolysieren und daraufhin wieder dissoziieren. Um diese Herausforderung zu bewältigen, habe ich die PACMAN-Methode entwickelt. Sie soll die Isolierung antigen-spezifischer proteolytischer Antikörper aus kombinatorischen Bibliotheken ermöglichen, indem die Mikrobead-gebundene DNA einzelner Bibliotheksvarianten in pikolitergroßen Wasser-in-Öl-Emulsionen *in vitro* exprimiert wird und anschließend Mikrobeads mit aktiven Bibliotheksvarianten mittels Fluoreszenz-aktivierte Zellsortierung (FACS) detektiert und isoliert werden, falls diese erfolgreich zusätzlich an die Mikrobeads gebundene, doppelt fluoreszent markierte Antigen-Substrate gespalten haben, welche als Reporter dienen. In dieser Arbeit wurde das Prinzip von PACMAN erfolgreich validiert, indem DNA, welche die Tabakmosaikvirus-Protease kodiert, aus einer verdünnten Mischung mit überschüssiger, irrelevanter DNA zurückgewonnen wurde.

Der zweite Schwerpunkt dieser Arbeit liegt auf der Untersuchung der Bildung von Amyloid-β-Oligomeren (AβO) und deren pathophysiologischen Auswirkungen bei der Alzheimer-Krankheit. Das „dimAβ”-Modell, das metastabile AβO bildet, wurde verwendet, um den Einfluss von AβO auf die Fibrillenaggregation, die Biogenese von AβO und ihre Auswirkungen auf neuronale Prozesse selektiv zu untersuchen. Es wurde gezeigt, dass AβO unabhängig von der Fibrillenbildung entstehen und zusätzlich die Proliferation von bestehenden Amyloid-Fibrillen aktiv behindern. Darüber hinaus wurde ein potenzieller *in vivo* Entstehungsweg von AβO entdeckt. Ein leicht saurer pH-Wert von 4,5–5,5, der physiologisch in endolysosomalen Vesikeln

vorkommt, beschleunigte die Bildung von AβO durch $A\beta_{42}$ um etwa das 8.000-fache. Unter diesen Bedingungen wurde die kritische $A\beta_{42}$-Konzentration, welche für die Bildung von AβO erforderlich ist, auf ca. 3 µM verringert. Diese Konzentration wurde in endolysosomalen Vesikeln bereits nachgewiesen. Diese Ergebnisse deuten darauf hin, dass das endolysosomale System möglicherweise einen wichtigen Ort für die *in vivo* Bildung von toxischen AβO darstellt. Schließlich wurde der spezifische Einfluss von AβO auf primäre Mausneuronen untersucht. Die Ergebnisse zeigten, dass AβO an dendritischen Spines binden können und dass Neurone, die AβO ausgesetzt wurden, verringerte spontane Ca^{2+}-Oszillationen aufwiesen. Am interessantesten war allerdings, dass eine deutliche Translokation des Mikrotubuli-assoziierten Proteins Tau von den Axonen der Neurone in ihre somatodendritischen Kompartimente stattfand. Diese Translokation von Tau ist als ein entscheidendes Ereignis während der Pathogenese der Alzheimer-Krankheit bekannt.

Zusammenfassend präsentiert diese Arbeit die Entwicklung der PACMAN-Methode, sowie eine eingehende Untersuchung von AβO und ihrer Rolle im Bezug auf die Alzheimer-Krankheit. Dabei liefert die PACMAN-Methode einen vielversprechenden Ansatz zur Isolation proteolytischer Antikörper gegen Amyloide aus kombinatorischen Bibliotheken, während die gewonnenen Erkenntnisse über die Bildung von AβO und ihre Auswirkungen auf die Fibrillenaggregation und ihr Einfluss auf neuronale Prozesse zu einem tieferen Verständnis der zugrunde liegenden Pathologie der Alzheimer-Krankheit beitragen.

Acknowledgements

Here, I would like to thank and acknowledge all the contributions of my supervisors, coworkers, funding organizations, friends and family who made this thesis possible.

First and foremost, particular thanks is due to Jun.-Prof. Dr. Wolfgang Hoyer, Prof. Dr. Dieter Willbold and Dr. Lothar Gremer, who sufficiently trusted in my project pitch to grant me access to their laboratory facilities and provided supervision to me and my project enabling this PhD thesis. On that note, I also want to express my gratitude towards the Hans und Ilse Breuerstiftung who funded my PhD position.

As this project grew, I acquired further support by winning over Anne Pfitzer who joined on this project as another PhD student and henceforth shared the dreadful ups and downs associated with this project. They say, a sorrow shared is a sorrow halved. In this regards, I would like to thank the Jürgen Manchot Stiftung who provided funding for her position and the project. And on the same note, I would like to thank Anne Pfitzer for her continued effort contributed to the project and joyful entertainment in the lab and office.

Further thanks are due to the many collaborators of this project. I would like to thank Prof. Dr. Gesine Kögler of the José Carreras Stammzellbank and Dr. Erik Lehnert of the central blood donation center as well as Prof. Dr. Markus Uhrberg who helped in the acquisition of a voting from the ethics committee and the acquisition of buffy coat donations. Many thanks to Prof. Dr. Charlotte Esser, Dr. Nadine Teichweyde, Prof. Dr. Ilka Maria Axmann and Dennis Hasenklever for access and support with FACS and flow cytometry.

Thanks to the office crew: Marie Schützmann, Melissa Jansing and Anne Pfitzer for the lively atmosphere and breaks in between the daily grind.

I am thankful for many fruitful discussions and suggestions from Dr. Hamed Shaykhalishahi.

But my utmost gratitude belongs to Lina Marie Raubold who I share my life with. You always backed me up in situations of doubt and picked me up from failed experiments, setbacks and exhaustion. Something I did not believe to be possible,

but you also changed my perspective on a healthy work-life balance. Just know, my life is best when I am with you.

Last but not least, I would like to thank my family who always supported me in my academic endeavors and trusted in the process. I anticipate my academic future to be equally strenuous, but I always know I can trust and build on your support.

List of Publications

Listed are publications to which I have contributed during my doctoral studies:

1. Filip Hasecke †, Tatiana Miti †, Carlos Perez, Jeremy Barton, Daniel Schölzel, Lothar Gremer, Clara S. R. Grüning, Garrett Matthews, Georg Meisl, Tuomas P. J. Knowles, Dieter Willbold, Philipp Neudecker, Henrike Heise, Ghanim Ullah, Wolfgang Hoyer and Martin Muschol — **Origin of metastable oligomers and their effects on amyloid fibril self-assembly.** Chem. Sci., 2018

2. Carlos Perez, Tatiana Miti, Filip Hasecke, Georg Meisl, Wolfgang Hoyer, Martin Muschol and Ghanim Ullah — **Mechanism of Fibril and Soluble Oligomer Formation in Amyloid Beta and Hen Egg White Lysozyme Proteins.** J. Phys. Chem. B, 2019

3. Filip Hasecke †, Chamani Niyangoda †, Gustavo Borjas, Jianjun Pan, Garrett Matthews, Martin Muschol and Wolfgang Hoyer — **Protofibril–Fibril Interactions Inhibit Amyloid Fibril Assembly by Obstructing Secondary Nucleation.** Angew. Chem. Int. Ed., 2021

4. Marie P. Schützmann †, Filip Hasecke †, Sarah Bachmann †, Mara Zielinski, Sebastian Hänsch, Gunnar F. Schröder, Hans Zempel and Wolfgang Hoyer — **Endo-lysosomal Aβ concentration and pH trigger formation of Aβ oligomers that potently induce Tau missorting.** Nat Commun, 2021

† Equal contributions, joint first authorship.

Contents

List of Figures

List of Tables

Abbreviations

aa	amino acids
Aβ	amyloid-β
AβO	amyloid-β oligomer
ACN	acetonitrile
AD	Alzheimer’s disease
AGE	advanced glycation endproducts
APP	amyloid precursor protein
APS	ammonium persulfate
ARIA	amyloid-related imaging abnormalities
BBB	blood-brain-barrier
BCR	B-cell receptor
CAA	cerebral amyloid angiopathy
CDR	complementarity determining region
CF	curvilinear fibril
CNS	central nervous system
COC	critical oligomer concentration
CRAA	covalently reactive antigen analog
CSF	cerebrospinal fluid
DBCO-NHS	dibenzocyclooctin n-hydroxysuccinimide ester conjugate
DFP	diisopropyl fluorophosphat
dimAβ	recombinant dimeric $A\beta_{40}$ construct
DMEM	Dulbecco’s modified eagle’s medium
DMF	N,N-Dimethylformamide
DMII	Diabetes Mellitus type II
DMSO	dimethyl sulfoxide

DTT	dithiothreitol
EDTA	ethylenediaminetetraacetic acid
EGCG	epigallocatechingallat
EMA	European Medicines Agency
emPCR	emulsion PCR
FACS	fluorescence-activated cell sorting
FDA	Food and Drug Administration
FRET	fluorescence resonance energy transfer
Fv	variable fragment domain of antibodies
gO	globular oligomer
GSI	γ-secretase inhibitor
GSM	γ-secretase modulator
HEPES	4-(2-hydroxyethyl)-1-piperazineethanesulfonic acid
HPLC	high-pressure liquid chromatography
HSA	human serum albumin
IgV_2	single-chain antibody composed of two V domains
IMAC	immobilized metal affinity chromatography
IVC	*in vitro* compartmentalization
IVTT	*in vitro* transcription and translation
MCS	multiple cloning site
MHC II	major histocompatibility complex II
NaN_3	sodium azide
NCC	nucleated conformational conversion
PACMAN	Proteolytic Antigen Cleavage-Mediated AmplificatioN
PBS	phosphate buffered saline
PDMS	polydimethylsiloxane
PEG	polyethylene glycole
pL	picoliter
POI	protein of interest
RBS	ribosome binding site
RF	rigid fibril
RP-HPLC	reverse phase high-pressure liquid chromatography

RPM	rotations per minute
scFv	single-chain variable fragment
sdAb	single-domain antibody
TCEP	tris(2-carboxyethyl)phosphine hydrochloride
TEMED	tetramethylethylenediamine
TEV	tobacco etch virus
TFA	trifluoroacetic acid
TGN	trans-golgi network
Th	T helper
ThT	thioflavin T
Tricine	n-tris(hydroxymethyl)methylglycin
Tris	tris(hydroxymethyl)aminomethane
UTR	untranslated region
VH	variable domain of an antibody heavy-chain
VK	variable domain of an antibody kappa light-chain
VL	variable domain of an antibody lambda light-chain
WHO	World Health Organization

1. Introduction

1.1 Amyloid Diseases

A diverse range of pathologies is linked to various amyloid diseases (reviewed in [2]). A non-exhaustive list of amyloid diseases is shown in Table 1.1. As virtually all organs can be affected by some amyloid disease, their symptomatic expressions are equally divers and differ substantially between diseases. Alzheimer's Disease (AD) for instance, as the most reknown amyloid disease, represents the most common form of dementia characterized by progressive decline in cognitive skills and motor function [3–5].

On the other hand, gelatinous drop-like corneal dystrophy affects the eye of a patient. Gelatinous nodules accumulate in the subepithelial space of the cornea leading to severe opacification and loss of vision (reviewed in [6]).

Seminal vesicle amyloidosis manifests as prostatitis, an acute or chronic inflammation of the prostate gland often associated with hematospermia, the presence of blood in the ejaculatory output [7–10].

Furthermore, an amyloid component might also be involved in type 2 diabetes. Here, leading to insulin resistance associated with increased blood sugar levels and a diffuse set of symptoms including polyuria, polydipsia, polyphagia, blurred vision, itchiness, fatigue, nausea and many more [11, 12].

These diseases emphasize the manifold, fundamentally distinct manifestations of amyloid diseases. Yet, the unifying property of these diseases is to be found on the molecular level. In all amyloid diseases, a peptide or protein is abberantly processed and thereby gains the tendency to aggregate. Consequently, a multitude of distinct aggregate species emerge that are resistant to degradation. Oftentimes, these abberant proteinogenic aggregates progressively accumulate forming microscopic deposits in the extra- or intracellular spaces of the affected tissues.

Table 1.1: A non-exhaustive list of amyloid diseases and their associated aggregating peptides or proteins. [1]

Disease	Aggregating protein or peptide
Neurodegenerative diseases	
Alzheimer's disease	Amyloid-β peptide; Tau protein
Tauopathies	Microtubule-associated protein Tau (Tau protein)
Spongiform encephalopathies	Prion protein or its fragments
Parkinson's disease	α-synuclein
Amyotrophic lateral sclerosis	Superoxide dismutase 1
Huntington's disease	Huntingtin fragments
Familial amyloidotic polyneuropathy	Transthyretin mutants
Ageing pituitary, prolactinomas	Prolactin
British familial dementia	ABri
Non-neuropathic systemic amyloidosis	
Amyloid light chain (AL) amyloidosis	Immunoglobulin (Ig) light chains or its fragments
Amyloid A (AA) amyloidosis	Serum amyloid A1 protein fragments
Senile systemic amyloidosis	Wild-type transthyretin
Haemodialysis-related amyloidosis	β2-microglobulin
Lysozyme amyloidosis	Lysozyme mutants
Finnish hereditary systemic amyloidosis	Gelsolin
Renal amyloidosis	Leukocyte cell-derived chemotaxin-2
Non-neuropathic localized amyloidosis	
Apolipoprotein A1 (Apo A-1) amyloidosis	Apo A-1 fragments
Diabetes mellitus Type II	Amylin
Injection-localized amyloidosis	Insulin
Atrial amyloidosis	Atrial natriuretic factor
Medullary carcinoma of the thyroid	Calcitonin
Aortic medial amyloidosis	Medin
Gelatinous drop-like corneal dystrophy	Lactotransferrin
Pulmonary alveolar proteinosis	Pulmonary surfactant-associated protein C
Lichen amyloidosis and Macular amyloidosis	Galectin 7
Hypotrichosis simplex of the scalp	Corneodesmosin
Seminal vesicle amyloidosis	Semenogelin-1

The plethora of pathological processes triggered by these aggregates is similarly diverse as their symptomatic expressions. Acute cytotoxicity, activation of inflammatory immune responses and disturbance of cellular homeostasis pathways are among the list.
In the following sections AD and its pathophysiology will be discussed in more detail.

1.2 Alzheimer's Disease

Alzheimer's Disease, as the most reknown amyloid disease, was first described by Dr. Alois Alzheimer in 1906 [3]. In 1901, Dr. Alzheimer performed a long-term study on his patient Auguste Deter who presented a paranoid symptomatology with increasing intensity — experiencing sleep disorders, disturbances of memory, aggressiveness, crying, and progressive confusion. After the death of his patient in 1906 he performed an autopsy and noticed an evenly atrophic brain with arteriosclerotic changes to the vasculature and prominent lesions scattered throughout her brain tissue. These lesions are now famously known as senile plaques and neurofibrillary tangles.

Since the discovery of AD the number of affected individuals continually rose concomitantly with our aging society and viciously gained notoriety as a devastating and deadly disease. According to the World Health Organization (WHO) 55 million people worldwide were diagnosed with dementia in 2020 [13]. The numbers were projected to reach 150 million by 2050 [14], which will, on top of the interpersonal tragedies, load a substantial burden on public healthcare systems and nursing home capacities. To this day, no effective treatment against AD is available. This emphasizes the need for in-depth investigations into the pathophysiology of the disease and the need to develop effective treatments to alleviate its symptoms or possibly cure or prevent the manifestation of the disease.

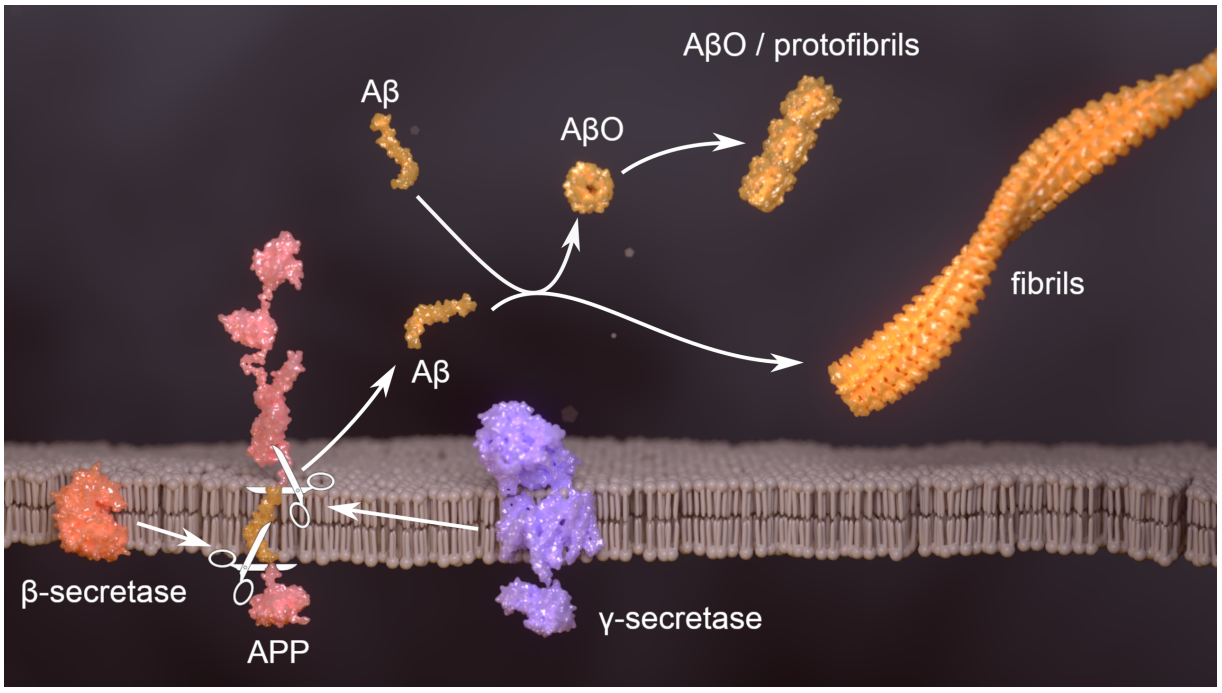

Figure 1.1: Processing of the Amyloid Precursor Protein (APP): The amyloidogenic pathway. The amyloidogenic pathway describes the proteolytic cleavage of the membrane protein APP by β- and γ-secretase resulting in the release of Aβ which proceeds to aggregate into oligomers, protofibrils and fibrils.

1.2.1 Pathophysiology of Alzheimer's Disease

AD is defined as an amyloid disease with the Amyloid-β (Aβ) peptide and the microtubule-associated protein Tau being responsible for the formation of the characteristic lesions observed in the diseased brain tissue.

Aβ originates from sequential, proteolytic cleavage of the Amyloid Precursor Protein (APP). APP is a single-pass transmembrane protein that resides in the outer cell membrane of neurons and might act as a receptor regulating neuronal survival, cell adhesion, neurite outgrowth and synaptic plasticity [15–17] . Furthermore, APP underlies dualistic proteolytic processing which results either in secretion of a soluble APP fragment that acts as a receptor ligand [18] or secretion of the amyloidogenic Aβ peptide [19]. APP processing and Aβ production takes place in the ER and Golgi/TGN during vesicular transport of APP to the cell membrane [20]. Additionally, Aβ is also

proposed to be produced within endo-/lysosomal compartments after reinternalization of APP during homeostatic recycling processes [21, 22]. The amyloidogenic cleavage is facilitated by β- and γ-secretase excising and releasing the Aβ peptide, while the non-amyloidogenic cleavage involves α-secretase instead of β-secretase [19] (see Figure 1.1). There is a certain leeway in the cleavage performed by γ-secretase leading to the production of Aβ isoforms of 36–43 amino acid residues in length [23]. The most abundant isoforms are $A\beta_{1\text{-}40}$ and $A\beta_{1\text{-}42}$, while the latter is considered more pathogenic and its abundance in AD patients is increased. Nevertheless, the exact insults leading to Aβ accumulation and eventually AD are still elusive, however the most widely accepted hypothesis on the origin of AD states that either overproduction or reduced clearence of Aβ leads to its accumulation in the cortex eliciting toxicity and ultimately leading to AD [24].

After production of Aβ (especially $A\beta_{1\text{-}42}$), it proceeds to aggregate, forming a plethora of distinct structures including soluble oligomers [25–27], fibrils [28–30] and eventually senile plaques which are dense Aβ-rich foci found in the cortex that further include co-deposition of complement proteins, clusterin and ApoE, they are modified by ubiquitination and advanced glycation endproducts (AGE) and are surrounded by microglia and reactive astrocytes [31–33]. All of these Aβ agglomerates are believed to excert neurotoxicity and to ultimately lead to the progression of AD. Nevertheless, there is a lively debate on the disease-relevance and the extent of toxicity attributable to specific aggregate species [34–40]. Currently, small soluble Aβ oligomers (AβO) are considered as the main culprit driving AD pathology. Some hypothesized that Aβ fibrils, in contrast to AβO, may act as a sink by sequestering soluble Aβ species into an insoluble form and thereby attenuating their toxicity [41, 42].

The mechanism of AβO toxicity is still a matter of debate. AβO were suggested to trigger toxicity by ligand-like binding to several receptors [43, 44]. Due to the multivalency of AβO, candidate receptors might cluster and hence erroneously activate pathological signaling cascades [45–48]. AβO were observed to preferentially cluster at dendritic spines which degenerate after prolonged exposure [49]. Furthermore, AβO hamper long-term potentiation [50, 51], induce oxidative stress [52, 53], plasmamembrane damage [54], endoplasmic reticulum stress [55], mitochondrial

dysfunction [55], neuroinflammation [56–60], and facilitate Tau missorting into the somatodendritic compartment paired with Tau hyperphosphorylation which leads to microtubule destabilization [31, 43, 56, 61–67]. Tau missorting is one of the first hallmarks of tauopathies and its induction by AβO might present a link in the Aβ-Tau axis in AD pathogenesis. Nevertheless, further details on the Tau aspect of AD pathogenesis is beyond the scope of this thesis.

The notion that Aβ aggregation and deposition in the brain parenchyma and downstream induced pathology constitutes the prime insult leading to AD was coined by John Hardy as the Amyloid Cascade Hypothesis [68] in 1992. Since then, the majority of AD research focused on advancing our understanding of Aβ pathogenesis and means to eliminate Aβ from the diseased brain. In the following section, an overview of current advances in Aβ-targeting therapeutics as well as pitfalls are presented.

1.3 Strategies to mitigate disease pathology

Since the discovery of AD, there has been a hunt for therapeutic medications to treat AD patients. Most of these aimed to remove or reduce the amount of Aβ in AD patients. In the recent years, the amount of clinical studies performed on AD therapeutics has surged, but unfortunately, virtually none of them made it to the clinic [69–72]. Due to the complexity of AD, increasingly divers mechanisms of action are being persued by AD therapeutics.

Among the earliest strategies was the utilization of the immune system to remove Aβ. This was intended to be achieved either by active immunization (i.e. vaccination against Aβ) or passive immunization by providing biologics, mostly in the form of monoclonal antibodies, that bind Aβ or its aggregates and recruit the patients' immune system to ultimately eliminate them [73–75].

Another persued approach is the modulation of specific enzymes that are involved in the production of Aβ. Specifically, small molecules have been and are still being developed to inhibit or modify the activity of β- or γ-secretase and thereby reduce the amount of toxic Aβ production [76].

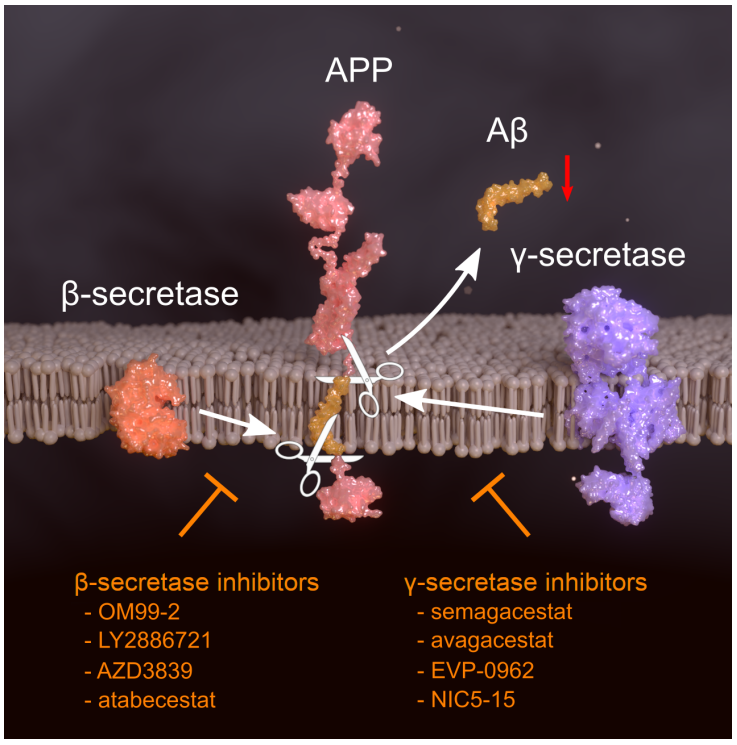

Figure 1.2: Disease mitigation by β- and γ-secretase inhibitors and modulators. Using compounds that specifically inhibit or modulate the activity of β- or γ-secretase, the production of Aβ shall be reduced. Either less APP is processed via the amyloidogenic pathway or APP cleavage is modulated to produce preferentially the shorter, less toxic Aβ variants rather than the longer, more toxic variants.

A more recent trend is the strategy to develop means to inhibit individual aggregation processes of Aβ or Tau fibrillization or oligomerization [77–83].

The following sections will provide an overview on current trends in therapeutic development and elaborate on obstacles faced on their way.

1.3.1 Modulation of Aβ production

A large portion of therapeutic research resides around the development of inhibitors or modulators of β- or γ-secretase activity. The rationale is the assumption that reduction of β- and γ-secretase activity might attenuate Aβ production [84] (see Figure 1.2).

In 2000, the first β-secretase inhibitor OM99-2 has been developed [85], proving

the feasibility of reducing Aβ production by inhibiting β-secretase. However, OM99-2 and several successor compounds were peptidomimetic inhibitors with relatively large molecular sizes which unfortunately eliminated their chances for applicability *in vivo* due to short half-life, deficiency in blood-brain-barrier (BBB) transmissibility and low oral availability [86]. Consequently, the next generation of β-secretase inhibitors were derived from high-throughput screenings of small molecule libraries with improved pharmacokinetics. This led to the development of compounds like Verubecestat (Merck)[87], LY2886721 (Eli Lilly)[88], AZD3839 (AstraZeneca)[89], atabecestat (JNJ-54,861,911, Janssen)[90], and lanabecestat (AZD3293, LY3314814, AstraZeneca and Eli Lilly)[91, 92]. These compounds proved to be effective in reducing Aβ levels in brain and cerebrospinal fluid (CSF), not only in animal models, but also in human clinical trials. Nevertheless, all clinical trials were discontinued due to lack of clinical benefit [93, 94]. Quite contrary, a significant cognitive worsening was reported associated with verubecestat and atabecestat [95–97]. A recurrent theme was detrimental liver toxicity induced by the inhibitors owing to β-secretase also being active in the liver and other organs exhibiting a crucial role governing and executing signaling pathways and enzymatic reactions [76].

At the same time, development of γ-secretase inhibitors (GSIs) and later γ-secretase modulators (GSMs) has been persued as well. Initial attempts included substrate-based GSIs that competitively bound to the binding site of APP. Of these, semagacestat (Eli Lilly) was one of the most sophisticated compounds which was advanced into a phase III clinical trial [98]. However, the trial was terminated before completion due to severe toxicity and increased risk of skin cancer and infections. Participants presented broad alterations to their immune system with reduced counts of CD19+ T cells and monocytes, and eosinophilia. But also cognitive worsening, renal and hepatic changes, increased QT intervals, and weight loss was observed [98, 99]. However, this clinical worsening might easily be explained accounting for the fact that more than 90 γ-secretase substrates, beyond APP, are known [100, 101], including Notch, a cardinal key receptor of highly conserved cell-cell-communication pathways, most reknown for its involvement in embryonic development, but also in renewal and maintenance of most adult tissues [102].
To overcome these adverse effects, ”notch-sparing” GSMs were developed that

should not interfere with γ-secretases' physiological Notch processing. Merely its cleavage activity excerted on APP should be altered, aiming to shift its cleavage site preference towards Aβ38 production, away from Aβ42 [103–105]. EVP-0962 (FORUM Pharmaceuticals Inc.), a small-molecule GSM that was shown to selectively modulate γ-secretase activity in preclinical trials [106], was advanced into a human phase II trial, but discontinued in 2016 [70, 107]. In 2013, Humanetics Corporation was enrolling 40 patients with mild to moderate AD in a second single-site phase IIb study with their GSM compound NIC5-15 (a natural compound, also called pinitol) but no results have been published [108, 109]. To date, clinical trials on GSIs and GSMs similarly to β-secretase inhibitors dampened enthusiasm for their therapeutic applicability.

As framed by Bart De Strooper [110], there is a 'critical knowledge gap in γ-secretase pharmacology'. With failed clinical trials stacking up, it became evident that there is a glooming lack of understanding on the complex physiological interconnections and enzymatic pathways involving β- and γ-secretase. This is further aggravated by our appalling ignorance concerning the structural biology of γ-secretase which limits our ability to develop precise and safe GSMs. Much more research would be necessary to safely derive beneficial effects for AD patients without disturbing the yet inscrutable, but vital, physiological processes exhibited by β- and γ-secretase.

1.3.2 Aggregation inhibitors

Aβ self-assembly is governed by distinct kinetic processes [123]. Primary nucleation describes the initial step of Aβ fibril formation in which a few Aβ monomers assemble into a growth-competent nucleus, a prerequisite and seed for further fibril formation. Elongation is an addition process of Aβ monomers to fibril ends leading to fibril growth. Secondary nucleation describes the catalytic production of new fibril nuclei by template-dependent conversion of Aβ monomers into nuclei via interaction with fibril surfaces. Secondary nucleation-derived oligomeric fibril nuclei were suggested to represent a potent neurotoxic agent in AD [124–127]. Yet another mode of Aβ self-assembly yields neurotoxic AβO which are off-pathway to fibril formation [128, 129].

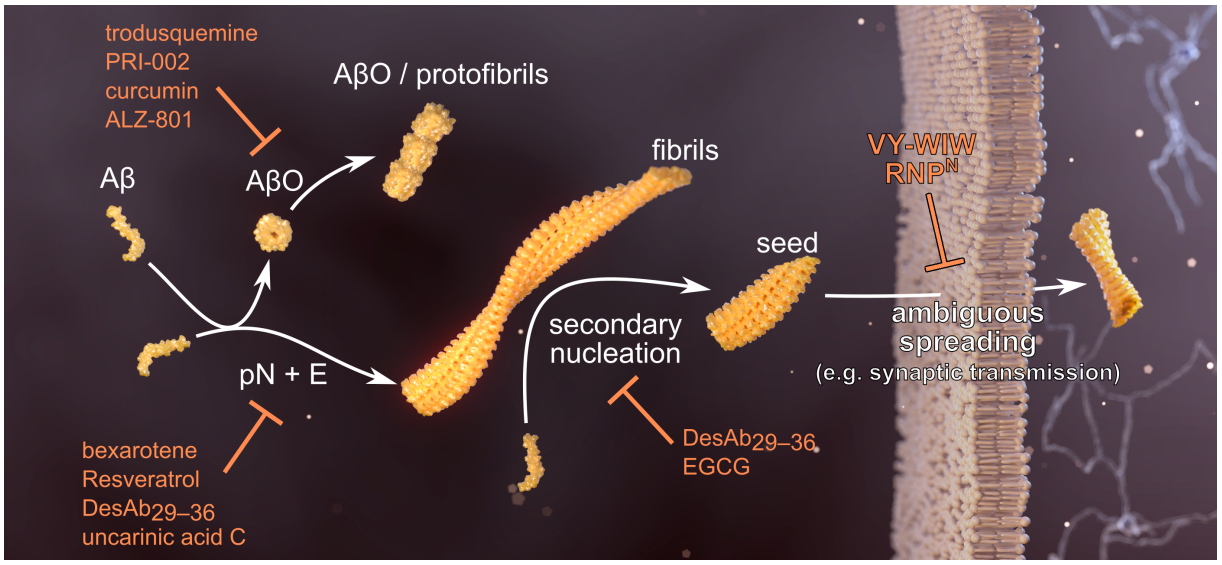

Figure 1.3: Overview of a selection of small molecule inhibitors of Aβ aggregation. PRI-002 [111], curcumin [112], ALZ-801 [113, 114] and trodusquemine [115] are compounds believed to prevent oligomerization or shift oligomers into a non-toxic state. Bexarotene [116], Resveratrol [117], $DesAb_{29\text{-}36}$ [118] and uncarinic acid C [119] either prevent primary nucleation or elongation of Aβ fibrils. EGCG [120] and $DesAb_{29\text{-}36}$ [118] were shown to hamper secondary nucleation processes. VY-WIW [121] and RNP^{N} [122] were proposed to prevent ambiguous spreading events (e.g. synaptic transmission) of Aβ aggregates. pN, primary nucleation and E, elongation.

All these assembly mechanisms might represent potential targets for disease-modifying therapeutic interventions (see Figure 1.3). Many groups developed small molecules or screened natural compound libraries for inhibitors targeting individual Aβ aggregation mechanisms [130, 131].

In the latter category, several natural compounds repeatedly lived through hypes as potential cures for AD and gained popularity in public media but also in scientific literature. Albeit the therapeutic potential of these compounds was regularly, comically exaggerated. Curcumin, for example, was hailed as an all-round, natural, miracle cure interfering with Aβ oligomerization, fibrilization and plaque formation as well as promoting disassembly of Aβ aggregates, while also acting as an anti-inflammatory, anti-oxidant, anti-proliferative, anti-atherosclerotic and anti-arthritis compound [112, 132]. Nevertheless, clinical studies on curcumin failed to derive any positive effects in AD patients [133]. A similar story unfolded around Resveratrol [134], a compound found in the skin of grapes and red wine. This case was

particularly grim, as Resveratrol further aggravated brain volume loss in recipients as compared to placebo group in a phase II study [134]. Another compound, Epigallocatechingallat (EGCG), found in green tea, was anticipated to inhibit secondary nucleation and entered clinical trials in 2009, but any publications on results are still pending [135].

On the other hand, there are also highly sophisticated, tailor-made aggregation inhibitors that might stand a chance in clinical trials. The most promising candidates aim to shift toxic AβO towards non-toxic conformers or to disassemble them entirely. Among these, ALZ-801 [113, 114] and PRI-002 [111] are currently persuing promising phase III and phase II clinical trials, respectively.
Another set of inhibitors specifically target isolated fibril aggregation mechanisms. These compounds target fibril elongation, secondary nucleation or synaptic propagation individually. Compounds include: Bexarotene [116], $DesAb_{29\text{-}36}$ [118], VY-WIW [121] and RNP^{N} [122], but most are still in the preclinical stage.
Nevertheless, it remains to be elucidated which exact aggregation mechanisms relevantly contribute to AD pathology and therefore pose worthwhile therapeutic targets. Furthermore, aggregation inhibitors need to be administered with sufficient caution as unanticipated liberation of Aβ from aggregates might provide substrate for toxic oligomer formation *in vivo*. Let alone shifting AβO into alternative conformers might pose unforeseen adverse effects, considering research on AβO is still a highly dynamic area with many unknowns.

1.3.3 Immunotherapy

Immunotherapy describes a set of medical interventions that utilize the abilities of the host's immune system or components thereof (e.g. antibodies) to mitigate a disease's pathology. In the context of AD, active and passive immunization are the most intensively persued immunotherapeutic strategies [72, 136, 137]. In active immunization the aim is to train the immune system to recognize and eliminate the amyloidogenic agents involved in AD by vaccination. Therefore, the immune system is confronted with prominent epitopes from an amyloid antigen, typically coupled to a protein carrier and mixed with adjuvants to provoke a proper immune

response with immune memory formation directed against the amyloid antigen. The benefit of active immunization is that after successful establishment of an immune response, the immune system should henceforth be equipped with the means to eliminate amyloid antigens on its own without the necessity for further, regular drug applications, which is a major drawback of virtually all other therapeutic approaches.

The first attempt of an anti-Aβ vaccine was AN1792 (JANSSEN & Pfizer) that enrolled in a clinical phase II trial in 2001 [138]. AN1792 utilized a synthetic full-length $A\beta_{1\text{-}42}$ peptide coupled to a saponin-based adjuvant as the immunogen. It was able to provoke the desired immune response with robust antibody production. These antibodies were able to target and reduce Aβ plaque burden by solubilization and efflux of Aβ through the perivascular pathway. Furthermore, a reduction in hippocampal Tau pathology was noted. Unfortunately, the phase II study had to be terminated, despite these positive effects, due to severe, adverse inflammatory reactions. 6% of the participants elicited sterile meningoencephalitis attributed to infiltration of the brain parenchyma by proinflammatory T-lymphocytes. It was later determined that T helper (Th)-1 cells, upon immunization, became reactive to the C-terminal and central regions of Aβ resulting in unanticipated autoimmunity [139, 140].

Subsequent active immunization strategies omitted these T-lymphocyte-reactive regions and focused on N-terminal B-cell epitopes. Some of the next-generation active anti-Aβ vaccines are listed in Table 1.2. So far, most clinical trials were unfortunately terminated prematurely due to adverse effects or inefficiency and none of them were approved, yet.

On the other hand, by far the most research, but also hope, went into the development of passive immunization as a means to treat AD [137]. In passive immunization, purified polyclonal or monoclonal antibodies specific to Aβ or its aggregates are administered to the patient in hopes to facilitate removal. The anticipated mechanisms of action are quite versatile. Anti-Aβ antibodies administered to the peripheral blood stream are believed to scavenge soluble Aβ from the blood stream reducing the Aβ concentration in the periphery. This is anticipated to create an increased Aβ concentration gradient across the blood-brain barrier, shifting Aβ equillibrium and

Table 1.2: Anti-Aβ vaccines in clinical trials

Drug	Composition	Clinical trial status	References
ACC-001 (Janssen)	$A\beta_{1\text{-}7}$ coupled to CRM197 and QS-21	Halted in phase II due to inefficacy	[141–143]
AD01 (AFFiRiS AG)	$A\beta_{1\text{-}6}$ mimic with Alum adjuvant	Phase I trial completed	[144–147]
AD02 (AFFiRiS AG)	$A\beta_{1\text{-}6}$ mimic with Alum adjuvant	Phase II trial terminated due to inefficacy	[144, 145, 148]
AD03 (AFFiRiS AG)	Pyroglutamate-Aβ with Alum adjuvant	Terminated due to organizational reasons	[144, 145]
ACI-24 (AC Immune SA)	Tetra-palmitolated $A\beta_{1\text{-}15}$ locked in β conformation by incorporation into liposome membranes	Phase I completed, phase IIa withdrawn (decision to proceed with an optimized study design and optimized vaccine formulation)	[149–151]
CAD-106 (Novartis)	$A\beta_{1\text{-}6}$ coupled to 180 copies of the bacteriophage QB coat protein	In phase II/III	[152, 153]
Lu AF20513 (Lundbeck, Otsuka Pharmaceutical Co., Ltd.)	$A\beta_{1\text{-}12}$ attached to Th epitopes of P2 and P30 from tetanus toxin	Terminated, no outcomes published yet	[154, 155]
UB-311 (United Neuroscience)	$A\beta_{1\text{-}14}$ coupled to CpG and Alum as adjuvants	In Phase II	[156, 157]
V-950 (Merck Sharp & Dohme Corp.)	$A\beta_{1\text{-}15}$ coupled to Alum/ISCOMATRIX	Halted after phase I for unknown reasons	[158]

consequently inducing enhanced efflux of Aβ into the periphery, where it is subsequently again sequestered by the antibodies and removed by endogenous degradation pathways (e.g. the liver). This ultimately results in progressive Aβ drainage from the brain. This concept was coined 'peripheral-sink hypothesis' (see Figure 1.4) [159–162].

In addition, a small portion of the antibodies were shown to enter the brain through receptor-mediated transcytosis [163]. Subsequently, these antibodies are believed to engage Aβ aggregates *in situ*, either resulting in their active disassembly or their opsonization, recruiting microglia through Fc-domain recognition. After microglia bind to these antibody-Aβ immune complexes, uptake is facilitated via receptor-mediated phagocytosis and elimination through the endo-/lysosomal system is commenced [164–168].

Table 1.3: Anti-Aβ monoclonal antibodies in clinical trials

Drug	Isoform and target	Clinical trial status	References
Bapineuzumab (Janssen, Pfizer)	humanized IgG1 monoclonal antibody targeting N-terminal $A\beta_{1\text{-}5}$	Terminated in phase III due to inefficacy and adverse effects	[169–172]
Ponezumab (Pfizer)	humanized IgG2 monoclonal antibody against the C-terminus of $A\beta_{40}$	Halted after two phase II studies revealed inefficiency	[173–175]
Solanezumab (Eli Lilly)	humanized IgG1 monoclonal antibody selective for $A\beta_{16\text{-}26}$	Failed in phase III as primary endpoints were not met	[176–178]
Crenezumab (AC Immune SA, Genentech, Hoffmann-La Roche)	human IgG4 monoclonal antibody engineered from a mouse antibody against pentameric Aβ oligomers, plaques and fibrils	Failed in phase II. No cognitive or clinical benefit, but adverse effects like ARIA-H. Nevertheless, a phase III study is conducted on prodromal-to-mild AD patients	[179–182]
Donanemab (Eli Lilly & Co)	humanized IgG1 monoclonal antibody derived from mouse antibody mE8-IgG2a, selective for pyroglutamate Aβ(p3-42). It is aimed to specifically target plaques	In phase II/III	[183, 184]
Ganterenumab (Chugai Pharmaceutical Co., Ltd., Hoffmann-La Roche)	human IgG1 monoclonal antibody against Aβ fibrils	In phase II until 2023. But another phase II/III trial failed to meet primary endpoints	[185–187]
Aducanumab (Biogen)	human IgG1 monoclonal antibody selective for $A\beta_{3\text{-}7}$ and aggregates	FDA approved, in phase IV	[114, 188–191]
Lecanemab (Biogen, Eisai Co., Ltd.)	humanized IgG1 monoclonal antibody against large soluble Aβ protofibrils	In phase III until 2024. First promising results published	[192–194]

The first monoclonal antibody developed against Aβ was bapineuzumab, a humanized IgG1 antibody targeting the N-terminus of Aβ ($A\beta_{1\text{-}5}$) [169]. This antibody was developed after AN1792 was terminated and subsequent analyses revealed that targeting N-terminal regions of Aβ might be regarded as a safer epitope, reducing undesirable inflammatory responses. Bapineuzumab entered clinical trials and was advanced into multiple phase III studies. Unfortunately, these had to be

terminated owing to severe adverse reactions including amyloid-related imaging abnormalities (ARIA) edema and ARIA-hemorrhages [169–172].

In the past 15 years, several successor antibodies were developed and advanced into clinical trials targeting virtually all thinkable epitopes and conformers of Aβ (see Table 1.3). ARIA-related adverse side-effects were recurrently observed in all trials, albeit to different extent for each antibody. Owing to the plethora of trials performed so far, a sophisticated model of the drug-induced pathophysiology leading to these adverse effects was derived (see Figure 1.4) [195, 196]. A prominent effect during immunotherapy efforts was the relocalization of Aβ from the brain's parenchyma to the vasculature [188, 197, 198]. It was suggested that increased antibody-mediated efflux of Aβ — especially when Aβ fibrils were targeted — facilitated trapping of Aβ within capillary vessel walls and linings promoting cerebral amyloid angiopathy (CAA). Deposits of Aβ aggregates within vascular vessel walls were suggested to then further sequester even more Aβ by continued aggregation. Concomittantly, a continued influx of anti-Aβ antibodies engage the trapped Aβ leading to further accumulation of Aβ and antibodies in the vessel walls initiating a proinflammatory feedback loop leading to therapy-induced exacerbation of CAA [195, 197, 198]. Chronic CAA-related inflammation in the vicinity of the vasculature increases vulnerability to vasogenic edema, microhemmorhages, damage to and leakage of the BBB and defective blood supply [199, 200].

Another detrimental implication regarding anti-Aβ passive immunotherapies is resolubilization of insoluble Aβ aggregates promoting AβO formation [201–204]. This effect was dubbed the "dust-raising effect" [201]. Mobilization of Aβ from well-established plaques transforms relatively inert, localized deposits into highly neurotoxic agile pathogens. This effect was particularly impressive in the vaccination studies of AN1792, which drastically reduced plaque burden, but increased soluble Aβ concentration which was conspicuously harmful and aggravated brain volume loss [205].

Furthermore, antibodies targeting the N-terminal sequence of Aβ, were shown to bind APP off-target, which interestingly enhanced Aβ production, possibly by initiation of endocytosis and subsequent proteolytic degradation of the APP-antibody complex [206, 207]. This effect might therefore be anticipated for antibodies like

bapineuzumab, ganterenumab and aducanumab which all target the N-terminal regions of Aβ [208]. Further, when acknowledging that certain antibodies are able to bind to APP on neuronal membranes via the exposed N-terminal Aβ sequence, it would be negligent to dismiss the consequential risk of imminent Fc-domain-mediated immune attacks on neurons, that are decorated by these antibodies. Furthermore, an over-the-top precarious situation culminates in the already inflamed cerebral milieu by additional cues from the Fc-region of the administered anti-Aβ antibodies. Once an antibody has bound to its Aβ antigen, its Fc-domain shifts conformation and becomes receptive to Fc receptors [209]. Many immune cells express and present Fc receptors and are thereby able to detect these immune complexes, which triggers activation upon binding. Thereby, antibody-Aβ immune complexes elicit a broad proinflammatory mediator function, which leads to activation of immune cells, including microglia, prompting release of proinflammatory cytokines and chemokines [165]. Another mediator function of the antibodies, anticipated in this context, is complement protein recruitment and activation which further promotes central nervous system (CNS) inflammation [210, 211]. Altogether, these complications might collectively explain the adverse effects and poor efficacies seen in clinical trials.

Despite the aforementioned shortcomings of passive immunization, currently the most promising candidate to root for is lecanemab. Lecanemab primarily targets protofibrillar Aβ, which is considered to be the most potent neurotoxic agent in AD. To a lesser degree lecanemab binds to plaques and fibrils. A phase IIb study with 28 patients receiving the highest dose of 10 mg/kg, biweekly, revealed a promising 47% reduction in progression of cognitive decline and a 93% reduction in brain amyloid, while merely 10% of the participants experienced ARIA-related adverse events [192]. Just recently, first results of a phase III study of lecanemab underscored its promising potential [194]. In an 18 month trial with 1795 participants 50 to 90 years of age with early AD, lecanemab slowed cognitive decline by 27% compared to placebo, albeit incidents of adverse events were observed more frequently compared to its phase IIb study. 12.6% of the participants experienced ARIA-edema and 17.3% ARIA-hemorrhages. These were exciting news, but the optimism was met by caution, as safety concerns remain and need to be addressed in extended trials

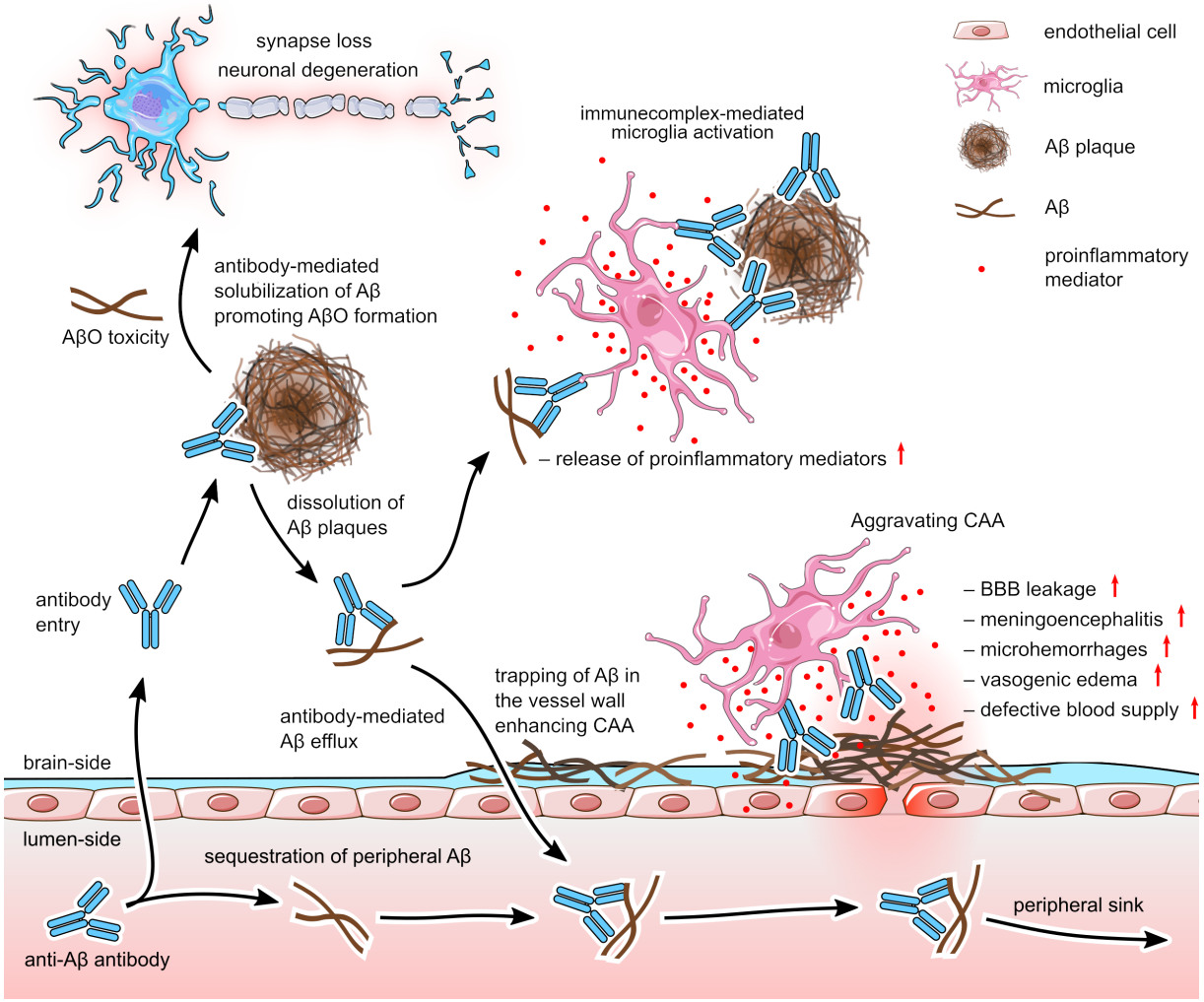

Figure 1.4: Anticipated beneficial impact of anti-Aβ passive immunization and mechanisms of adverse antibody-mediated effects. Microglia and neuron sprites were adapted from Servier Medical Art. Servier Medical Art by Servier is licensed under a Creative Commons Attribution 3.0 Unported License (https://creativecommons.org/licenses/by/3.0/).

[212, 213]. Nevertheless, these results once more signify the disease-relevance of protofibrillar AβO and strengthen the call for in-depth investigations into their pathophysiology.

Another special case is aducanumab which deserves to be mentioned separately. Aducanumab is a human monoclonal IgG1 antibody targeting aggregated Aβ, which was originally developed by Neurimmune and later advanced by Biogen into successful phase I and II studies suggesting cognitive benefit in AD patients.

But in 2019, two almost identical phase III clinical trials were shut down prematurely, as a futility analysis by an independent monitoring committee could not detect a beneficial effect in patients. Beyond, 41.3% of the participants receiving the highest dose of aducanumab experienced ARIA, 35.2% ARIA-edema, 19.1% ARIA-microhemorrhage and 14.7% ARIA–superficial siderosis which raised serious safety concerns [189, 214].
Nevertheless, Biogen later reported, upon reanalysis of their datasets, that participants receiving the highest dose of aducanumab in one of the two trials showed a slight slowdown of cognitive decline. Biogen then applied for approval by the U.S. Food and Drug Administration (FDA) and indeed became the first approved drug that claimed to treat the underlying pathophysiology of AD and to slowdown its progression.

1.3.3.1 Aduhelm: a backlash unfolds

Aduhelm, the brand name of aducanumab, became an increasingly controversial topic in the AD field and beyond. On 7th June 2021, the FDA gave the green light for the marketing authorization of Aduhelm utilizing an accelerated approval pathway. This requires Biogen to confirm the efficacy and benefit of Aduhelm in a follow-up phase IV study. But, this whole process was remarkable, as this approval was granted despite the almost unanimous advise against the approval by the FDA's scientific advisory committee.

> *"Ten voted against and one was uncertain." — The New York Times* [215]

The events following the approval were nothing shy of a thriller. On June 11th, three FDA advisors resigned over the approval, on June 25th, two Congressional House committees launched joint investigations into the approval process, on July 9th, the FDA's acting commissioner requested an independent investigation, on August 4th, investigations by the Department of Health and Human Service were launched [216, 217]. Entanglements of Biogen and FDA individuals were uncovered and are further discussed in [216, 218].
On top of this political fiasco, as Aduhelm is now effectively approved, clinicians are

now facing difficult discussions and decisions with patients and their families regarding the vague promise of clinical benefit, but potentially severe side-effects and the high costs associated with Aduhelm. Annual costs for the drug itself were initially listed at 56.000 US$, but were later reduced to 28.200 US$ due to public outrage. This does not yet include costs for mandatory periodic follow-up MRI scans and hospital stays. This further raised questions about equity and affordability. Aduhelm was also picked up as a strengthening argument to push for reforms on drug pricing legislations in the US.

In response to these uncertainties, the European Medicines Agency (EMA) refused a marketing authorization for Aduhelm in europe [219].

Heretofore, passive immunization with monoclonal antibodies, like aducanumab, unfortunately still constitutes our ray of hope to tackle AD, despite the off-putting risk benefit ratios, precarious side-effects and incomprehensible, trust deteriorating regulatory decision rulings. But, we have to admit that after all these iterations of monoclonal anti-Aβ antibodies entering clinical trials and not or barely succeeding, although targeting virtually all possible epitopes and conformers of Aβ (see table 1.3), chances of a breakthrough game-changer are exhausted. Negative side-effects (see Figure 1.4) appear to render these therapeutic applications futile or at least ineffective. In my opinion, it is time to lay conventional antibodies against Aβ to rest and approach novel techniques.
Unfortunately, all these accumulated failed iterations also came with another caveat: No return on investments. After repeated loss of investments, as clinical trials were terminated, investors are now increasingly reluctant to invest in AD therapeutics. Pfizer, for example, called it quits on Alzheimer's and Parkinson's research, entirely [220]. Consequently, novel developments will have a hard time and will have to increasingly rely on public financial support or might not be able to advance into clinical phases at all.

But, if one positive learning could be derived from aducanumab and more recently lecanemab, it would be the first indications that reduction of Aβ in AD patients might actually yield a beneficial effect, if not masked by the inflicted additional burden attributable to the negative side-effects of the drug itself. Reinforced by these

findings, I want to shed some light onto a novel, potential therapeutic approach that might surpass its predecessors by avoiding the aforementioned negative side-effects while yet improving the anticipated Aβ clearing effect.

1.4 Proteolytic antibodies

To ease the mood of the previous sections, let me introduce a refreshingly ingenious avenue that might resolve the aforementioned shortcomings of conventional antibody therapeutics and might represent a worthwile addition to our therapeutic repertoire against amyloid diseases.

Catalytic antibodies, i.e. proteolytic antibodies with an inherent ability to hydrolyse their antigen [221]. These antibodies would instead of merely binding to their antigen, cleave it and release hydrolysis products. In the case of Aβ, these hydrolysis products are believed to be inert in terms of amyloidogenic potential [222, 223]. Furthermore, proteolytic functionality might resolve virtually all shortcomings of conventional antibody immunotherapeutics as observed in clinical trials by: (1) Elimination of antibody-Aβ immune complex-induced activation of microglia, as no stable immune complexes are formed at any point. Antibody-Aβ contact is merely transient due to cleavage-mediated antigen release. (2) Circumvention of microglial uptake to get rid of Aβ aggregates. Once the proteolytic antibodies engage Aβ it would be hydrolysed on the spot, no need for microglial uptake of aggregates. (3) Increase in clearance efficiency, as proteolytic antibodies are not consumed once an Aβ molecule is hydrolysed, as is the case for conventional antibodies which upon antigen binding are eliminated alongside their bound antigen by microglial uptake or clearance by the liver. Contrary to that, proteolytic antibodies can engage an Aβ molecule, cleave it and then continue to eliminate further Aβ molecules (see Figure 1.5). Therefore, one proteolytic antibody might eliminate ten thousands of Aβ molecules during its lifetime. Consequently, they might not only drastically increase the efficiency of Aβ clearance, but could possibly reduce the necessary amount of antibody to be administered in therapy. (4) Sparing of the BBB from aggravating CAA, owing to the mode of action of proteolytic antibodies. Neither Aβ aggregates would be shuttled through the BBB nor antibodies would be trapped in the vessel

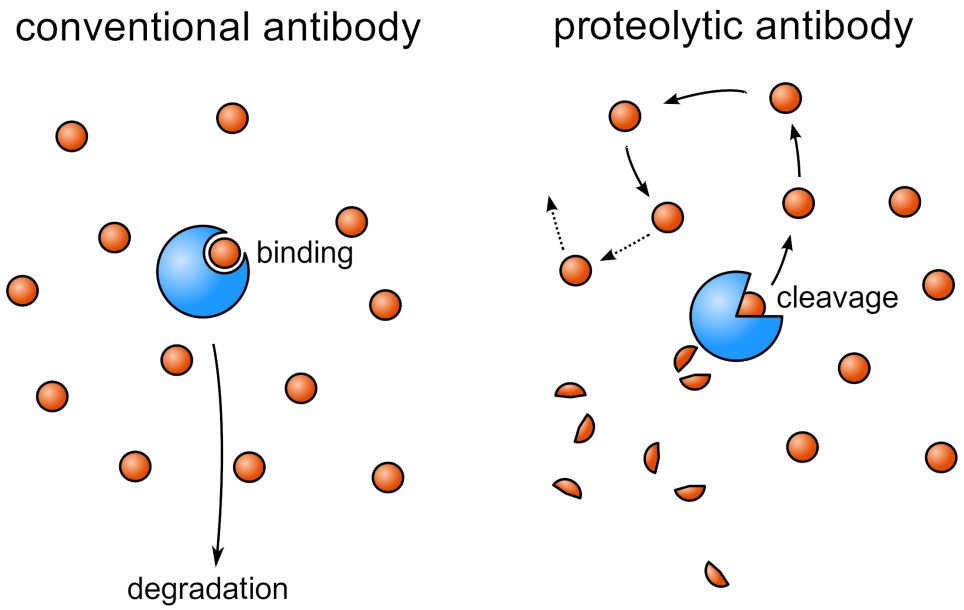

Figure 1.5: Increased efficiency anticipated for proteolytic antibodies. A conventional antibody may bind one or two antigens before being degraded alongside its bound antigen. On the other hand, a proteolytic antibody is not consumed when hydrolysing an antigen. Therefore, proteolytic antibodies might successively cleave thousands of antigens and thereby drastically increase clearance efficiency and might reduce necessary therapeutic doses.

linings. Quite the opposite, Aβ in proximity to the vasculature would possibly be among the first to be cleared by the catalytic action of the proteolytic antibodies, which would attenuate CAA. (5) Proteolytic antibodies act independent of endogenous, homeostatic degradation pathways. Protein homeostatic maschinery is already impaired in AD and in the case of conventional antibody immunotherapeutics further stress is inflicted on these pathways by the need to additionally process the antibody-Aβ complexes. This is not the case for proteolytic antibodies, which act by themselves.

Proteolytic antibodies might constitute a novel class of immunotherapeutic drugs that combine the superior antigen-specificity of antibodies with the catalytic clearance ability of proteases. They bear a tremendously promising potential and might pose a valuable addition to our therapeutic arsenal which might be applied to a wide range of amyloid diseases.

1.4.1 Naturally occurring proteolytic antibodies

Proteolytic antibodies have first been reported in 1989 [221]. Naturally occurring proteolytic antibodies able to degrade vasoactive intestinal peptide (VIP), a bronchodilator, were discovered in patients with autoimmunity [221]. Several other proteolytic antibodies were discovered in the following years including antibodies against thyroglobulin in Hashimoto's thyroiditis [224], factor VIII in hemophilia patients [225] and monoclonal myeloma light chains were shown to hydrolytically cleave prothrombin [226] and vasopressin [227]. Furthermore, transthyretin [228] and Aβ [229, 230] have been identified as targets of proteolytic antibodies.

At first glance, the ubiquitous natural occurrence of proteolytic antibodies against distinct antigens might appear as an intellectually challenging concept. Activation of B-cells and subsequent antibody production is dependent on B-cell receptor (BCR)-mediated signal transduction upon antigen binding. Therefore, antigen cleavage, as is the case for proteolytic antibodies, would diametrically contradict this requirement, as the antigen would be prematurely released upon cleavage and would therefore abbrogate development of proteolytic adaptive immunity. According to our classical understanding, there is yet another prerequisite for B-cell activation and expansion — contemporaneous T-helper cell stimulation. Here, T-helper cells need to specifically recognize processed fragments of the antigen, presented on the B-cell's major histocompatibility complex II (MHC II) molecules. After successful recognition, the T-helper cell releases cytokines, highly localized, directed towards the B-cell, promoting and enabling activation, clonal expansion and class-switching of the B-cell. But in addition, the B-cell needs to simultaneously grip onto another antigen molecule via its BCR. This co-stimulation is required for proper activation, clonal expansion and appropriate class-switching of the B-cell [231, 232]. Consequently, when pondering about the chances of proteolytic antibody existence, the intuitive stance would be to assume: They must be obscure and rare immunological oddballs. But the conflicting observation of many proteolytic antibodies with distinct targets, leads to the challenging question of: How can proteolytic antibodies be so ubiquitously induced?

Antigen proteolysis by BCRs only allows subsequent B-cell activation and clonal expansion in case transmembrane BCR signaling, as a consequence of antigen binding, is faster than antigen proteolysis and release [233]. Elevated abundance of proteolytic antibodies in patients with autoimmunities characterized by reduced thresholds in BCR signalling supports this assumption [234, 235]. Furthermore, B-cell activation in proteolytic immunity might follow a T-helper cell-independent activation route. Strong BCR signaling alone, induced by multivalent antigens (e.g. polysaccharides on the surface of bacteria), was shown to be sufficient to induce B-cell activation with proper antibody production [236, 237]. Albeit, this activation mechanism exclusively results in the production of IgM-class antibodies, as T-helper cell signalling is imperative for class-switching to occur and is missing in this case. A supporting argument of the T-helper cell-independent induction hypothesis is that superior catalytic activity was consistently found in IgM-class antibodies and almost none in class-switched IgG antibodies [238, 239].
One exemption of T-helper cell-dependency in antibody class-switching is present in IgA antibodies. IgA class-switching is facilitated through both T-helper cell-dependent and T-helper cell-independent pathways [240]. Accordingly, proteolytic IgA antibodies have been reported and surprisingly elicited profound activities surpassing IgM activities [241, 242].

Interestingly, all proteolytic antibodies that have been identified so far exhibited serine protease-like activity, featuring the typical catalytic triads or diads characteristic for serine proteases, consisting of serine, histidine and aspertate residues. Independent catalytic domains and antigen-binding domains were consistently found in proteolytic antibodies and therefore a split-site model of spatially separated antigen recognition and hydrolysis has been posited [239, 243]. The catalytic domains, which presented prominent nucleophilic activity, were found within the conserved framework regions of the V domains and their nucleophilic activity was not abbrogated by experimental complementarity determining region (CDR) exchange, while on the other hand CDRs were indispensable for antigen recognition and binding [244]. Nucleophilic sites were found to be encoded in conserved, heritable germline

sequences and promiscuous nucleophilic reactivity was found in essentially all V domains, when probed with phosphonate diesters (strong electrophiles able to covalently bind nucleophiles, such as the catalytic domains of serine proteases) [245]. The ubiquity and conservation of the nucleophilic sites in heritable, germline V domains allowed speculations that catalytic activity might evolutionarily preceed classic, adaptive immunity and might serve an important protective purpose [243]. In support of this assumption, high levels of catalytic antibodies have been correlated with survival chances in sepsis patients [246].

In the case of proteolytic antibodies against amyloid peptides, the induction requirements are readily met, as amyloids present a high degree of multivalency, which might be sufficient for T-helper cell-independent activation. Furthermore, amyloids present conformational neoantigens which might circumvent developmental negative selection of autoreactive B-cells during B-cell development.
In line with this notion, proteolytic anti-Aβ antibodies were found in AD patients, healthy elderly but also in healthy young individuals (<35 y.o.). The catalytic activity was superior in IgM-class antibodies and virtually absent in IgG-class antibodies. Polyclonal IgM preparations from healthy elderly donors (>70 y.o.) displayed catalytic activities against $A\beta_{1\text{-}40}$ that were 3 orders of magnitude higher than those of IgG preparations from the same donors [229]. Correlation of catalytic activity with age and AD pathology hints at adaptive processes involved in these antibodies. However, analyses suggested that this adaptivity occured only by affinity maturation of the antigen-binding sites while the nucleophilic, catalytic sites were devoid of adaptive processes [229].
Proteolytic anti-Aβ antibodies were shown to reduce Aβ levels, prevent its aggregation and reduce toxicity in AD mouse models and cell culture [229, 247]. Another positive finding in experiments in mice, was that a proteolytic anti-Aβ single-chain variable fragment (scFv) did not activate microglia and the number of microhemorrhages found in the neocortex was slightly reduced compared to control group, which was treated with an irrelevant scFv. These results support the superiority of proteolytic antibodies over conventional antibodies in terms of safety and infers promising potential for proteolytic antibodies as a treatment opportunity for AD.

1.5 Selection methods

The following sections will focus on the evolution of selection methods and how these have been utilized for proteolytic antibody development in the past — pitfalls of these early attempts will be discussed and finally, my proposed method to develop proteolytic antibodies will be introduced in section 3.1 and its advantages will be emphasized.

1.5.1 Harnessing *in vitro* evolution — survival of the fittest

In biochemistry, methods for isolation and development of compounds with tailor-made properties (e.g. antibodies that bind a certain antigen, enzymes that catalyze a defined reaction or whole organisms that produce a valuable resource) rely heavily on the concept of evolution, which can be condensed down to the utilization of mutations and specific selection pressures leading to the enrichment of entities with the desired functionality.
Conceptually, in an evolution-driven system traits of an entity are passed on to its successors. Individual traits are subject to random alterations. Beneficial alterations to traits are more likely to be passed on to the next generation. Effects of evolution can be seen in any living species over the course of several thousands of generations due to mutations in their genetic information. But evolution is not limited to living creatures, as evidenced by viruses which are also subject to evolution. This also shows that evolutionary processes are not limited to the inherited information being encoded in DNA, but can also act on RNA which encodes the information of certain forms of viruses. Generalized, evolution may act on any system in which a genotype — the code harbouring the information about the traits of an entity — is connected to the corresponding phenotype — the functional expression of the traits encoded in the genotype. But there are two more conditions: First, the genotype must be subject to intergenerational variability due to mutations/alterations and second, the probability of survival/reproduction of the entity must be subject to selection pressures.

We have learnt to harness the potential that lies in these evolutionary processes to our advantage. To date, artificial evolutionary processes were ubiquitously adapted in tightly controlled setups to develop functional proteins (e.g. antibodies and enzymes) or catalytic and binding DNAs or RNAs (e.g. aptamers and DNAzymes).

1.5.2 First-generation selection methods

Early selection methods focused on the provision of means to physically connect a proteinogenic expression of a variant with its encoding DNA. These methods were widely used to isolate antibodies against specific antigens from large combinatorial libraries by repeated panning and recovery of variants, that were able to bind to the desired, immobilized antigens. As the corresponding encoding DNA was physically connected to the captured antibodies, active variant sequences could easily be recovered. Probably the most famous and routinely used selection method is phage display [248]. Here, antibodies or other proteins are conjugated to a coat protein (mostly pIII) of the bacteriophage M13. Therefore, *E.coli* bacteria are infected with phagemids that harbour the code for an entire phage and in addition a conjugation construct of the proteins of interest (POI) with the pIII coat protein. Subsequently, the infected *E.coli* produce phages which clonally display a POI-variant on their surface. These phages are then subjected to immobilized ligands and phages that are able to bind are recovered. These phages are then reused in subsequent selection cycles or maturation experiments by mutagenesis to further increase the binding affinities or for down-stream analyses of selected variants.
Similar and more advanced display methods have been developed including ribosome display, mRNA display, CIS display, yeast surface display, SNAP-BG display and many more, which all have their individual advantages and disadvantages and are reviewed in [249–251]. But unfortunately, all these methods still have the inherent disadvantage of a pretty narrow scope of application, limited exclusively to non-covalent or covalent binding events. Proteolytic antibodies on the other hand do exactly the opposite by hydrolysing peptide bonds of their antigens. Therefore, early attempts to isolate proteolytic antibodies using phage display had to come up

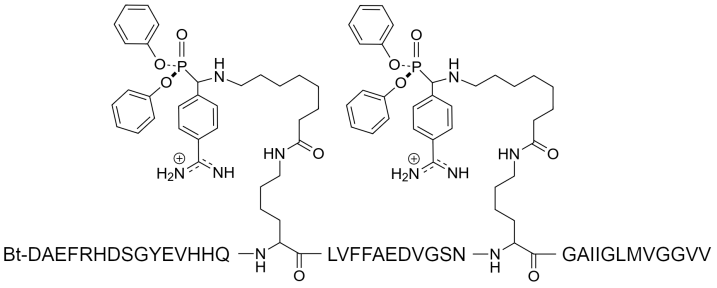

Figure 1.6: Chemical structure of the Aβ CRAA used by Taguchi *et al.* The Aβ CRAA features two large phosphonate ester probes conjugated to the lysine residues of the Aβ sequence and an N-terminal biotin. Image recreated according to [230].

with unconventional means to circumvent the cleaving nature of proteolytic antibodies during selection.

1.5.3 An early success — enrichment of proteolytic antibodies via phage display

In 2001, the group of Paul Sudhir published a method to isolate single-chain proteolytic antibodies from combinatorial libraries by phage display [252]. The group — inspired by the serine protease and serine esterase inhibitor diisopropyl fluorophosphate (DFP) — developed phosphonate diester probes, that were utilized to develop covalently reactive antigen analogs (CRAAs). In CRAAs, inhibitory phosphonate esters are conjugated to certain residues of the target antigen. Thereby, CRAA probes are able to irreversibly and covalently bind to the active site of proteolytic antibodies, while at the same time presenting antigen epitopes, favouring the isolation of antigen-specific, proteolytic antibodies. In a subsequent study, an Aβ CRAA (see Figure 1.6) was developed by coupling phosphonate esters to the lysine residues of Aβ and it was used to isolate single-chain proteolytic anti-Aβ antibodies [230]. Phage display was used wherein phages that displayed proteolytic antibodies which were able to engage the Aβ-coupled phosphonate diester moieties, were covalently captured and recovered. The method design was affirmed, by successful isolation of single-chain antibodies which exhibited prominent catalytic activies against Aβ.

At that time, it was a formidable achievement to successfully utilize the limited versatility of phage display to isolate antigen-specific, proteolytic antibodies. Two antibodies from these selections were published: 2E6, a non-physiological single-chain antibody consisting of two lambda light chain Fvs, and 5D3, a single-domain kappa light chain Fv antibody. Both presented superior catalytic activity against Aβ compared to polyclonal and monoclonal IgM preparations. Furthermore, 2E6 was able to reduce Aβ plaque burden in an AD mouse model, while microglia activation and incidences of microhemmorhages were indistinguishable from control [247]. Nevertheless, unfortunately, the stability of these antibodies turned out to be unsuitable for therapeutic applications. The purification process of 2E6 drastically diminished its specific activity.
On a side note, multiple attemts I performed to reproduce the claimed proteolytic activity of 2E6 and 5D3, failed to recapitulate any proteolytic activity against Aβ, which adds a grain of salt to the afforementioned achievements.

Generally, a set of disadvantages inherent to the afforementioned phage display method utilizing CRAAs to develop antigen-specific, proteolytic single-chain antibodies limits its applicability and needs to be overcome, to successfully develop antibodies fit for therapeutic applications: 1) Instability of antibodies is a major concern and currently needs to be met by extensive engineering post-isolation. 2) CRAAs favour the isolation of antibodies featuring nucleophilic activity, irrespective of antigen-specificity. Any antibody with nucleophilic activity, that is able to engage the phosphonate ester probes, will be isolated. 3) Presence of nucleophilic activity does not equate to the presence of proteolytic activity. This necessitates further extensive manual screening of individual variants post-isolation for antigen-specific proteolytic activity. 4) the antigen is modified by conjugation with large phosphonate ester probes across multiple residues, altering the structural appearence of epitopes originally presented by the antigen, potentially tampering with achievable antigen-specificity.

Table 1.4: Applications of IVC in biomolecule engineering

Type of molecule	Functionality	Selection method	References
Proteins	Site-specific methylation by HaeIII methyltransferase	Protection from nuclease degradation by DNA methylation	[253, 254]
	Enhanced thiolactonase activity	W/o/w emulsion sorting by FACS, fluorescence produced by thiolactonase activity	[255]
	Site-specific endonuclease	Incorporation of dUTP-biotin into cohesive ends after successful nuclease cleavage by DNA polymerase	[256]
	Enhanced phosphotriesterases for degradation of organophosphate pesticides and nerve agents (soman, sarin and VX)	Microbead display and FACS sorting of microbeads conjugated with variant DNA and harbouring product, if the variant was active	[257]
	Protein-ligand binding, development of enhanced HA-tags	FACS sorting of microbeads displaying a POI	[258]
	Protein-ligand binding, mutant ligand peptides recognized by anti-His antibody	FACS sorting of microbeads displaying mutant His-tags recognized by fluorescent anti-His antibody	[259]
	Protein-ligand binding	Attachment of encoding DNA to the POI via BG-SNAP covalent bonding, selection panning performed as in phage display	[250, 260–262]
RNAs	Trans-acting ligase ribozymes	Microbead display and FACS sorting, active variants attach fluorophors to RNA oligonucleotides	[263]
	Ribozymes catalyzing multiple-turnover Diels-Alder cycloadditions	Library DNA variants are modified with an anthracene moeity and are conjugated to a biotin-maleimide by active ribozymes	[264]
Other	T7 promotor variants with enhanced *in vitro* activity	Microbead display and FACS sorting of microbeads which gain fluorescence upon successful *in vitro* expression	[265]

1.5.4 Next-generation selection methods — miniturizing the laboratory with artificial cell-like compartments

Earlier selection methods were essentially limited to simple binding or bond-forming reactions to physically capture variants with the desired properties from a bulk mixture.

The advent of next-generation selection methods, arrived with the invention of *in vitro* compartmentalized (IVC), cell-sized, picoliter reactors provided via emulsification. With *in vitro* transcription and translation (IVTT) formulations becoming commercially available, proteins and enzymes could be produced in reaction tubes, devoid of any cells. This was utilized in combination with IVC to establish artificial cell-like compartments with custom compositions to allow millions of paralleled enzymatic reactions to be performed simultaneously, which enabled development of sophisticated, custom enzymes performing complex and tailor-made chemical reactions. These methods allowed the development of a broad range of enzymes with functionalities beyond bond formation. Table 1.4 contains a compiled, but non-exhaustive list of successful developments achieved using IVTT IVC applications.

The next leap forward in selection methods was achieved by the introduction of a solid phase to IVC IVTT in the form of microbeads. These microbeads could be funtionalized by tethering chemicals, proteins or nucleic acids to their surfaces alongside with a variant-encoding DNA. Selection setups were formulated, so that functional groups could be manipulated by the desired variant-induced enzymatic reactions yielding a readout for isolation. A popular readout was generated by attachment, detachment or modification of fluorescences as a result of catalysis induced by active variants. Afterwards, microbeads harbouring DNA encoding active variants could be collected via fluorescence-activated cell sorting (FACS).

1.5.5 Microfluidics

The current state-of-the-art technique predicted to soon dominate the enzyme and biomolecule engineering field is microfluidics with chip-based microfluidic devices. Microfluidics applications feature pressure pumps capable of reliably pumping fluids on a nanoliter to milliliter per minute scale. These pumps are used together with carefully designed microfluidic chips, which are usually made of polydimethylsiloxane (PDMS) and feature miniscule, intricate, interconnected channels that allow a broad range of fluid manipulations. Their main purpose in enzyme engineering is the establishment of highly homogeneous aqueous droplets in oil [266]. Furthermore, the chip design allows not only for droplet generation but also for droplet

mixing [266], splitting [266, 267], fusion [266, 268], incubation [266], microbead or cell encapsulation [269, 270], sorting via fluorescence or absorbance readouts [268, 269, 271, 272] and also sorting by droplet load or size [273, 274]. The versatility of this platform never ceases to amaze with ever more elaborate applications emerging in the field of directed evolution and biomolecule development.
Unfortunately, microfluidics has a relatively high entrance barrier, as it necessitates the use of highly specialized equipment, which is only available to a handful of laboratories. But as costs for equipment drop, it is expected to quickly dominate the field of biochemical engineering.

1.6 The scope of this study

This study was divided into two parts. The first part focused on the investigation of an AβO model, which was derived from a recombinant dimeric Aβ construct (dimAβ). The second and main part of this thesis revolved around the development of means to enable the isolation of antigen-specific proteolytic antibodies from combinatorial antibody libraries against amyloid peptides, in this case against Aβ.

1.6.1 Investigations into AβO using dimAβ

dimAβ is a recombinantly produced $Aβ_{40}$ dimer, which is composed of two $Aβ_{40}$ subunits tethered head-to-tail via a $(G_4S)_4$ linker. In initial experiments, dimAβ presented a conspicuous kinetic behavior in Thioflavin T (ThT)-monitored aggregation experiments. Typically, amyloid aggregation is characterized by sigmoidal assembly kinetics. The aggregation of dimAβ on the other hand presented highly concentration-dependent biphasic assembly kinetics. Intriguingly, the first phase was dominated by rapid generation of AβO, while the second phase represented the conversion of AβO into mature fibrils. The first part of my thesis aimed to elucidate on the assembly mechanisms of dimAβ-derived AβO, their interactions with mature fibrils, and to probe their suitability as a model to study AβO-induced pathophysiology.

1.6.2 Development of a method to enable the isolation of antigen-specific proteolytic antibodies from combinatorial libraries

To conquer the pressing need for an effective AD treatment, I sought out to provide means to enable investigations into the potential of antigen-specific proteolytic antibodies as novel anti-Aβ therapeutics. Proteolytic antibodies were so far largely neglected as potential drugs, probably due to their elusive nature and lack of sophisticated methods to isolate them from combinatorial antibody libraries. Therefore, as a self-proclaimed goal of this study, I aimed to develop a method which allows for the isolation of proteolytic antibodies and thereby makes them tangible for therapeutic research. The pinnacle of this work was intended to be an initial application of my method to isolate proteolytic anti-Aβ antibodies from combinatorial antibody libraries derived from naive human blood donations.

2. Results: Aβ Oligomers

We previously developed an AβO model by connecting two $Aβ_{40}$ molecules head-to-tail via a $(G_4S)_4$ linker. This recombinant peptide was termed dimAβ. By the spatial proximity of the two Aβ subunits the local Aβ concentration was artificially elevated, which promoted a highly concentration-dependent formation of AβO. Under quiescent conditions, AβO formation by dimAβ was kinetically favored over fibril formation, enabling the generation of metastable AβO. In contrast to AβO generated by $Aβ_{40}$ and $Aβ_{42}$, dimAβ-derived AβO, once formed, could be studied for elongated periods of time, without interfering progression of aggregation into fibrillar conformations. This was true for quiescent incubation conditions, but could be overcome by agitation which lead to proper fibril formation, possibly induced by interactions with the water-air interphase. Using dimAβ as an AβO model, I investigated the interactions of AβO with Aβ fibrils, demonstrating that AβO were able to bind and decorate fibril surfaces and thereby hamper fibril growth by inhibition of secondary nucleation processes (see original publication abstracts in infoboxes 2.1 and 2.2 and original publications 1 and 2 in 2.4) [128, 275]. My results supported the notion that AβO might be sequestered and thereby inactivated via interactions with Aβ fibrils, albeit beyond that they also antagonize their fixation at the same time by inhibition of fibril formation and thereby might elude their inactivation. Regardless, it remains to be elucidated whether AβO fixation by fibrils or senile plaques reduces their specific toxicity or might even promote toxicity elicited in the vicinity of plaques [276–278].

The origin of AβO *in vivo* is yet an open question. There is a long-standing paradox by which AβO formation *in vitro* is depend on elevated two- to three-digit micromolar concentrations of Aβ [65, 279–283], but these concentrations far exceed the estimated pico- to nanomolar concentrations found in brain tissue or cerebrospinal fluid (CSF) by several orders of magnitude [284–286]. Nevertheless, AβO were found

in post-mortem AD brain homogenates suggesting the existence of alternative formation mechanisms or factors promoting AβO production *in vivo* [287].

Together with colleagues, I was able to demonstrate a possible route of *in vivo* AβO formation [288]. We investigated the effect of pH on the concentration-dependent generation of AβO by dimAβ as well as native $Aβ_{42}$. At neutral pH, fibril formation of $Aβ_{42}$ and dimAβ was favoured until a critical oligomer concentration was exceeded giving rise to rapid AβO formation. These AβO were off-pathway to fibril formation. The critical oligomer concentration at neutral pH was ~30 µM for $Aβ_{1\text{-}42}$ far exceeding physiological concentrations. But we were able to show that upon reduction of pH to endo-/lysosomal pH of 4.5–5.5 the formation of AβO was accelerated ~8,000-fold and the critical oligomer concentration was reduced to ~3 µM.

The endo-/lysosomal system is known to naturally enrich Aβ. Endo-/lysosomal Aβ concentration has previously been reported to be well above 2.5 µM [289] suggesting that, together with its acidic pH, the endo-/lysosomal system might be a major contributor to spawning AβO *in vivo* (see original publication abstract in infobox 2.3 and original publication 3 in 2.4).

Furthermore, using dimAβ as a metastable AβO model, we were able to recapitulate a hallmark event of AD in primary mouse neurons that has been linked to AβO: Tau missorting. AβO formed by dimAβ potently induced Tau missorting in primary mouse cortical neurons and decreased spontaneous calcium oscillations. These results highlight the potential of our dimAβ-derived AβO model to faithfully recapitulate AβO pathology and might thereby provide a valuable model to investigate this usually elusive key-player of AD pathogenesis and might contribute to the development of novel therapeutics against AβO.

Original Publication: Hasecke *et al.*

2.1 Origin of metastable oligomers and their effects on amyloid fibril self-assembly [128]

Assembly of rigid amyloid fibrils with their characteristic cross-β sheet structure is a molecular signature of numerous neurodegenerative and non-neuropathic disorders. Frequently, large populations of small globular amyloid oligomers (gOs) and curvilinear fibrils (CFs) precede the formation of late-stage rigid fibrils (RFs), and have been implicated in amyloid toxicity.

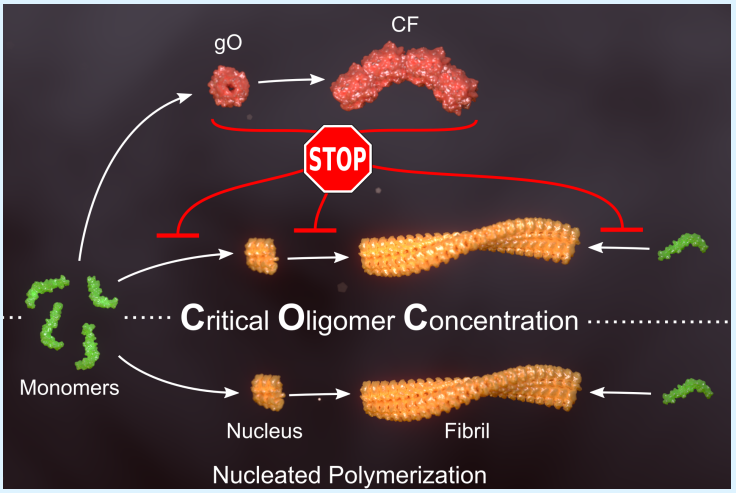

Figure 2.1: Aβ gO/CFs form at concentrations above the COC and inhibit fibril growth.

Yet our understanding of the origin of these metastable oligomers, their role as on-pathway precursors or off-pathway competitors, and their effects on the self-assembly of amyloid fibrils remains incomplete. Using two unrelated amyloid proteins, amyloid-β and lysozyme, we find that gO/CF formation, analogous to micelle formation by surfactants, is delineated by a “critical oligomer concentration” (COC). Below this COC, fibril assembly replicates the sigmoidal kinetics of nucleated polymerization.

Upon crossing the COC, assembly kinetics becomes biphasic with gO/CF formation responsible for the lag-free initial phase, followed by a second upswing dominated by RF nucleation and growth. RF lag periods below the COC, as expected, decrease as a power law in monomer concentration. Surprisingly, the build-up of gO/CFs above the COC causes a progressive increase in RF lag periods. Our results suggest that metastable gO/CFs are off-pathway from RF formation, confined by a condition-dependent COC that is distinct from RF solubility, underlie a transition from sigmoidal to biphasic assembly kinetics and, most importantly, not only compete with RFs for the shared monomeric growth substrate but actively inhibit their nucleation and growth.

Abstract from [128].

Original Publication: Hasecke *et al.*

2.2 Protofibril–Fibril Interactions Inhibit Amyloid Fibril Assembly by Obstructing Secondary Nucleation [275]

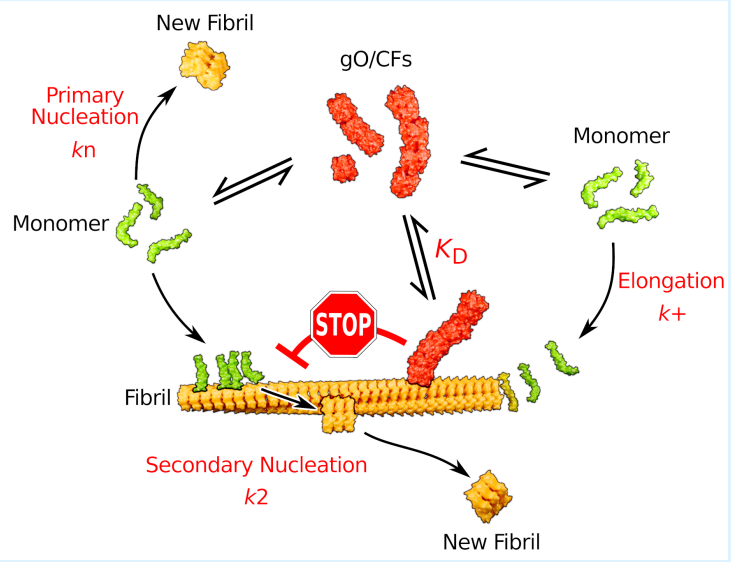

Figure 2.2: Aβ gO/CFs are able to bind to the surface of Aβ fibrils. This obscures secondary nucleation sites and thereby inhibits fibril formation.

Amyloid-β peptides assemble into both rigid amyloid fibrils and metastable oligomers termed AβO or protofibrils. In Alzheimer's disease, Aβ fibrils constitute the core of senile plaques, but Aβ protofibrils may represent the main toxic species. Aβ protofibrils accumulate at the exterior of senile plaques, yet the protofibril–fibril interplay is not well understood. Applying chemical kinetics and atomic force microscopy to the assembly of Aβ and lysozyme, protofibrils are observed to bind to the lateral surfaces of amyloid fibrils. When utilizing Aβ variants with different critical oligomer concentrations, the interaction inhibits the autocatalytic proliferation of amyloid fibrils by secondary nucleation on the fibril surface. Thus, metastable oligomers antagonize their replacement by amyloid fibrils both by competing for monomers and blocking secondary nucleation sites. The protofibril—fibril interaction governs their temporal evolution and potential to exert specific toxic activities.

Abstract from [275].

2.3 Endo-lysosomal Aβ concentration and pH enable formation of Aβ oligomers that potently induce Tau missorting [288]

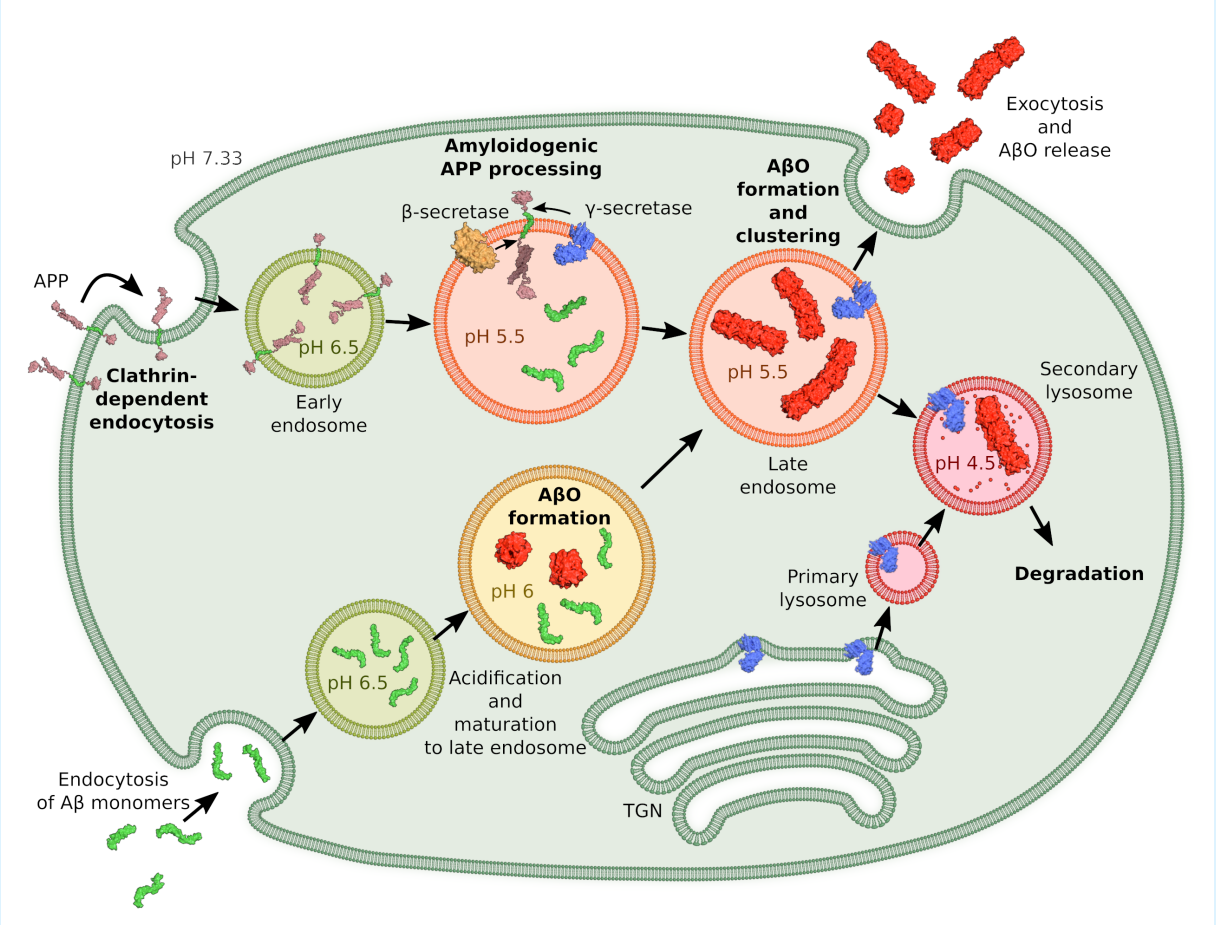

Figure 2.3: Scheme of intracellular APP processing and AβO formation. APP is endocytosed via clathrin-dependent mechanisms. Cleavage of APP by β- and γ-secretase present in the endosomal membrane releases Aβ into the endosomal lumen. The locally increased Aβ concentration together with progressive lumen acidification promotes AβO formation and subsequent release.

Amyloid-β peptide (Aβ) forms metastable oligomers >50 kDa, termed AβOs, that are more effective than Aβ amyloid fibrils at triggering Alzheimer's disease-related processes such as synaptic dysfunction and Tau pathology, including Tau mislocalization. In neurons, Aβ accumulates in endo-lysosomal vesicles at low pH. Here, we show that the rate of AβO

assembly is accelerated 8,000-fold upon pH reduction from extracellular to endo-lysosomal pH, at the expense of amyloid fibril formation. The pH-induced promotion of AβO formation and the high endo-lysosomal Aβ concentration together enable extensive AβO formation of Aβ42 under physiological conditions. Exploiting the enhanced AβO formation of the dimeric Aβ variant dimAβ we furthermore demonstrate targeting of AβOs to dendritic spines, potent induction of Tau missorting, a key factor in tauopathies, and impaired neuronal activity. The results suggest that the endosomal/lysosomal system is a major site for the assembly of pathomechanistically relevant AβOs.

Abstract from [288].

2.4 Original publications

In the following part of the chapter, (shared) first author publications are presented as originally published. These publications address insights into the emergence and pathological relevance of AβO as well as their interactions with Aβ fibrils and their effects on amyloid aggregation kinetics.
Publications are reprinted as originally published by the corresponding publisher. The Supplementary Information are attached as deposited by the corresponding publisher. Copyrights are governed by Creative Commons licenses as stated below:

Details on my contributions can be found in appendix B.

Chemical Science

EDGE ARTICLE

View Article Online
View Journal | View Issue

Cite this: *Chem. Sci.*, 2018, **9**, 5937

Origin of metastable oligomers and their effects on amyloid fibril self-assembly†

Filip Hasecke,‡[a] Tatiana Miti,‡[b] Carlos Perez,[b] Jeremy Barton,[b] Daniel Schölzel,[ac] Lothar Gremer,[ac] Clara S. R. Grüning,[a] Garrett Matthews,[b] Georg Meisl,[d] Tuomas P. J. Knowles,[d] Dieter Willbold,[ac] Philipp Neudecker,[ac] Henrike Heise,[ac] Ghanim Ullah,[b] Wolfgang Hoyer*[ac] and Martin Muschol*[b]

Assembly of rigid amyloid fibrils with their characteristic cross-β sheet structure is a molecular signature of numerous neurodegenerative and non-neuropathic disorders. Frequently large populations of small globular amyloid oligomers (gOs) and curvilinear fibrils (CFs) precede the formation of late-stage rigid fibrils (RFs), and have been implicated in amyloid toxicity. Yet our understanding of the origin of these metastable oligomers, their role as on-pathway precursors or off-pathway competitors, and their effects on the self-assembly of amyloid fibrils remains incomplete. Using two unrelated amyloid proteins, amyloid-β and lysozyme, we find that gO/CF formation, analogous to micelle formation by surfactants, is delineated by a "critical oligomer concentration" (COC). Below this COC, fibril assembly replicates the sigmoidal kinetics of nucleated polymerization. Upon crossing the COC, assembly kinetics becomes biphasic with gO/CF formation responsible for the lag-free initial phase, followed by a second upswing dominated by RF nucleation and growth. RF lag periods below the COC, as expected, decrease as a power law in monomer concentration. Surprisingly, the build-up of gO/CFs above the COC causes a progressive increase in RF lag periods. Our results suggest that metastable gO/CFs are off-pathway from RF formation, confined by a condition-dependent COC that is distinct from RF solubility, underlie a transition from sigmoidal to biphasic assembly kinetics and, most importantly, not only compete with RFs for the shared monomeric growth substrate but actively inhibit their nucleation and growth.

Received 1st April 2018
Accepted 12th June 2018

DOI: 10.1039/c8sc01479e

rsc.li/chemical-science

Introduction

Deposits of protein aggregates forming non-branching rigid fibrils (RFs) with a characteristic cross-β sheet architecture are closely associated with a wide range of human disorders including Alzheimer's and Parkinson's disease, as well as non-neuropathic amyloidoses such as type-II diabetes and hereditary lysozyme amyloidosis.[1–9] More recently, amyloid formation has also been associated with functional biological responses.[10] Beyond late-stage RFs, amyloid formation frequently involves morphologically distinct, long-lived and highly populated metastable intermediates. Globular amyloid oligomers (gOs) and their associated highly curvilinear fibrils (CFs), often referred to as protofibrils, have been observed with large numbers of amyloid proteins and over a wide range of growth conditions.[11–21] Substantial evidence suggests that early-stage gOs are potent sources of cytotoxicity in amyloid diseases.[19,22–30] Metastable oligomers also affect the aggregation of pharmaceuticals,[31] and might hold answers to the question what distinguishes functional from pathological amyloid species.[3,10] Formation of metastable precursors relates to a variety of physiochemical and biomedical problems.[32] This includes metastable liquid phases as precursor of protein crystallization[33] or sickle-cell hemoglobin fibrillation,[34] as well as the significance of membrane-less organelles in promoting ALS fibril formation.[35] Some amyloid oligomers themselves have been suggested to share characteristics of disordered liquid-like states.[36,37]

Characterizing the mechanisms and developing solutions to kinetic schemes that replicate RF nucleation and growth kinetics in the absence of long-lived, metastable intermediates has made significant progress.[38,39] These models helped identify secondary nucleation mechanisms as critical contributors to the process of fibril nucleation. Analysis of the scaling behavior of reaction half-times *vs.* monomer concentrations now permits

[a]*Institut für Physikalische Biologie, Heinrich-Heine-Universität, 40204 Düsseldorf, Germany. E-mail: wolfgang.hoyer@hhu.de*

[b]*Department of Physics, University of South Florida, Tampa, FL 33620, USA. E-mail: mmuschol@usf.edu*

[c]*Institute of Complex Systems (ICS-6), Structural Biochemistry, Research Centre Jülich, Germany*

[d]*Department of Chemistry, University of Cambridge, Lensfield Road, Cambridge CB2 1EW, UK*

† Electronic supplementary information (ESI) available. See DOI: 10.1039/c8sc01479e

‡ Equal contributions, joint first authors.

View Article Online
Chemical Science Edge Article

quantification of the relative contributions of distinct growth mechanisms to fibril formation.[39–41] In contrast, the conditions required for the formation of significant concentrations of long-lived, metastable amyloid oligomers, which are distinct from the inherently minor populations of small, on-pathway fibril seeds, remain uncertain. Similarly, the mechanisms by which these metastable oligomers are replaced by late-stage RFs continue to be elusive. The role metastable states play in the nucleation and growth of late-stage RFs has important implications for our understanding of amyloid pathogenesis and informs efforts at intervening with their formation. Yet, it remains unresolved whether metastable globular oligomers are obligatory or optional precursors of fibril growth, and whether they serve as on-pathway precursors or represent off-pathway competitors of late-stage RFs.[13] Two prevalent models for the role of globular oligomers are nucleated conformational conversion (NCC) *vs.* nucleated polymerization with competing off-pathway oligomers (cNP) (Fig. 1A). In NCC, oligomers are on-pathway but structurally distinct precursors of RFs; restructuring of oligomers into RF seeds represents the rate-limiting nucleation step.[42,43] In cNP, RFs nucleate *via* "classical nucleation" from the monomer pool while metastable oligomers and curvilinear fibrils are off-pathway competitors to RF nucleation and growth.[44,45] It is difficult to distinguish these scenarios since both predict qualitatively identical temporal sequences of aggregate populations and growth kinetics.

We have previously reported the separation of the parameter space for amyloid assembly of lysozyme in dependence of protein and salt concentration (Fig. 1B).[46,50] One regime is typified by nucleated polymerization of rigid amyloid fibrils without discernible populations of metastable intermediates. The other regime results in lag-free formation of readily detectable globular oligomer (gOs) which tend to assemble into highly curvilinear fibrils (CFs), *i.e.* fibrils with distinctly shorter persistence lengths than their rigid fibril (RF) counterparts. A colloidal model accounting for the free-energy cost of charge

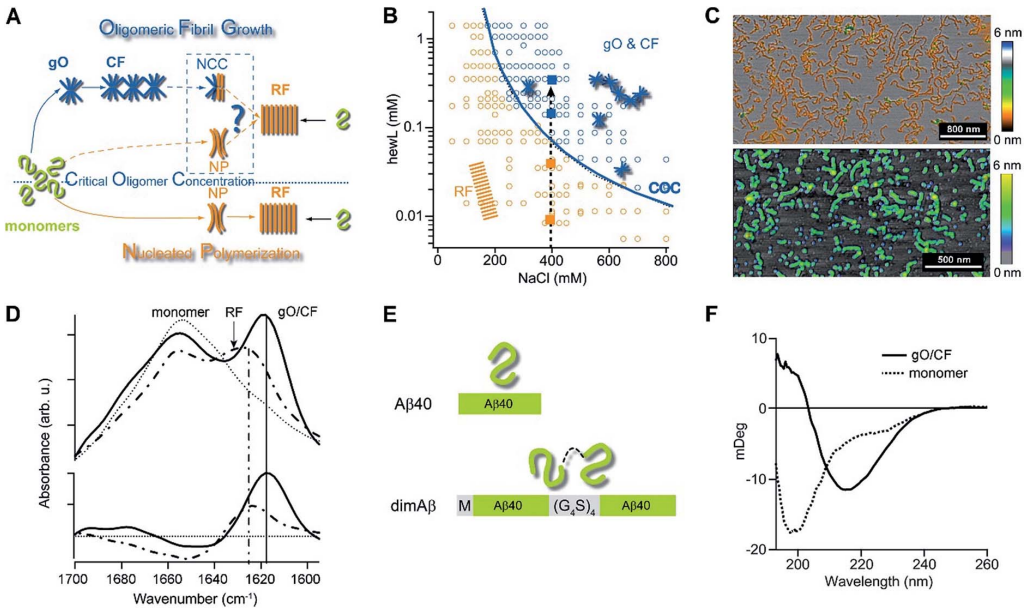

Fig. 1 Amyloid oligomer model systems. (A) Schematic of potential roles for globular oligomers (gOs) and their curvilinear fibrils (CFs) in late-stage rigid fibril (RF) formation. (Top) Globular oligomers (gOs) and their curvilinear fibrils (CFs) are presumed to assemble prior to late-stage formation of RFs. The dashed lines represent the potential nucleation pathways for RFs either *via* nucleated conformational conversion (NCC) from gO/CFs or *via* nucleated polymerization from monomers, with RFs competing with off-pathway gO/CF formation (cNP). (Bottom) Nucleated polymerization (NP) of RFs from monomers only, *i.e.* in the absence of metastable gO/CFs. The transition for fibril formation in the absence or presence of gO/CF occurs upon crossing some monomer threshold called the "critical oligomer concentration" (COC, blue dotted line) (B) phase diagram for lysozyme at pH 2, 52 °C (adapted from ref. 46). Open orange circles indicate protein/salt concentrations resulting in RFs without gO/CF formation, as assessed by thioflavin T (ThT) and light scattering kinetics as well as time-resolved atomic force microscopy (AFM). Blue circles specify conditions for lag-free onset of gO/CF growth. The blue curve represents the fit from a colloidal model to the protein- and salt-dependent COC. The dashed vertical line indicates the transition from RF growth without build-up of metastable oligomeric species (below COC) to oligomeric RF growth (above COC) upon increasing monomer concentration, as applied in this study. (C) Morphologies of lysozyme (top) and dimAβ (bottom) gOs and CFs formed above their respective COCs, imaged using AFM. Color scale: height in nm. (D) Top: Amide I band infrared spectra of hewL monomers *vs.* gO/CFs or RFs, both after separation from monomers. Bottom: gO/CF and RF spectra after subtraction of monomer reference (adapted from ref. 54) (E) scheme of the dimeric Aβ40 construct dimAβ. Two Aβ40 units are linked in a single chain in a head-to-tail fashion. An N-terminal methionine affords recombinant expression. A flexible $(G_4S)_4$ linker was chosen to provide the Aβ40 units with conformational freedom. (F) Far-UV CD spectra of dimAβ before and after gO/CF formation, recorded at 4 °C or 20 °C, respectively, at a protein concentration of 20 μM.

View Article Online
Edge Article Chemical Science

repulsion among monomers upon confinement to an oligomer replicated the prominent protein- and salt-dependence of the sudden onset of gO formation in hen egg-white lysozyme (hewL) (Fig. 1B).[46] Due to these strong similarities with the onset of micelle formation in charged surfactant system we labelled this transition the "critical oligomer concentration" or COC.[47] Our observations also resembled a transition of β2-microglobulin amyloid assembly upon changes in solution pH.[48,49] The gOs formed by hewL above the COC displayed the basic characteristics of small oligomers observed with multiple amyloid proteins, including those of β2-microglobulin, transthyretin, Aβ40/42, and α-synuclein.[14,20,21,51–53] These characteristics include the globular morphology, the size of a few nanometers (Fig. 2E-I), the propensity to assemble into curvilinear fibrils (Fig. 1C, top, and Fig. 2E-II), and the muted ThT responses they elicit.[54] Their IR spectra showed prominent peaks in the characteristic "amyloid band", which were slightly but consistently shifted with respect to those of their RF counterparts (Fig. 1D).[55] An additional weak peak near 1690 cm^{-1} hints at a potential antiparallel β-barrel architecture, now reported for multiple amyloid oligomers.[56] The tinctorial and spectroscopic features of hewL gOs therefore replicate the limited number of high-resolution structures of early-stage amyloid gOs in other systems.[57,58] We also confirmed that gO/CFs were metastable as RFs seeded above the COC readily grew while gO/CFs seeded below the COC slowly decayed. In short, metastable gO/CFs of hewL are confined by their COC to a subset of conditions permissive of fibril growth and are therefore nonobligatory intermediates of fibril growth (Fig. 1B).

These results raised a series of questions we set out to answer. First, is formation of metastable gO/CFs typically confined above a threshold protein concentration, *i.e.* a COC? Does it depend whether a folded or an intrinsically disordered protein undergoes amyloid assembly? Are these metastable gO/CFs on-pathway precursors or off-pathway byproducts of amyloid assembly? Most importantly, does the emergence of metastable gO/CFs above the COC alter RF nucleation and growth, and if so, in what ways? We chose to address these questions by comparing a single-chain Aβ dimer (dimAβ) against the behaviour of hen egg-white lysozyme (hewL). While Aβ is a disordered monomer and the key component of protein deposits associated with Alzheimer's disease, hewL is a folded protein closely related to hereditary lysozyme amyloidosis. The dimeric Aβ construct increases the local concentration of Aβ monomers and, thereby, lowers the threshold for oligomer formation *in vitro*. As detailed below, it also promotes the separation of timescales for gO/CF *vs.* RF formation and, thereby, permits separate analysis of their intrinsic kinetics. We show that, for both dimAβ and hewL, RF assembly kinetics changes from purely sigmoidal to biphasic upon crossing a protein- and condition-specific COC. The initial phase in biphasic kinetics represents the lag-free formation of gO/CFs while the second phase indicates RF nucleation and growth. Analysing the RF component, we find that the increasing levels of gO/CFs above the COC progressively slow RF formation, as evident in increasing RF lag periods. As we argue below, the formation of metastable gO/CFs therefore alters RF nucleation and growth in ways that neither of the currently dominant models of NCC and cNP fully captures.

Results

Single-chain Aβ dimer as amyloid oligomer model system

Formation of metastable gO/CFs of Aβ has been linked to neurotoxicity in Alzheimer's disease.[11,12,22,24,26,28–30,59] To facilitate determination of the effects of gO/CFs on Aβ fibril formation, we introduce here a single-chain dimeric variant of Aβ40 termed dimAβ. In dimAβ, two Aβ40 units are connected through a flexible glycine–serine-rich linker in a head-to-tail fashion (Fig. 1E). A relatively long (20 amino acids), flexible linker was chosen to guarantee minimal disturbance of the conformational properties of Aβ in monomeric as well as aggregated states. This is especially important in the light of previous work on Aβ dimer constructs that suggested that short linkages *via* disulfide bridges restrict the accessibility of the RF state.[30,60–62] In the case of dimAβ, solution NMR of the monomeric construct retrieves the resonances of monomeric Aβ40, indicating that the two Aβ subunits in dimAβ do not affect each other's largely disordered conformation (Fig. S1†). According to AFM (Fig. S2A†) and solid-state NMR spectroscopy (Fig. S2B and C†) the end product of dimAβ assembly, as for Aβ40, are RFs. A 2D INEPT MAS spectrum, which only displays mobile regions of the fibrils, almost exclusively picks up signals from glycine and serine residues. This indicates that the linker in dimAβ RFs remains flexible, while both Aβ subunits are incorporated into the RF β-sheet core (Fig. S2B†). Aβ40 and Aβ42 were previously shown to exhibit biphasic assembly kinetics at elevated protein concentrations.[63–66] The linkage of two Aβ units was chosen to increase the local Aβ concentration, thereby promoting the highly concentration-dependent gO/CF formation. Compared to Aβ40 and Aβ42, this provides the separation of the two kinetics phases, *i.e.* the time regimes with dominant gO/CF or RF formation, at much reduced total incubation times and protein concentrations, important for the subsequent analysis of gO/CF and RF kinetics (see below). As seen by AFM and CD spectroscopy, dimAβ does readily form gO/CFs with morphologies (Fig. 1C) and β-structure (Fig. 1F) similar to those observed with hewL.

Formation of gO/CFs induces switch from sigmoidal to biphasic assembly kinetics

The time courses of amyloid fibril assembly for both hewL and dimAβ undergo a discontinuous transition from purely sigmoidal to biphasic kinetics, as monitored by the amyloid indicator dye ThT (Fig. 2A and C). Below the transition (orange traces), ThT shows no discernible increase during an extended lag period lasting many hours to days. The flatness of the initial plateaus is highlighted in Fig. 2A and D by using a logarithmic axis for the ThT signal. This initial plateau is followed by a dramatic upswing in ThT emission which eventually saturates. Upon crossing a monomer concentration of about 1.5 μM dimAβ or 40 μM hewL, at their respective solution conditions, the kinetics changes discontinuously (blue traces, Fig. 2A and

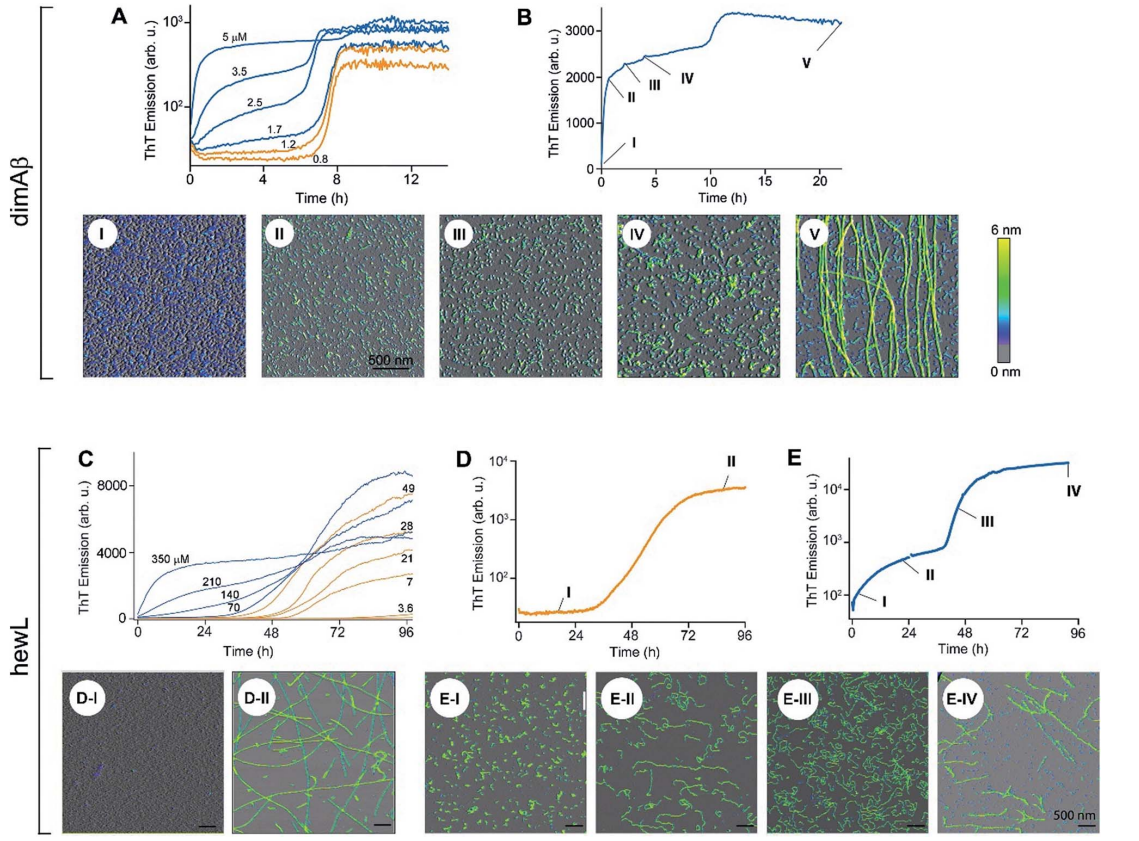

Fig. 2 Transition from sigmoidal to biphasic growth kinetics upon oligomer formation. Transition from sigmoidal (orange) to bimodal (blue) amyloid growth kinetics of dimAβ (A, B) and hewL (C–E), as monitored by ThT fluorescence. Concentration dependent time traces of (A, B) dimAβ assembly in 50 mM Na-phosphate, 50 mM NaCl, pH 7.4, 37 °C, and (C–E) hewL assembly in 25 mM K-phosphate, pH 2.0, 52 °C, with 450 (C, E) and 500 (D) mM NaCl, respectively. Typical sigmoidal (D) and bimodal (B, E) growth kinetics correlated to AFM images of aggregate morphologies at the indicated time points (I–V) and concentrations of 20 μM dimAβ (B), 21 μM hewL (D), and 280 μM hewL (E), respectively.

C). Slightly above the transition, ThT responses display a small but steady upward drift from the outset, followed by a prominent upswing at a time point consistent with RF nucleation and growth. By further raising monomer concentration the biphasic character of the kinetics becomes increasingly prominent, with the initial phase reaching a saturation plateau well before the second upswing in ThT response. The hewL traces shown in Fig. 2C emphasize another features of biphasic kinetics. The second upswing above the COC, while present, becomes less pronounced and the ThT amplitude at 96 hours decreases even though monomer concentration increases. As shown below, the progressive decrease in ThT response at this time point correlates with the increasing concentrations of residual gO/CFs. Both of these features support the model of RF assembly in the presence of gO/CFs put forth below. The ThT trace for hewL in Fig. 2E emphasize the biphasic character of hewL kinetics. The biphasic kinetics reported here extend our prior observation that the onset of a lag-free increase in ThT and light scattering kinetics in hewL coincided with the onset of gO/CF formation.

Using AFM imaging, we confirmed that the sigmoidal kinetics indicated RF growth without detectable intermediates while biphasic kinetics represented the sequential growth of gO/CFs during the initial phase and RF nucleation and growth during the secondary phase. AFM images of aliquots sampled for hewL growth below the COC indeed only detect monomers within the lag phase and accumulating numbers of fibrils of increasing length during the rise and subsequent plateau in ThT (Fig. 2D). The extended lag periods with no discernible fibril nucleation/growth matches well with the predictions from nucleated polymerization dominated by autocatalytic secondary nucleation mechanisms (see fits below). In contrast, AFM images of aggregate populations sampled during the initial phase of biphasic growth only show significant buildup of small gOs and CFs. This matches with the high reaction-order of gO/CF formation discussed below. Following the second upswing, in turn, AFM detects RFs in the solution (Fig. 2B and E). While AFM images of samples taken near the end of the kinetics traces clearly show RFs, significant populations of residual gO/CFs

persist and their concentrations increase with monomer concentration above the COC. For hewL, for example, an additional two weeks of incubation were required before RFs had completely replaced gO/CFs. Hence, the apparent decline in the ThT amplitude above the COC (Fig. 2C) arises from the increasing populations of (weakly ThT positive) residual gO/CFs and their glacial pace of depolymerisation into (strongly ThT positive) RFs.

Inherent metastability of gO/CFs

The slow depletion of gO/CFs by RFs highlights perhaps the most distinctive feature of gO/CFs: their intrinsic metastability against RF formation.[13,46] We previously corroborated the metastability of hewL gO/CFs by seeding solutions above the COC with RFs, which readily grew and replaced gO/CFs. Similarly, isolated gO/CFs, when seeded into monomeric solutions below the COC, dissolved and did so at progressively faster rates the further monomer concentrations were below the COC.[46] Fig. 3A exemplifies this behavior by showing the kinetics of an unseeded, RF seeded and gO/CF seeded monomer solution, with the total monomer concentration after seeding remaining below the COC. While seeding with isolated RFs induced lag-free RF elongation, seeding with isolated gO/CFs at identical concentrations caused their slow decay and increased the RF lag period compared to the unseeded sample. Moreover, we previously established that the binding protein ZAβ3, which sequesters monomeric Aβ, achieves dissolution of Aβ42 gO/CFs but not of Aβ42 RFs.[65,67] Here, we used ZAβ3 as a tool to monitor the slow depletion of gO/CFs and the concomitant RF growth (Fig. 3B). When an excess of ZAβ3 is added to dimAβ assembly reactions before the second ThT upswing, fluorescence vanishes almost completely on the time scale of hours, indicating dissolution of gO/CFs at the expense of formation of the dimAβ:ZAβ3 complex. In contrast, when ZAβ3 is added after the second ThT upswing, the amplitude of the fluorescence drop progressively decreases the later ZAβ3 is added, reflecting the increasing formation of stable RFs and concomitant decrease of gO/CFs susceptible to disaggregation into the dimAβ:ZAβ3 complex (Fig. 3B). Incubation of preformed dimAβ:ZAβ3 complexes in the presence of sonicated dimAβ RF seeds resulted in the dissociation of the dimAβ:ZAβ3 complex at the expense of RF growth (Fig. S3†). Thus the dimAβ states can be ordered according to their thermodynamic stability: RF-incorporated > ZAβ3-bound > gO/CF-incorporated (Fig. 3C). This indicates substantially higher thermodynamic stability of RFs compared to gO/CFs.

High reaction order of gO formation

As noted above, using the dimeric Aβ construct helped to separate the time regimes of dominant gO/CF *vs.* RF formation sufficiently to allow separate analysis of the gO/CF assembly kinetics (Fig. 4A and B). A global fit to the concentration-dependent time course of the initial fluorescence increase with a primary nucleation-growth model,[68] assuming a common nucleus size as well as common nucleation and elongation rate constants, shows clear systematic deviations (Fig. 4A). However, it could be fit to an n^{th}-order oligomerization reaction with a global rate constant for all concentrations (Fig. 4B). The reaction order obtained from global fits to three independent data sets was 3.3 ± 0.2, reflecting the high concentration dependence of gO/CF formation. This high reaction order explains the observability of a well-defined COC. Considering that one dimAβ molecule contains two Aβ units, the reaction order of ~3.3 suggests an oligomer size of six to seven Aβ units, which is compatible with previous studies indicating a prominent role of hexamers in Aβ assembly.[69–72] For hewL, gO/CF and RF kinetics overlapped, requiring a simultaneous fit to both gO/CF and RF growth (Fig. 4C), with the gO/CF portion better

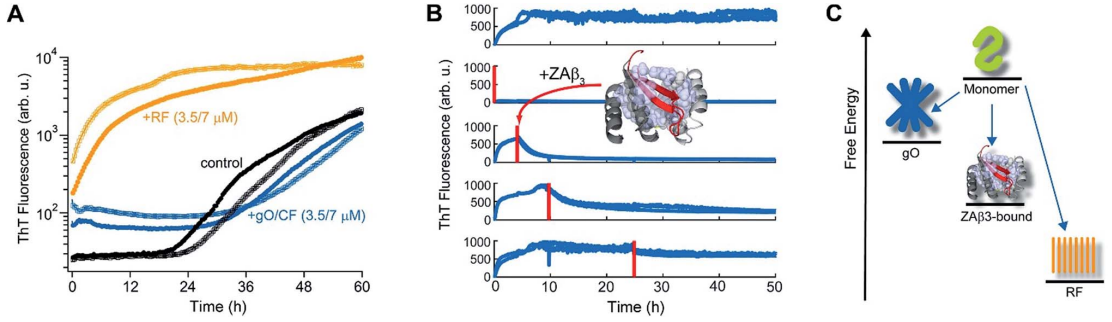

Fig. 3 Metastability and RF seeding incompetence of gO/CFs. (A) HewL RF kinetics below the COC (38 μM hewL, 400 mM NaCl) without seeding (black), or after seeding with isolated gO/CFs (blue) or RFs (orange) at either 3.5 or 7 μM each, and incubated at pH 2, $T = 52\,^{\circ}C$. (B) ThT-detected dissociation of pre-assembled dimAβ upon addition of the binding protein ZAβ3 (grey), which sequesters monomeric dimAβ in a β-hairpin conformation (red, see ref. 65 and 67). The complex is shown in ribbon representation, hydrophobic side chains of ZAβ3 in direct contact with the Aβ40 β-hairpin are shown as spheres (Protein Data Bank entry 2OTK). The assembly of 6 μM dimAβ was monitored by ThT fluorescence, with addition of 14 μM ZAβ3 at different time points, indicated by red lines. Addition of ZAβ3 during the gO/CF formation-dominated time regime results in nearly complete loss of ThT fluorescence, while ZAβ3 addition during the RF-dominated time regime leads to a progressive decrease in the amplitude of the fluorescence drop. (C) Energy diagram illustrating the order of thermodynamic stability of different states of Aβ, above the COC and under the present experimental conditions.

View Article Online
Chemical Science Edge Article

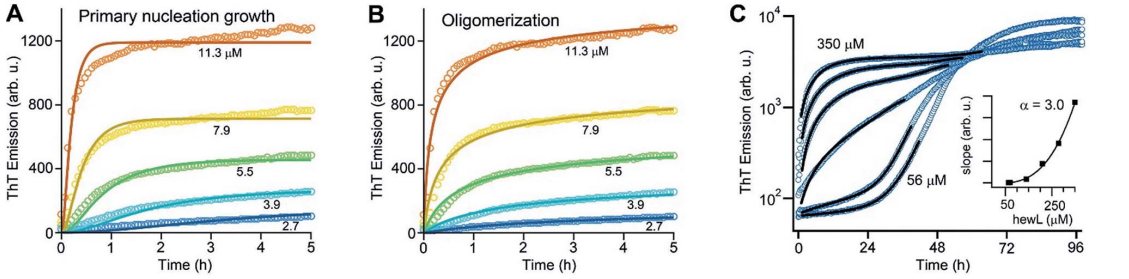

Fig. 4 gO formation kinetics. (A, B) Concentration-dependent kinetics of gO/CF formation of dimAβ monitored by ThT fluorescence. Global fits to the data were performed using (A) a primary nucleation-growth model (eqn (2); see Materials and methods in the ESI†) or (B) a one-step oligomerization model (eqn (3)†). The reaction order obtained from the global fit to the data set in (B) was 3.4 ± 0.1. (C) Fits to the early stages of hewL ThT kinetics combining a single-exponential with the model for nucleated polymerization (eqn (4) & (1)†). The inset shows the power-law increase in the exponential growth rate required to fit the data.

represented by first-order kinetics. The near first-order kinetics of hewL gO/CFs probably reflects the propensity of hewL gOs to assemble further into CFs (see Fig. 2E), with a simultaneous decrease in net reaction order. However, the exponential rate constant fitting the gO/CF data increased as a non-linear 3rd-order function in monomer concentration (Fig. 4C, inset), again suggesting a high reaction-order for the initial gO formation step. In both cases, the concentration dependence of gO/CF formation is much higher than the one for RF formation, for which negative scaling exponents down to only −1.7 were reported.[73] These observations indicate once more that gO/CF formation occurs through a fundamentally different reaction mechanism than RF formation and rapidly becomes the initially dominant growth process above the COC.

GO/CFs are retarding RF nucleation and growth

Crossing the COC results in a sharp transition from RF nucleation and growth in the absence of metastable gO/CFs to their concurrent growth. This provides the unique opportunity to evaluate how gO/CFs alter the mechanisms of RF nucleation and growth, while maintaining fixed solution conditions and monomer conformations. Theoretical considerations indicate that RF lag periods follow specific scaling laws as function of monomer concentration, with the magnitude of the scaling coefficients providing information about the underlying molecular mechanisms of fibril nucleation and growth.[39,74] Here we investigated whether and how the presence of increasing concentrations of gO/CFs above the COC altered these scaling laws for RF nucleation and growth. It is worth mentioning that this comparison is valid irrespective of whether RFs nucleate *via* homogeneous or heterogeneous nucleation mechanism(s). In the absence of metastable gOs (*i.e.* below the COC) we fit RF kinetics with the analytical expression for nucleated polymerization with secondary mechanisms that ignores late-stage monomer depletion (early time approximation of eqn (1), see Materials and methods in the ESI† and ref. 38). Besides the quality of the individual fits (Fig. 5A), the net rate for primary and secondary nucleation extracted varied within a narrow range (Fig. 5B). The dominance of secondary over primary nucleation (Fig. 5B) reflects the highly cooperative character of RF nucleation, as already apparent from the initially completely flat ThT responses. The critical importance of autocatalytic nucleation mechanisms replicates prior observations with a multitude of amyloid proteins.[38,74]

To fit RF kinetics of dimAβ above the COC, we first subtracted the global fits of the gO/CF formation time regime to an oligomerization reaction from the entire time traces (Fig. 5D). The resulting time courses represent the RF portion of the ThT signal. This treatment disregards the depletion of gO/CFs after the second ThT upswing. However, this introduces only a negligible error into the determination of lag-times, as gO/CF depletion is slow and becomes significant only long after the lag phase (see AFM images for Fig. 2B and E). Lag-times were obtained from the RF portions of the data by applying the same fits as for RF kinetics below the COC. In the case of hewL the time regimes of dominant gO/CF formation and dominant RF formation above the COC were not as clearly separated. We therefore fitted the data simultaneously to a combination of the above analytical approximation for RF growth (eqn (1)†) with a saturating exponential growth for gO/CFs (eqn (4)†). Fig. 4C indicates that the resulting fits were good when limited to the early stages of RF nucleation. Subtraction of the gO/CF component of the fits from the raw data again yielded the sigmoidal time traces expected for the RF portion of the ThT data (Fig. 5C).

Several striking features emerge from the log–log plots for RF lag time *vs.* protein concentration (Fig. 5E and F). The lag periods below the COC (orange) do decrease as a power law in monomer concentration, with scaling exponents yielding values of $\alpha = -(0.24 \pm 0.07)$ and $\alpha = -(0.32 \pm 0.05)$ for hewL and dimAβ, respectively. As recently shown, scaling exponents below a magnitude of 0.5 indicate that dock and lock steps upon monomer addition at the growing fibril end become rate-limiting of fibril elongation.[39] Neglecting gO/CF formation, one would expect lag periods above the COC to continue to shorten as indicated by the extrapolation of the power law obtained below the COC (Fig. 5E and F, solid black lines). While this holds true for some data points just above the COC, rapidly increasing formation of gO/CFs above the COC not only arrests

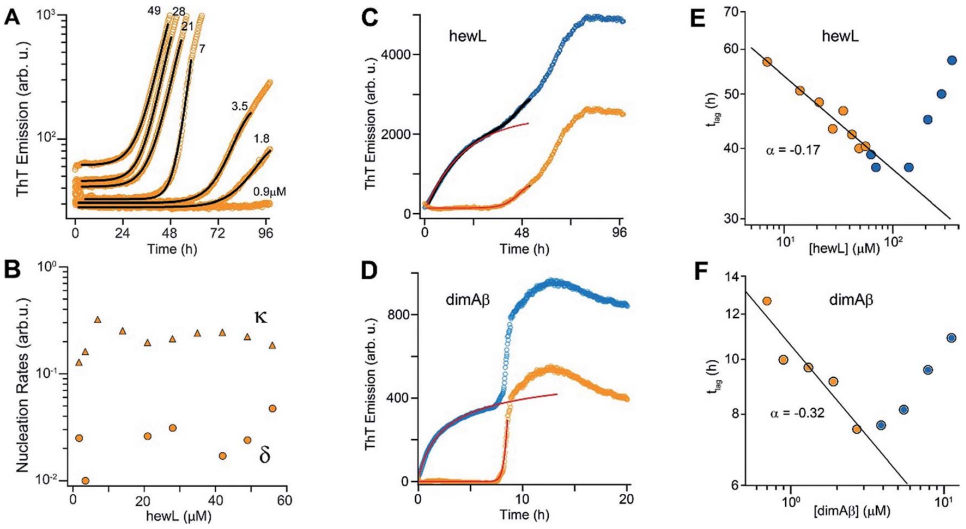

Fig. 5 gO/CFs are retarding RF nucleation and growth. (A) Fit to ThT kinetics of hewL RFs below the COC with the analytical solution for nucleated polymerization (eqn (1)†). (B) Primary (δ) and secondary (κ) nucleation parameters obtained by the fits. (C, D) Typical ThT kinetics above the COC (blue circles), and their underlying RF kinetics (orange circles) obtained after subtracting the oligomeric portion of the fit (red line) from the data for hewL (C) and dimAβ (D). (E, F) RF lag times of hewL (E) and dimAβ (F) extracted from fits to experimental kinetics below (orange) and above (blue) the COC. The solid lines are power-law fits through these specific data sets below the COC (exponent $\alpha = -(0.17 \pm 0.02)$ (hewL) and $-(0.32 \pm 0.06)$ (dimAβ)). Three or four, respectively, independent repeats of these measurements yielded power law values of $\alpha = -(0.24 \pm 0.07)$ (hewL) and $\alpha = -(0.32 \pm 0.05)$ (dimAβ).

the decrease but progressively increases RF lag periods with increasing protein concentration, as shown by the blue data points. A leveling off of the lag periods would be consistent with gO/CFs as off-pathway competitors of RFs. As monomer concentrations exceed the COC, the increasingly rapid pace of gO/CF formation eventually depletes monomers down to their value at the COC. As a result RF nucleation rates from monomers would be reduced to their value at the COC. The experimentally observed rapid increase in RF lag periods, though, implies that gO/CFs actively inhibit RF nucleation beyond the capacity for off-pathway aggregates to buffer monomer concentrations.

GO/CFs act as off-pathway competitors of RFs, not as on-pathway precursors

The above changes in scaling behaviour of lag periods upon onset of oligomer formation speak to the broader question whether gO/CFs are on-pathway precursors or off-pathway competitors of RF growth. To be effective precursors of RF seed formation, gO/CFs should decrease the lag periods upon crossing the COC. Even if gO/CFs are only slowly converting to RFs, lag periods above the COC should, at best, level off. Instead, lag periods increase. Hence, nucleated conformational conversion (NCC) of the gO/CFs observed here into RF seeds is not a feasible mechanism. Our qualitative observation that AFM imaging of samples with particularly high concentrations of gO/CF failed to generate RFs for weeks further corroborates the off-pathway character of gO/CFs.

As additional confirmation that hewL gO/CFs are incapable of conversion into RFs on the time scale of spontaneous RF nucleation from monomers we seeded isolated gO/CFs or RFs into solutions below the COC. As shown in Fig. 3A, controls without addition of seeds (black traces) underwent traditional nucleated polymerization. Seeding with preformed and isolated RFs (orange traces) eliminated the lag period and resulted in immediate fibril elongation. In contrast, adding identical concentrations of gO/CF seeds (blue traces) increased RF lag periods just as observed above the COC. This further supports the conclusion that gO/CFs, instead of being on-pathway for RF nucleation, retard the process of RF nucleation from monomers. The data in Fig. 3A also address the unlikely scenario that we might have missed small populations of gO/CFs already present below the COC, which in turn dominate nucleation rates under those conditions. The significant increase in the ThT baseline upon adding gO/CFs indicates that their concentrations are well above any vanishingly small levels of gO/CF present below the COC. Yet, even at those high concentrations, they do not promote RF formation. Notably, the progressively prominent inhibitory effect of gO/CF formation on RF nucleation and growth with increasing protein concentration falls outside the current versions for off-pathway oligomer formation as well.

Numerical simulations of biphasic off-pathway oligomer growth

The above data suggest that gO/CFs are off-pathway products that emerge only over the limited range of amyloid fibril growth

View Article Online
Chemical Science Edge Article

conditions above the COC. They are non-obligatory since RFs can readily form above and below the COC. To gain a better understanding of the transition from sigmoidal to biphasic growth kinetics not just during the initial stage of RF nucleation but over the entire range of reaction time scales, we adopted the off-pathway kinetics model originally proposed by Powers and Powers,[75] but modified it in two significant ways. First, off-pathway oligomer formation was limited to concentrations above the COC. In addition, we needed to include secondary nucleation mechanisms for on-pathway fibril growth in order to replicate the experimentally observed RF kinetics. Details of the numerical scheme are provided in the ESI.† An example of fitting experimental kinetics below and above the COC to simulated growth kinetics is illustrated in Fig. 6 (for further examples see Fig. S4†). This off-pathway kinetic model readily replicates the transition from sigmoidal to biphasic behavior seen in our experimental data. Equally important, it provides a natural decomposition of the ThT signal into its gO/CF and RF components. Since the current model does not include mechanisms to account for active inhibition of RFs by gO/CF formation, the parameters for RF formation rates had to be adjusted to match the individual kinetic curves.

Discussion

The combined kinetics and imaging data reported here show that the sharp transition in amyloid assembly from sigmoidal to biphasic kinetics coincides with the onset of gO/CF formation above a protein and solution-condition dependent COC (Fig. 2A and C). Prior reports of biphasic ThT kinetics for Aβ[43,63,66] and Sup35 yeast protein[42] suggest that biphasic kinetics represent a generic mode for amyloid assembly. Similarly, there are previous reports associating a micelle-like transition in Aβ40,[64,76,77] amylin,[78] β-microglobulin,[21] and lysozyme,[46] with the formation of gO/CFs. Our data indicate that biphasic kinetics represents a generic mode of amyloid assembly that is directly related to the formation of metastable gO/CF formation, and is distinct from the sigmoidal kinetics associated with nucleated polymerization of RFs from monomers. The lack of any detectable gO/CFs below the COC (Fig. 2D) and their inability to accelerate RF nucleation and growth under those conditions (Fig. 3A) indicates that metastable gO/CFs are not precursors of RFs. This distinguishes gO/CFs from any on-pathway oligomeric fibril seeds transiently formed below the COC.

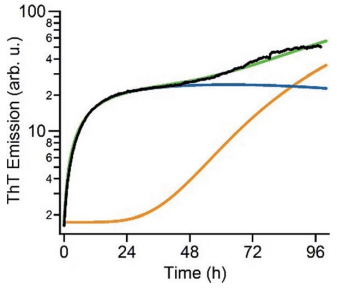

Fig. 6 Numerical simulation of biphasic ThT kinetics. Fit of the experimental ThT kinetics for 280 μM hewL (black) to the dual-pathway assembly model (green) and corresponding decomposition into its RF (orange) and gO/CF (blue) components.

We presume that the commonly observed formation of gO/CFs and RFs by various amyloid proteins, and over a wide range of solution conditions, arises from two basic yet distinct features of polypeptide chains: their amphiphilic nature and their propensity to form intermolecular hydrogen bonds across their backbone. The latter is well established as the fundamental driving force underlying RF formation.[79] Similarly, the amphiphilic character of polypeptide chains has been repeatedly suggested to contribute to the existence of a COC and gO formation.[77,78] We have previously provided a quantitative colloidal model replicating both the salt and protein concentration dependence of the COC of hewL.[46] The available structural data suggest that gOs are short anti-parallel β-barrels,[80] clearly distinct from the steric zipper structure of RFs. GO/CFs arising from amphiphilic phase separation *vs.* RFs *via* intermolecular hydrogen bonding also rationalizes the existence of two distinct aggregate species formed along separate assembly pathways. Furthermore, it explains why they have distinct morphologies and mechanical rigidities (sterically constrained gOs polymerizing into weakly-linked CFs *vs.* mechanically rigid hydrogen-linked RFs), their relative thermodynamic stabilities (weaker linked gO/CFs *vs.* strongly bonded RFs), the distinct reaction orders of their formation (as reported here), their dependence on various solution parameters such as pH, ionic strength, specific ion effects, and of course, their dependence on the primary sequence of the polypeptide chain itself.

Recently, it has been proposed that the switch from RFs to gO/CFs in β-lactoglobulin at strongly hydrolyzing conditions (90 °C, pH 2) results from concentration-dependent changes to the distributions of hydrolyzed fragments.[81] It is possible that different peptides do undergo either gO/CF or RF formation at identical solution conditions. For our hewL assembly conditions (52 °C, pH 2) we have shown that the switch from RF to gO/CF formation can be readily induced by increasing salt at fixed protein concentrations (see horizontal lines in Fig. 1B),[46] while hydrolysis rates across the COC were unchanged (Fig. 4 in ref. 54). Here we show that pre-hydrolyzing hewL for multiple days has no discernible effect on RF kinetics which, due to its long lag periods, would be most susceptible to hydrolysis (see Fig. S5†). Hence, we believe hydrolysis is not fundamental to the switch from RF to gO/CF formation.

The sharp transition from "oligomer-free" to "oligomeric" RF growth upon crossing the COC allowed us to address a long-standing question: what role do metastable gO/CFs play in the nucleation–polymerization of RFs? Qualitatively, NCC fits well with the lag-free emergence of gO/CFs and the biphasic kinetics for gO/CF growth with late-stage RF nucleation and growth. However, the inability of gO/CFs to seed RF growth below the COC (Fig. 3A) and their inhibitory effects on RF formation above the COC (Fig. 5E and F) are inconsistent with NCC. We note, however, that protein-specific factors such as the structure of the protein undergoing assembly or the size and structure of its

oligomers might affect whether NCC is a feasible RF nucleation mechanism under other conditions. Large liquid-like droplets have been reported to arise during polyQ fibril assembly or β2 microglobulin disassembly.[82,83] Hence, there remains uncertainty whether there are multiple, potentially distinct metastable states, and how those might be related to each other and to late-stage fibrils.

Extrapolating NP scaling laws, established below the COC, to monomer concentrations above the COC allowed us to quantify how gO/CF formation altered NP. Crossing the COC, the scaling law for lag periods with monomer concentration initially developed a kink. Kinks in the scaling behavior of RF lag periods, albeit to a lesser degree, have been reported for insulin, bovine serum albumin and lysozyme.[39,41,84] Even inverse relationships between half-time and/or lag-time of amyloid fibril growth have been observed before for the light chain variable domain LEN,[85] ribosomal protein S6,[86] glucagon-like peptide-1,[31] and Aβ[66] and have been explained with competing off-pathway aggregation. A model for competing off-pathway aggregation by Powers and Powers[75] did generate an inverse relationship between half-time for reaction completion (but not lag-time) of amyloid formation at high protein concentration, due to monomer depletion by off-pathway precipitates. Importantly, though, COC-limited monomer depletion can only explain an arrest but not the increase in the RF lag-times reported here. The identified active inhibition of RF formation by gO/CFs necessitates modification of the standard cNP model (Fig. 7).

The COCs observed here are relatively high compared to typical *in vivo* protein concentrations. For example, dimAβ, although showing increased oligomerization propensity due to covalent linkage of two Aβ units, has a COC of the order of 1 μM (in low salt buffer at neutral pH), whereas physiological Aβ concentrations are in the nanomolar range.[87] Similar discrepancies, though, exist for Aβ fibril solubilities, with the latter ranging from hundreds of nanomolar to millimolars. It is important to realize in this context that there are multiple factors that can significantly reduce COCs or increase local protein concentrations *in vivo*. These include salt concentration and pH (see Fig. 1B) (*e.g.*, accumulation of micromolar concentrations of Aβ in acidic vesicles[87]); interfaces, such as membrane or fibril surfaces;[88] post-translational modifications such as cross-links;[30] macromolecular crowding;[89] and disease-related mutations, some of which strongly promote gO/CF formation.[17,90,91] Moreover, interactions with other cellular components may affect gO/CF formation. For example, interaction with another aggregation-prone protein, TDP-43, was shown to strongly promote gO/CF formation of Aβ at the expense of RF formation.[92] The relatively high COCs observed for the two model systems therefore likely result from the present experimental conditions. Interestingly, reduced expression of APP in mouse models that did not affect plaque load led to reduced formation of plaque-unrelated oligomers, suggesting that the concentration dependence of gO/CF formation has a correlate *in vivo*.[93,94]

The above results paint a complex picture of how RF formation proceeds in the presence of gO/CFs. The mutual interactions among gO/CFs and RFs, either direct or *via* the monomer pool, are likely to feature prominently in the temporal evolution of gO/CFs *vs.* RF populations *in vivo*, as well. There are solid indications that gO/CFs and RFs have distinct biological/pathological activity profiles that might vary with protein identity, its growth conditions, and its cellular environment.[20,27,57,95–98] The retarding effects of early-stage gOs on the nucleation and growth of late-stage RFs might result in extended exposure to toxic oligomers and low rates of RF formation and gO/CF depletion *in vivo*. This provides one possible explanation for the paradoxical observations that post-mortem RF loads correlate poorly with the severity of clinical symptoms.[99,100] Overall, systematic investigation of the thermodynamic and kinetic factors regulating the assembly of distinct amyloid species *in vitro* and their mutual interplay can provide important insights into the mechanisms regulating amyloid assembly *in vivo*.

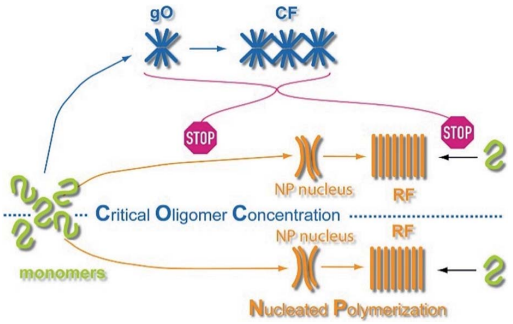

Fig. 7 Scheme of amyloid oligomer and fibril formation. GO/CFs are metastable off-pathway assemblies formed to a significant extent above the COC. GO/CFs inhibit RF formation not only by buffering monomer concentration to the COC level, thereby slowing fibril nucleation and elongation, but also by actively disrupting either process (STOP signs). The precise mechanism of this active inhibition remains to be elucidated.

Conflicts of interest

There are no conflicts to declare.

Acknowledgements

This work was supported by NIH grant 2R15GM097723-02 (M. M.), NIH grant R01AG053988 (G. U.), ERC Consolidator grant 726368 (W. H.), Alzheimer Forschungs Initiative (W. H.), and Sidney Sussex College Cambridge (G. Me.). Access to the Jülich-Düsseldorf Biomolecular NMR Center is acknowledged.

Notes and references

1 E. H. Koo, J. Lansbury, P. T. Lansbury Jr and J. W. Kelly, *Proc. Natl. Acad. Sci. U. S. A.*, 1999, **96**, 9989–9990.
2 C. A. Ross and M. A. Poirier, *Nat. Med.*, 2004, **10**, S10–S17.

3 F. Chiti and C. M. Dobson, *Annu. Rev. Biochem.*, 2006, **75**, 333–366.
4 M. Stefani, *Biochim. Biophys. Acta*, 2004, **1739**, 5–25.
5 M. Sunde and C. F. F. Blake, *Q. Rev. Biophys.*, 1998, **31**, 1–39.
6 J. N. Buxbaum, *Curr. Opin. Rheumatol.*, 2004, **16**, 67–75.
7 L. M. Blancas-Mejia and M. Ramirez-Alvarado, *Annu. Rev. Biochem.*, 2013, **82**, 745–774.
8 D. Eisenberg and M. Jucker, *Cell*, 2012, **148**, 1188–1203.
9 M. B. Pepys, P. N. Hawkins, D. R. Booth, D. M. Vigushin, G. A. Tennent, A. K. Soutar, N. Totty, O. Nguyen, C. C. F. Blake, C. J. Terry, T. G. Feest, A. M. Zalin and J. J. Hsuan, *Nature*, 1993, **362**, 553–557.
10 D. M. Fowler, A. V. Koulov, W. E. Balch and J. W. Kelly, *Trends Biochem. Sci.*, 2007, **32**, 217–224.
11 I. Benilova, E. Karran and B. De Strooper, *Nat. Neurosci.*, 2012, **15**, 349–357.
12 R. Kayed, E. Head, J. L. Thompson, T. M. McIntire, S. C. Milton, C. W. Cotman and C. G. Glabe, *Science*, 2003, **300**, 486–489.
13 R. Kodali and R. Wetzel, *Curr. Opin. Struct. Biol.*, 2007, **17**, 48–57.
14 D. M. Walsh, A. Lomakin, G. B. Benedek, M. M. Condron and D. B. Teplow, *J. Biol. Chem.*, 1997, **272**, 22364–22372.
15 H. A. Lashuel, C. Wurth, L. Woo and J. W. Kelly, *Biochemistry*, 1999, **38**, 13560–13573.
16 Y. E. Kim, F. Hosp, F. Frottin, H. Ge, M. Mann, M. Hayer-Hartl and F. U. Hartl, *Mol. Cell*, 2016, **63**, 951–964.
17 K. A. Conway, S.-J. Lee, J.-C. Rochet, T. T. Ding, R. E. Williamson and P. T. Lansbury, *Proc. Natl. Acad. Sci. U. S. A.*, 2000, **97**, 571–576.
18 C. A. Lasagna-Reeves, D. L. Castillo-Carranza, M. J. Guerrero-Muñoz, G. R. Jackson and R. Kayed, *Biochemistry*, 2010, **49**, 10039–10041.
19 V. Novitskaya, O. V. Bocharova, I. Bronstein and I. V. Baskakov, *J. Biol. Chem.*, 2006, **281**, 13828–13836.
20 W. B. Stine Jr, K. N. Dahlgren, G. A. Krafft and M. J. LaDu, *J. Biol. Chem.*, 2003, **278**, 11612–11622.
21 W. S. Gosal, I. J. Morten, E. W. Hewitt, D. A. Smith, N. H. Thompson and S. E. Radford, *J. Mol. Biol.*, 2005, **351**, 850–864.
22 R. Kayed, Y. Sokolov, B. Edmonds, T. M. McIntire, S. C. Milton, J. E. Hall and C. G. Glabe, *J. Biol. Chem.*, 2004, **279**, 46363–46366.
23 M. N. N. Vieira, L. Forny-Germano, L. M. Saraiva, A. Sebollela, A. M. B. Martinez, J.-C. Houzel, F. G. De Felice and S. T. Ferreira, *J. Neurochem.*, 2007, **103**, 736–748.
24 K. Ono, M. M. Condron and D. B. Teplow, *Proc. Natl. Acad. Sci. U. S. A.*, 2009, **106**, 14745–14750.
25 L. V. Kalia, S. K. Kalia, P. J. McLean, A. M. Lozano and A. E. Lang, *Ann. Neurol.*, 2013, **73**, 155–169.
26 K. N. Dahlgren, A. M. Manelli, W. B. Stine, J. Baker, K. Lorinda, G. A. Krafft and M. J. LaDu, *J. Biol. Chem.*, 2002, **277**, 36046–36053.
27 M. Malisauskas, A. Darinskas, V. Zamotin, A. Gharibyan, I. Kostanyan and L. Morozova-Roche, *Biochemistry*, 2006, **71**, 505–512.
28 M. P. Lambert, A. K. Barlow, B. A. Chromy, C. Edwards, R. Freed, M. Liosatos, T. E. Morgan, I. Rozovsky, B. Trommer, K. L. Viola, P. Wals, C. Zhang, C. E. Finch, G. A. Krafft and W. L. Klein, *Proc. Natl. Acad. Sci. U. S. A.*, 1998, **95**, 6448–6453.
29 R. Kayed and C. A. Lasagna-Reeves, *J. Alzheimer's Dis.*, 2013, **33**, S67–S78.
30 B. O'Nuallain, D. B. Freir, A. J. Nicoll, E. Risse, N. Ferguson, C. E. Herron, J. Collinge and D. M. Walsh, *J. Neurosci.*, 2010, **30**, 14411–14419.
31 K. L. Zapadka, F. J. Becher, S. Uddin, P. G. Varley, S. Bishop, A. L. Gomes dos Santos and S. E. Jackson, *J. Am. Chem. Soc.*, 2016, **138**, 16259–16265.
32 A. L. Fink, *Folding Des.*, 1998, **3**, R9–R23.
33 M. Muschol and F. Rosenberger, *J. Chem. Phys.*, 1997, **107**, 1953–1962.
34 S. M. Vaiana, M. B. Palma-Vittorelli and M. U. Palma, *Proteins: Struct., Funct., Bioinf.*, 2003, **51**, 147–153.
35 A. Patel, H. O. Lee, L. Jawerth, S. Maharana, M. Jahnel, M. Y. Hein, S. Stoynov, J. Mahamid, S. Saha, T. M. Franzmann, A. Pozniakovski, I. Poser, N. Maghelli, L. A. Royer, M. Weigert, E. W. Myers, S. Grill, D. Drechsel, A. A. Hyman and S. Alberti, *Cell*, 2015, **162**, 1066–1077.
36 L. Wei, P. Jiang, W. Xu, H. Li, H. Zhang, L. Yan, M. B. Chan-Park, X.-W. Liu, K. Tang, Y. Mu and K. Pervushin, *J. Biol. Chem.*, 2011, **286**, 6291–6300.
37 C. Bleiholder, N. F. Dupuis, T. Wyttenbach and M. T. Bowers, *Nat. Chem.*, 2010, **3**, 172.
38 T. P. J. Knowles, C. A. Waudby, G. L. Devlin, S. I. A. Cohen, A. Aguzzi, M. Vendruscolo, E. M. Terentjev, M. E. Welland and C. M. Dobson, *Science*, 2009, **326**, 1533–1537.
39 G. Meisl, J. B. Kirkegaard, P. Arosio, T. C. T. Michaels, M. Vendruscolo, C. M. Dobson, S. Linse and T. P. J. Knowles, *Nat. Protoc.*, 2016, **11**, 252–272.
40 G. Meisl, X. Yang, B. Frohm, T. P. J. Knowles and S. Linse, *Sci. Rep.*, 2016, **6**, 18728.
41 G. Meisl, L. Rajah, S. A. I. Cohen, M. Pfammatter, A. Saric, E. Hellstrand, A. K. Buell, A. Aguzzi, S. Linse, M. Vendruscolo, C. M. Dobson and T. P. J. Knowles, *Chem. Sci.*, 2017, **8**, 7087–7097.
42 T. R. Serio, A. G. Cashikar, A. S. Kowal, G. J. Sawicki, J. J. Moslehi, L. Serpell, M. F. Arnsdorf and S. L. Lindquist, *Science*, 2000, **289**, 1317–1321.
43 J. Lee, E. K. Culyba, E. T. Powers and J. W. Kelly, *Nat. Chem. Biol.*, 2011, **7**, 602–609.
44 M. Necula, R. Kayed, S. Milton and C. G. Glabe, *J. Biol. Chem.*, 2007, **282**, 10311–10324.
45 S. Matsumura, K. Shinoda, M. Yamada, S. Yokojima, M. Inoue, T. Ohnishi, T. Shimada, K. Kikuchi, D. Masui, S. Hashimoto, M. Sato, A. Ito, M. Akioka, S. Takagi, Y. Nakamura, K. Nemoto, Y. Hasegawa, H. Takamoto, H. Inoue, S. Nakamura, Y.-i. Nabeshima, D. B. Teplow, M. Kinjo and M. Hoshi, *J. Biol. Chem.*, 2011, **286**, 11555–11562.
46 T. Miti, M. Mulaj, J. D. Schmit and M. Muschol, *Biomacromolecules*, 2015, **16**, 326–335.

47 J. N. Israelachvili, in *Intermolecular and Surface Forces*, Academic Press, Burlington, MA, 3rd edn, 2011, ch. 19.
48 M. Adachi, M. So, K. Sakurai, J. Kardos and Y. Goto, *J. Biol. Chem.*, 2015, **290**, 18134–18145.
49 T. R. Jahn and S. E. Radford, *Arch. Biochem. Biophys.*, 2008, **469**, 100–117.
50 S. E. Hill, T. Miti, T. Richmond and M. Muschol, *PLoS One*, 2011, **6**, e18171.
51 S. E. Hill, J. Robinson, G. Matthews and M. Muschol, *Biophys. J.*, 2009, **96**, 3781–3790.
52 D.-P. Hong, A. L. Fink and V. N. Uversky, *J. Mol. Biol.*, 2008, **383**, 214–223.
53 R. H. Pires, Á. Karsai, M. J. Saraiva, A. M. Damas and M. S. Z. Kellermayer, *PLoS One*, 2012, **7**, e44992.
54 J. Foley, S. E. Hill, T. Miti, M. Mulaj, M. Ciesla, R. Robeel, C. Persichilli, R. Raynes, S. Westerheide and M. Muschol, *J. Chem. Phys.*, 2013, **139**, 121901–121912.
55 G. Zandomeneghi, M. R. H. Krebs, M. G. McCammon and M. Fändrich, *Protein Sci.*, 2004, **13**, 3314–3321.
56 E. Cerf, R. Sarroukh, S. Tamamizu-Kato, L. Breydo, S. Derclaye, Y. F. Dufrêne, V. Narayanaswami, E. Goormaghtigh, J.-M. Ruysschaert and V. Raussens, *Biochem. J.*, 2009, **421**, 415–423.
57 A. Laganowsky, C. Liu, M. R. Sawaya, J. P. Whitelegge, J. Park, M. Zhao, A. Pensalfini, A. B. Soriaga, M. Landau, P. K. Teng, D. Cascio, C. Glabe and D. Eisenberg, *Science*, 2012, **335**, 1228–1231.
58 M. I. Apostol, K. Perry and W. K. Surewicz, *J. Am. Chem. Soc.*, 2013, **135**, 10202–10205.
59 U. Sengupta, A. N. Nilson and R. Kayed, *Exp. Biol. Med.*, 2016, **6**, 42–49.
60 T. T. O'Malley, N. A. Oktaviani, D. Zhang, A. Lomakin, B. O'Nuallain, S. Linse, G. B. Benedek, M. J. Rowan, F. A. A. Mulder and D. M. Walsh, *Biochem. J.*, 2014, **461**, 413–426.
61 T. T. O'Malley, W. M. Witbold, S. Linse and D. M. Walsh, *Biochemistry*, 2016, **55**, 6150–6161.
62 T. Yamaguchi, H. Yagi, Y. Goto, K. Matsuzaki and M. Hoshino, *Biochemistry*, 2010, **49**, 7100–7107.
63 Z. Fu, D. Aucoin, J. Davis, W. E. Van Nostrand and S. O. Smith, *Biochemistry*, 2015, **54**, 4197–4207.
64 A. Lomakin, D. S. Chung, G. B. Benedek, D. A. Kirschner and D. B. Teplow, *Proc. Natl. Acad. Sci. U. S. A.*, 1996, **93**, 1125–1129.
65 L. M. Luheshi, W. Hoyer, T. P. de Barros, I. van Dijk Härd, A.-C. Brorsson, B. Macao, C. Persson, D. C. Crowther, D. A. Lomas, S. Ståhl, C. M. Dobson and T. Härd, *PLoS Biol.*, 2010, **8**, e1000334.
66 M. Nick, Y. Wu, N. W. Schmidt, S. B. Prusiner, J. Stöhr and W. F. DeGrado, *Biopolymers*, 2018, e23096.
67 C. S. R. Grüning, S. Klinker, M. Wolff, M. Schneider, K. Toksöz, A. N. Klein, L. Nagel-Steger, D. Willbold and W. Hoyer, *J. Biol. Chem.*, 2013, **288**, 37104–37111.
68 S. I. A. Cohen, M. Vendruscolo, M. E. Welland, C. M. Dobson, E. M. Terentjev and T. P. J. Knowles, *J. Chem. Phys.*, 2011, **135**, 065105.
69 R. Roychaudhuri, M. Yang, M. M. Hoshi and D. B. Teplow, *J. Biol. Chem.*, 2009, **284**, 4749–4753.
70 S. L. Bernstein, N. F. Dupuis, N. D. Lazo, T. Wyttenbach, M. M. Condron, G. Bitan, D. B. Teplow, J.-E. Shea, B. T. Ruotolo, C. V. Robinson and M. T. Bowers, *Nat. Chem.*, 2009, **1**, 326–331.
71 M. Wolff, B. Zhang-Haagen, C. Decker, B. Barz, M. Schneider, R. Biehl, A. Radulescu, B. Strodel, D. Willbold and L. Nagel-Steger, *Sci. Rep.*, 2017, **7**, 2493.
72 M. Cernescu, T. Stark, E. Kalden, C. Kurz, K. Leuner, T. Deller, M. Göbel, G. P. Eckert and B. Brutschy, *Anal. Chem.*, 2012, **84**, 5276–5284.
73 G. Meisl, X. Yang, C. M. Dobson, S. Linse and T. P. J. Knowles, *Chem. Sci.*, 2017, **8**, 4352–4362.
74 S. I. A. Cohen, S. Linse, L. M. Luheshi, E. Hellstrand, D. A. White, L. Rajah, D. E. Otzen, M. Vendruscolo, C. M. Dobson and T. P. J. Knowles, *Proc. Natl. Acad. Sci. U. S. A.*, 2013, **110**, 9758–9763.
75 E. T. Powers and D. L. Powers, *Biophys. J.*, 2008, **94**, 379–391.
76 R. Sabaté and J. Estelrich, *J. Phys. Chem. B*, 2005, **109**, 11027–11032.
77 B. Soreghan, J. Kosmoski and C. Glabe, *J. Biol. Chem.*, 1994, **269**, 28551–28554.
78 E. Rhoades and A. Gafni, *Biophys. J.*, 2003, **84**, 3480–3487.
79 M. Fändrich and C. M. Dobson, *EMBO J.*, 2002, **21**, 5682–5690.
80 J. C. Stroud, C. Liu, P. K. Teng and D. Eisenberg, *Proc. Natl. Acad. Sci. U. S. A.*, 2012, **109**, 7717–7722.
81 X. Ye, M. S. Hedenqvist, M. Langton and C. Lendel, *RSC Adv.*, 2018, **8**, 6915–6924.
82 S. L. Crick, K. M. Ruff, K. Garai, C. Frieden and R. V. Pappu, *Proc. Natl. Acad. Sci. U. S. A.*, 2013, **110**, 20075–20080.
83 K. W. Tipping, T. K. Karamanos, T. Jakhria, M. G. Iadanza, S. C. Goodchild, R. Tuma, N. A. Ranson, E. W. Hewitt and S. E. Radford, *Proc. Natl. Acad. Sci. U. S. A.*, 2015, **112**, 5691–5696.
84 K. Eden, R. Morris, J. Gillam, C. E. MacPhee and R. J. Allen, *Biophys. J.*, 2015, **108**, 632–643.
85 P. O. Souillac, V. N. Uversky, I. S. Millett, R. Khurana, S. Doniach and A. L. Fink, *J. Biol. Chem.*, 2002, **277**, 12666–12679.
86 T. Deva, N. Lorenzen, B. S. Vad, S. V. Petersen, I. Thørgersen, J. J. Enghild, T. Kristensen and D. E. Otzen, *Biochim. Biophys. Acta, Proteins Proteomics*, 2013, **1834**, 677–687.
87 X. Hu, S. L. Crick, G. Bu, C. Frieden, R. V. Pappu and J.-M. Lee, *Proc. Natl. Acad. Sci. U. S. A.*, 2009, **106**, 20324–20329.
88 A. Quist, I. Doudevski, H. Lin, R. Azimova, D. Ng, B. Frangione, B. Kagan, J. Ghiso and R. Lal, *Proc. Natl. Acad. Sci. U. S. A.*, 2005, **102**, 10427–10432.
89 L. Huang, R. Jin, J. Li, K. Luo, T. Huang, D. Wu, W. Wang, R. Chen and G. Xiao, *FASEB J.*, 2010, **24**, 3536–3543.
90 C. Nilsberth, A. Westlind-Danielsson, C. B. Eckman, M. M. Condron, K. Axelman, C. Forsell, C. Stenh, J. Luthman, D. B. Teplow, S. G. Younkin, J. Naslund and L. Lannfelt, *Nat. Neurosci.*, 2001, **4**, 887–893.

91 T. Tomiyama, T. Nagata, H. Shimada, R. Teraoka, A. Fukushima, H. Kanemitsu, H. Takuma, R. Kuwano, M. Imagawa, S. Ataka, Y. Wada, E. Yoshioka, T. Nishizaki, Y. Watanabe and H. Mori, *Ann. Neurol.*, 2008, **63**, 377–387.
92 Y.-S. Fang, K.-J. Tsai, Y.-J. Chang, P. Kao, R. Woods, P.-H. Kuo, C.-C. Wu, J.-Y. Liao, S.-C. Chou, V. Lin, L.-W. Jin, H. S. Yuan, I. H. Cheng, P.-H. Tu and Y.-R. Chen, *Nat. Commun.*, 2014, **5**, 4824.
93 S. W. Fowler, A. C. A. Chiang, R. R. Savjani, M. E. Larson, M. A. Sherman, D. R. Schuler, J. R. Cirrito, S. E. Lesné and J. L. Jankowsky, *J. Neurosci.*, 2014, **34**, 7871–7885.
94 P. Liu, M. N. Reed, L. A. Kotilinek, M. K. O. Grant, C. L. Forster, W. Qiang, S. L. Shapiro, J. H. Reichl, A. C. A. Chiang, J. L. Jankowsky, C. M. Wilmot, J. P. Cleary, K. R. Zahs and K. H. Ashe, *Cell Rep.*, 2015, **11**, 1760–1771.
95 W. L. Klein, G. A. Krafft and C. E. Finch, *Trends Neurosci.*, 2001, **24**, 219–224.
96 M. F. Mossuto, A. Dhulesia, G. Devlin, E. Frare, J. R. Kumita, P. P. de Laureto, M. Dumoulin, A. Fontana, C. M. Dobson and X. Salvatella, *J. Mol. Biol.*, 2010, **402**, 783–796.
97 N. Reixach, S. Deechongkit, X. Jiang, J. W. Kelly and J. N. Buxbaum, *Proc. Natl. Acad. Sci. U. S. A.*, 2004, **101**, 2817–2822.
98 W.-F. Xue, A. L. Hellewell, W. S. Gosal, S. W. Homans, E. W. Hewitt and S. E. Radford, *J. Biol. Chem.*, 2009, **284**, 34272–34282.
99 D. W. Dickson, *Neurobiol. Aging*, 1997, **18**, S21–S26.
100 B. T. Hyman, *Neurobiol. Aging*, 1997, **18**, S27–S32.

Electronic Supplementary Material (ESI) for Chemical Science.

Electronic supplementary information

Origin of Metastable Oligomers and their Effects on Amyloid Fibril Self-Assembly

Filip Hasecke,‡[a] Tatiana Miti,‡[b] Carlos Perez,[b] Jeremy Barton,[b] Daniel Schölzel,[ac] Lothar Gremer,[ac] Clara S.R. Grüning,[a] Garrett Matthews,[b] Georg Meisl,[d] Tuomas P.J. Knowles,[d] Dieter Willbold,[ac] Philipp Neudecker,[ac] Henrike Heise,[ac] Ghanim Ullah,[b] Wolfgang Hoyer*[ac] and Martin Muschol*[b]

[a.] *Institut für Physikalische Biologie, Heinrich-Heine-Universität, 40204 Düsseldorf, Germany. E-mail: wolfgang.hoyer@hhu.de*
[b.] *Department of Physics, University of South Florida, Tampa, FL 33620, USA. E-mail: mmuschol@usf.edu*
[c.] *Institute of Complex Systems (ICS-6), Structural Biochemistry, Research Centre Jülich, Germany.*
[d.] *Department of Chemistry, University of Cambridge, Lensfield Road, Cambridge CB2 1EW, UK.*

Contents

Materials and methods

Protein and chemicals

Two times recrystallized, dialyzed, and lyophilized hewL was purchased from Worthington Biochemicals (Lakewood, NJ) and used for all experiments. Ultrapure grade ThT was obtained from Anaspec (Freemont, CA) and standard grade ThT from Sigma Aldrich. All other chemicals were from Fisher Scientific (Pittsburgh, PA) and were reagent grade or better.

Preparation of hewL solutions

HewL was dissolved at twice its final concentration in 25 mM KH_2PO_4 pH 2 buffer and was placed in a water bath for 3 minutes at 42 °C to help dissolve preformed assemblies. Samples were successively filtered through 220 nm nitrile (Fisherbrand, Fisher Scientific, Pittsburgh, PA) and 50 nm polyethersulfone (Tisch Scientific, North Bend, OH) pore size syringe filters. The concentrated hewL stock was mixed 1:1 with a NaCl/25 mM KH_2PO_4 pH 2 stock solution at double the desired final salt concentrations. Final lysozyme concentrations were determined from UV absorption measurements at 280 nm (ε_{280} = 2.64 mL mg^{-1} cm^{-1}).

Preparation of DimAβ

Following a strategy previously established for recombinant production of Aβ,[1] bacterial expression of dimAβ was achieved by co-expression of ZAβ3, a binding protein that shields aggregation-prone sequence segments of Aβ. The gene encoding dimAβ, including an N-terminal methionine, followed by a Aβ40 unit, a $(G_4S)_4$ linker, and a second Aβ40 unit, was obtained from Life Technologies, and was cloned into the pACYCDuet-1 vector for co-expression with the ZAβ3 gene using NcoI and HindIII restriction sites. The coexpression vector contains the genes for dimAβ and $(His)_6$-tagged ZAβ3 in the following order: T7promoter-1 – dimAβ – T7promoter-2 – $(His)_6$ZAβ3 – T7 terminator. The protein was expressed as described.[1]

For purification, cell pellets were resuspended in 50 mM Na-phosphate, 0.3 M NaCl, 20 mM imidazole, pH 8, containing EDTA-free protease inhibitor (Roche Applied Sciences) and lysed by a cell disrupter (Constant Systems). The cell debris was removed by centrifugation in a Beckman J2-21 centrifuge mounting a JA20.1 rotor at 18,000 RPM, 4 °C for 40 minutes. For capture of the dimAβ:ZAβ3 complex by immobilized metal ion affinity chromatography (IMAC), the supernatant was loaded on a HisTrap FF column (GE Healthcare). DimAβ was separated from the resin-bound ZAβ3 and eluted with 8 M urea, 20 mM Na-phosphate, pH 7. For further purification, including removal of residual ZAβ3, reverse phase high-performance liquid chromatography (RP-HPLC) was performed. For this purpose the IMAC eluate was concentrated in a Vivaspin 20 centrifugal concentrator (Sartorius), followed by addition of 5 mM TCEP to reduce the disulfide bond of ZAβ3, and loading onto a semi-preparative Zorbax 300SB-C8 RP-HPLC column (9.4 mm × 250 mm, Agilent) connected to an Agilent 1260 Infinity system with UV detection at 214 nm. Monomeric dimAβ was eluted in a gradient from 30% (v/v) to 36% acetonitrile in water, 0.1% (v/v) trifluoroacetic acid at 80 °C. DimAβ containing fractions were pooled, lyophilized, dissolved in HFIP, aliquoted in 1 mg portions, lyophilized again, and stored at -20 °C. Immediately before use in experiments, lyophilized dimAβ was reconstituted in 6 M guanidinium-HCl, 50 mM Na-phosphate, 50 mM NaCl, pH 7.4, and sonicated for 30 minutes in a sonicator bath. Subsequently, the solution was loaded onto a Superdex 75 10/300 GL column (GE Healthcare) equilibrated with 35 mM Na_2HPO_4, 50 mM NaCl, 5 mM NaOH, pH 11.

DimAβ eluted at 13.5 ml. Protein concentration was determined by spectrophotometry. Immediately before the start of an experiment, 1.5% 1 M NaH_2PO_4 was added, yielding 50 mM Na-phosphate, 50 mM NaCl, pH 7.4, as final buffer.

Atomic force microscopy

For imaging of hewL assemblies, 50 µL of sample solutions were diluted 20-100 fold into the same solvent used during growth, deposited onto freshly cleaved mica for 3 minutes, rinsed with deionized water and dried with dry nitrogen. Amyloid fibrils were imaged in air with a MFP-3D atomic-force microscope (Asylum Research, Santa Barbara, CA) using NSC36/NoAl (Mikromasch, San Jose, CA) or PFP-FMR-50 (Nanosensor, Neuchatel, Switzerland) silicon tips with nominal tip radii of 10 and 7 nm, respectively. The cantilever had a typical spring constant and resonance frequency of 2 nN/nm and 80 kHz, respectively. It was driven at 60−70 kHz in alternating current mode and at a scan rate of 0.25-0.75 Hz. Images were acquired at 512 × 512 pixel resolution. Raw image data were corrected for image bow and slope. Amplitude, phase, and height images were collected for areas of 5x5 µm.

For imaging of dimAβ assemblies, 25 µL of sample solutions were directly deposited onto freshly cleaved mica for 1 minute, rinsed with deionized water and dried with dry nitrogen. Imaging was performed in air with a NanoWizard 2 (JPK instruments) with OMCLAC160TS silicon cantilevers (Olympus) with a nominal tip radius of 7 nm. The cantilever had a typical spring constant and resonance frequency of 26 nN/nm and 300 (±100) kHz, respectively. It was driven at 250−370 kHz in intermittent contact mode and at scan rates of 0.5-1.0 Hz. Images were acquired at 1024 × 1024 pixel resolution. Raw image data were corrected for image bow and slope. Amplitude, phase, and height images were collected for areas of 2x2 or 10x10 µm. Height images were superimposed over either amplitude or phase images using Gimp – GNU Image Manipulation Program.

Circular dichroism spectroscopy

Far-UV CD spectra of dimAβ were measured on a JASCO J-815 spectropolarimeter at a protein concentration of 20 µM in 1 mm Suprasil Quarz cuvettes (Hellma). To obtain a spectrum of monomeric dimAβ the sample was measured at 4°C, immediately after elution of the monomer fraction from SEC. The spectrum of dimAβ in the gO/CF state was recorded at 20°C, after 24 hours of quiescent incubation in 50 mM Na-phosphate, 50 mM NaCl, pH 7.4. The gO/CF state of the sample was confirmed by AFM.

Thioflavin T (ThT) fluorescence-monitored amyloid formation

ThT stock solutions were prepared by dissolving 1 mM dye in distilled water and then filtering through 220 nm syringe filters. Final ThT concentrations were obtained from absorption at λ = 412 nm (ε_{412} = 32 000 M^{-1} cm^{-1}).

HewL amyloid growth kinetics measurements with ThT were performed using a SpectraMax M5 fluorescence plate reader (Molecular Devices). ThT fluorescence was excited at 440 nm, and emission collected at 488 nm. Protein solutions at concentrations ranging from 0.3 mg/ml (21 µM, below the COC) to 5 mg/ml (350 µM, above the COC) were incubated in the presence of either 450 or 500 mM NaCl. Protein concentrations were more closely spaced near the COC for a given salt concentration, and more widely spaced above the COC. Typically, six identical 300 µL samples were incubated in a 96 well plate at 52 °C.

ThT at final concentrations of 5-10 µM was added to each well. Measurements were taken every 20 minutes and the plate was shaken for 3 seconds before each measurement.

DimAβ amyloid growth kinetics measurements were performed using an Infinite M200 Pro fluorescence plate reader (Tecan) with ThT excitation at 445 nm, and emission collected at 482 nm. Protein concentrations ranged from 0.6 µM (below the COC) to 40 µM (above the COC) in 50 mM Na-phosphate, 50 mM NaCl, pH 7.4. Typically, three identical 100 µL samples were incubated in a 96 well plate at 37 °C. ThT at final concentrations of 100 µM was added to each well. Measurements were taken every 3 minutes and the plate was shaken for 2 seconds before each measurement. The slow thermal equilibration of the multiwell plates causes an initial decrease in ThT fluorescence, which is equally present in ThT/buffer control wells. This thermal transient was either removed from the traces (lysozyme) or ignored for the analysis of the more rapidly assembling dimAβ samples.

Determination of the COC

We frequently refer to the COC, which is the phase boundary for the onset of gO/CF formation in both hewL and dimAβ. For hewL, we relied on our prior measurements of a sharp transition in ThT and light scattering kinetics from traces with extended lag periods to the onset of a lag-free drift.[2] This transition coincided with a sudden switch in aggregate morphology from RFs past the lag period to immediate presence of gOs and CFs. In addition, we showed that pre-formed gO/CFs grew above and decayed below the COC and that RFs seeded above the COC continued to grow. These measurements indicated that the COC is a (metastable) phase boundary, and the resulting phase diagram is shown in Fig. 1B. For dimAβ, the COC was similarly taken as the concentration for which ThT kinetics transitioned from pure sigmoidal to weakly bimodal kinetics - again reflecting the lack of a lag period for gO/CF formation.

Data analysis of ThT kinetics

The sigmoidal kinetics of RF formation in the absence of oligomers (below the COC) was fit to the analytical approximation of nucleated polymerization with secondary nucleation mechanisms.[3] Specifically, in the absence of fibril seeding

$$M_{RF}(t) = M_0[1 - \exp\left(C_- e^{-\kappa t} - C_+ e^{+\kappa t} + \frac{\delta^2}{\kappa^2}\right)] \quad (1)$$

where M_{RF} is the fibril mass, M_0 the total protein concentration, $C_\pm = \pm(\delta/2\kappa)^2$, and δ and κ represent the primary and secondary nucleation rates.

The biphasic kinetics of dimAβ and hewL, in turn, were fit to a superposition of a one-step oligomerization reaction and the above nucleated-polymerization reaction. For dimAβ, the time regimes of dominant gO/CF formation and dominant RF formation were sufficiently separated to allow separate analysis of the gO/CF assembly kinetics. Two alternative reaction models were fit to gO/CF kinetics in the initial time regime, namely primary nucleation-growth and one-step oligomerization. For a match to primary nucleation-growth the expression for classical nucleated polymerization was used[4]

$$M_{gO/CF}(t) = M_0[1 - \mathrm{sech}^{2/n_c}\left(\sqrt{n_c k_n k_+ M_0^{\,n_c}}\, t\right)] \quad (2)$$

with $M_{gO/CF}$(t) the mass concentration of polymer, M_0 the total protein concentration, k_n the nucleation rate constant, k_+ the elongation rate constant, and n_c the critical nucleus size. Global fits to the concentration-dependent gO/CF formation were performed with n_c and the product $k_n k_+$ as shared fit parameters. For one-step oligomerization $n\,\mathrm{M} \rightarrow \mathrm{M_n}$, the mass concentration of oligomer, $M_{gO/CF}$, evolves in time according to the following expression

$$M_{gO/CF}(t) = M_0 - [M_0^{1-n} + (n-1)nkt\,]^{1/(1-n)} \quad (3)$$

with M_0 the total protein concentration, k the oligomerization rate constant, and n the oligomer size or reaction order. Global fits to the concentration-dependent gO/CF formation data were performed with n and k as shared fit parameters. For both fits, the proportionality constant relating M(t) to ThT fluorescence intensity was treated as a fit parameter with an individual value for every sample.

In the case of hewL, the time scales for gO/CF and RF formation overlapped, particularly at monomer concentrations just slightly above the COC. We therefore fit the data to the superposition of the above nucleated polymerization reaction (eqn. 1) and an oligomerization reaction. In addition, the initial hewL oligomerization kinetics were better approximated using a 1st-order forward reaction with an exponential growth in time.

$$M_{gO,CF}(t) = M_\infty(1 - \exp(-at)) \quad (4)$$

where $M_{gO/CF}$(t) is the mass concentration of oligomer, and M_∞ is the gO/CF mass that would be reached in the absence of RF formation. The neglect of a backward rate for oligomers is justified by two observations. First of all, we had previously shown that gO/CF decay rates are exceedingly small.[2] In addition, as discussed below, CFs did not fully depolymerize for many days after RFs had nucleated.

Determination of lag periods

We defined the RF lag time as the point at which the amplitude of the RF portion of the ThT signal increases beyond a fixed threshold. To determine RF lag periods below the COC (sigmoidal growth) ThT kinetics were directly fit to Eqn. (1). Above the COC (biphasic growth) our kinetics data were fit as the superposition of oligomeric and RF growth, as described above. The oligomeric fits were then subtracted from the entire time traces, resulting in the RF portion of the ThT signal. RF lag periods where then determined as below the COC. In both cases, using semi-logarithmically scaled ThT intensities significantly improves visual detection for deviations of ThT kinetics from its flat baseline and onset of significant RF growth. Error bars for individual lag periods (see Figs. 5E &F), which are derived from analytical fits to individual kinetic traces, are difficult to assign. However, the scatter among the data points is a reasonable measure of underlying experimental and fitting uncertainties. The uncertainty in the slope of the resulting power law fit through the lag periods, as well as the average of the slopes for three independent repeats of these experiments, is provided in the figure caption.

Stability assessment of dimAβ assembly states by ZAβ3

The affibody protein ZAβ3 and its tryptophan-containing derivative ZAβ3W were prepared as described previously.[5,6] To monitor the stability of dimAβ assemblies formed during ThT assays, 14 μM ZAβ3

was added to assembly reactions of 6 µM dimAβ at different time points, and ThT fluorescence was recorded. To test if RFs of dimAβ are thermodynamically or only kinetically stable against dissolution in the presence of ZAβ3, 15 µM preformed dimAβ:ZAβ3W complex was incubated over one week in the presence of 48 µM (in monomer equivalents) sonicated dimAβ RF seeds and the wavelength of maximum tryptophan fluorescence emission was recorded as previously described.[6]

Modeling of biphasic assembly kinetics

To replicate the experimentally observed transition from sigmoidal to biphasic growth we performed numerical simulations for fibril growth in the presence of off-pathway aggregation. To do so we modified the model of Powers and Powers (for details, see ref. 7) in three ways. We (i) accounted for secondary nucleation of fibril growth; (ii) replaced the off-pathway amorphous precipitates with off-pathway oligomers that could only form after crossing a well-defined solubility threshold we had previously identified;[2] and again following our experimental results, we (iii) assumed that RF fibrils, once nucleated, elongate faster than gO/CFs grow. A more detailed description of this model is provided further below.

To connect ThT responses to the kinetics of gO/CF vs. RF formation, we built on our prior measurements indicating that ThT responses to gO/CFs are weaker than to equivalent concentrations of RFs (about ten times in the case of hewL).[8] We further considered the ThT fluorescence to be the linear superposition of the response evoked by gO/CFs and RFs, each with their distinct response factors, i.e.

$$\Delta ThT = \alpha\,[gO, CF] + \beta\,[RF]$$

The fits used α, β as global fitting parameters for a given protein. This implicitly assumes that binding of ThT to gO/CFs and RFs remains linear over the range of concentrations we consider.

Assessing role of hewL hydrolysis

We have previously shown that hewL hydrolysis under our growth conditions requires in excess of 18 hours to generate distinct peptide fragments (see Fig. 4 in ref. 8). Since gO/RF formation is lag-free and the total amounts of gO/CFs formed at the plateau phase matched monomer concentrations above the COC (see ref. 2), hydrolysis is unlikely to underlie gO/CF formation in our system. In contrast, RF formation does show lag periods that stretch into the time frame for weak hewL hydrolysis. To investigate whether hydrolysis does affect RF formation under our growth conditions, we pre-hydrolyzed 20 mg/ml of hewL monomers in 25 mM KH_2PO_4 buffer (RF growth conditions) for either 3 or 7 days at 45 °C, ie. slightly below the threshold temperature of 50 °C for any amyloid aggregation.

NMR spectroscopy

For solution NMR spectroscopy, [U-^{15}N]-dimAβ was freshly eluted in 20 mM Na-phosphate, 50 mM NaCl, pH 10, from a Superdex 75 10/300 column (GE Healthcare). 375 µl eluate at ca. 130 µM protein concentration was diluted with 75 µl of 20 mM NaH_2PO_4, 50 mM NaCl, and 50 µl D_2O to a final [U-^{15}N]-dimAβ concentration of ca. 100 µM. The solution had a pH of 7.9. For comparison with dimAβ, [U-^{15}N]-Aβ40 was prepared with an N-terminal methionine as described previously.[1] Solution NMR data were collected at 5 °C using a 600 MHz spectrometer (Varian). [^{1}H,^{15}N]-HSQC spectra were collected at 5.0°C on a Bruker AVANCE III HD 600 MHz or Varian VNMRS 900 MHz NMR spectrometer equipped with cryogenic probes with z-axis pulsed field gradient capabilities.

For solid-state NMR spectroscopy, [U-^{15}N-^{13}C]-dimAβ was freshly eluted in 20 mM Na-phosphate, pH 10, from a Superdex 75 16/60 column (GE Healthcare). To form RFs samples were incubated in 5 ml Qualyvials (Zinsser). 1035 µl isotopically labeled dimAβ were mixed with 3915 µl 20 mM Na-phosphate, 50 mM NaCl, pH 7.4, and 50 µl 10% NaN_3. The vials were incubated at 37 °C while being stirred with a micro stir bar. After 20 h of incubation fibril formation was confirmed by AFM analysis. The remaining sample was centrifuged for 10 min at 16.100 x g at 4 °C, and the pellet was centrifuged into a 3.2 mm MAS NMR rotor. MAS NMR spectra were recorded at sample temperatures of 25 °C $\pm$ 5 °C (INEPT spectrum, Fig. S2B) and 0 °C $\pm$ 5 °C (PDSD spectrum with CP excitation, Fig. S2C), respectively on a 14.1 T (^{1}H Larmor frequency: 600 MHz) spectrometer (Varian). NMR data were processed with NMRPipe[9] using squared and shifted sine bell functions for apodization and analyzed with CcpNmr.[10]

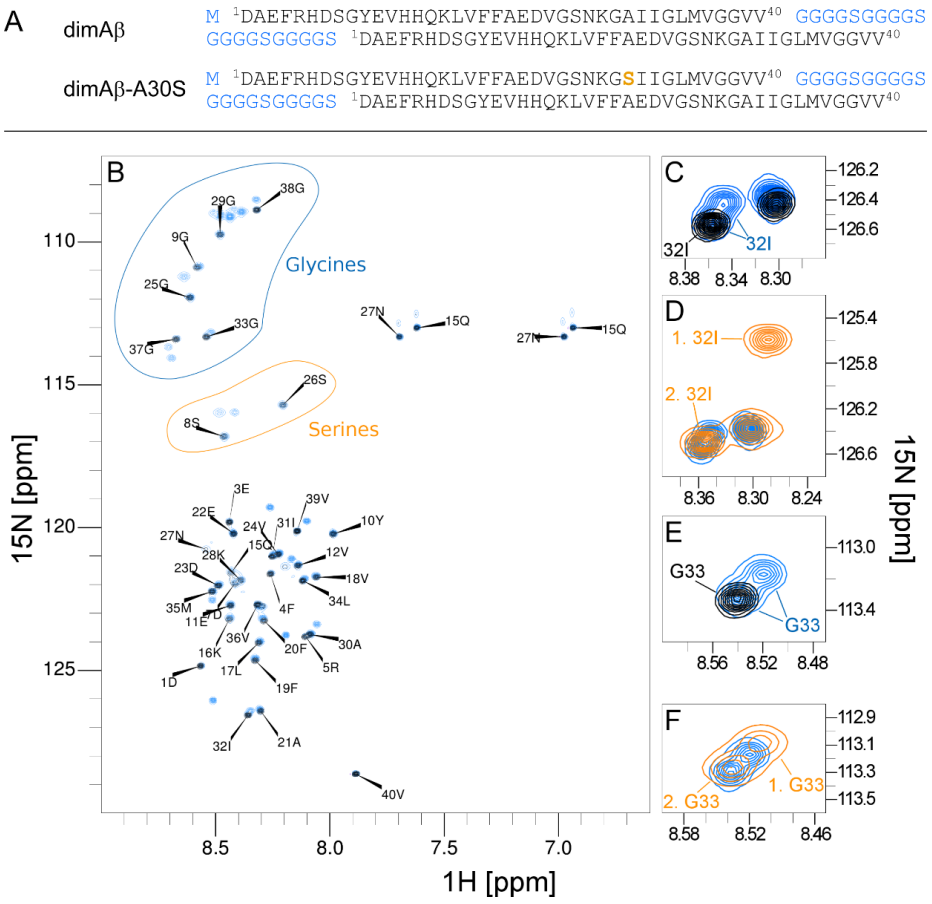

Figure S1. The conformation of monomeric Aβ40 is retained in dimAβ. To assess differences in conformation, solution NMR spectra of monomeric Aβ40 were compared to those of monomeric dimAβ and the mutant dimAβ-A30S. (**A**) Amino acid sequences of dimAβ and dimAβ-A30S. DimAβ-A30S contains an Ala-to-Ser exchange at position 30 of only the first Aβ40 unit, in order to locally perturb the NMR spectrum and abolish spectral overlap of the two Aβ40 units. (**B**) Overlay of (^{1}H-^{15}N) HSQC NMR spectra of [U-^{15}N]-Aβ40 (black) and [U-^{15}N]-dimAβ (blue). Assignments are shown for Aβ40. In the spectrum of [U-^{15}N]-dimAβ the resonances of Aβ40 are recovered, indicating that the conformation of monomeric Aβ40 is retained in dimAβ. In addition, further peaks are observed mainly in the glycine and serine regions of the spectrum and can be attributed to the $(G_4S)_4$ linker. For some resonances in the central/C-terminal region of the Aβ sequence, e.g., Ile-32 and Gly-33, peak splittings are evident in the spectrum of dimAβ (**C**,**E**). To evaluate if the peak splittings originate from a symmetric interaction between both Aβ units, or if it is due to the asymmetric placement of the Aβ units within dimAβ (preceding vs. following the linker), the variant dimAβ-A30S was generated and compared to dimAβ. In dimAβ-A30S (orange spectrum), one of the two split resonances observed for dimAβ is shifted as a consequence of local perturbation by the A30S mutation (**D**,**F**). This indicates that the peak splittings are not due to a symmetric interaction between both Aβ units, as in this case quadruple peaks would be expected for Ile-32 and Gly-33. Instead, specifically the one dimAβ resonance is shifted in dimAβ-A30S (D,F) that does not overlay with the Aβ40 resonance (C,E). This suggests that the peak splittings in dimAβ result from a slightly altered electronic environment of the central/C-terminal region in the N-terminal Aβ unit within dimAβ, likely resulting from proximity to, or transient interaction with, the linker region.

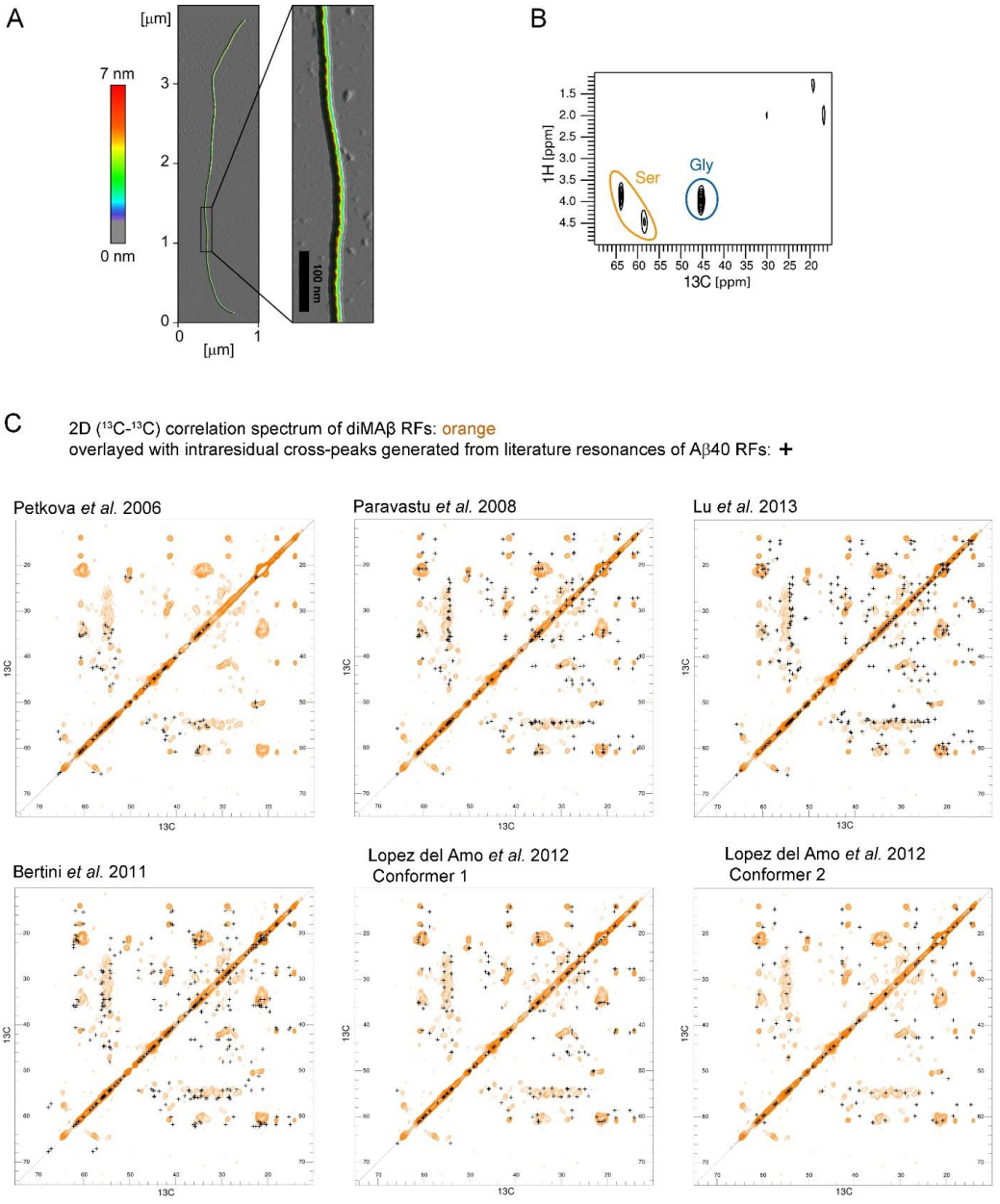

Figure S2. Both Aβ subunits of dimAβ are incorporated into the RF β-sheet core. (**A**) AFM image of a dimAβ RF. Color scale: height in nm. (**B**) 2D (^{1}H-^{13}C) HETCOR spectrum obtained with refocused INEPT as magnetization transfer[11] of diMAβ RFs. Only signals from mobile regions of the fibrils are detected.[12] Almost exclusively signals from glycine and serine residues (encircled) in dimAβ RFs are visible, indicating that the $(G_4S)_4$ linker remains flexible, while both Aβ units are incorporated into the RF β-sheet core. The sample temperature was ~25 °C ± 5°C, the MAS spinning speed was 11 kHz. For the 2D spectrum, 64 t_1 increments with 32 scans each were recorded. During ^{13}C detection, high-power proton decoupling (~83 kHz) was applied. (**C**) 2D (^{13}C-^{13}C) correlation spectrum of diMAβ RFs (orange) overlayed with intraresidual cross-peaks generated from resonances previously reported for six preparations of Aβ40 RFs (crosses). Initial proton to carbon magnetization transfer was achieved by cross polarization with a contact time of 200 µs,

homonuclear mixing was achieved by proton driven spin diffusion with a mixing time of 50 ms. High-power proton decoupling (~83 kHz) was employed during ^{13}C evolution and detection periods. Sample temperature was ~0 °C ± 5°C, the spinning speed was 11 kHz. In total 256 t_1 increments with 128 scans each were recorded. MAS NMR was performed at a magnetic field strength of 14.1 T corresponding to a proton Larmor frequency of 600 MHz. Spectra were processed using squared and shifted sine-bell apodization (shift of 0.35·π). The Aβ40 RF literature resonances are from Petkova *et al.* (BMRB entry 18127),[13] Paravastu *et al.* (BMRB entry 18129),[14] Lu *et al.* (BMRB entry 19009),[15] Bertini et al.,[16] and Lopez del Amo *et al*.[17] The spectrum of diMAβ RFs particularly overlaps with the cross-peaks of conformer 1 of Lopez del Amo *et al.*, but also with those of Bertini et al., Petkova *et al.*, and Paravastu *et al.*, suggesting structural similarity of the diMAβ RF polymorph investigated here with the Aβ40 RF polymorphs of these studies.

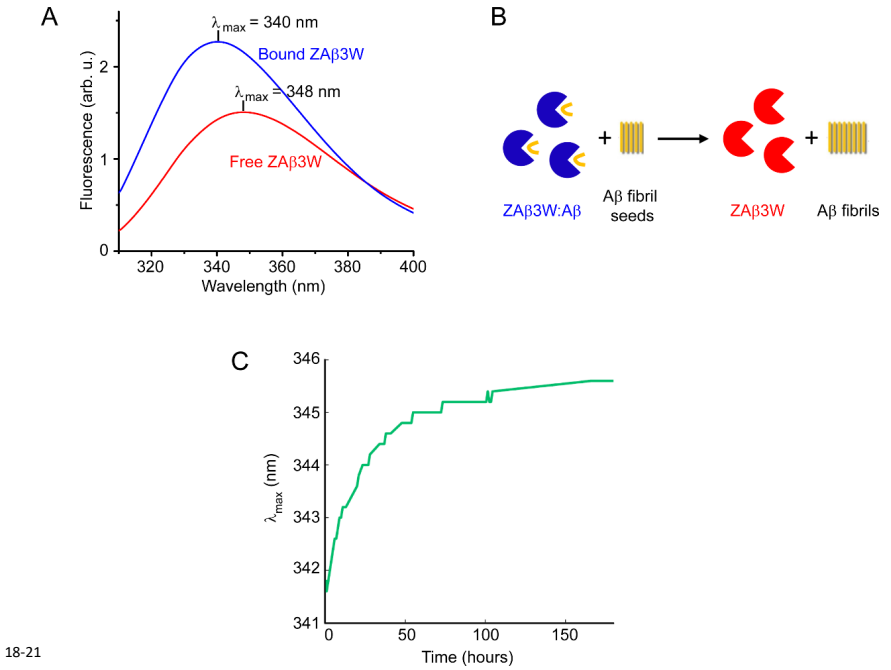

Figure S3. DimAβ possesses higher thermodynamic stability in the RF state than in the ZAβ$_3$-bound state. (**A**) ZAβ3W, a tryptophan-containing version of ZAβ3, is a probe for the stability of Aβ assembly states.[6] The fluorescence emission spectrum of ZAβ3W exhibits a blue shift upon binding of Aβ and can therefore report on dissociation of Aβ monomers from Aβ assemblies. (**B**) Scheme of the experiment to compare the thermodynamic stability of dimAβ in the ZAβ$_3$-bound and RF state. 15 µM preformed dimAβ:ZAβ3W complex was incubated over one week in the presence of 48 µM (in monomer equivalents) sonicated dimAβ RF seeds and the wavelength of maximum tryptophan fluorescence emission was recorded as described previously.[6] (**C**) The wavelength of maximum tryptophan fluorescence emission exhibits a red shift, indicating that dimAβ dissociates from the dimAβ:ZAβ3W complex and is incorporated into RFs.

Kinetic Model of Competing Oligomer and Fibril Pathways

Our formalism for the transition from sigmoidal to biphasic growth upon crossing the COC builds on the model of Powers and Powers.[22] Their original model has two assembly pathways: (1) on-pathway assembly leads to RF formation, and (2) off-pathway assembly generating gOs. We include both pathways in our model. Along the on-pathway, the fibril nucleation barrier is represented by unfavorable association constants for monomer addition up to n=5 (nucleus size). Note that the reaction rates can be adjusted to fit the model to the data when a nucleus size smaller or larger than 5 is considered. The reaction from nucleus to RF is irreversible (note that $b_2 = 0$). The unstructured oligomer growth is treated as unstable aggregates that may grow to some specified maximum size, m (we take m=8), and follow the off-pathway that essentially buffers the monomer concentration temporarily. This, for now, neglects subsequent assembly of gOs in CFs.

To replicate our observations, we make four key changes to the model by Powers and Powers. (1) We use rate constants that are significantly smaller than those in (Powers and Powers 2008).[22] (2) In the original model, the same on-rate for monomer addition was used along the entire on-pathway, while the off-rate below and above the nucleus size were different. In our model, both the on- and off rates (a_1 vs. a, and b_1 vs. b in Fig. S4) are different for aggregates that are smaller than the nucleus size and RFs. (3) We included a secondary nucleation mechanism, as proposed by Knowles et al.[3,4,23,24] where already formed RFs facilitate nucleation of new seeds (blue arrows, k_2 binding constant in Fig. S4). This was necessary to replicate the sharp autocatalytic rise in the experimental ThT fluorescence upon RFs nucleation. (4) To incorporate the lack of gO formation below the COC and the dependence of experimental gO growth rates on monomer concentration, we replicated the increase in off-pathway assembly rates seen in experiment (see Fig. 4C, insert). With these changes, the amount of different species in the solution are given by the following rate equations.

$$\frac{d[X_1]}{dt} = -[X_1](2a_1[X_1] + a_1\sum_{j=2}^{n}[Y_j] + a[F^{(0)}]) + 2b_1[Y_2] + b_1\sum_{j=3}^{n}[Y_j] + c[F^{(0)}] - [X_1](2\alpha_1[X_1] + \alpha\sum_{j=2}^{m}[Z_j]) + 2\beta[Z_2] + \beta\sum_{j=3}^{m}[Z_j] - k_2 n[X_1]^n[F^{(1)}] \quad (1)$$

$$\frac{d[Y_2]}{dt} = (a_1[X_1]^2 - b_1[Y_2]) - (a_1[X_1][Y_2] - b_1[Y_3]) \quad (2)$$

$$\frac{d[Y_j]}{dt} = (a_1[X_1][Y_{j-1}] - b_1[Y_j]) - (a_1[X_1][Y_j] - b_1[Y_{j+1}]),\ j=3,4. \quad (3)$$

$$\frac{d[Y_n]}{dt} = (a_1[X_1][Y_{n-1}] - b_1[Y_n]) - a[X_1][Y_n] + k_2[X_1]^n[F^{(1)}] \quad (4)$$

$$\frac{d[Z_2]}{dt} = (\alpha_1[X_1]^2 - \beta\ \ [Z_2]) - (\alpha[X_1][Z_2] - \beta[Z_3]) \quad (5)$$

$$\frac{d[Z_j]}{dt} = (\alpha[X_1][Z_{j-1}] - \beta[Z_j]) - (\alpha[X_1][Z_j] - \beta[Z_{j+1}]),\ j=3,4,\ldots 7. \quad (6)$$

$$\frac{d[Z_m]}{dt} = (\alpha_1[X_1][Z_{m-1}] - \beta[Z_m]) \quad (7)$$

$$\frac{d[F^{(0)}]}{dt} = a[X_1][Y_n] \quad (8)$$

$$\frac{d[F^{(1)}]}{dt} = (n+1)a[X_1][Y_n] + a[X_1]\left[F^{(0)}\right] - c[F^{(0)}], \quad (9)$$

where $[X_1]$, $[Y_j]$, $[Z_j]$, $[F^{(0)}]$, and $[F^{(1)}]$ represent the concentration of monomers, i-mers along the on-pathway, j-mers along the off-pathway, the RF number concentration, and the amount of monomers incorporated in RFs respectively in μM. The last term in eqs (1 – 5) each corresponds to secondary nucleation of new fibrils catalyzed by already established ones. The rate constants, a, b_1, c, and β are fixed at 1.98×10^{11} $M^{-1}hr^{-1}$, 3.96×10^{-4} hr^{-1}, 7.2×10^{2} hr^{-1}, and 3.6×10^{-2} hr^{-1} respectively. The on rate, α_1, is given by $7.2\times10^{10} \times f([X_1],[NaCl])$ (in $M^{-1}hr^{-1}$), where $f([X_1],NaCl)$ is given by the following equation

$$f([X1], NaCl) = \frac{1}{1 + exp^{(COC-[X_1])/0.5}}$$

$$COC = 3.522e^{-[NaCl]/45.3107} + 45.3107$$

where COC is the critical oligomer concentration. This assures that the oligomer reaction only becomes significant upon crossing the COC. In the model, the primary and secondary nucleation rates a_1 and k_2 are varied over the range 6.336 $M^{-1}hr^{-1}$ – 10.296 $M^{-1}hr^{-1}$ and 3.6×10^{-15} $M^{-1}hr^{-1}$ – 5.04×10^{-10} $M^{-1}hr^{-1}$ to obtain the best fit for fibril and aggregation growth with varying initial monomer concentration. The rate constant α is varied between 72.0 $M^{-1}hr^{-1}$ – 1.728×10^{3} $M^{-1}hr^{-1}$ to stay consistent with the power law behavior of the initial slope of gOs growth curve as a function of monomer concentration.

Representative time traces from the model with initial monomer concentration below and above the COC are shown in Figure S4B. In order to compare the theoretical mass concentrations to experimental ThT kinetics, we measured a slope of 125 ThT units / 1 μM RF for our plate reader. Based on our earlier measurements, the ThT response of gO/CFs was taken to be ten-fold weaker than that of RFs.[8]

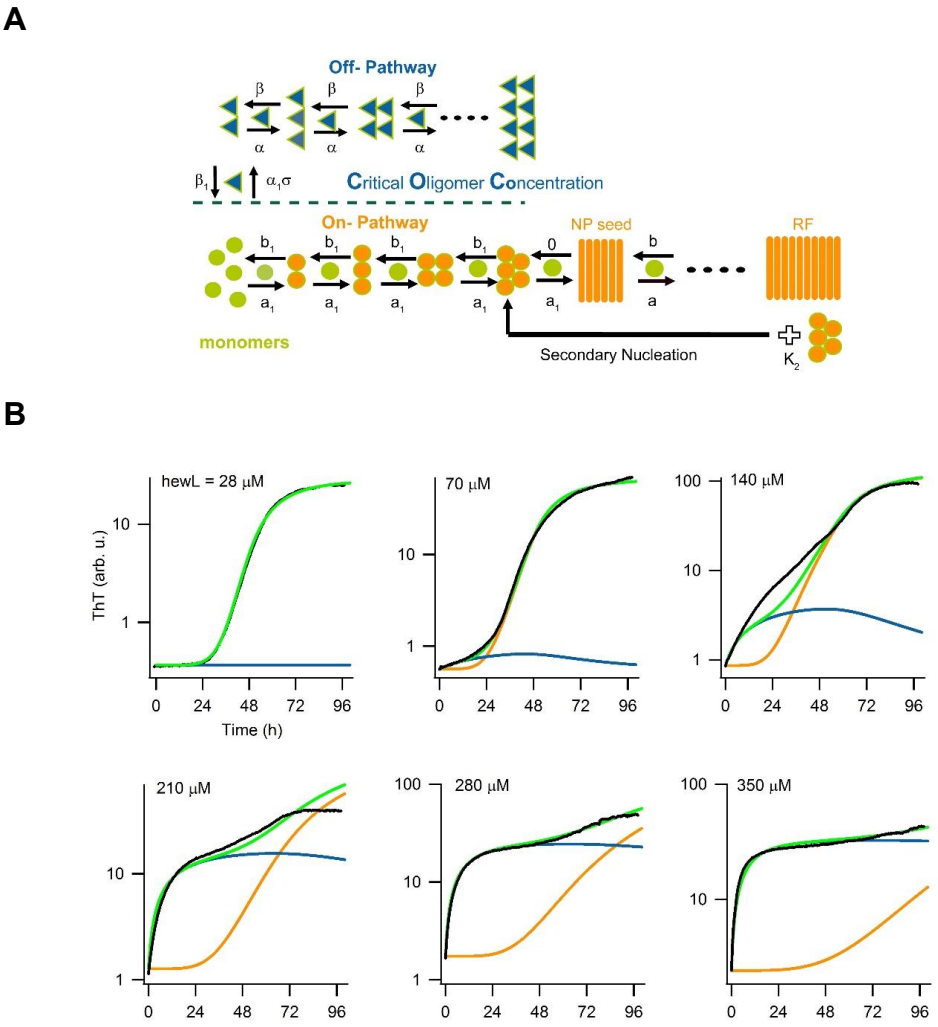

Figure S4: (**A**) Diagram of on- and off-pathways in the kinetic model. The on-pathway is displayed using orange symbols, where in addition to primary nucleation, secondary nucleation contributes to RF seed formation. Within the on-pathway, monomers (green) associate, forming pre-fibrillar multimers (orange) until eventually reaching a nucleus size (orange bars) consisting of n monomers. Beyond this specified nucleus, fibril growth begins. Already existing fibrils catalyze the formation of new ones through secondary nucleation with rate constant K_2. On the off-pathway monomers form gOs, but can only do so once monomer concentrations cross the COC. This limits the pool of monomers available for gO growth (indicated by using triangles instead of spheres) (**B**) Comparison of simulated with experimental kinetics. Experimental observed time-traces (black) showing ThT kinetics in response to the presence of hewl gOs and RFs and theoretical fits (green) plotted alongside their contributions from gOs (blue) and RFs (orange) concentrations at the indicated total monomer concentrations. ThT increases are in arbitrary units but account for the 10-fold smaller ThT response to equivalent mass concentrations from gO/CFs vs. RFs.

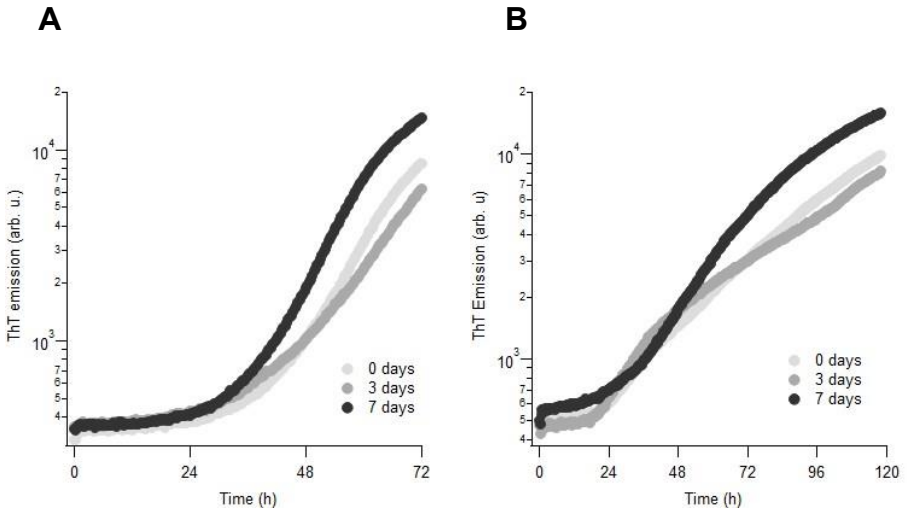

Figure S5: Effect of hewL pre-hydrolysis on RF nucleation and growth. HewL monomers, either freshly prepared or pre-hydrolyzed for 3 or 7 days, were incubated at (A) 30 uM hewL and 350 mM NaCl or (B) 350 uM and 100 mM NaCl in the presence of 15 uM ThT. Both are RF growth conditions, but at more than 10-fold different protein concentrations. As shown, pre-hydrolysis did not affect the RF lag periods in our system. Some acceleration in RF elongation occurred during the latter parts of the incubation periods, and only for the 7 day pre-hydrolyzed sample. This suggests that hewL hydrolysis, under our growth conditions, is not the cause of RF nucleation but can accelerate RF elongation rates at the late-stages of growth.

References

1. B. Macao, W. Hoyer, A. Sandberg, A.-C. Brorsson, C. M. Dobson and T. Härd, *BMC Biotechnol.*, 2008, **8**, 82.
2. T. Miti, M. Mulaj, J. D. Schmit and M. Muschol, *Biomacromolecules*, 2015, **16**, 326-335.
3. T. P. J. Knowles, C. A. Waudby, G. L. Devlin, S. I. A. Cohen, A. Aguzzi, M. Vendruscolo, E. M. Terentjev, M. E. Welland and C. M. Dobson, *Science*, 2009, **326**, 1533-1537.
4. S. I. A. Cohen, M. Vendruscolo, M. E. Welland, C. M. Dobson, E. M. Terentjev and T. P. J. Knowles, *J. Chem. Phys.*, 2011, **135**, 065105.
5. E. A. Mirecka, H. Shaykhalishahi, A. Gauhar, Ş. Akgül, J. Lecher, D. Willbold, M. Stoldt and W. Hoyer, *Angew. Chem. Int. Ed.*, 2014, **53**, 4227-4230.
6. C. S. R. Grüning, S. Klinker, M. Wolff, M. Schneider, K. Toksöz, A. N. Klein, L. Nagel-Steger, D. Willbold and W. Hoyer, *J. Biol. Chem.*, 2013, **288**, 37104-37111.
7. E. T. Powers and D. L. Powers, *Biophys. J.*, 2008, **94**, 379-391.
8. J. Foley, S. E. Hill, T. Miti, M. Mulaj, M. Ciesla, R. Robeel, C. Persichilli, R. Raynes, S. Westerheide and M. Muschol, *J. Chem. Phys.*, 2013, **139**, 121901/121901-121912.
9. F. Delaglio, S. Grzesiek, G. W. Vuister, G. Zhu, J. Pfeifer and A. Bax, *J. Biomol. NMR*, 1995, **6**, 277-293.
10. W. F. Vranken, W. Boucher, T. J. Stevens, R. H. Fogh, A. Pajon, M. Llinas, E. L. Ulrich, J. L. Markley, J. Ionides and E. D. Laue, *Proteins*, 2005, **59**.
11. R. Freeman and G. A. Morris, *J. Am. Chem. Soc.*, 1979, **101**, 760-762.
12. H. Heise, W. Hoyer, S. Becker, O. C. Andronesi, D. Riedel and M. Baldus, *Proc. Natl. Acad. Sci. USA*, 2005, **102**, 15871-15876.
13. A. T. Petkova, W. M. Yau and R. Tycko, *Biochemistry*, 2006, **45**, 498-512.
14. A. K. Paravastu, R. D. Leapman, W. M. Yau and R. Tycko, *Proc. Natl. Acad. Sci. USA*, 2008, **105**, 18349-18354.
15. J. X. Lu, W. Qiang, W. M. Yau, C. D. Schwieters, S. C. Meredith and R. Tycko, *Cell*, 2013, **154**, 1257-1268.
16. I. Bertini, L. Gonnelli, C. Luchinat, J. Mao and A. Nesi, *J. Am. Chem. Soc.*, 2011, **133**, 16013-16022.
17. J. M. Lopez del Amo, M. Schmidt, U. Fink, M. Dasari, M. Fandrich and B. Reif, *Angew. Chem. Int. Ed. Engl.*, 2012, **51**, 6136-6139.
18. Z. Fu, D. Aucoin, J. Davis, W. E. Van Nostrand and S. O. Smith, *Biochemistry*, 2015, **54**, 4197-4207.
19. A. Lomakin, D. S. Chung, G. B. Benedek, D. A. Kirschner and D. B. Teplow, *Proc. Natl. Acad. Sci. USA*, 1996, **93**, 1125-1129.
20. L. M. Luheshi, W. Hoyer, T. P. de Barros, I. van Dijk Härd, A.-C. Brorsson, B. Macao, C. Persson, D. C. Crowther, D. A. Lomas, S. Ståhl, C. M. Dobson and T. Härd, *PLoS Biol.*, 2010, **8**, e1000334.
21. M. Nick, Y. Wu, N. W. Schmidt, S. B. Prusiner, J. Stöhr and W. F. DeGrado, *Biopolymers*, 2018, e23096.
22. E. T. Powers and D. L. Powers, *Biophys J*, 2008, **94**, 379-391.
23. S. I. A. Cohen, M. Vendruscolo, C. M. Dobson and T. P. J. Knowles, *J. Chem. Phys.*, 2011, **135**, 065106/065101-065118.
24. S. I. A. Cohen, S. Linse, L. M. Luheshi, E. Hellstrand, D. A. White, L. Rajah, D. E. Otzen, M. Vendruscolo, C. M. Dobson and T. P. J. Knowles, *Proceedings of the National Academy of Sciences*, 2013, **110**, 9758-9763.

GDCh Research Articles Angewandte International Edition Chemie

Check for updates

How to cite: *Angew. Chem. Int. Ed.* **2021**, *60*, 3016–3021
International Edition: doi.org/10.1002/anie.202010098
German Edition: doi.org/10.1002/ange.202010098

Proteins

Protofibril–Fibril Interactions Inhibit Amyloid Fibril Assembly by Obstructing Secondary Nucleation

Filip Hasecke[+], Chamani Niyangoda[+], Gustavo Borjas, Jianjun Pan, Garrett Matthews, Martin Muschol, and Wolfgang Hoyer**

Abstract: *Amyloid-β peptides (Aβ) assemble into both rigid amyloid fibrils and metastable oligomers termed AβO or protofibrils. In Alzheimer's disease, Aβ fibrils constitute the core of senile plaques, but Aβ protofibrils may represent the main toxic species. Aβ protofibrils accumulate at the exterior of senile plaques, yet the protofibril–fibril interplay is not well understood. Applying chemical kinetics and atomic force microscopy to the assembly of Aβ and lysozyme, protofibrils are observed to bind to the lateral surfaces of amyloid fibrils. When utilizing Aβ variants with different critical oligomer concentrations, the interaction inhibits the autocatalytic proliferation of amyloid fibrils by secondary nucleation on the fibril surface. Thus, metastable oligomers antagonize their replacement by amyloid fibrils both by competing for monomers and blocking secondary nucleation sites. The protofibril—fibril interaction governs their temporal evolution and potential to exert specific toxic activities.*

Introduction

Amyloid fibrils are cross-β structured protein assemblies that represent the hallmark of many protein aggregation disorders.[1] For several disease-related proteins, amyloid fibrils correspond to the thermodynamic minimum of the free energy landscape for folding and aggregation.[2] For example, Aβ amyloid fibrils are the core components of the senile plaques found in Alzheimer's disease (AD)-affected brains.[3] Aβ fibrils are polymorphic, variably constructed from in-register parallel β-sheets.[4–6] They form by nucleated polymerization, where initial fibril nuclei grow by monomer addition to the fibril ends.[7] A frequent contributor to the typical sigmoidal growth profile of amyloid fibrils is fibril-mediated secondary nucleation. In this process, the fibril surface acts as the preferential site for new fibril nucleation, leading to the autocatalytic proliferation of amyloid fibrils.[7]

A second type of assemblies that Aβ is prone to form are metastable globular oligomers with a molecular weight > 50 kD, and their associated curvilinear fibrils with typical lengths up to 200 nm.[8–14] These oligomers are collectively referred to as AβO or protofibrils.[8,12,15] As these oligomers are formed in a reaction distinct from fibril formation (i.e., off-pathway),[8,11,13,16] the term protofibril can be misleading. Similarly, the term AβO is used interchangeably for on-pathway oligomers. Below we use the designations globular oligomer (gO) and curvilinear fibril (CF) to refer specifically to the off-pathway, metastable assemblies. GO/CFs form in a lag-free oligomerization reaction with a much higher reaction order than that observed for fibril formation.[11] Like amyloid fibrils, gO/CFs are rich in β-sheets, but their structure has not been resolved to the same level of detail yet.[17] GO/CFs have been reported for several amyloidogenic proteins, suggesting that they are a general alternative assembly type of this class of proteins.[16,18–20]

Aβ gO/CFs may represent the main toxic species in AD, as they are more effective than amyloid fibrils at inducing synaptic dysfunction, inhibiting long-term potentiation, triggering inflammation, and disrupting membranes.[8,13] Several receptors that mediate toxic signaling of extracellular Aβ gO/CFs have been identified.[21] In addition, intracellular Aβ gO/CFs show cytotoxic effects.[8] Aβ gO/CFs are enriched in a halo surrounding senile plaques, pointing to a potential role of gO/CF-fibril interactions.[22,23] For example, fibril plaques have been suggested to serve as a reservoir, or buffer, of Aβ oligomers.[22,23] However, gO/CF–fibril interactions have not been characterized in detail.

We have recently reported that the high concentration dependence of gO/CF formation results in a threshold monomer concentration required for gO/CF formation, denoted critical oligomer concentration (COC), which is significantly higher than the threshold for fibril formation.[11,20] Above the COC, the assembly kinetics are biphasic, with an initial lag-free gO/CF formation phase, followed by a sigmoidal phase representing the nucleation and growth of fibrils which slowly replace the metastable gO/CFs. Surprisingly, we observed that gO/CF formation above the COC

[*] F. Hasecke,[+] W. Hoyer
Institut für Physikalische Biologie
Heinrich-Heine-Universität Düsseldorf
40204 Düsseldorf (Germany)
E-mail: wolfgang.hoyer@hhu.de
W. Hoyer
Strukturbiochemie (IBI-7), Forschungszentrum Jülich
52425 Jülich (Germany)
C. Niyangoda,[+] G. Borjas, J. Pan, G. Matthews, M. Muschol
Department of Physics, University of South Florida
Tampa, FL 33620 (USA)
E-mail: mmuschol@usf.edu
[+] These authors contributed equally to this work.

Supporting information and the ORCID identification number(s) for the author(s) of this article can be found under: https://doi.org/10.1002/anie.202010098.

progressively increased the lag period for subsequent fibril nucleation and growth, revealing that gO/CFs inhibit fibril formation not only by competing for monomers, but also in an active fashion. These observations were made with two distinct amyloid proteins, a dimeric variant of Aβ40 (dimAβ) and hen egg-white lysozyme (hewL).[11]

Here, we investigate how gO/CFs actively inhibit fibril formation. We first show that the inhibitory effects of off-pathway gO/CF formation on subsequent fibril nucleation and growth are similarly present in the two dominant AD peptides Aβ40 and Aβ42. We then demonstrate for Aβ as well as for hewL that gO/CFs bind to fibril surfaces. GO/CF binding also promotes fibril bundling, thereby further reducing fibril surface area. We finally take advantage of the Aβ-dimAβ system to show that the gO/CF-fibril interaction interferes with secondary nucleation and blocks the proliferation of amyloid fibrils.

Results and Discussion

To investigate gO/CF formation of Aβ, we have generated dimAβ, a dimeric Aβ variant in which two Aβ40 units are linked in one polypeptide chain through a flexible glycerin-serine-rich linker.[11] The conformational properties of the Aβ40 units in dimAβ are the same as those of unlinked Aβ40.[11] However, due to the increased local Aβ concentration, gO/CF formation of dimAβ is strongly promoted, which is reflected in the comparatively low COC of ≈1.5 μM at neutral pH.[11] Above the COC, Thioflavin T (ThT) fluorescence indicates biphasic assembly kinetics of dimAβ (Figure 1 A). During the first phase, gO/CFs form (Figure 1 C) in an oligomerization reaction with a high reaction order of ≈3.[11] After a lag-time, amyloid fibril formation is observed, in agreement with a nucleation-polymerization reaction (Figure 1 A,C).[11] Upon prolonged incubation, the metastable gO/CFs are slowly replaced by amyloid fibrils.[11] Above the COC, the lag-time of amyloid fibril formation develops an inverse dependence on protein concentration, i.e., the lag-time increases with protein concentration (Figure 1 B), indicating that gO/CFs actively interfere with amyloid fibril formation.[11]

We tested if these observations, previously made for dimAβ and hewL, are reproduced for Aβ40 and Aβ42. A logarithmic plot of the ThT time course of Aβ40 assembly at a concentration of 20 μM or below shows a sigmoidal curve with a lag-time of several hours. This is in agreement with amyloid formation by a nucleation-polymerization reaction with prominent contributions from secondary nucleation (Figure 1 D). In contrast, for Aβ40 concentrations of 40 μM or above, an additional, lag-free kinetic phase occurred during which gO/CFs assembled (Figure 1 D,F). These gO/CFs were replaced by amyloid fibrils during a second kinetic phase (Figure 1 D,F). Aβ40 assembly thus follows the same pattern as dimAβ assembly, albeit with an approximately 20-fold higher COC (≈30 μM), which is expected considering the lack of a covalent connection between Aβ monomers in unlinked Aβ40. ThT kinetics recorded with Aβ40 by the deGrado and Prusiner lab, for concentrations at or above those used here, generated similar biphasic kinetics and produced long-lived Aβ gOs.[24] As with dimAβ and hewL, the lag-time of amyloid fibril formation of Aβ40 started to increase above the COC (Figure 1 E). This indicates that Aβ40 gO/CFs share the ability to interfere actively with fibril formation. For Aβ42, the ThT time courses indicated a transition to biphasic kinetics at a concentration between 10 and 30 μM (Figure 1 G), in line with previous observations.[25] The short lag times of Aβ42 amyloid fibril formation undermined our efforts of correlating biphasic ThT kinetics with the onset of gO/CF formation in that system. Never-

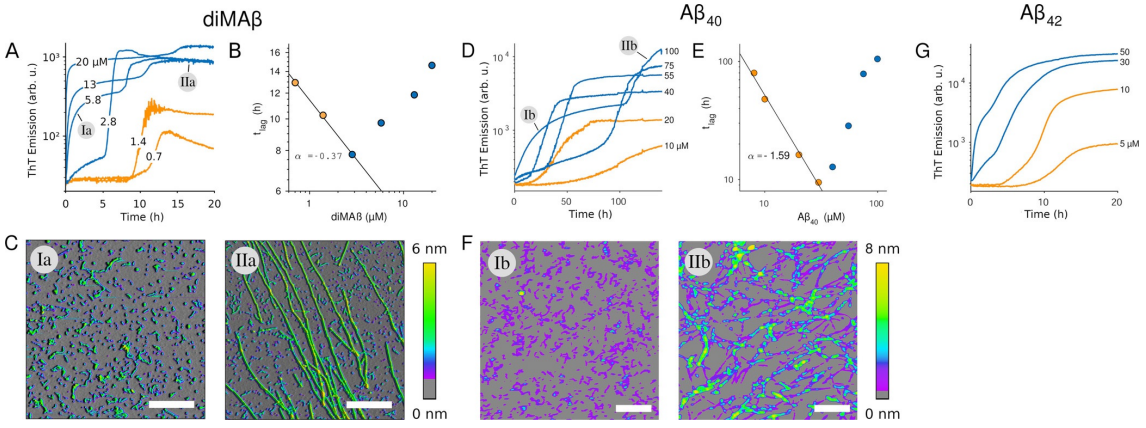

Figure 1. Biphasic assembly kinetics of Aβ. A), D), G) Transition from sigmoidal (orange) to bimodal (blue) amyloid growth kinetics of dimAβ, Aβ40, and Aβ42, monitored by ThT fluorescence. Concentration dependent time traces of A) dimAβ assembly in 50 mM Na-phosphate, 50 mM NaCl, pH 7.4, 37 °C, and D) Aβ40 or G) Aβ42 assembly in 50 mM Na-phosphate, pH 7.4, 27 °C. ThT fluorescence is plotted logarithmically to highlight the stable low signal during the lag-time under sigmoidal growth conditions. B), E) Dependence of the lag-time of the second kinetic phase on protein concentration. C), F) AFM images corresponding to the early oligomeric and subsequent fibril-dominated kinetic phases observed above the COC.

theless, the data for Aβ40 and Aβ42 show that the observations made for dimAβ and hewL extend to the two prevalent Aβ variants, with higher COCs of the unlinked peptides.

One possible mechanism by which gO/CFs might actively inhibit amyloid formation would be by interfering with secondary nucleation. GO/CFs might bind to amyloid fibril surfaces, where they could block the sites capable of catalyzing fibril nucleation. To test this hypothesis, we first investigated if gO/CFs bind to amyloid fibril surfaces. Fibrils were formed from Aβ40 at a concentration of 10 μM. Since this concentration is below the COC of Aβ40, only fibrils but no gO/CFs were formed. Upon centrifugation, the fibrils were found in the pellet (Figure 2A, left). GO/CFs were formed by quiescently incubating dimAβ at a concentration of 10 μM for 24 hours. Under these conditions dimAβ assembled into gO/CFs whereas amyloid fibrils were still absent. The gO/CFs were collected from the supernatant after centrifugation (Figure 2A, middle). When Aβ40 fibrils and dimAβ gO/CFs were mixed and subsequently centrifuged, the pellet contained amyloid fibrils decorated with gO/CFs (Figure 2A, right). This indicates that the fibril surfaces have an affinity for gO/CFs, leading to co-precipitation of the two species. The experiment was repeated for hewL. HewL amyloid fibrils grown under sigmoidal (sub-COC) conditions (Figure 2B, left) and hewL gO/CFs formed during the early phases of biphasic growth (Figure 2B, middle) were mixed, resulting in binding of gO/CFs to the lateral surfaces of the fibrils (Figure 2B, right). In addition, mixing of hewL gO/CFs with fibrils at growth temperatures dramatically increased lateral bundling and precipitation of fibrils, while isolated fibrils remained unchanged (Figure 2C). Both binding and bundling reduce the fibril surface area available for secondary nucleation.

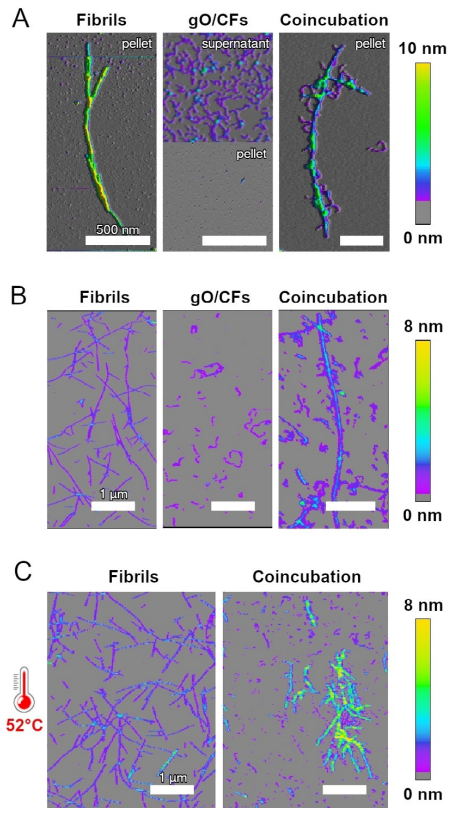

Figure 2. GO/CFs bind to amyloid fibril surfaces. AFM images of assemblies of A) dimAβ and Aβ40 or B),C) hewL. A) Amyloid fibrils formed from 10 μM Aβ40 were found in the pellet upon centrifugation at 14000 g (left); gO/CFs formed from 10 μM dimAβ remained in the supernatant (middle). Upon mixing equimolar amounts, dimAβ gO/CFs co-precipitated with Aβ40 fibrils and decorated fibril surfaces (right). B) Amyloid fibrils and gO/CFs formed from 1.75 mM hewL were grown below (50 mM NaCl) or above (250 mM NaCl) the COC, respectively. After isolation and adjusting NaCl for both to 450 mM,100 μM of fibrils were mixed with 1 mM of gO/CFs at room temperature and in 450 mM NaCl. C) Mixing hewL gO/CFs and fibrils at growth temperature (52 °C), instead, induced rapid fibril bundling and precipitation while, under the same conditions, fibrils themselves remained unchanged.

In order to isolate the consequences of this gO/CF and fibril interaction on fibril growth mechanisms we performed seeded fibril growth experiments with increasing gO/CF admixtures. To do so, we took advantage of the different COCs for dimAβ vs. Aβ40: at low μM concentrations dimAβ assembles into gO/CFs, whereas Aβ40 continues to exhibit the sigmoidal kinetics of nucleated-polymerization with secondary nucleation. Furthermore, dimAβ gO/CFs possess high kinetic stability and persist even for several hours after dilution to sub-COC concentrations, thereby allowing to investigate effects of gO/CFs down to sub-μM concentrations.[26] Amyloid fibril formation is a multistep reaction (Figure 3G).[27] To test the effects of gO/CFs specifically on fibril elongation and secondary nucleation, we seeded Aβ40 monomers with different concentrations of sonicated Aβ40 fibrils in the presence of increasing concentrations of dimAβ gO/CFs (Figure 3A). When 10% Aβ40 seeds were added to 2.5 μM Aβ40 monomers, fibril elongation was the dominant reaction as evident from the immediate linear increase in ThT signal (Figure 3B). Addition of 1.25 μM dimAβ gO/CFs (corresponding to an Aβ40 subunit concentration of 2.5 μM) did not have a substantial effect, showing that gO/CFs do not actively interfere with amyloid fibril elongation (Figure 3B). When a lower amount, that is, 0.1%, of Aβ40 seeds was applied, sigmoidal time traces were obtained, indicating the importance of autocatalytic amplification of amyloid fibrils by secondary nucleation (Figure 3C). In this case, addition of dimAβ gO/CFs led to a concentration-dependent increase in lag-time (Figure 3C). Since primary nucleation does not contribute to the ThT signal on this time scale at this Aβ40 monomer concentration (Figure 1D) and fibril elongation is not affected by gO/CFs (Figure 3B), we conclude that gO/CFs inhibit secondary nucleation. The inhibitory effect was already discernible at a concentration of 60 nM gO/CFs, which corresponds to a gO/CF:monomer ratio of 1:20 in numbers of Aβ40 units. Such a substoichiometric effect is compatible with inhibition of an autocatalytic process. To confirm that inhibition of Aβ40 fibril formation is in fact caused by gO/CFs and not due to any other activity of dimAβ on Aβ40, we compared the effects of i) dimAβ gO/CFs

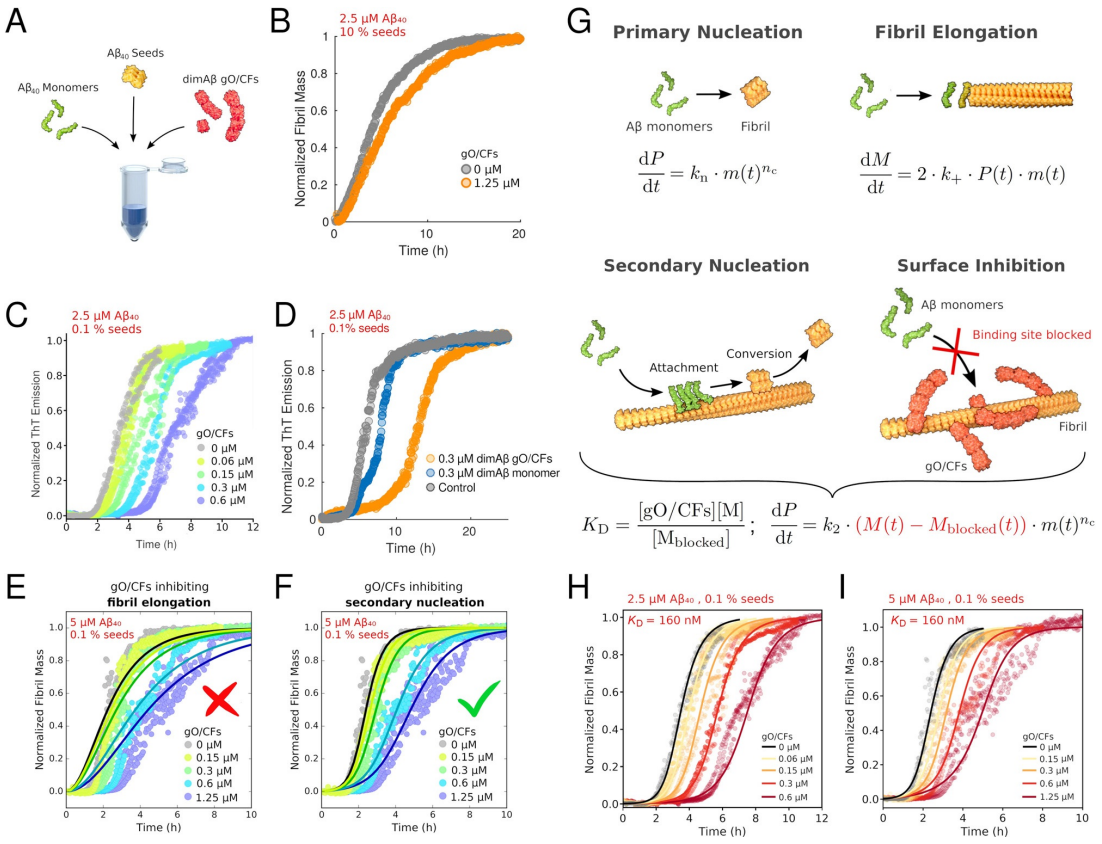

Figure 3. GO/CFs inhibit secondary nucleation of amyloid fibrils. A) Scheme of the kinetics assays. The effects of dimAβ gO/CFs on secondary nucleation and elongation of Aβ40 amyloid fibrils were probed. B) Elongation of Aβ40 fibril seeds by Aβ40 monomers in the absence and presence of dimAβ gO/CFs. C) Secondary nucleation-elongation of Aβ40 fibril seeds by Aβ40 monomers in the absence and presence of dimAβ gO/CFs. D) Secondary nucleation-elongation of Aβ40 fibril seeds by Aβ40 monomers in the absence (grey) and presence of dimAβ gO/CFs formed above the COC and diluted below the COC (orange) or dimAβ monomers below the COC (blue). E) Global fits to the data using a nucleation-elongation model. All parameters were shared apart from the elongation rate constants. F) Global fits to the data using a secondary nucleation-elongation model. All parameters were shared apart from the secondary nucleation rate constant. G) Nucleation-growth model including binding of gO/CFs to amyloid fibril surfaces, which inhibits secondary nucleation. P, fibril particle concentration; M, fibril mass concentration; m, monomer concentration; n_c, nucleus size; k_n, primary nucleation rate constant; k_2, secondary nucleation rate constant; k_+, elongation rate constant; K_D, affinity of gO/CF for the fibril surface. H), I) Numerical simulations applying the model outlined in G), using the rate constants obtained for the nucleation-elongation model in F) (uninhibited trace) and a K_D of 160 nM. Duplicate or triplicate measurements per condition are shown in panels (C), (E), (F), (H), (I).

prepared above the COC and diluted to a sub-COC concentration of 0.3 μM with those of ii) dimAβ monomers that were freshly eluted from size exclusion chromatography and kept at a sub-COC concentration of 0.3 μM. The dimAβ preparation that contained gO/CFs due to incubation above the COC exhibited a much stronger effect on fibril formation than the one kept below the COC (Figure 3 D). The inhibition is not an unspecific effect of any polypeptide assembly in the size range of gO/CFs, as it is not observed for ferritin, a 24-mer of helical bundles with a molecular weight of 440 kD (Figure S1).

To further confirm that the kinetics data are in agreement with inhibition of secondary nucleation, we computed global fits to the gO/CF concentration-dependent data for two different models of fibril formation using the software package Amylofit.[27] First, we applied a nucleation-elongation model and performed global fits that attributed the effects of gO/CFs to an altered rate constant of either primary nucleation or fibril elongation (all parameters were shared among the data sets apart from the rate constants of primary nucleation or fibril elongation, respectively). These fits showed clear deviations from the experimental data (Figures 3 E and S2A,B). Second, we applied a secondary nucleation-elongation model and performed global fits that attributed the effects of GO/CFs to altered rate constants of either primary nucleation, secondary nucleation, or fibril elongation (again, keeping all other fitting parameters the same among the data sets). The global fit to this model using a variable rate constant of primary nucleation did not reproduce the

decreasing slope during the exponential growth phase with increasing gO/CF concentration (Figure S2C). In contrast, when the rate constants of secondary nucleation or fibril elongation were variable, good agreement with the data was obtained (Figures 3F and S2D,E). These fits do not differentiate between effects on secondary nucleation and fibril elongation, as the rate constant of secondary nucleation occurs in the regression equation only in the form of its product with the rate constant of fibril elongation.[28] However, as we can exclude any substantial effect of gO/CF on fibril elongation (Figure 3B), the global fits further strengthen the case for gO/CFs inhibiting amyloid fibril formation through an effect on secondary nucleation. As gO/CFs bind to amyloid fibril surfaces, they likely inhibit secondary nucleation by blocking the sites capable of catalyzing secondary nucleation (Figure 3G). This mode of inhibition of Aβ fibril formation has previously been described for the BRICHOS chaperone.[29] The reduction in the number of active sites effectively corresponds to a reduction in the fibril surface available for autocatalytic amplification rather than to a decrease in the secondary nucleation rate constant. We extended the nucleation-polymerization model by including an equilibrium of gO/CF binding to fibrils that reduces the fibril mass engaged in secondary nucleation (Figure 3G). Numerical simulations with the modified model were performed, using the rate constants obtained by Amylofit for the uninhibited case of nucleation-polymerization with variable secondary nucleation (black fit in Figure 3F). In particular, the same secondary nucleation rate constant was used for all gO/CF concentrations, attributing the gO/CF concentration dependence of the kinetics solely to changes in the fibril mass available for secondary nucleation according to the gO/CF:fibril interaction equilibrium. The gO/CF:fibril interaction was treated as a 1:1 interaction in the number of Aβ subunits. When applying a dissociation constant of $K_D =$ 160 nM the numerical simulations yielded good agreement with data obtained both at 2.5 μM and 5 μM Aβ40 monomer concentration (Figure 3H,I).

Conclusion

We previously observed a remarkable inversion of the scaling relation between increasing protein concentration and decreasing lag-times for dimAβ and hewL amyloid fibril formation upon crossing the COC.[11] Here, we reproduced the surprising increase in lag-time with increasing protein concentration for Aβ40, which indicates that gO/CFs actively inhibit fibril formation (Figure 1E). Collectively, the AFM data (Figure 2) and chemical kinetics data (Figure 3) provide strong evidence that gO/CFs inhibit Aβ amyloid fibril formation by binding to amyloid fibril surfaces, blocking the sites that would otherwise promote secondary nucleation. The same mode of inhibition was observed for the BRICHOS chaperone, but not for a set of control proteins.[29] This suggests that this inhibitory activity is rather specific. It is also in line with the relatively high affinity of the gO/CF:fibril interaction, as indicated by the observed inhibition at low nM gO/CF concentration.

Our observations provide insight into the structure specificity of secondary nucleation. Decoration of amyloid fibril surfaces with gO/CFs formed from the same protein results in less efficient secondary nucleation. This demonstrates that gO/CF surfaces do not possess the same capacity as amyloid fibril surfaces to catalyze fibril nucleation, suggesting that the cross-β structure of amyloid fibrils is essential for efficient secondary nucleation. This is consistent with the distinct structural signatures of gO/CFs vs. fibrils seen in the amide-I bands of their respective infrared spectra that we have shown for hewL and that have been reported for Aβ, as well.[20,30]

Figure 4 shows an updated Scheme of oligomer and amyloid fibril formation. GO/CFs are an alternative (off-pathway), metastable assembly type and form rapidly and extensively above the COC. GO/CFs inhibit amyloid formation by competing for the monomers that are required for amyloid fibril nucleation and elongation.[11] In addition, as we show here, GO/CFs actively inhibit the autocatalytic amplification of fibrils by blocking secondary nucleation sites on amyloid fibrils.

Recently, protofibril–fibril interactions were observed under conditions of biphasic Aβ42 assembly, and the protofibrils were interpreted to represent nuclei formed by secondary nucleation.[31] This interpretation is in conflict with the off-pathway nature of protofibrils.[11,13] The results reported here show that protofibril–fibril interactions do not represent, but rather interfere with secondary nucleation.

The interplay between gO/CFs and amyloid fibrils has a high relevance for AD pathogenesis: GO/CFs, which are thought to represent the main toxic Aβ species,[8,13,21,32] were shown to associate with amyloid fibril plaques in vivo, with potential consequences for the neurotoxic activities of both assembly types.[22,23] For example, amyloid fibril plaques might serve as reservoir of toxic gO/CFs.[22,23] Our results demonstrate that the interaction of gO/CFs with amyloid fibrils affects the kinetics of formation and depletion of the

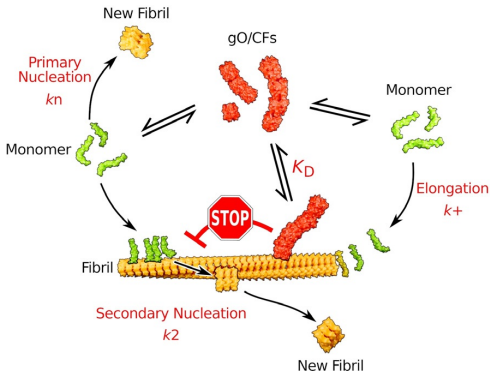

Figure 4. Scheme of oligomer and amyloid fibril formation. GO/CFs constitute an alternative (off-pathway) assembly type that competes with amyloid fibrils for monomers and that inhibits the autocatalytic amplification of amyloid fibrils by secondary nucleation. GO/CFs interfere with secondary nucleation by binding to amyloid fibrils surfaces and blocking the sites that catalyze nucleation.

two species. By binding to amyloid fibrils, gO/CFs inhibit formation of new fibrils and thereby delay their own replacement by amyloid fibrils. The dimAβ-Aβ40 system may serve as a valuable tool for further elucidation of the interplay between gO/CFs and amyloid fibrils.

Acknowledgements

This project was supported by ERC Consolidator Grant 726368 (W.H.), by the National Institutes of Health grant 2R15GM097723-02 (M.M), and by the Hans und Ilse Breuer-Stiftung (F.H.). Open access funding enabled and organized by Projekt DEAL.

Conflict of interest

The authors declare no conflict of interest.

Keywords: aggregates · fibrils · peptides · protein–protein interactions · self-assembly

[1] M. G. Iadanza, M. P. Jackson, E. W. Hewitt, N. A. Ranson, S. E. Radford, *Nat. Rev. Mol. Cell Biol.* **2018**, *19*, 755 – 773.
[2] A. J. Baldwin, T. P. Knowles, G. G. Tartaglia, A. W. Fitzpatrick, G. L. Devlin, S. L. Shammas, C. A. Waudby, M. F. Mossuto, S. Meehan, S. L. Gras, et al., *J. Am. Chem. Soc.* **2011**, *133*, 14160 – 14163.
[3] D. J. Selkoe, J. Hardy, *EMBO Mol. Med.* **2016**, *8*, 595 – 608.
[4] M. T. Colvin, R. Silvers, Q. Z. Ni, T. V. Can, I. Sergeyev, M. Rosay, K. J. Donovan, B. Michael, J. Wall, S. Linse, et al., *J. Am. Chem. Soc.* **2016**, *138*, 9663 – 9674.
[5] L. Gremer, D. Schölzel, C. Schenk, E. Reinartz, J. Labahn, R. B. G. Ravelli, M. Tusche, C. Lopez-Iglesias, W. Hoyer, H. Heise, et al., *Science* **2017**, *358*, 116 – 119.
[6] M. Kollmer, W. Close, L. Funk, J. Rasmussen, A. Bsoul, A. Schierhorn, M. Schmidt, C. J. Sigurdson, M. Jucker, M. Fändrich, *Nat. Commun.* **2019**, *10*, 4760.
[7] S. I. Cohen, S. Linse, L. M. Luheshi, E. Hellstrand, D. A. White, L. Rajah, D. E. Otzen, M. Vendruscolo, C. M. Dobson, T. P. Knowles, *Proc. Natl. Acad. Sci. USA* **2013**, *110*, 9758 – 9763.
[8] E. N. Cline, M. A. Bicca, K. L. Viola, W. L. Klein, *J. Alzheimer's Dis.* **2018**, *64*, S567 – S610.
[9] C. S. R. Grüning, S. Klinker, M. Wolff, M. Schneider, K. Toksöz, A. N. Klein, L. Nagel-Steger, D. Willbold, W. Hoyer, *J. Biol. Chem.* **2013**, *288*, 37104 – 37111.
[10] J. D. Harper, S. S. Wong, C. M. Lieber, P. T. Lansbury, *Chem. Biol.* **1997**, *4*, 119 – 125.
[11] F. Hasecke, T. Miti, C. Perez, J. Barton, D. Schölzel, L. Gremer, C. S. R. Grüning, G. Matthews, G. Meisl, T. P. J. Knowles, et al., *Chem. Sci.* **2018**, *9*, 5937 – 5948.
[12] A. Jan, D. M. Hartley, H. A. Lashuel, *Nat. Protoc.* **2010**, *5*, 1186 – 1209.
[13] K. Ono, M. Tsuji, *Int. J. Mol. Sci.* **2020**, *21*, 952.
[14] D. M. Walsh, A. Lomakin, G. B. Benedek, M. M. Condron, D. B. Teplow, *J. Biol. Chem.* **1997**, *272*, 22364 – 22372.
[15] B. A. Chromy, R. J. Nowak, M. P. Lambert, K. L. Viola, L. Chang, P. T. Velasco, B. W. Jones, S. J. Fernandez, P. N. Lacor, P. Horowitz, et al., *Biochemistry* **2003**, *42*, 12749 – 12760.
[16] R. Kodali, R. Wetzel, *Curr. Opin. Struct. Biol.* **2007**, *17*, 48 – 57.
[17] R. Tycko, *Cold Spring Harbor Perspect. Med.* **2016**, *6*.
[18] W. S. Gosal, I. J. Morten, E. W. Hewitt, D. A. Smith, N. H. Thomson, S. E. Radford, *J. Mol. Biol.* **2005**, *351*, 850 – 864.
[19] H. A. Lashuel, C. Wurth, L. Woo, J. W. Kelly, *Biochemistry* **1999**, *38*, 13560 – 13573.
[20] T. Miti, M. Mulaj, J. D. Schmit, M. Muschol, *Biomacromolecules* **2015**, *16*, 326 – 335.
[21] H. H. Jarosz-Griffiths, E. Noble, J. V. Rushworth, N. M. Hooper, *J. Biol. Chem.* **2016**, *291*, 3174 – 3183.
[22] D. L. Brody, H. Jiang, N. Wildburger, T. J. Esparza, *Alzheimer's Res. Ther.* **2017**, *9*, 62.
[23] R. M. Koffie, M. Meyer-Luehmann, T. Hashimoto, K. W. Adams, M. L. Mielke, M. Garcia-Alloza, K. D. Micheva, S. J. Smith, M. L. Kim, V. M. Lee, et al., *Proc. Natl. Acad. Sci. USA* **2009**, *106*, 4012 – 4017.
[24] M. Nick, Y. Wu, N. W. Schmidt, S. B. Prusiner, J. Stöhr, W. F. DeGrado, *Biopolymers* **2018**, *109*, e23096.
[25] Z. Fu, D. Aucoin, J. Davis, W. E. Van Nostrand, S. O. Smith, *Biochemistry* **2015**, *54*, 4197 – 4207.
[26] M. P. Schützmann, F. Hasecke, S. Bachmann, M. Zielinski, S. Hänsch, G. F. Schröder, H. Zempel, W. Hoyer, *bioRxiv* **2020**, https://doi.org/10.1101/2020.06.28.175885.
[27] G. Meisl, J. B. Kirkegaard, P. Arosio, T. C. Michaels, M. Vendruscolo, C. M. Dobson, S. Linse, T. P. Knowles, *Nat. Protoc.* **2016**, *11*, 252 – 272.
[28] S. I. Cohen, M. Vendruscolo, M. E. Welland, C. M. Dobson, E. M. Terentjev, T. P. Knowles, *J. Chem. Phys.* **2011**, *135*, 065105.
[29] S. I. A. Cohen, P. Arosio, J. Presto, F. R. Kurudenkandy, H. Biverstal, L. Dolfe, C. Dunning, X. Yang, B. Frohm, M. Vendruscolo, et al., *Nat. Struct. Mol. Biol.* **2015**, *22*, 207 – 213.
[30] J. M. Ruysschaert, V. Raussens, *Methods Mol. Biol.* **2018**, *1777*, 69 – 81.
[31] M. Törnquist, R. Cukalevski, U. Weininger, G. Meisl, T. P. J. Knowles, T. Leiding, A. Malmendal, M. Akke, S. Linse, *Proc. Natl. Acad. Sci. USA* **2020**, *117*, 11265 – 11273.
[32] I. H. Cheng, K. Scearce-Levie, J. Legleiter, J. J. Palop, H. Gerstein, N. Bien-Ly, J. Puolivali, S. Lesne, K. H. Ashe, P. J. Muchowski, et al., *J. Biol. Chem.* **2007**, *282*, 23818 – 23828.

Manuscript received: July 22, 2020
Revised manuscript received: October 16, 2020
Accepted manuscript online: October 23, 2020
Version of record online: December 11, 2020

Angewandte Chemie
Eine Zeitschrift der Gesellschaft Deutscher Chemiker

Supporting Information

Protofibril–Fibril Interactions Inhibit Amyloid Fibril Assembly by Obstructing Secondary Nucleation

Filip Hasecke[+], Chamani Niyangoda[+], Gustavo Borjas, Jianjun Pan, Garrett Matthews, Martin Muschol, and Wolfgang Hoyer**

anie_202010098_sm_miscellaneous_information.pdf

Table of contents

1. Supporting Experimental Section

Proteins and chemicals

DimAβ was recombinantly produced as previously described.[1] Aβ40 and Aβ42 were obtained from Bachem or rPeptide. Two-times crystallized and lyophyilized hen egg-white lysozyme (hewL) was obtained from Worthington Biochemical Corporation and used without further purification. Ferritin was obtained from Cytiva.

Preparation of Aβ40

Before use, Aβ40 peptide from Bachem was further purified. The lyophilized powder was reconstituted in 6M guanidinium chloride, 50 mM sodium-phosphate buffer, pH 7.4. Reverse phase high-performance liquid chromatography (RP-HPLC) was performed to remove residual impurities. The sample was loaded onto a semi-preparative Zorbax 300SB-C8 RP-HPLC column (9.4 mm × 250 mm, Agilent) connected to an Agilent 1260 Infinity system with UV detection at 214 nm. Monomeric Aβ40 was eluted in a gradient from 30% (v/v) to 36% acetonitrile in water, 0.1% (v/v) trifluoroacetic acid at 80 °C. Aβ40 containing fractions were pooled, lyophilized, dissolved in HFIP, aliquoted in 1 mg portions, lyophilized again, and stored at RT.

Preparation of monomeric Aβ species for ThT kinetics experiments

For aggregation kinetics experiments, the lyophilized protein (Aβ40 or dimAβ) was reconstituted in 6M guanidinium chloride, 50 mM sodium-phosphate buffer, pH 7.4, and incubated at room temperature for 30 min. The lyophilized powder from rPeptide (Aβ40 or Aβ42) was dissolved directly in 100 mM NaOH at pH 12. For all Aβ peptides, SEC was performed using a Superdex 75 increase column (GE Healthcare) equilibrated with 35 mM Na_2HPO_4 50 mM NaCl, 5 mM NaOH, pH 11. The concentration of the monomeric peptides was measured via UV absorption at 280 nm using the extinction coefficient of 1,490 M^{-1} cm^{-1} for Aβ40 and Aβ42, and 2,980 M^{-1} cm^{-1} for dimAβ. Solutions were kept on ice during subsequent sample preparation. Immediately before the start of ThT kinetics experiments, 1.5% 1 M NaH_2PO_4 was added, yielding 50 mM Na-phosphate, 50 mM NaCl, pH 7.4, as final buffer composition.

Preparation of dimAβ gO/CFs for kinetic assays

DimAβ lyophilisate was resuspended in a small volume (3-5 µl) 50 mM NaOH until completely dissolved. Next, 50 mM Na-phosphate buffer, 50 mM NaCl, pH 7.4, and 50 mM HCl (3-5 µl) were added and immediately mixed, obtaining a final concentration of 10 µM dimAβ. To induce gO/CF formation, dimAβ was incubated at 37°C for 16 – 24 hours.

Preparation of Aβ40 fibril seeds for kinetic assays

Aβ40 lyophilisate was resuspended in a small volume (3-5 µl) 50 mM NaOH until completely dissolved. Next, 50 mM Na-phosphate buffer, 50 mM NaCl, pH, 7.4, 10 µM ThT, and 50 mM HCl (3-5 µl) were added and immediately mixed, obtaining a final concentration of 10 µM Aβ40. Aβ amyloid growth was monitored using a BMG ClarioStar plate reader in 96-well low-binding plates (Greiner). After 16 – 24 hours samples with a steady plateau were taken and combined. Samples were sonicated using a Bandelin Sonopuls utilizing an MS72 sonicator tip. Sonication was performed in 3 pulses of one second sonication and five seconds waiting in between at 25% amplitude strength.

Preparation of isolated hewL fibrils and gO/CFs for interaction experiments

HewL fibrils and gO/CFs were grown and isolated following protocols previously described.[1] In short, lyophilized hewL was dissolved at 14 mM in 25 mM KH_2PO4 buffer with either 50 mM NaCl (fibrils) or 250 mM NaCl (gO/CFs) and incubated for 90 hours (fibrils) or 5 hours (gO/CFs), respectively. RFs and go/CFs were isolated from the residual monomeric background three repeated centrifugation (15,000 rpm for 12 hours, each) with the resulting pellet re-suspended in fresh buffer solution after each round.

Amyloid formation assays using Thioflavin T (ThT) fluorescence

ThT stock solutions were prepared by dissolving 2 mM dye in distilled water and then filtering through a 220 nm syringe filter. Final ThT concentrations were obtained from absorption at a wavelength of 412 nm (ε_{412} = 32,000 M^{-1} cm^{-1}). Aβ amyloid growth kinetics measurements were performed using either a BMG ClarioStar or a BMG Fluostar Optima plate reader with ThT excitation at 445 nm and emission collected at 482 nm in 96-well low-binding half-area plates (Greiner) which were sealed with transparent polypropylene films. Samples contained Aβ species as indicated in the Results and 10 µM ThT in 50 mM Na-phosphate buffer, 50 mM NaCl, pH7.4. Typically, three identical 100 µL samples were incubated at 37 °C. Measurements were taken every 3 minutes without shaking in between.

Data analysis of ThT kinetics

ThT data in Figure 1 was analyzed as described in ref.[1]. Briefly, sigmoidal amyloid growth kinetics below the COC were fit to analytical approximations of nucleated polymerization with secondary nucleation mechanisms. Biphasic growth kinetics above the COC were analyzed in two steps. First, the portion dominated by gO/CF formation was fit to a one-step oligomerization $n\ M \rightarrow M_n$ function. To be able to fit the fibril nucleation-growth dominated second part of the kinetics, the oligomerization fit was substracted from the raw data followed by a fit to analytical approximations of nucleated polymerization with secondary nucleation mechanisms as

described before. We defined the RF lag time as the point at which the amplitude of the RF portion of the ThT signal increases beyond a fixed threshold.

Primary and secondary nucleation and elongation models using AmyloFit

Data as shown in Figure 3 E and F was analyzed using the online software AmyloFit.[2] The ThT raw data was uploaded into the fitting software and the triplicates were grouped. Sample and seed concentrations were assigned to the individual groups. The seed particle concentration was defined assuming fibril seed sizes of 1,000 Aβ subunits per seed. The models "Nucleation Elongation" and "Secondary Nucleation Dominated" were used to analyze the data. The variables n_c and n_2 were kept at 2. Only one of the variables k_n, k_+ and k_2 was fitted individually while the others were fitted globally as indicated in the Results.

Secondary nucleation-growth model including binding of gO/CFs to amyloid fibril surface

The effect of gO/CFs on fibril growth was modeled using numerical simulations. The change of fibril mass concentration (M) and fibril particle concentration (P) was calculated over time in one thousand time increments over the observed timespan. The rates for primary nucleation (k_n), elongation (k_+) and secondary nucleation (k_2) for Aβ40 in the presence of 0.1% Aβ40 fibril seeds and in the absence of gO/CFs were obtained from analysis with AmyloFit.

Each time increment included the calculation of the following derivatives:

$\frac{\mathrm{d}P}{\mathrm{d}t} = k_\mathrm{n} \cdot m(t)^{n_c}$ | Change of fibril particle concentration due to primary nucleation-growth

$\frac{\mathrm{d}M}{\mathrm{d}t} = 2 \cdot k_+ P(t) m(t)$ | Change of fibril mass concentration due to fibril elongation

In our model of secondary nucleation inhibition in response to gO/CF binding to secondary nucleation sites, the formula for secondary nucleation was modified to include the reduction of available fibril surface for secondary nucleation:

$\frac{\mathrm{d}P}{\mathrm{d}t} = k_2 \cdot \left(M(t) - M_\mathrm{blocked}(t)\right) \cdot m(t)^{n_c}$ | Secondary nucleation including surface inhibition

The blocked fraction was calculated taking the inhibitor concentration [gO/CFs] and the dissociation constant (K_D) into account:

$$K_\mathrm{D} = \frac{[\mathrm{gO/CFs}_\mathrm{free}][\mathrm{M}_\mathrm{free}]}{[\mathrm{M}_\mathrm{blocked}]}$$

$$[\mathrm{M}]_\mathrm{blocked}(t) = \frac{([\mathrm{M}]_\mathrm{total}(t) + [\mathrm{gO/CFs}]_\mathrm{total} + K_\mathrm{D}) - \sqrt{([\mathrm{M}]_\mathrm{total}(t) + [\mathrm{gO/CFs}]_\mathrm{total} + K_\mathrm{D})^2 - 4[\mathrm{M}]_\mathrm{total}(t)[\mathrm{gO/CFs}]_\mathrm{total}}}{2}$$

Atomic force microscopy

For imaging of Aβ assemblies, 25 µl of the samples were applied onto freshly cleaved muscovite mica. After 1 minute of incubation at room temperature, samples were washed three time with 100 µl ddH_2O, and subsequently dried under N_2 gas stream. Imaging was performed

in intermittent contact mode (AC mode) in a JPK Nano Wizard 3 atomic force microscope (JPK, Berlin) using a silicon cantilever with silicon tip (OMCLAC160TS-R3, Olympus) with a typical tip radius of 9 ± 2 nm, a force constant of 26 N/m and resonance frequency around 250 kHz. The images were processed using JPK DP Data Processing Software (version spm-5.0.84) or Gwyddion (version 2.52). For the presented height profiles a polynomial fit was subtracted from each scan line first independently and then using limited data range. False colour height images were superimposed over either amplitude or phase images using Gimp – GNU Image Manipulation Program.

For hewL samples, each of isolated RFs and gO/CFs were brought to 450 mM NaCl, mixed and further diluted to a final concentration ratio of 30:300 μM. 16 μL of this mixture was deposited on freshly cleaved mica, either immediately after mixing or following 15 min of incubation at the amyloid growth temperature of 52 °C. After 5 minute incubation, samples were washed with dH_2O and dried with N_2 gas. AFM imaged were acquired on an MPF-3D (Asylum Research) in taping mode using PFP-FMR-50 silicon tips (Nanosensor) with nominal tip radii of 7 nm. The cantilever had a typical spring constant and resonance frequency of 2 nN/nm and 70 kHz, respectively. It was driven at 60−70 kHz in alternating current mode and at a scan rate of 0.25-0.5 Hz. Images were acquired at 512 × 512 pixel resolution. Amplitude, phase, and height images were collected and processed using the built-in acquisition software.

2. Supporting Figures

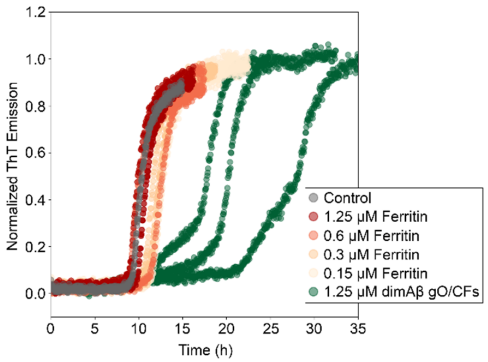

Figure S1: Inhibition of secondary nucleation is not a universal feature of polypeptide assemblies in the size range of gO/CFs. Secondary nucleation-elongation of Aβ40 fibril seeds by Aβ40 monomers in the absence (grey) or presence of either dimAβ gO/CFs (green) or the 440 kD-protein ferritin (red), which is a 24-mer of helical bundles.

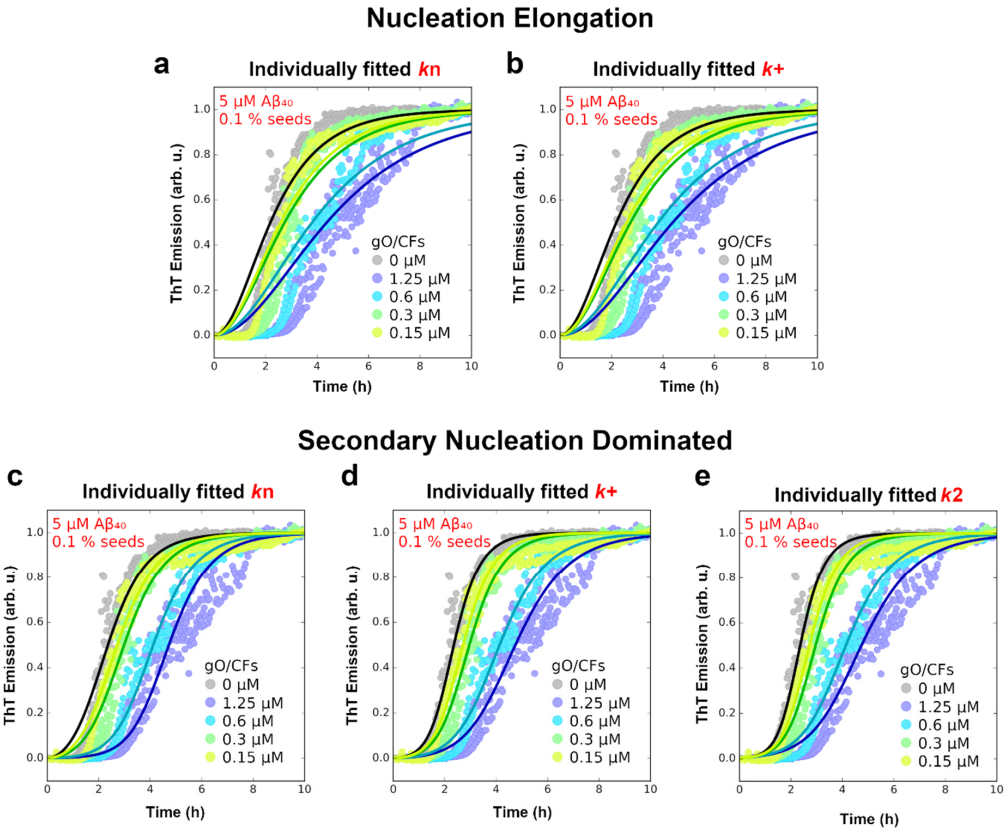

Figure S2: Comparison of the "Nucleation Elongation" and "Secondary Nucleation Dominated" models of AmyloFit. ThT traces from 5 µM Aβ40 seeded with 0.1 % Aβ40 seeds treated with inrcreasing concentrations of dimAβ gO/CFs were analyzed. The effect of gO/CFs on the kinetic rates of fibril nucleation and growth was analyzed by fitting one of the kinetic rates k_n, k_+, or k_2 individually while the other rates were fitted globally. a), b) Fits to the "Nucleation Elongation" model, either fitting k_n (a) or k_+ (b) individually. c)-e) Fits to the "Secondary Nucleation Dominated" model, either fitting k_n (c), k_+ (d), or k_2 (e) individually.

3. Supporting References

[1] F. Hasecke, T. Miti, C. Perez, J. Barton, D. Scholzel, L. Gremer, C. S. R. Gruning, G. Matthews, G. Meisl, T. P. J. Knowles, et al., *Chem. Sci.* **2018**, *9*, 5937-5948.

[2] G. Meisl, J. B. Kirkegaard, P. Arosio, T. C. Michaels, M. Vendruscolo, C. M. Dobson, S. Linse, T. P. Knowles, *Nat. Protoc.* **2016**, *11*, 252-272.

nature COMMUNICATIONS

ARTICLE

https://doi.org/10.1038/s41467-021-24900-4 OPEN

Endo-lysosomal Aβ concentration and pH trigger formation of Aβ oligomers that potently induce Tau missorting

Marie P. Schützmann[1,6], Filip Hasecke[1,6], Sarah Bachmann[2,6], Mara Zielinski[3], Sebastian Hänsch[4], Gunnar F. Schröder[3,5], Hans Zempel[2✉] & Wolfgang Hoyer[1,3✉]

Amyloid-β peptide (Aβ) forms metastable oligomers >50 kDa, termed AβOs, that are more effective than Aβ amyloid fibrils at triggering Alzheimer's disease-related processes such as synaptic dysfunction and Tau pathology, including Tau mislocalization. In neurons, Aβ accumulates in endo-lysosomal vesicles at low pH. Here, we show that the rate of AβO assembly is accelerated 8,000-fold upon pH reduction from extracellular to endo-lysosomal pH, at the expense of amyloid fibril formation. The pH-induced promotion of AβO formation and the high endo-lysosomal Aβ concentration together enable extensive AβO formation of Aβ42 under physiological conditions. Exploiting the enhanced AβO formation of the dimeric Aβ variant dimAβ we furthermore demonstrate targeting of AβOs to dendritic spines, potent induction of Tau missorting, a key factor in tauopathies, and impaired neuronal activity. The results suggest that the endosomal/lysosomal system is a major site for the assembly of pathomechanistically relevant AβOs.

[1] Institut für Physikalische Biologie, Heinrich-Heine-Universität Düsseldorf, Düsseldorf, Germany. [2] Institute of Human Genetics and Center for Molecular Medicine Cologne (CMMC), University of Cologne, Faculty of Medicine and University Hospital Cologne, Cologne, Germany. [3] Institute of Biological Information Processing (IBI-7) and JuStruct: Jülich Center for Structural Biology, Forschungszentrum Jülich, Jülich, Germany. [4] Department of Biology, Center for Advanced Imaging (CAi), Heinrich-Heine-Universität Düsseldorf, Düsseldorf, Germany. [5] Physics Department, Heinrich-Heine-Universität Düsseldorf, Düsseldorf, Germany. [6] These authors contributed equally: Marie P. Schützmann, Filip Hasecke, Sarah Bachmann. ✉email: hans.zempel@uk-koeln.de; wolfgang.hoyer@hhu.de

Aβ amyloid fibrils are highly stable protein aggregates of regular cross-β structure that constitute the main component of the senile plaques in the brains of Alzheimer's disease (AD) patients[1–3]. Although amyloid fibrils can exert toxic activities, metastable Aβ oligomers are thought to represent the main toxic species in AD[3–5]. At sufficiently high monomer concentration, Aβ readily forms oligomers with molecular weights (MWs) >50 kDa with spherical, curvilinear, and annular shapes, where the elongated structures appear as "beads-on-a-string"-like assemblies of spherical oligomers[4–11]. While multiple names have been given to these metastable Aβ oligomers, including AβOs, ADDLs, and protofibrils, they seem to be closely related with regard to their structures and detrimental activities and likely form along a common pathway[6,7,12]. Importantly, this pathway is distinct from that of amyloid fibril formation, i.e., AβOs are not intermediates on the pathway to amyloid fibrils (they are "off-pathway") but constitute an alternative Aβ assembly type with distinct toxic activities (Fig. 1a)[4,5,11,13]. The distinct nature of Aβ amyloid fibrils and AβOs is also reflected in their different formation kinetics. Aβ amyloid fibrils form by nucleated polymerization with crucial contributions from secondary nucleation processes, resulting in the characteristic sigmoidal growth time courses that feature an extended lag time[14]. AβOs, on the other hand, form in a lag-free oligomerization reaction that has a substantially higher monomer concentration dependence than amyloid fibril formation[11]. We note that in this work the term AβO refers exclusively to these off-pathway oligomers and does not include other oligomeric Aβ species, such as those transiently formed on the pathway to amyloid fibrils, through secondary nucleation, or through shedding by fibril fragmentation[15].

Several lines of evidence support a critical role of AβOs in AD pathogenesis. AβOs of sizes >50 kDa are the main soluble Aβ species in biological samples[16]. They are synaptotoxic, disrupt long-term potentiation, and cause cognitive impairment in mouse and non-human primate models[4,8,17–23]. Furthermore, AβOs induce oxidative stress, endoplasmic reticulum stress, neuroinflammation, and elicit Tau missorting, the earliest hallmark of tauopathy in AD[21,23–29]. The detrimental effects are enhanced by pathogenic Aβ mutations that specifically promote AβO formation, in particular the arctic (Aβ E22G) and the Osaka (Aβ ΔE22) mutations[22,23,28,30,31]. Consequently, targeting AβOs therapeutically is an important alternative to amyloid-centric approaches and has entered clinical evaluation[32–34].

AβOs were suggested to trigger toxic effects through ligand-like binding to a remarkably high number of candidate receptors[4,35]. AβOs achieve clustering of receptors in cell surface signaling platforms, probably promoted by the multivalency inherent to AβOs[4,35,36]. AβO clustering is especially prominent at dendritic spines, which deteriorate upon prolonged exposure to AβOs[18]. Importantly, this effect is mediated by Tau protein, providing a connection between the Aβ and the Tau aspects of AD pathogenesis. AβOs induce missorting of Tau into the somatodendritic compartment as well as Tau hyperphosphorylation, leading to microtubule destabilization and spine loss[23,37–39].

In addition to receptor binding of extracellular AβOs, intracellular AβOs are thought to contribute to AD pathogenesis[40]. The endosomal–lysosomal system is the main site not only for Aβ production but also for the uptake of Aβ monomers and AβOs[27,41–49]. Aβ accumulates in endosomes/lysosomes, which promotes aggregation with potential consequences for cellular homeostasis as well as for the spreading of Aβ pathology by exocytosis of aggregated Aβ species[27,28,41,44–46,48–51].

At neutral pH, high Aβ concentrations are required to convert a substantial fraction of the protein into AβOs. Widely used protocols for AβO preparation start from around 100 μM Aβ

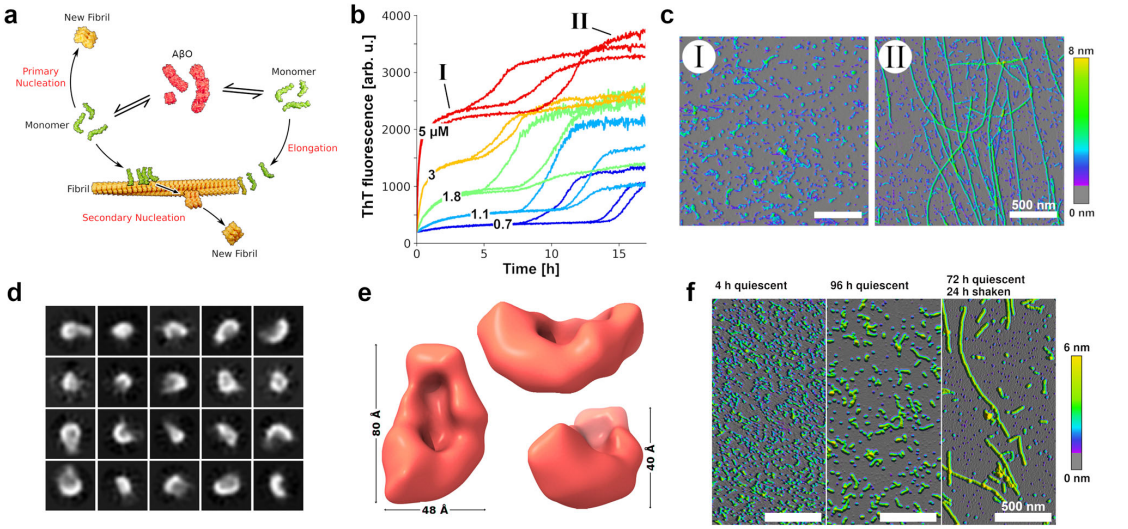

Fig. 1 AβOs assemble from dimAβ in a lag-free oligomerization reaction. a Scheme of AβO and amyloid fibril formation. **b** Biphasic assembly kinetics of dimAβ at pH 7.4 and indicated concentrations monitored by ThT fluorescence. The experimental replicates illustrate the good reproducibility of the nucleation-free oligomerization phase and the stochastic nature of the nucleation-dependent fibril growth phase. **c** AFM images corresponding to the two kinetic phases as indicated in **b**. **d** Exemplary 2D classes of the smallest dimAβ AβO species observed in cryo-EM micrographs. **e** 3D density reconstruction of this dimAβ AβO species at a resolution of 17 Å by cryo-EM. The comparatively low resolution is due to the small size and high degree of heterogeneity of the dimAβ AβO species. Consequently, only a rough estimate to size and volume can be made. **f** AFM images of dimAβ assemblies formed upon incubation at pH 7.4 in microcentrifuge tubes. Kinetics data as shown in **b** was obtained from at least three independently prepared assays with two to three replicates for each concentration for reproducibility. AFM images in **c** were prepared from two independent assays and at least three areas at different positions on the mica surface were scanned. The experiment in **f** was done once and at least two sections of the mica surface were scanned.

monomers[7,8,10]. At tenfold lower Aβ concentration, the formation of AβOs is already greatly disfavored, which enables the investigation of the pure sigmoidal time course of amyloid fibril formation, including the analysis of on-pathway oligomer formation[14,15,52]. These on-pathway oligomers, however, are short-lived, rapidly consumed in the process of fibril formation, and, as evident from the different assembly kinetics, clearly distinct from the neurotoxic off-pathway AβOs introduced above. To investigate AβO formation, we have generated a dimeric variant of Aβ termed dimAβ, in which two Aβ40 units are linked in one polypeptide chain through a flexible glycine–serine-rich linker[11]. In dimAβ, the conformational properties of the Aβ40 units are not altered as compared to free Aβ40 monomers[11]. The linkage of two Aβ units, however, increases the local Aβ concentration, which strongly promotes the highly concentration-dependent formation of AβOs[11] (Fig. 1b, c). The advantages in applying dimAβ for the study of AβOs are: First, AβOs form already above a threshold concentration (critical oligomer concentration (COC)) of ~1.5 μM dimAβ at neutral pH. Second, the increased local Aβ concentration preferentially accelerates AβO formation as compared to Aβ fibril formation, resulting in an enhanced separation of the kinetic phases of AβO and Aβ fibril formation, which facilitates analysis.

There is an apparent discrepancy between the obvious pathogenic relevance of AβOs and the high μM Aβ concentrations required for the conversion of a substantial fraction of the protein into AβOs at neutral pH in vitro, which exceeds the estimated picomolar to nanomolar concentrations of extracellular Aβ in normal brain by several orders of magnitude[44]. However, accumulation of Aβ in the endo-lysosomal system was shown to result in micromolar Aβ concentrations in late endosomes and lysosomes[44], suggesting that these acidic vesicles might be the prime sites of AβO formation. Acidic conditions have been reported to accelerate Aβ aggregation[53]. Here we applied dimAβ and Aβ42 to test whether pH reduction from neutral to endo-lysosomal pH affects AβO formation. We find that endo-lysosomal pH in fact strongly accelerates AβO formation, whereas amyloid fibril formation is delayed, suggesting that AβO formation is the dominant aggregation process in endosomes/lysosomes. We furthermore show that dimAβ is a disease-relevant model construct for pathogenic AβO formation by demonstrating that dimAβ AβOs target dendritic spines, induce AD-like somatodendritic Tau missorting, and reduce synaptic transmission in terminally matured primary neurons. This indicates that dimAβ-derived oligomers are suitable for the study of downstream mechanistic and neuropathological events in the progression of AD.

Results

DimAβ assembles into AβOs that bind to dendritic spines and potently induce Tau missorting. The assembly kinetics of dimAβ at neutral pH monitored by ThT show a biphasic behavior above a concentration (COC) of ~1.5 μM, with the first phase corresponding to the lag-free oligomerization into AβOs and the second phase reflecting amyloid fibril formation[11] (Fig. 1b, c). DimAβ AβOs are of spherical and curvilinear shape (Fig. 1c) and rich in β-structure[11], in agreement with the characteristics of AβOs formed from Aβ40 and Aβ42 (refs. [4–6,9,13,21]; for atomic force microscopic (AFM) data of AβOs formed from Aβ42, see below). We applied cryogenic electron microscopy (cryo-EM) to further characterize dimAβ AβOs structurally. Structure determination is hampered by the size and shape heterogeneity of AβOs[7,9,10], which is moreover evolving with time, as observed for AβOs formed from Aβ[9] as well as dimAβ[11]. As larger AβOs seem to be assemblies of small spherical structures, our analysis focused on the small AβOs observed in the micrographs (Fig. 1d, e and Supplementary Figs. 1–3). The fraction of small AβOs was 72 ± 12% in terms of particle number but only ~2–3% in terms of the number of Aβ molecules within AβOs (Supplementary Fig. 1c). The relation between the small and the elongated curvilinear AβOs cannot be inferred from the micrographs. Nevertheless, structure elucidation of the small AβOs could provide insight into a biologically relevant AβO substructure that may furthermore laterally associate and convert into protofibrillar AβOs[54]. We obtained a three-dimensional (3D) density reconstruction (Fig. 1e) at a resolution of 17 Å, which shows a bowl-shaped structure with dimensions of 80 × 48 × 40 Å. From this reconstruction, we were able to calculate the approximate molecular mass that fits into the density to be 62 kDa (Supplementary Fig. 3; see "Methods"). Therefore, the small AβO species, as visible on the micrographs, likely contains six dimAβ monomers (total MW of 60.2 kDa), which corresponds to 12 Aβ40 units. Dodecameric Aβ oligomers were observed before in AβO preparations from synthetic peptide or isolated from AD brain or mouse models and have been associated with neuronal dysfunction and memory impairment[55–58].

AβO formation occurred on the same time scale in the plate reader experiment as in microcentrifuge tubes (Fig. 1b, c, f). In contrast, extensive amyloid formation was observed in the plate reader experiment after ~10 h but was not detectable when AβOs were incubated in microcentrifuge tubes for several days, unless the microcentrifuge tube was agitated (Fig. 1b, c, f). This suggests that the movement of the microplate in the plate reader, caused by scanning of the wells during measurements every 3 min and 2 s of preceding orbital shaking, creates sufficient agitation to promote amyloid fibril nucleation. When the samples in the microplate were covered with a layer of mineral oil, AβO formation was unaffected but amyloid fibril formation was completely abrogated (Supplementary Fig. 4), in line with the essential role of the air–water interface in Aβ amyloid formation in vitro[59]. The strong effects of agitation[14] and air–water interface on Aβ amyloid fibril formation but not on AβO formation confirms again that their assembly mechanisms are different and is in line with the notion that AβO formation does not involve a nucleation step[11,60]. When AβOs, formed by incubation of dimAβ above the COC, were diluted to sub-COC concentrations, they persisted for >24 h, indicating high kinetic stability (Supplementary Fig. 5). We conclude that AβOs formed from dimAβ under quiescent conditions are kinetically stable, not replaced by amyloid fibrils for several days, and can be applied at sub-μM concentrations. DimAβ AβOs may therefore serve as a favorable AβO model.

To test whether dimAβ AβOs cause the same biological effects as reported for AβOs formed from Aβ40 or Aβ42, we investigated their binding to dendritic spines, their direct cytotoxicity, their capacity to induce Tau missorting, and their consequences for neuronal function. AβOs were formed from 20 μM dimAβ and added to primary mouse neurons (days in vitro 15 (DIV15)–22) to a final concentration of 0.5 μM (all dimAβ AβO concentrations given in dimAβ equivalents). One micromolar Aβ40 was used as monomeric control. DimAβ localized to neuronal dendrites both after 3 and 24 h of treatment, where it partially co-localized with dendritic protrusions positive for filamentous actin (stained by phalloidin), which mark synaptic spines (Fig. 2a). In contrast, Aβ40 monomers did not show substantial localization to dendrites (Fig. 2a). Direct cytotoxicity was assessed by analysis of the sizes and shapes of neuronal nuclei upon staining with NucBlue. The fractions of normal and dense nuclei did not change significantly after incubation with dimAβ AβOs (Fig. 2b, c), indicating the absence of direct cytotoxicity, in line with previous reports on AβOs[61].

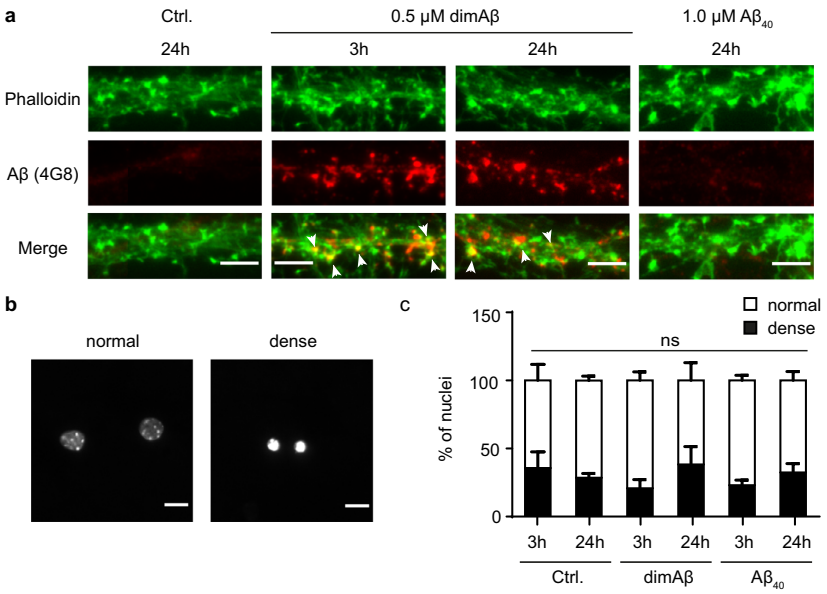

Fig. 2 DimAβ AβOs bind to dendrites and postsynaptic spines but have no direct cytotoxic effect on primary mouse neurons. Primary mouse neurons (DIV15–22) were treated with 0.5 µM dimAβ AβOs or 1 µM Aβ40 for 3 and 24 h. **a** DimAβ AβOs localized to neuronal dendrites both after 3 and 24 h of treatment, where they partially co-localized with phalloidin, a marker for synaptic spines. Arrows indicate co-localization of dimAβ with phalloidin. Scale bar, 5 µm. The experiment was independently repeated four times with similar results. **b** Nuclei of primary neurons were stained with NucBlue and analyzed with respect to shape and size. Representative images of normal and dense nuclei. Scale bar, 10 µm. **c** Quantification of normal and dense nuclei of primary neurons after vehicle control, Aβ40, or dimAβ AβO treatment revealed no direct cytotoxicity. $N = 3$; around 300 nuclei were analyzed for each condition. Error bars represent SEM. Statistical analysis was done by two-way ANOVA with Tukey's test for multiple comparisons and yielded no significant differences between the experimental groups.

Tau cellular distribution was analyzed with an anti-Tau (K9JA) antibody. DimAβ AβO-treated neurons showed strong enhancement of the fluorescence signal of Tau in the soma after 24 h of treatment (Fig. 3), indicating pathological somatodendritic Tau missorting as previously reported for AβOs[38,39]. In contrast, Aβ40 monomers did not induce Tau missorting in our experimental setting (Fig. 3). In previous studies, Tau missorting and spine loss were reversible within 12–24 h due to loss of AβO potency (transformation of AβOs over time to larger, non-toxic aggregates)[38,62]. Here we observe an increase of Tau missorting over time, which indicates remarkable kinetic stability and persistent ability of dimAβ AβOs to induce pathological Tau missorting.

Next, we investigated the consequences of AβO exposure for neuronal function. As readout, we measured spontaneous calcium oscillations in our neuronal cultures after dimAβ AβO treatment as an indicator for neuronal activity with live-cell imaging, using the fluorescent cell-permeable calcium indicator Fluo-4 as previously described[38]. A significant decrease of calcium oscillations was observed after 24 h but not after 3 h of treatment with dimAβ AβOs (Fig. 4). As calcium oscillations in our conditions depend on action potentials and neurotransmission, this indicates that dimAβ AβOs impair neuronal activity and function. With regard to dendritic spine binding, lack of direct cytotoxicity, potent induction of Tau missorting as well as decreased neuronal activity, dimAβ AβOs thus faithfully reproduce the observations previously made for AβOs formed from Aβ40 or Aβ42 or from 7:3 Aβ40:Aβ42 mixtures regarded as particularly toxic[38]. Of note, dimAβ AβOs effects appeared later (24 vs. 3 h) than for the previously studied oligomers, hinting toward their kinetic and structural stability in cell culture conditions.

Aβ42 as well as dimAβ accumulate within endo-lysosomal compartments. Next, we aimed to test the uptake of dimAβ AβOs in neuronal cells. First, SH-SY5Y neuroblastoma cells were subjected to a mixture of 0.1 µM HiLyte Fluor 647-labeled Aβ42 and 1 µM unlabeled Aβ42. After 24 h of incubation, Aβ42 accumulated within vesicular foci within the cytoplasm of the cells. Co-staining with a LysoTracker dye showed prominent colocalization suggesting the accumulation of Aβ42 within endo-lysosomal compartments (Fig. 5). This is in line with previous studies that showed Aβ42 accumulation in acidic vesicles of neuroblastoma cells and primary murine cortical neurons[41,44–46]. Hu et al. measured local Aβ42 concentrations >2.5 µM within endo-lysosomal compartments, which exceeds the extracellular concentration by approximately four orders of magnitude[44].

In a second attempt, SH-SY5Y cells were treated with 1.1 µM Abberior Star 520SXP-labeled dimAβ AβOs, formed from a mixture of 91% unlabeled and 9% fluorophore-labeled dimAβ (i.e., same final concentrations of unlabeled and fluorophore-labeled Aβ as in the Aβ42 experiment above). This experiment revealed a similar colocalization in acidic vesicles as for Aβ42 (Fig. 5). This confirms that both Aβ monomers and AβOs are readily taken up by neuron-like cells and accumulate in the endo-lysosomal system. Our results, however, do not reveal the assembly state of Aβ, and it is possible that the applied Aβ species undergo structural alterations upon cell entry and accumulation in endo-lysosomes, such as higher-order assembly as described below.

Endo-lysosomal pH promotes AβO assembly but delays amyloid fibril formation. Due to the accumulation of Aβ, endosomes/lysosomes might constitute the dominant site of the highly

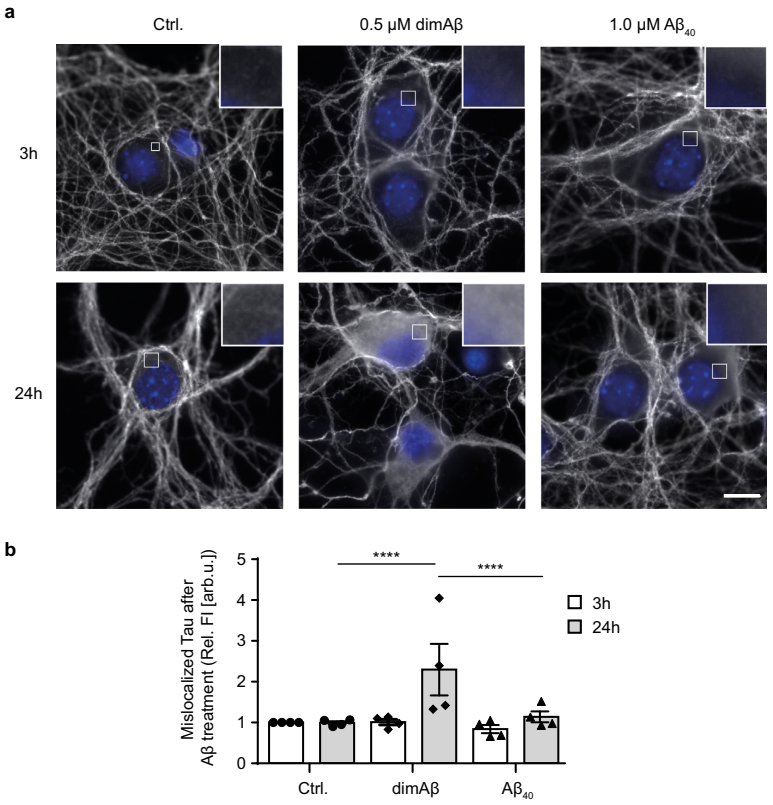

Fig. 3 DimAβ AβOs induce pathological somatodendritic missorting of Tau. Primary mouse neurons (DIV15–22) were treated with 0.5 µM dimAβ AβOs or 1 µM Aβ40 for 3 and 24 h. **a** Representative images of cell bodies of primary neurons after treatment with Aβ. Neurons were stained with anti-Tau (K9JA) antibody; nuclei were stained with NucBlue. DimAβ AβO-treated neurons show strong enrichment of fluorescence signal of Tau in the soma only after 24 h of treatment. Insets show magnification of white boxed areas in the somata. Scale bar, 10 µm. **b** Quantification of Tau enrichment in the soma of primary neurons. Fluorescence intensities of cell bodies were quantified and normalized to control-treated neurons after 3 h of treatment. $N = 4$, 30 cells were analyzed for each condition. Error bars represent SEM. Statistical analysis was done by two-way ANOVA with Tukey's test for multiple comparisons. Statistical significance: $^{****}p < 0.0001$.

concentration-dependent AβO formation. Apart from the increased Aβ concentration in endosomes/lysosomes, the low pH in late endosomes (~5.5) and lysosomes (~4.5) might promote AβO formation. We used dimAβ to simultaneously determine the specific effects of pH on AβO formation and on amyloid fibril formation. Lyophilized dimAβ was dissolved in 6 M buffered guanidinium chloride, followed by size-exclusion chromatography (SEC) into 1 mM NaOH, leading to a pH of 10.9, and added to the wells of a microplate. The basic pH conditions prohibit premature aggregation of Aβ[63]. The pH-dependent aggregation reaction was initiated in the microplate reader by injection of a 10× buffer yielding the desired final pH, allowing for monitoring of ThT fluorescence without any substantial delay. We determined the kinetics of dimAβ assembly between pH 4.8 and 7.6 in the concentration range 0.65–5.0 µM. At neutral pH, the initial kinetic phase reflecting AβO formation spanned several hours, but upon pH reduction, AβO formation was continuously accelerated and occurred within a few seconds at pH 4.8 (Fig. 6a–g). ThT fluorescence intensity decreased at acidic pH[64] but was still sufficiently sensitive to detect the signal of AβO formation at pH 4.8 and 0.65 µM dimAβ (Fig. 6g). For pH 7.4, we have previously shown that a global fit of an *n*th-order oligomerization reaction to the concentration-dependent assembly kinetics is in good agreement with the data and yields a reaction order of ~3.3 for dimAβ AβO formation[11]. Here we found that a reaction order of three applied to global fitting of the concentration-dependent data results in fits that reproduce the kinetic traces at all pH values (Fig. 6a–g). This indicates that the fundamental mechanism of AβO formation is not affected by pH reduction. A logarithmic plot of the obtained oligomerization rate constants against pH shows a linear trend with a slope of −1.56, i.e., the rate constant decreases 36-fold per pH unit within the investigated pH range (Fig. 6h). At pH 4.8, in between lysosomal and endosomal pH, AβO formation is 7900-fold faster than at interstitial pH (7.3).

In order to test whether the acceleration of AβO formation kinetics is accompanied by thermodynamic stabilization, we evaluated the effect of pH reduction on the COC of dimAβ. In the AβO formation assay at pH 7.4, the fluorescence intensity increase during the lag-free oligomerization phase scaled linearly with protein concentration at dimAβ concentrations above ~2 µM, whereas no lag-free oligomerization was detectable below ~0.5 µM, indicative of a COC of around 1 µM (Supplementary Fig. 6a, b). At pH 5.6, however, there is no indication of disappearance of the oligomerization phase down to a concentration of 0.4 µM dimAβ (Supplementary Fig. 6c, d). Due to the limited sensitivity of ThT at acidic pH[64], it is not possible to reliably monitor oligomerization at lower concentrations and to

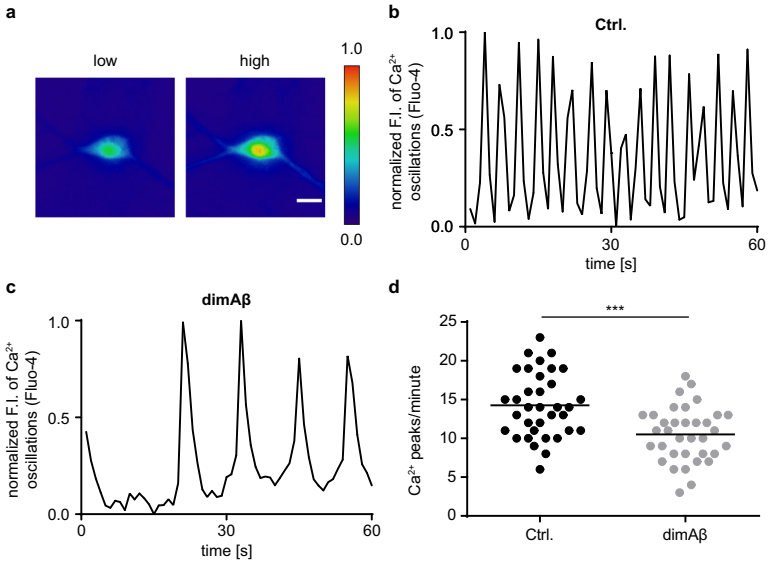

Fig. 4 DimAβ AβOs decrease spontaneous calcium oscillations of primary mouse neurons. Primary mouse neurons (DIV15–22) were treated with 0.5 µM dimAβ AβOs for 24 h. Cells were labeled with calcium-sensitive Fluo-4 dye and spontaneous calcium oscillations were recorded by time-lapse movies. **a** Representative ratiometric images of low and high calcium concentrations in the soma of a neuron. Scale bar, 20 µm. **b**, **c** Representative graphs of spontaneous Ca^{2+} oscillations in **b** vehicle control- and **c** dimAβ AβO-treated primary neurons. Fluorescence intensities were normalized to minimum values and plotted over time. **d** Quantification of spontaneous Ca^{2+} oscillations in primary neurons after vehicle control or dimAβ AβO treatment. Fluorescence intensities were normalized to minimum values and peaks per minute were counted for each sample. In total, 35 cells were analyzed; statistical analysis was done by two-tailed unpaired *t* test. Statistical significance: $^{***}p = 0.0001$.

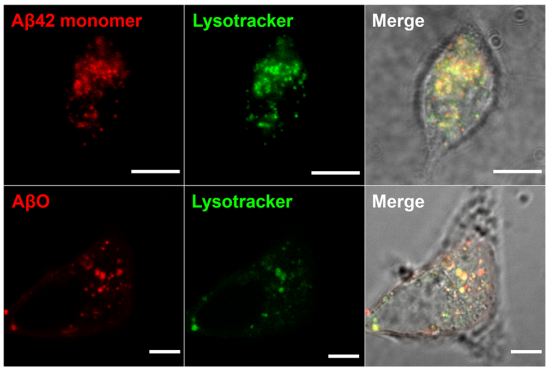

Fig. 5 Aβ42 and dimAβ AβOs accumulate in endosomes/lysosomes. SH-SY5Y cells were treated with Aβ42 monomers (top row) or dimAβ AβOs (bottom row) and co-localization with endo-lysosomal compartments was analyzed. 1.1 µM Aβ42 (containing 9% HiLyte 647-labeled Aβ42, top row) or 1.1 µM dimAβ AβOs (in monomer equivalents, formed from a dimAβ solution containing 9% AbberiorStar 520SXP-labeled dimAβ, bottom row) were added to the cells. After 24 h, the medium was exchanged with fresh medium supplemented with 50 nM Yellow HCK-123 LysoTracker dye. Scale bar, 5 µm. $N = 3$, at least three images were acquired for each treatment to ensure reproducibility.

determine the COC at this pH. Nevertheless, the COC at pH 5.6 is clearly lower than the COC at neutral pH, indicative of thermodynamic stabilization of AβOs at acidic pH.

AβOs formed at different pH values were imaged by AFM (Fig. 6i–o). From pH 7.6 to pH 6.8, AβOs were mainly spherical and curvilinear structures, the latter apparently resulting from bead-chain-like association of the spherical AβOs[6]. At pH 6.4, AβOs showed an increased tendency to form more compact structures, such as annular protofibrils and denser clusters. Below pH 6.0, AβOs associated into large clusters, in line with a previous description of Aβ40 aggregates at pH 5.8[53]. In AFM, these AβO clusters have average heights of ~100 nm, compared to heights of ~4 nm observed for AβOs formed between pH 6.0 and 7.2 (Fig. 6p). Thus, while the fundamental mechanism of AβO formation seems to be unaffected by pH reduction, there is an additional level of particle aggregation involved below pH 6.0.

The second kinetic phase in the ThT time course of dimAβ aggregation reports on amyloid fibril formation[11]. It is characterized by a lag time, which reflects the primary and secondary nucleation events involved in nucleated polymerization[14,52]. In contrast to the acceleration of AβO formation, the lag time of amyloid formation did not decrease with decreasing pH. On the contrary, the amyloid fibril formation phase could not be observed within 10 h experiments at pH values of 6.8 and below. This can be explained by the inhibition that the rapidly forming AβOs entail on amyloid formation: First, AβOs compete for the monomer growth substrate of amyloid fibril growth; second, AβOs actively inhibit amyloid fibril growth[11,65].

AβO assembly of Aβ42 is enabled under endo-lysosomal conditions. We investigated whether the promotion of AβO formation at endo-lysosomal pH is sufficient to also support AβO formation from Aβ42 at relevant endo-lysosomal Aβ concentrations, determined to be well above 2.5 µM[44]. At pH 7.2, Aβ42 in the concentration range 1.9–9 µM displayed sigmoidal assembly kinetics typical for amyloid fibril formation (Fig. 7a). The absence of a lag-free oligomerization phase is in agreement with the observation that the COC of Aβ42 in in vitro assay at neutral pH

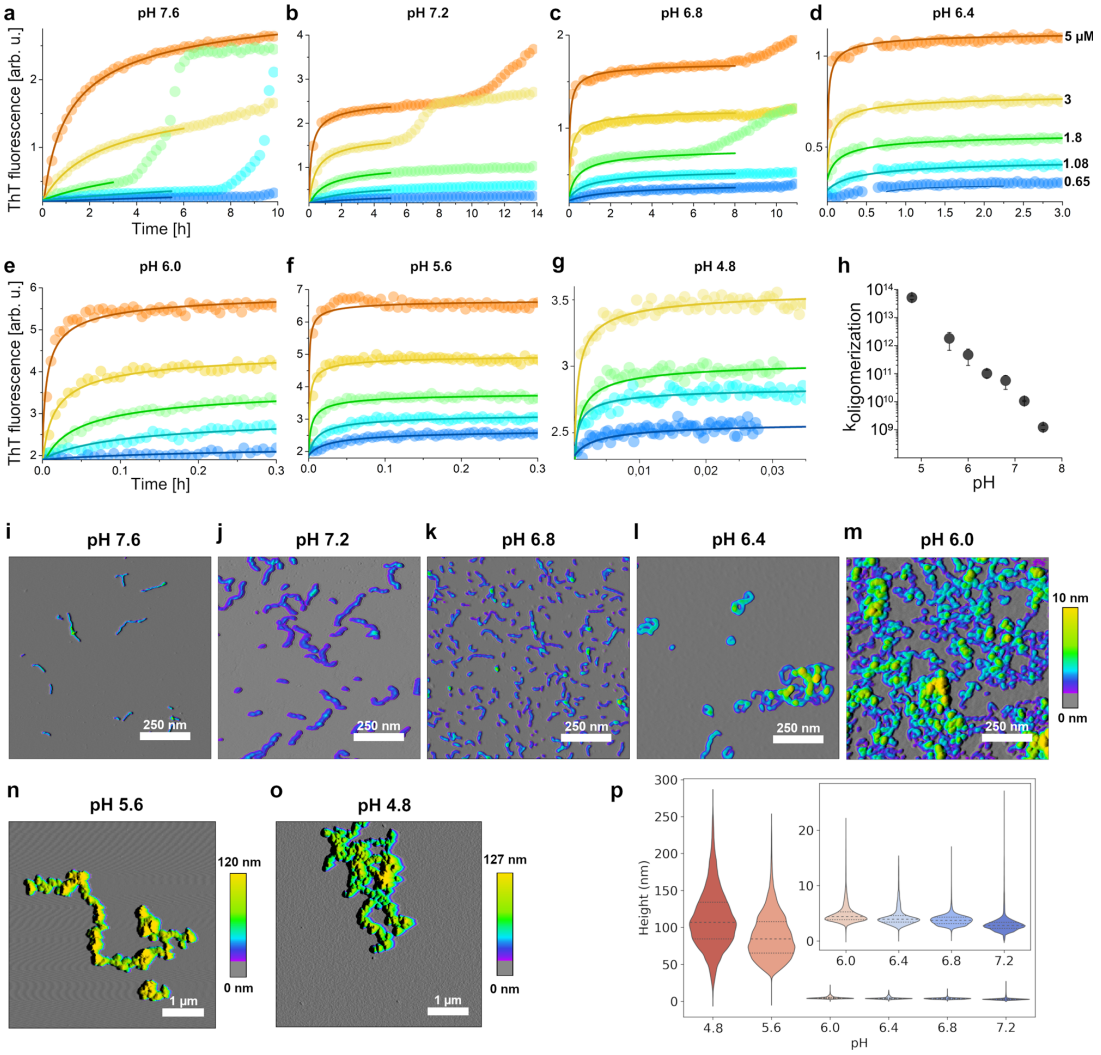

Fig. 6 pH dependence of dimAβ assembly kinetics. a–**g** DimAβ assembly at concentrations between 0.65 and 5 µM and at pH values between 4.8 and 7.6 monitored by ThT fluorescence. Solid lines represent global fits to the data using a one-step oligomerization model with a shared reaction order of 3 for all pH values and concentrations and an individual oligomerization rate constant per pH value. **h** Logarithmic plot of the obtained oligomerization rate constants vs. pH. The rate constants were obtained from global fits to *n* concentration dependence data sets obtained from *m* independently prepared assays, with *n*/*m* being 2/2 (pH 4.8), 6/4 (pH 5.6), 8/4 (pH 6.0), 5/4 (pH 6.4), 6/2 (pH 6.8), 6/2 (pH 7.2), and 6/2 (pH 7.6). One of the *n* repeats is shown in **a**–**g**. Replicates are given in Supplementary Fig. 8. Data points represent mean and standard deviation, except for pH 4.8, where the error bar indicates the higher and lower value of the $n = 2$ experiments. **i**–**o** AFM images of dimAβ AβO formed at different pH values. Note the dramatic change in the height scale bar upon pH decrease to <6.0 due to formation of large AβO clusters. Between 7 and 25 micrographs of at least 2 independent assays were recorded for each pH value to ensure reproducibility. **p** Particle height distributions determined from AFM images, displayed as violin plots. All pixels assigned to AβOs by the image analysis software in five micrographs per pH value were evaluated. Dashed lines represent medians; dotted lines represent interquartile ranges. Inset, zoom on the data for pH 6.0 to pH 7.2.

is >10 µM[65]. Consequently, the aggregation products under this condition are amyloid fibrils (Fig. 7c, f). In contrast, at pH 4.5 lag-free aggregation occurred at a concentration of ≥5.4 µM (Fig. 7b). The change from lag-containing to lag-free conditions at pH 4.5 was accompanied by a switch in aggregate morphology from amyloid fibril networks to large AβO clusters identical to those observed for dimAβ at endo-lysosomal pH (Fig. 7d, e, g, h). This indicates that under endo-lysosomal conditions the local Aβ concentration can exceed the COC of AβO formation, suggesting that endosomes/lysosomes may represent crucial sites of AβO formation in vivo.

Aβ aggregates can leak from endosomes/lysosomes into the cytosol and to other cell compartments or can be secreted and spread to other cells, potentially contributing to the propagation of Aβ pathology[27,28,44,45,51]. Upon transfer from endosomes/lysosomes to the cytosol or interstitial fluid, AβOs experience a shift from acidic to neutral pH. We tested the kinetic stability of AβOs formed at pH 4.5 after a shift to neutral pH by monitoring

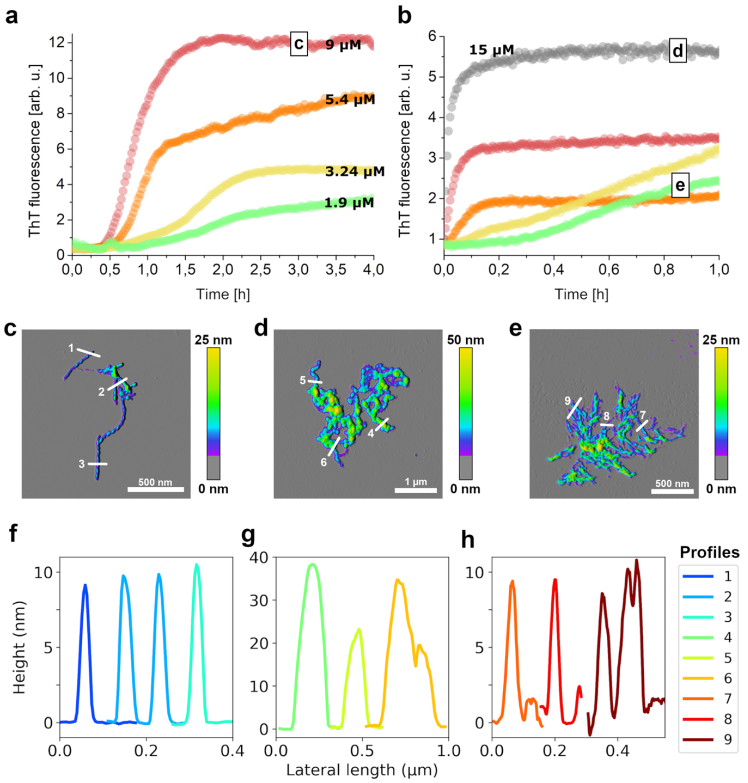

Fig. 7 Aβ42 rapidly forms AβOs at endo-lysosomal pH. a, **b** Aβ42 assembly at **a** pH 7.2 or **b** pH 4.5 at concentrations between 1.9 and 15 µM monitored by ThT fluorescence. Replicates are given in Supplementary Fig. 9. **c**–**e** AFM images of **c** amyloid fibrils formed by 9 µM Aβ42 at pH 7.2, **d** AβOs formed by 15 µM Aβ42 at pH 4.5, and **e** amyloid fibril networks formed by 1.9 µM Aβ42 at pH 4.5. At least three micrographs each of two independently prepared sample repeats were recorded to ensure reproducibility of the AFM data. **f**–**h** Height profiles of the sections indicated in **c**–**e**.

the ThT intensity and by imaging of the aggregate morphology by AFM. We applied Aβ42 at a concentration of 10 µM in this experiment, as Aβ42 does not form AβOs de novo at this concentration at neutral pH. Any AβOs observed after the pH shift can therefore safely be ascribed to the kinetic stability of AβOs pre-formed under acidic conditions. As before, a pH shift from basic pH to pH 4.5 was applied to initiate AβO formation. After AβO formation had reached a steady state, pH was adjusted to 7.2 by a further injection of a corresponding buffer stock. After the adjustment to neutral pH, there was an instantaneous increase in ThT fluorescence (Supplementary Fig. 7), which can be explained by the pH dependence of ThT fluorescence[64]. Thereafter, the ThT fluorescence did not exhibit any other larger changes that would be expected in the case of disassembly of AβOs or replacement of AβOs by an alternative type of aggregate. Apart from dense clusters like those observed for low pH AβOs, AFM images showed spherical and curvilinear structures typical for AβOs formed at neutral pH, indicating dissociation of the AβO clusters into their constituents (Fig. 8a). In fact, the AFM images suggest that smaller AβOs detach from fraying AβO clusters. The height of the cluster-released Aβ42 AβOs was 3.5–4.5 nm as measured by AFM in the dried state (Fig. 8b, c), identical to that of Aβ42 AβOs (Fig. 8d, e) and dimAβ AβOs (Fig. 6p) that were directly formed at neutral pH. Taken together, the ThT and AFM data demonstrate that AβOs formed at endo-lysosomal pH possess a high kinetic stability after shifting to neutral pH, which is, however, accompanied by dissociation of large AβO clusters into spherical and curvilinear AβOs.

Discussion

AβOs have been identified as the main neurotoxic Aβ species in AD. The characterization of the most critical disease-related AβOs has revealed that they are metastable oligomers >50 kDa in size that do not represent intermediates of amyloid fibril formation but are an alternative Aβ assembly type. However, the conditions required for AβO formation and the underlying mechanism have not been elucidated in detail. Here we show that AβO formation is highly pH dependent and is accelerated ~8000-fold upon a change in pH from neutral to endo-lysosomal pH. At the same time, the COC of AβO formation is reduced. This enables AβO formation at physiologically relevant Aβ concentrations, determined to be well above 2.5 µM in endo-lysosomal vesicles[44]. The strong acceleration of AβO formation at pH 4.5–5.5 suggests that the endosomal/lysosomal system might be a major site of AβO formation. AβOs may either form from Aβ monomers that have been newly generated by amyloid precursor protein (APP) processing or from endocytosed monomers (Fig. 9)[40–42,44,47,48]. APP processing in endo-lysosomal compartments by γ-secretase containing presenilin 2 generates a prominent pool of intracellular Aβ that is enriched in Aβ42 (ref. [48]). Esbjörner et al. applied fluorescence lifetime and

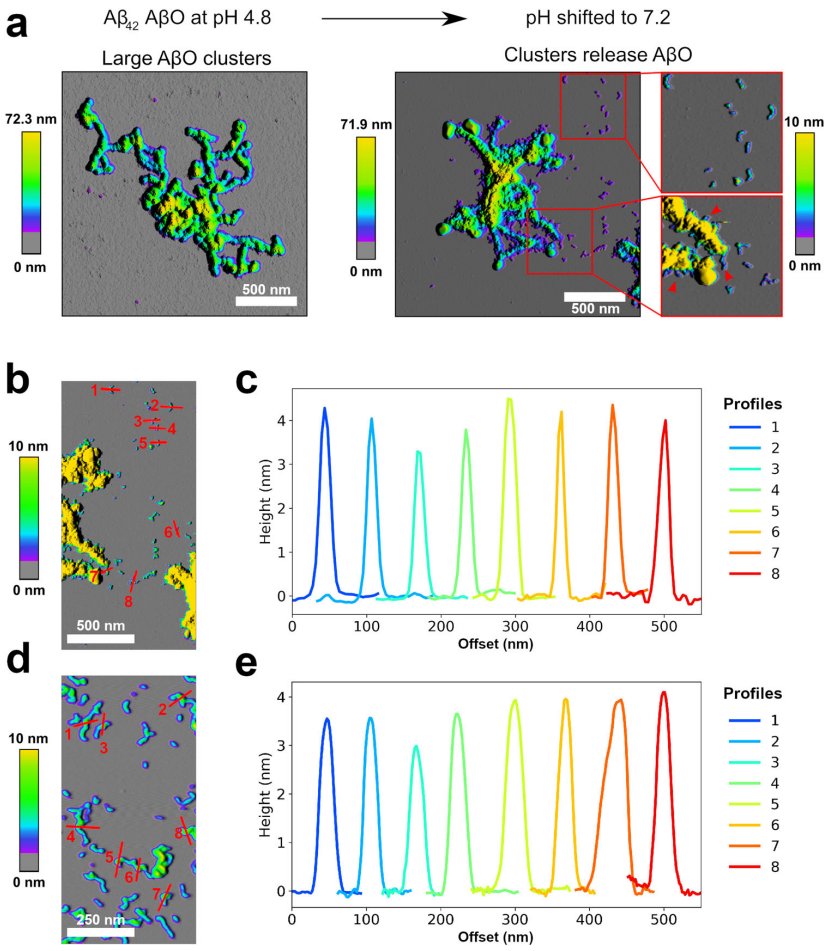

Fig. 8 Stability of AβOs formed by Aβ42 at endo-lysosomal pH after shifting to neutral pH. a AFM images of AβOs formed by 10 µM Aβ42 at pH 4.5 before (left) and after (right) shift to pH 7.2. Red arrowheads point to a few of the sites where AβOs seem to detach from AβO clusters. In all, 3–7 micrographs were recorded per condition to ensure reproducibility. **b**, **c** Height profiles of small AβOs after pH shift to neutral pH. Height profiles in **c** correspond to the sections in **b**. **d**, **e** Height profiles of AβOs formed by 110 µM Aβ42 at pH 7.2. Height profiles in **e** correspond to the sections in **d**.

super-resolution imaging to determine the kinetics of Aβ aggregation in live cells and found that aggregation occurred in endo-lysosomal compartments[41]. Importantly, they reported that Aβ42 aggregated without a lag time into compact, dense structures[41]. Both the absence of a lag time and the structural characterization are in line with the low pH AβO clusters described here, suggesting that AβO clusters indeed form in endo-lysosomal compartments and represent the dominant Aβ aggregate species in live cells. Subsequently, AβOs might cause lysosomal impairment, leak into the cytosol and cause intracellular damage, or might be secreted and spread to neighboring cells, where they could contribute to the propagation of pathology[40,42,44–46,48,49].

Enhanced aggregation at acidic pH is a known property of Aβ with established relevance for sample preparation[63]. Our results are in line with a study on the aggregation of Aβ40 (at a concentration of 230 µM) at pH 5.8 that reported the rapid formation of large clusters with (proto)fibrillar and globular substructures that were not able to seed, but rather inhibited, amyloid fibril formation[53]. Our analysis of the aggregation kinetics reveals that these low pH Aβ aggregates, often termed amorphous aggregates, form along the same pathway as neutral pH AβOs and therefore represent particle aggregates of AβOs. This is supported by the observation that low pH AβO clusters release spherical and curvilinear AβOs upon a shift to neutral pH (Fig. 8a). Nevertheless, there may be differences between atomic-level structures and between intermolecular interactions in AβOs formed at different pH, just as atomic-level structures and protofilament interfaces of amyloid fibril polymorphs can differ significantly.

The increasing clustering of AβOs upon pH reduction from neutral to pH 6 points to the high propensity of AβOs to associate. At neutral pH, self-association of spherical AβOs results in curvilinear assemblies. A decrease of pH leads to an increase in annular and compact assemblies and finally to large AβO clusters (Fig. 6). This propensity of AβOs to associate likely also contributes to their clustering with neuronal receptors[35,36] and to their accumulation around amyloid fibril plaques[66].

In contrast to AβO formation, amyloid fibril formation of dimAβ is slowed down at acidic pH. This pH dependence is not an inherent property of Aβ amyloid fibril formation: in the absence of AβOs, Aβ42 amyloid fibril formation occurs rapidly at

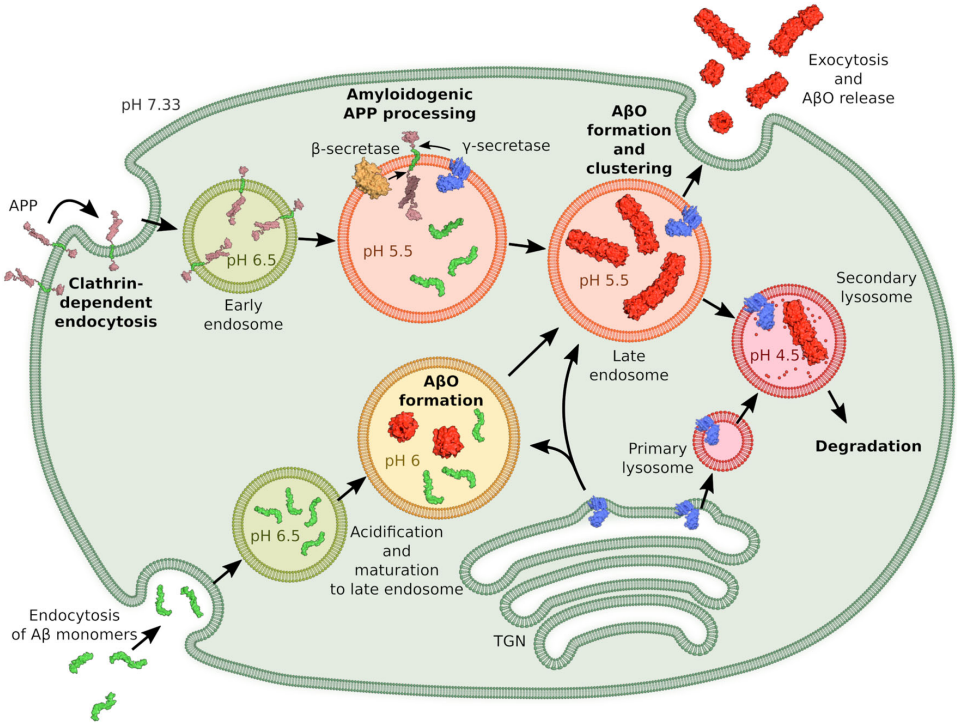

Fig. 9 Scheme of intracellular APP processing, Aβ uptake, and AβO formation. This is an extension of previous schemes of APP processing and Aβ uptake[48,76,77], now including potential formation of AβOs especially in endo-lysosomal compartments. Using a conservative estimate of the endo-lysosomal Aβ concentration of 2.5 μM[44] and assuming an endosome volume of 0.3 μm^3, there are on average 450 Aβ molecules in an endosome. Protein structure images were prepared using pdb entries 1OWT, 1IYT, 1RW6, 3DXC, 4UIS, and 1SGZ. TGN trans-Golgi network.

pH 4.5 (Fig. 7b, 1.9 μM trace). Delayed amyloid fibril formation upon pH reduction is only observed in combination with accelerated AβO formation and can be explained by the two inhibitory activities of AβOs on amyloid fibril formation: AβOs compete with amyloid fibrils for monomers (Fig. 1a) and furthermore inhibit amyloid fibril growth actively[11,65].

DimAβ AβOs show dendritic spine binding, lack direct cytotoxicity, potently induce Tau missorting, and decrease neuronal activity, suggesting that they constitute a suitable AβO model construct to study the pathomechanism of AD. Previous AβO preparations showed a loss of potency to induce Tau missorting within 12 h due to transformation to non-toxic larger Aβ aggregates[38,62]. In contrast, dimAβ AβOs led to extensive and persistent Tau missorting 24 h after application. The sustained activity of dimAβ AβOs is likely a consequence of the kinetic stabilization of the AβO state achieved by the dimer linkage. DimAβ might therefore be an advantageous model for eliciting Tau missorting and downstream consequences, as it represents a model of chronic stress corresponding to the human disease rather than acute insult.

Methods

Preparation of dimAβ. DimAβ was produced recombinantly[11]. Expression of dimAβ was achieved by co-expression of ZAβ3, a binding protein that shields aggregation-prone sequence segments of Aβ[67]. The gene encoding dimAβ included an N-terminal methionine, followed by a Aβ40 unit, a $(G_4S)_4$ linker, and a second Aβ40 unit. DimAβ and $(His)_6$-tagged ZAβ3 were co-expressed from a pACYCDuet-1 vector that contained the genes in the following order: T7promoter-1–dimAβ–T7promoter-2–$(His)_6$ZAβ3–T7 terminator. BL21(DE3) *E. coli* cells (Novagen) were transformed with the expression vector and grown for ~16 h at 37 °C on LB agar plates containing 34 μg/ml chloramphenicol. Single colonies were picked and grown for ~16 h in 50 ml M9 medium, containing 2×YT medium and 34 μg/ml chloramphenicol. In all, 40 ml of the pre-culture was transferred to 2 l of M9-Celtone medium in a 5 l baffled Erlenmeyer flask. The culture was grown at 37 °C with shaking and induced at OD_{600} ~ 0.8 by the addition of IPTG to a final concentration of 1 mM. After further growth for 4 h, the cells were harvested and frozen at −20 °C.

For purification, cell pellets were resuspended in 50 mM Na-phosphate, 0.3 M NaCl, 20 mM imidazole, pH 8, containing EDTA-free protease inhibitor (Roche Applied Sciences), and lysed by a cell disrupter (Constant Systems). The cell debris was removed by centrifugation in a Beckman J2-21 centrifuge mounting a JA20.1 rotor at 18,000 RPM, 4 °C for 40 min. For capture of the dimAβ:ZAβ3 complex by immobilized metal ion affinity chromatography (IMAC), the supernatant was loaded on a HisTrap FF column (GE Healthcare). DimAβ was separated from the resin-bound ZAβ3 and eluted with 8 M urea and 20 mM Na-phosphate, pH 7. For further purification, including removal of residual ZAβ3, reverse-phase high-performance liquid chromatography (RP-HPLC) was performed. For this purpose, the IMAC eluate was concentrated in a Vivaspin 20 centrifugal concentrator (Sartorius), followed by addition of 5 mM TCEP to reduce the disulfide bond of ZAβ3, and loading onto a semi-preparative Zorbax 300SB-C8 RP-HPLC column (9.4 mm × 250 mm, Agilent) connected to an Agilent 1260 Infinity system with UV detection at 214 nm. Monomeric dimAβ was eluted in a gradient from 30% (v/v) to 36% acetonitrile in water and 0.1% (v/v) trifluoroacetic acid at 80 °C. DimAβ-containing fractions were pooled, lyophilized, dissolved in hexafluoroisopropanol (HFIP), aliquoted in 1 mg portions, lyophilized again, and stored at −20 °C.

For aggregation kinetic experiments, the lyophilized protein was reconstituted in 6 M guanidinium chloride and 50 mM sodium-phosphate buffer, pH 7.4, and incubated at room temperature (RT) for 30 min. Subsequently, SEC was performed using a Superdex 75 increase column (GE Healthcare) equilibrated with 1 mM NaOH. The concentration of the monomeric dimAβ in the alkaline eluate was measured via tyrosine fluorescence using a pH-adjusted extinction coefficient of 2685 M^{-1} cm^{-1}. Samples were always kept on ice until further needed.

ThT aggregation kinetics. ThT, NaN_3, NaCl, protein, and 1 mM NaOH were given into the wells of a 96-well low-binding plate (Greiner) such that if filled up to 100 μl, concentrations of 1 μM ThT, 0.02% NaN_3, 150 mM NaCl, and the desired final protein concentration were reached. The outermost wells of the plate were left

blank due to the risk of aberrant aggregation behavior. The plate was put in a BMG ClarioStar platereader fitted with two injectors and tempered at 37 °C. One syringe of the injector was equilibrated with 1 ml 10× buffer concentrate. The reaction was started using the injector of the platereader by dispensing 10 µl of the concentrate at highest available speed into each of the wells. This adjusted the pH value in situ and initiated oligomerization. Data points were collected in evenly spaced intervals depending on the velocity of the reaction using the BMG Reader Control software (version 5.40).

For shifting the pH in situ twice, both syringes were equilibrated with 10× buffer concentrate; the first one resulting in a final buffer concentration of 20 mM and pH 4.5 and the second one resulting in a final buffer concentration of 50 mM and pH 7.2. The first syringe was used to inject 10 µl to initiate oligomerization, whereas the second one was used to inject 11 µl to achieve the shift to neutral pH at a time point where the oligomerization reaction had reached its plateau.

For analysis of the kinetics of AβO formation, the initial phase of the ThT kinetics was fit to one-step oligomerization $n\mathrm{M} \rightarrow \mathrm{M}_n$ (ref. [11]). The AβO mass concentration, $M_{\mathrm{A\beta O}}$, evolves in time according to the following expression

$$M_{\mathrm{A\beta O}}(t) = M_0 - \left[M_0^{1-n} + (n-1)nkt\right]^{1/(1-n)} \quad (1)$$

with M_0 the total protein concentration, k the oligomerization rate constant, and n the oligomer size or reaction order. Global fits to the pH- and concentration-dependent AβO formation data were performed using the Origin 9.0 software with a reaction order of $n = 3$ shared between all data sets, and the oligomerization rate constant k as a pH-dependent parameter, which was shared within the concentration-dependency data sets at a given pH. The proportionality constant relating $M(t)$ to ThT fluorescence intensity was treated as a fit parameter with an individual value for every sample.

Atomic force microscopy. In all, 10 µl of the dimAβ samples were taken directly from the plate after the ThT assays at a concentration of 5 µM and applied onto freshly cleaved muscovite mica. They were left to dry, washed with 500 µl ddH_2O, and dried with a stream of N_2 gas. For imaging dimAβ at pH 4.8, the aforementioned method did not work, likely due to sticking of the sample to the well. Instead, all reaction components apart from the buffer concentrate were premixed and loaded into a micropipette tip. By adding the reaction components to a vial containing the buffer concentrate and thorough mixing, the reaction was started, before pulling the solution back into the tip. Immediately afterwards, the micropipette was relocated into a 37 °C incubation cabinet, where a drop was pushed out to the point where it still stuck to the tip. After 45 s, the drop was pushed onto the freshly cleaved muscovite mica and preparation commenced as with the other pH values.

For the Aβ42 samples, 5 µl of the respective concentrations were taken, applied onto freshly cleaved muscovite mica, and left to dry for 15 min before carefully washing with 200 µl ddH_2O and drying under a stream of N_2 gas.

Imaging was performed in intermittent contact mode (AC mode) in a JPK Nano Wizard 3 atomic force microscope (JPK, Berlin) using a silicon cantilever with silicon tip (OMCL-AC160TS-R3, Olympus) with a typical tip radius of 9 ± 2 nm, a force constant of 26 N/m, and resonance frequency around 250 kHz. The images were processed using the JPK DP Data Processing Software (version spm-5.0.84). For the presented height profiles, a polynomial fit was subtracted from each scan line first independently and then using limited data range. False-color height images were overlaid onto the amplitude profile.

Particle height distributions were extracted from AFM images. Therefore, the Morphological Active Contours without Edges (MorphACWE) function of python's scikit-image module was used to distinguish and separate AβOs from background (see Supplementary Fig. 10 for examples of AFM image segmentation). Histographical height profiles of AβOs at different pH were determined as per pixel heights of the MorphACWE-isolated areas.

Cryo-EM. For cryo-EM imaging, the AβO sample was plunge-frozen on glow-discharged Quantifoil 1.2/1.3 grids. In total, 1308 micrographs were recorded as focal pairs at high defocus (6 µm) and low defocus (using a range of −0.5 to −2 µm) on a Tecnai Arctica (200 kV) using a Falcon III direct electron detector, yielding a pixel size of 0.935 Å. Particle selection was performed automatically using crYOLO[68]. In total, 32,211 particles were selected on the high defocus micrographs. The contrast transfer function of the micrographs was determined using CTFFIND4[69]. Further image processing was performed using the software package RELION 3.0.5[70]. Two-dimensional and 3D classification was conducted on the high-defocus images to clean the data set. A box size of 128 pix, which corresponds to 119.7 Å, and a radial mask with a diameter of 100 Å were used.

The high-defocus micrographs were aligned to the low-defocus micrographs. The relative shifts obtained from this alignment were applied to all particles (that were picked from the high-defocus micrographs) and then the particles were extracted from the low-defocus micrographs with the shifted particle coordinates, while keeping the Euler angles from the high-defocus 3D refinements. A 3D reconstruction calculated from the high-defocus images was low-pass filtered to 60 Å and was used as an initial model for further low-defocus 3D refinements. For further processing steps, only micrographs that contain a signal beyond a resolution of 5 Å were used. The final resolution of 17 Å was assessed by Fourier shell correlation.

In order to obtain an estimate for the molecular mass within the reconstructed density, 110 pseudo-atomic models with varying number of pseudo-atoms (molecular masses between 10 and 120 kDa) were generated from the density map using the program VISDEM[71], which is part of the software package DireX[72]. In VISDEM, atoms are randomly placed into a density region with density above a provided threshold. The density threshold was set to yield a volume such that the mass density is fixed at 0.714 ml/g (average mass density observed in proteins). The pseudo-atomic model has a composition of 62.2% C atoms, 20.6% O atoms, and 17.2% N atoms, which corresponds to the average composition observed in proteins. Afterwards, a density map was computed from each of the 110 pseudo-atomic models. The VISDEM method was used to sharpen these pseudo-atomic model maps as well as the EM reconstruction. The sharpening was performed with a resolution cutoff of 17 Å and the mass of the corresponding pseudo-atomic model. Finally, the cross-correlation between the sharpened EM reconstruction and the sharpened pseudo-atomic model map was computed and plotted for each tested mass. The highest cross-correlation was found for the pseudo-atomic model map that contains a molecular mass of 62 kDa. One dimAβ monomer (101 amino acids) has a molecular mass of 10.0 kDa. Thus, the reconstructed density likely holds six dimAβ monomers. The final 3D reconstruction of the oligomer was sharpened by VISDEM using a mass of 62 kDa and a resolution cutoff of 17 Å.

Preparation of dimAβ AβOs and Aβ40 monomers for treatment of primary neurons. Aβ preparations were performed under sterile conditions. DimAβ lyophilisate was resuspended in 50 mM NaOH until completely dissolved. Next, phosphate-buffered saline (PBS) and 50 mM HCl were added and immediately mixed, obtaining a final concentration of 20 µM dimAβ and 40 µM Aβ40. To induce AβO formation, dimAβ was incubated at 37 °C for 16 h. Aβ40 controls were prepared in the same manner without subsequent incubation. Primary neurons (DIV15–22) were treated with either 0.5 µM dimAβ AβO or 1 µM Aβ40 monomers diluted in conditioned neuronal maintenance media for 3 and 24 h under normal growth conditions (see below). In addition, control cells were treated with a vehicle control (PBS containing 50 mM NaOH and 50 mM HCl). Afterwards, cells were fixed and stained as described below.

Primary neuron culture. Primary neurons were isolated and cultured as described before[73] with slight modifications: In brief, the brains of FVB/N mouse embryos were dissected at embryonic day 13.5. Brainstem and meninges were removed and whole cortex was digested with 1× Trypsin (Panbiotech). Neurons were diluted in pre-warmed (37 °C) neuronal plating medium (Neurobasal media (Thermofisher Scientific), 1% fetal bovine serum (FBS; Biochrom AG), 1× antibiotic/antimycotic solution (Thermofisher Scientific), 1× NS21 (Panbiotech)) and seeded onto poly-D-lysine (Merck) coated coverslips. Neurons were cultivated in a humidified incubator at 37 °C, 5% CO_2. Four days after plating, media was doubled with neuronal maintenance media (Neurobasal media (Thermofisher Scientific), 1× antibiotic/antimycotic solution (Thermofisher Scientific), 1× NS21 (Panbiotech)) and cells were treated with 0.5 µg/ml Cytosine β-D-arabinofuranoside (AraC; Sigma-Aldrich). The isolation of primary neurons was reviewed and approved (§4 TschG) by the Animal Welfare Officer of University of Cologne and the Landesamt für Natur-, Umwelt- und Verbraucherschutz (LANUV), Germany.

Somatodendritic missorting of Tau. To analyze Tau somatodendritic localization, neurons were fixed with 3.7% formaldehyde/4% sucrose in PBS (both Sigma-Aldrich) for 30 min at RT using gentle agitation after treatment with Aβ or vehicle control for the indicated time points. Afterwards, cells were permeabilized and blocked for 5–10 min in 5% bovine serum albumin/0.2% TX-100 in PBS (both Carl Roth), washed with PBS, and stained with a polyclonal rabbit anti-Tau (K9JA, Dako A0024; dilution: 1:1000) antibody overnight at 4 °C. The next day, coverslips were washed again with PBS, incubated with NucBlue (Thermofisher Scientific) for 15 min, and subsequently stained with a secondary antibody coupled to an AlexaFluor dye (Thermofisher Scientific) for 1 h at RT. Coverslips were mounted onto glass slides using Aqua-Poly/Mount (Polysciences) and dried overnight at RT (for further details on immunofluorescence staining procedure, see ref. [73]). Images of neuronal cell bodies were taken with a wide-field fluorescence microscope (Axioscope 5, Zeiss) and the ZenBlue Pro imaging software (V2.5, Zeiss). Fluorescence intensities of cell bodies were quantified using the ImageJ software[74,75]. Fluorescence intensity values were normalized to vehicle-treated control cells after 3 h of treatment. All experiments were performed 4 times; 30 cells were analyzed for each condition. Statistical analysis was done by two-way analysis of variance (ANOVA) with Tukey's test for multiple comparisons using GraphPad Prism v6 (GraphPad Software).

Cytotoxic effect of dimAβ. To evaluate AβO toxicity, cells were fixed and stained with NucBlue (Thermofisher Scientific) after dimAβ AβO treatment. Shape and density of nuclei were analyzed and counted: cells were considered dead, when nuclei appeared condensed and smaller, compared to viable cell nuclei. All experiments were conducted for 3 times; around 300 nuclei were analyzed for each condition. Statistical analysis was done by two-way ANOVA with Tukey's test for multiple comparisons using GraphPad Prism v6 (GraphPad Software).

Aβ targeting to postsynaptic spines and imaging of spontaneous calcium oscillations. To analyze Aβ binding to synapses, neurons were fixed and stained for F-actin with phalloidin as a marker of synaptic spines (Thermofisher Scientific) and a monoclonal mouse anti-Aβ (clone 4G8, Merck, #MAB1561; dilution: 1:300) antibody. The experiment was repeated independently for four times and colocalization of AβO with synapses was observed for all replicates.

To monitor spontaneous Ca^{2+} oscillations, primary neurons were labeled with 2 µM Fluo-4 (Thermofisher Scientific) and 0.02% Pluronic F127 (Merck) for 20 min after 24 h of dimAβ treatment. Time-lapse movies of different fields were recorded for 1 min each (frame rate: 1 s) using a Leica DMi8 microscope (Leica) and the Leica LAS X imaging software (v3.7.3). Fluorescence intensity changes of cell bodies were quantified over time with ImageJ[74,75] and corrected for background signal. Fluorescence intensities were normalized to minimum values and peaks per minute were counted for each sample. In total, 35 cells were analyzed; statistical analysis was done by two-tailed unpaired *t* test.

Preparation of fluorescently labeled Aβ for cell culture experiments. For preparation of AbberiorStar 520SXP-labeled Cys0-dimAβ, a mutant of dimAβ with an N-terminal cysteine residue was expressed as described above. For fluorophore labeling, TCEP-reduced Cys0-dimAβ lyophilisate was incubated in 200 mM HEPES pH 7.0 with a twofold molar excess of maleimide-conjugated AbberiorStar 520SXP fluorophore, which was dissolved in dimethylformamide. After 2 h of incubation, the labeled dimAβ was purified using reverse-phase HPLC. Samples were lyophilized, redissolved in HFIP, and aliquots were prepared. These aliquots were lyophilized and stored at RT for later use. Abberior STAR 520SXP-labeled AβOs were prepared from a 1:10 molar ratio of Abberior STAR 520SXP-labeled dimAβ and unlabeled dimAβ, in order to avoid that the fluorophore alters AβO properties. In all, 10 µl of 1:10 mixture of Abberior STAR 520SXP-labeled dimAβ and unlabeled dimAβ was prepared in 50 mM NaOH. Quickly, 490 µl phenol red-free Dulbecco's Modified Eagle's Medium (DMEM) supplemented with 100 U/ml penicillin–streptomycin was added, and the pH was readjusted by adding 10 µl 50 mM HCl. The final dimAβ concentration was 10 µM. The sample was quiescently incubated at 37 °C in the dark for 24 h. AβO formation was confirmed using AFM.

For Aβ42 cell culture experiments, Aβ42-HiLyte Fluor 647 (Anaspec) was dissolved in HFIP and lyophilized into smaller aliquots (30 µg). For cell culture experiments, aliquots were first dissolved in 3 µl 50 mM NaOH. In all, 544 µl phenol red-free DMEM supplemented with 100 U/ml penicillin–streptomycin was added, and the pH was recalibrated by the addition of 3 µl 50 mM HCl. To avoid exposure of the Aβ peptide to local low pH environments, the HCl was pipetted into the lid of the tube, closed, and quickly vortexed. This procedure yields a 10 µM mostly monomeric stock solution of Aβ42-HiLyte Fluor 647 suitable for cell culture experiments.

Neuroblastoma cell culture. SH-SY5Y cells were grown to 80% confluency in DMEM with phenol red, 10% FBS, and 100 U/ml penicillin–streptomycin in T75 flasks. Experiments were performed in Ibidi collagen IV-coated µ-Slide VI 0.4. A total of 7500 cells (250,000 cells/ml) were seeded into each channel of the slide. Cells adhered to the surface of the channels within an hour of incubation at 37 °C, 5% CO_2, in a humidified chamber. Subsequently, the feeding reservoirs of the channels were filled with further medium. Each day, the medium in the reservoirs was replaced with fresh medium until the cell density was satisfactory for coincubation experiments.

Coincubation experiments and imaging. For coincubation and imaging experiments, phenol red was removed by flushing the channels three times with phenol red-free DMEM supplemented with 100 U/ml penicillin–streptomycin. Subsequently, channels were filled with medium containing corresponding Aβ species. Cells were incubated for 24 h. Channels were flushed with fresh medium and supplemented with 50 nM Yellow HCK-123 LysoTracker. Imaging was performed either on a Leica Infinity TIRF microscope or on a confocal microscope using the Leica LAS AF software. Confocal measurements were performed using a TCS SP8 STED 3× (Leica Microsystems) equipped with an HC PL APO CS2 ×100 objective (NA 1.4) at a scan speed of 600 Hz and a line accumulation of 6. A 488 nm of a pulsed white light laser was chosen as excitation for Yellow HCK-123 LysoTracker and AbberiorSTAR520XPS. The emitted fluorescent signal was detected by counting-mode hybrid detectors in the spectral range of 500–531 nm for Yellow HCK-123 LysoTracker and 650–765 nm for AbberiorStar520SXP. Additionally, a time-gating of 0.1 ns was used to avoid laser reflection.

Reporting summary. Further information on research design is available in the Nature Research Reporting Summary linked to this article.

Data availability

The cryo-EM density map of dimAβ AβOs has been deposited in the Electron Microscopy Data Bank under accession code EMD-11327. The authors declare that all the data necessary to interpret, verify, and extend the research of the article are available within the article (and Supplementary Information files). All data are available from the corresponding authors on reasonable request. Source data are provided with this paper.

Received: 1 July 2020; Accepted: 14 July 2021;
Published online: 30 July 2021

References

1. Gremer, L. et al. Fibril structure of amyloid-β(1-42) by cryo-electron microscopy. *Science* **358**, 116–119 (2017).
2. Kollmer, M. et al. Cryo-EM structure and polymorphism of Aβ amyloid fibrils purified from Alzheimer's brain tissue. *Nat. Commun.* **10**, 4760 (2019).
3. Selkoe, D. J. & Hardy, J. The amyloid hypothesis of Alzheimer's disease at 25 years. *EMBO Mol. Med.* **8**, 595–608 (2016).
4. Cline, E. N., Bicca, M. A., Viola, K. L. & Klein, W. L. The Amyloid-β oligomer hypothesis: beginning of the third decade. *J. Alzheimers Dis.* **64**, S567–S610 (2018).
5. Ono, K. & Tsuji, M. Protofibrils of amyloid-β are important targets of a disease-modifying approach for Alzheimer's disease. *Int. J. Mol. Sci.* **21**, 952 (2020).
6. Chromy, B. A. et al. Self-assembly of Aβ(1-42) into globular neurotoxins. *Biochemistry* **42**, 12749–12760 (2003).
7. Jan, A., Hartley, D. M. & Lashuel, H. A. Preparation and characterization of toxic Aβ aggregates for structural and functional studies in Alzheimer's disease research. *Nat. Protoc.* **5**, 1186–1209 (2010).
8. Lambert, M. P. et al. Diffusible, nonfibrillar ligands derived from Aβ1-42 are potent central nervous system neurotoxins. *Proc. Natl Acad. Sci. USA* **95**, 6448–6453 (1998).
9. Walsh, D. M. et al. Amyloid β-protein fibrillogenesis. Structure and biological activity of protofibrillar intermediates. *J. Biol. Chem.* **274**, 25945–25952 (1999).
10. Walsh, D. M., Lomakin, A., Benedek, G. B., Condron, M. M. & Teplow, D. B. Amyloid β-protein fibrillogenesis. Detection of a protofibrillar intermediate. *J. Biol. Chem.* **272**, 22364–22372 (1997).
11. Hasecke, F. et al. Origin of metastable oligomers and their effects on amyloid fibril self-assembly. *Chem. Sci.* **9**, 5937–5948 (2018).
12. Bitan, G., Fradinger, E. A., Spring, S. M. & Teplow, D. B. Neurotoxic protein oligomers—what you see is not always what you get. *Amyloid* **12**, 88–95 (2005).
13. Kodali, R. & Wetzel, R. Polymorphism in the intermediates and products of amyloid assembly. *Curr. Opin. Struct. Biol.* **17**, 48–57 (2007).
14. Cohen, S. I. et al. Proliferation of amyloid-β42 aggregates occurs through a secondary nucleation mechanism. *Proc. Natl Acad. Sci. USA* **110**, 9758–9763 (2013).
15. Michaels, T. C. T. et al. Dynamics of oligomer populations formed during the aggregation of Alzheimer's Aβ42 peptide. *Nat. Chem.* **12**, 445–451 (2020).
16. Sehlin, D. et al. Large aggregates are the major soluble Aβ species in AD brain fractionated with density gradient ultracentrifugation. *PLoS ONE* **7**, e32014 (2012).
17. Fowler, S. W. et al. Genetic modulation of soluble Aβ rescues cognitive and synaptic impairment in a mouse model of Alzheimer's disease. *J. Neurosci.* **34**, 7871–7885 (2014).
18. Lacor, P. N. et al. Aβ oligomer-induced aberrations in synapse composition, shape, and density provide a molecular basis for loss of connectivity in Alzheimer's disease. *J. Neurosci.* **27**, 796–807 (2007).
19. Forny-Germano, L. et al. Alzheimer's disease-like pathology induced by amyloid-β oligomers in nonhuman primates. *J. Neurosci.* **34**, 13629–13643 (2014).
20. Hartley, D. M. et al. Protofibrillar intermediates of amyloid β-protein induce acute electrophysiological changes and progressive neurotoxicity in cortical neurons. *J. Neurosci.* **19**, 8876–8884 (1999).
21. Yasumoto, T. et al. High molecular weight amyloid β1-42 oligomers induce neurotoxicity via plasma membrane damage. *FASEB J.* **33**, 9220–9234 (2019).
22. Klyubin, I. et al. Soluble Arctic amyloid β protein inhibits hippocampal long-term potentiation in vivo. *Eur. J. Neurosci.* **19**, 2839–2846 (2004).
23. Tomiyama, T. et al. A mouse model of amyloid β oligomers: their contribution to synaptic alteration, abnormal tau phosphorylation, glial activation, and neuronal loss in vivo. *J. Neurosci.* **30**, 4845–4856 (2010).
24. De Felice, F. G. et al. Aβ oligomers induce neuronal oxidative stress through an N-methyl-D-aspartate receptor-dependent mechanism that is blocked by the Alzheimer drug memantine. *J. Biol. Chem.* **282**, 11590–11601 (2007).
25. Maezawa, I., Zimin, P. I., Wulff, H. & Jin, L. W. Amyloid-β protein oligomer at low nanomolar concentrations activates microglia and induces microglial neurotoxicity. *J. Biol. Chem.* **286**, 3693–3706 (2011).
26. Paranjape, G. S., Gouwens, L. K., Osborn, D. C. & Nichols, M. R. Isolated amyloid-β(1-42) protofibrils, but not isolated fibrils, are robust stimulators of microglia. *ACS Chem. Neurosci.* **3**, 302–311 (2012).
27. Söllvander, S. et al. Accumulation of amyloid-β by astrocytes result in enlarged endosomes and microvesicle-induced apoptosis of neurons. *Mol. Neurodegener.* **11**, 38 (2016).

28. Umeda, T. et al. Intraneuronal amyloid β oligomers cause cell death via endoplasmic reticulum stress, endosomal/lysosomal leakage, and mitochondrial dysfunction in vivo. *J. Neurosci. Res.* **89**, 1031–1042 (2011).
29. Zempel, H. & Mandelkow, E. Lost after translation: missorting of Tau protein and consequences for Alzheimer disease. *Trends Neurosci.* **37**, 721–732 (2014).
30. Lord, A. et al. Amyloid-β protofibril levels correlate with spatial learning in Arctic Alzheimer's disease transgenic mice. *FEBS J.* **276**, 995–1006 (2009).
31. Tomiyama, T. et al. A new amyloid β variant favoring oligomerization in Alzheimer's-type dementia. *Ann. Neurol.* **63**, 377–387 (2008).
32. Kutzsche, J. et al. Safety and pharmacokinetics of the orally available antiprionic compound PRI-002: a single and multiple ascending dose phase I study. *Alzheimers Dement.* **6**, e12001 (2020).
33. Logovinsky, V. et al. Safety and tolerability of BAN2401—a clinical study in Alzheimer's disease with a protofibril selective Aβ antibody. *Alzheimers Res. Ther.* **8**, 14 (2016).
34. Overk, C. R. & Masliah, E. Toward a unified therapeutics approach targeting putative amyloid-β oligomer receptors. *Proc. Natl Acad. Sci. USA* **111**, 13680–13681 (2014).
35. Jarosz-Griffiths, H. H., Noble, E., Rushworth, J. V. & Hooper, N. M. Amyloid-β receptors: the good, the bad, and the prion protein. *J. Biol. Chem.* **291**, 3174–3183 (2016).
36. Rösener, N. S. et al. A d-enantiomeric peptide interferes with heteroassociation of amyloid-β oligomers and prion protein. *J. Biol. Chem.* **293**, 15748–15764 (2018).
37. De Felice, F. G. et al. Alzheimer's disease-type neuronal tau hyperphosphorylation induced by Aβ oligomers. *Neurobiol. Aging* **29**, 1334–1347 (2008).
38. Zempel, H. et al. Amyloid-β oligomers induce synaptic damage via Tau-dependent microtubule severing by TTLL6 and spastin. *EMBO J.* **32**, 2920–2937 (2013).
39. Zempel, H., Thies, E., Mandelkow, E. & Mandelkow, E. M. Aβ oligomers cause localized Ca(2+) elevation, missorting of endogenous Tau into dendrites, Tau phosphorylation, and destruction of microtubules and spines. *J. Neurosci.* **30**, 11938–11950 (2010).
40. LaFerla, F. M., Green, K. N. & Oddo, S. Intracellular amyloid-β in Alzheimer's disease. *Nat. Rev. Neurosci.* **8**, 499–509 (2007).
41. Esbjörner, E. K. et al. Direct observations of amyloid β self-assembly in live cells provide insights into differences in the kinetics of Aβ(1-40) and Aβ(1-42) aggregation. *Chem. Biol.* **21**, 732–742 (2014).
42. Orr, M. E. & Oddo, S. Autophagic/lysosomal dysfunction in Alzheimer's disease. *Alzheimers Res. Ther.* **5**, 53 (2013).
43. Rushworth, J. V., Griffiths, H. H., Watt, N. T. & Hooper, N. M. Prion protein-mediated toxicity of amyloid-β oligomers requires lipid rafts and the transmembrane LRP1. *J. Biol. Chem.* **288**, 8935–8951 (2013).
44. Hu, X. et al. Amyloid seeds formed by cellular uptake, concentration, and aggregation of the amyloid-β peptide. *Proc. Natl Acad. Sci. USA* **106**, 20324–20329 (2009).
45. Soura, V. et al. Visualization of co-localization in Aβ42-administered neuroblastoma cells reveals lysosome damage and autophagosome accumulation related to cell death. *Biochem. J.* **441**, 579–590 (2012).
46. Marshall, K. E., Vadukul, D. M., Staras, K. & Serpell, L. C. Misfolded amyloid-β−42 impairs the endosomal-lysosomal pathway. *Cell. Mol. Life Sci.* **77**, 5031–5043 (2020).
47. Koo, E. H. & Squazzo, S. L. Evidence that production and release of amyloid β-protein involves the endocytic pathway. *J. Biol. Chem.* **269**, 17386–17389 (1994).
48. Sannerud, R. et al. Restricted location of PSEN2/γ-secretase determines substrate specificity and generates an intracellular Aβ pool. *Cell* **166**, 193–208 (2016).
49. Vadukul, D. M. et al. Internalisation and toxicity of amyloid-β 1-42 are influenced by its conformation and assembly state rather than size. *FEBS Lett.* **594**, 3490–3503 (2020).
50. Lord, A. et al. The Arctic Alzheimer mutation facilitates early intraneuronal Aβ aggregation and senile plaque formation in transgenic mice. *Neurobiol. Aging* **27**, 67–77 (2006).
51. Yang, A. J., Chandswangbhuvana, D., Margol, L. & Glabe, C. G. Loss of endosomal/lysosomal membrane impermeability is an early event in amyloid Aβ1-42 pathogenesis. *J. Neurosci. Res.* **52**, 691–698 (1998).
52. Meisl, G. et al. Molecular mechanisms of protein aggregation from global fitting of kinetic models. *Nat. Protoc.* **11**, 252–272 (2016).
53. Wood, S. J., Maleeff, B., Hart, T. & Wetzel, R. Physical, morphological and functional differences between ph 5.8 and 7.4 aggregates of the Alzheimer's amyloid peptide Aβ. *J. Mol. Biol.* **256**, 870–877 (1996).
54. Fu, Z., Aucoin, D., Davis, J., Van Nostrand, W. E. & Smith, S. O. Mechanism of nucleated conformational conversion of Aβ42. *Biochemistry* **54**, 4197–4207 (2015).
55. Barghorn, S. et al. Globular amyloid β-peptide oligomer - a homogenous and stable neuropathological protein in Alzheimer's disease. *J. Neurochem.* **95**, 834–847 (2005).
56. Gong, Y. et al. Alzheimer's disease-affected brain: presence of oligomeric Aβ ligands (ADDLs) suggests a molecular basis for reversible memory loss. *Proc. Natl Acad. Sci. USA* **100**, 10417–10422 (2003).
57. Lesne, S. et al. A specific amyloid-β protein assembly in the brain impairs memory. *Nature* **440**, 352–357 (2006).
58. Liu, P. et al. Quaternary structure defines a large class of amyloid-β oligomers neutralized by sequestration. *Cell Rep.* **11**, 1760–1771 (2015).
59. Morinaga, A. et al. Critical role of interfaces and agitation on the nucleation of Aβ amyloid fibrils at low concentrations of Aβ monomers. *Biochim. Biophys. Acta* **1804**, 986–995 (2010).
60. Carrotta, R., Manno, M., Bulone, D., Martorana, V. & San Biagio, P. L. Protofibril formation of amyloid β-protein at low pH via a non-cooperative elongation mechanism. *J. Biol. Chem.* **280**, 30001–30008 (2005).
61. Zempel, H. & Mandelkow, E. M. Linking amyloid-β and tau: amyloid-β induced synaptic dysfunction via local wreckage of the neuronal cytoskeleton. *Neurodegener. Dis.* **10**, 64–72 (2012).
62. Kuperstein, I. et al. Neurotoxicity of Alzheimer's disease Aβ peptides is induced by small changes in the Aβ42 to Aβ40 ratio. *EMBO J.* **29**, 3408–3420 (2010).
63. Fezoui, Y. et al. An improved method of preparing the amyloid β-protein for fibrillogenesis and neurotoxicity experiments. *Amyloid* **7**, 166–178 (2000).
64. Hackl, E. V., Darkwah, J., Smith, G. & Ermolina, I. Effect of acidic and basic pH on Thioflavin T absorbance and fluorescence. *Eur. Biophys. J.* **44**, 249–261 (2015).
65. Hasecke, F. et al. Protofibril-fibril interactions inhibit amyloid fibril assembly by obstructing secondary nucleation. *Angew. Chem. Int. Ed.* **60**, 3016–3021 (2021).
66. Brody, D. L., Jiang, H., Wildburger, N. & Esparza, T. J. Non-canonical soluble amyloid-β aggregates and plaque buffering: controversies and future directions for target discovery in Alzheimer's disease. *Alzheimers Res. Ther.* **9**, 62 (2017).
67. Macao, B. et al. Recombinant amyloid beta-peptide production by coexpression with an affibody ligand. *BMC Biotechnol.* **8**, 82 (2008).
68. Wagner, T. et al. SPHIRE-crYOLO is a fast and accurate fully automated particle picker for cryo-EM. *Commun. Biol.* **2**, 218 (2019).
69. Rohou, A. & Grigorieff, N. CTFFIND4: fast and accurate defocus estimation from electron micrographs. *J. Struct. Biol.* **192**, 216–221 (2015).
70. Zivanov, J. et al. New tools for automated high-resolution cryo-EM structure determination in RELION-3. *Elife* **7**, e42166 (2018).
71. Spiegel, M., Duraisamy, A. K. & Schröder, G. F. Improving the visualization of cryo-EM density reconstructions. *J. Struct. Biol.* **191**, 207–213 (2015).
72. Schröder, G. F., Brunger, A. T. & Levitt, M. Combining efficient conformational sampling with a deformable elastic network model facilitates structure refinement at low resolution. *Structure* **15**, 1630–1641 (2007).
73. Zempel, H. & Mandelkow, E. M. Tracking Tau in neurons: how to grow, fix, and stain primary neurons for the investigation of Tau in all developmental stages. *Methods Mol. Biol.* **1523**, 327–334 (2017).
74. Schindelin, J. et al. Fiji: an open-source platform for biological-image analysis. *Nat. Methods* **9**, 676–682 (2012).
75. Schneider, C. A., Rasband, W. S. & Eliceiri, K. W. NIH Image to ImageJ: 25 years of image analysis. *Nat. Methods* **9**, 671–675 (2012).
76. Campion, D., Pottier, C., Nicolas, G., Le Guennec, K. & Rovelet-Lecrux, A. Alzheimer disease: modeling an Aβ-centered biological network. *Mol. Psychiatry* **21**, 861–871 (2016).
77. Hu, Y. B., Dammer, E. B., Ren, R. J. & Wang, G. The endosomal-lysosomal system: from acidification and cargo sorting to neurodegeneration. *Transl. Neurodegener.* **4**, 18 (2015).

Acknowledgements

This project has received funding from the European Research Council under the European Union's Horizon 2020 research and innovation program, grant agreement No. 726368. We acknowledge support from the Hans und Ilse Breuer-Stiftung, the Else-Kröner-Fresenius Stiftung, and Köln Fortune. We thank Raimond B.G. Ravelli, P.J. Peters, and C. López-Iglesias for advice and helpful discussions; H. Duimel for help with sample preparation; and the M4I Division of Nanoscopy of Maastricht University for microscope access and support. We acknowledge the Center of Advanced Imaging (CAI) at the Heinrich Heine University Düsseldorf for providing access to the TCS SP8 STED 3× and support during image acquisition. WT mice were provided by CMMC animal facility (Cologne, Germany) and CECAD in vivo research facility (Cologne, Germany); live-cell imaging was conducted at the CMMC imaging facility. We thank Jennifer Klimek for excellent technical support.

Author contributions

M.P.S., F.H., S.B., G.F.S., H.Z., and W.H. designed the experiments. M.P.S., F.H., S.B., M. Z., S.H., G.F.S., H.Z., and W.H. performed the experiments and analyzed the data. M.P.S., F.H., S.B., M.Z., G.F.S., H.Z., and W.H. wrote the manuscript. All authors commented on the manuscript.

Funding

Open Access funding enabled and organized by Projekt DEAL.

Competing interests

The authors declare no competing interests.

Additional information

Supplementary information The online version contains supplementary material available at https://doi.org/10.1038/s41467-021-24900-4.

Correspondence and requests for materials should be addressed to H.Z. or W.H.

Peer review information *Nature Communications* thanks Jan Bieschke and the other anonymous reviewer(s) for their contribution to the peer review of this work. Peer reviewer reports are available.

Reprints and permission information is available at http://www.nature.com/reprints

Publisher's note Springer Nature remains neutral with regard to jurisdictional claims in published maps and institutional affiliations.

Endo-lysosomal Aβ concentration and pH trigger formation of Aβ oligomers that potently induce Tau missorting

Marie P. Schützmann[1,†], Filip Hasecke[1,†], Sarah Bachmann[2,†], Mara Zielinski[3], Sebastian Hänsch[4], Gunnar F. Schröder[3,5], Hans Zempel[2,*], and Wolfgang Hoyer[1,3,*]

[1]Institut für Physikalische Biologie, Heinrich-Heine-Universität Düsseldorf, 40204 Düsseldorf, Germany

[2]Institute of Human Genetics and Center for Molecular Medicine Cologne (CMMC), University of Cologne, Faculty of Medicine and University Hospital Cologne, 50931 Cologne, Germany

[3]Institute of Biological Information Processing (IBI-7) and JuStruct: Jülich Center for Structural Biology, Forschungszentrum Jülich, 52425 Jülich, Germany

[4]Department of Biology, Center for Advanced Imaging (CAi), Heinrich-Heine-Universität Düsseldorf, 40204 Düsseldorf, Germany

[5]Physics Department, Heinrich-Heine-Universität Düsseldorf, 40204 Düsseldorf, Germany

Correspondence and requests for materials should be addressed to H.Z. (email: hans.zempel@uk-koeln.de) or W.H. (email: wolfgang.hoyer@hhu.de)

† These authors contributed equally.

Supplementary Figures

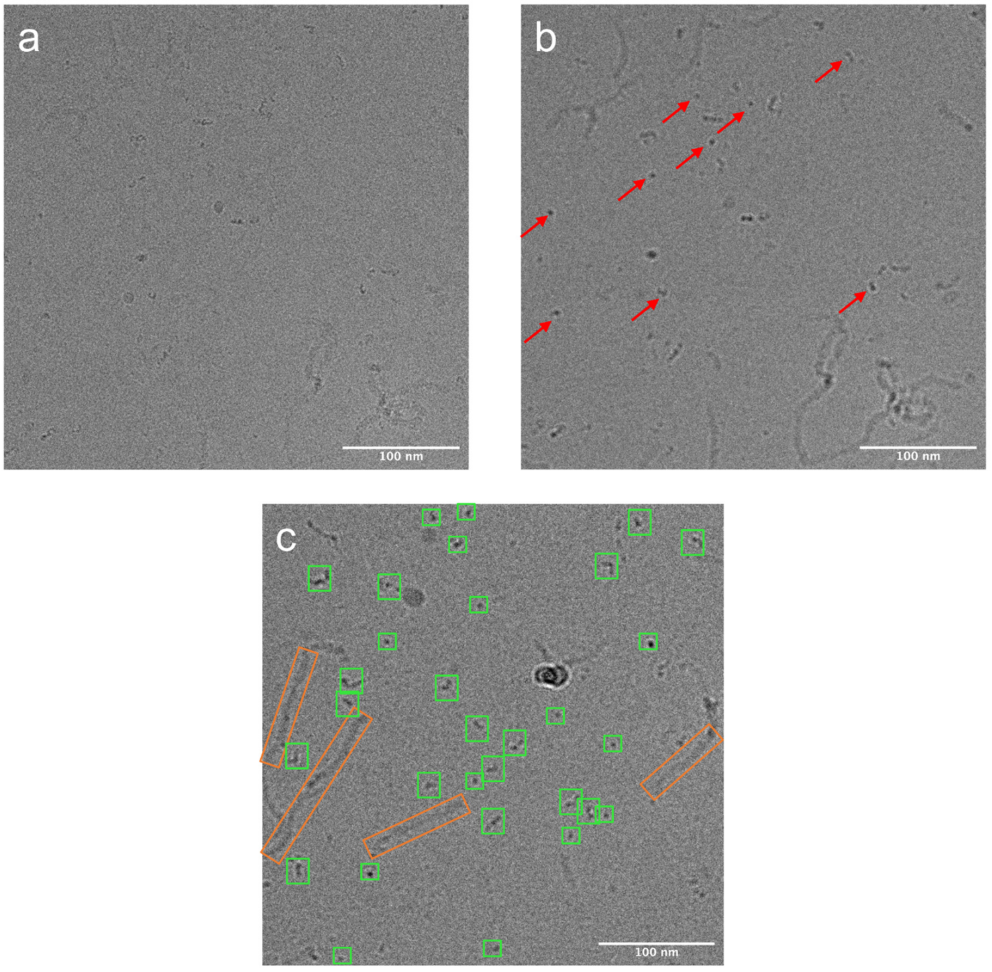

Supplementary Fig. 1 Representative examples from a total of 1308 cryo-EM micrographs collected of dimAβ AβOs. Micrographs were recorded at a defocus of **a** -1.6 µm or **b** -6 µm, respectively. Small AβO particles, indicated by red arrows, were selected on the high defocus micrographs for density reconstruction. **c** Thirty micrographs were analyzed to estimate the relative abundance of the small AβOs (green boxes) and AβO protofibrils (orange boxes). All clearly discernible objects were counted. Small AβOs accounted for 72±12% of all particles. Considering the particles' dimensions, we estimated that small AβOs contain 2-3% of all Aβ molecules within AβOs.

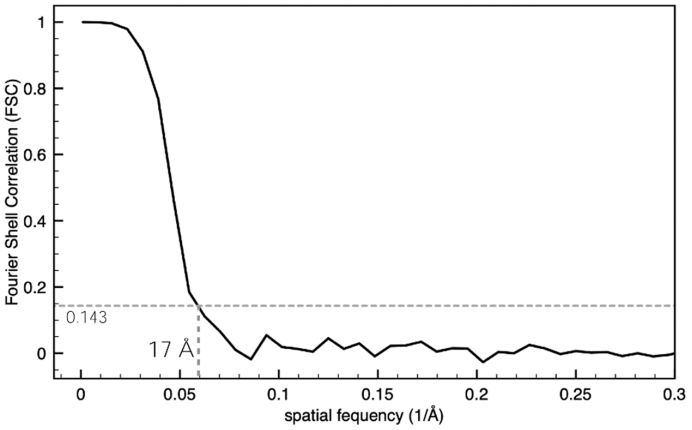

Supplementary Fig. 2 Fourier shell correlation (FSC) for the 3D reconstruction of the smallest dimAβ AβOs observed on the cryo-EM micrographs yields a resolution estimate of 17 Å.

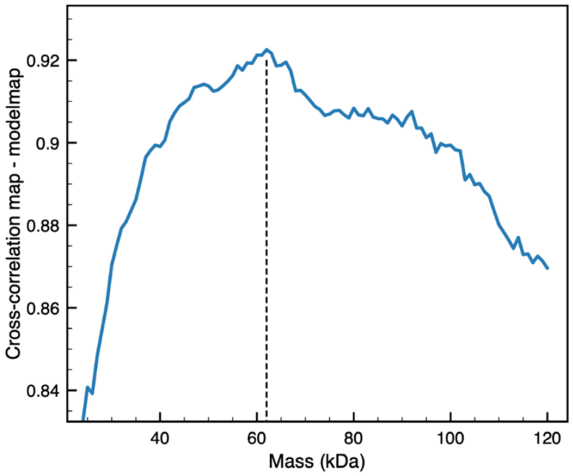

Supplementary Fig. 3 Density cross-correlation computed for each of the 110 pseudo-atomic model maps with the EM reconstruction after sharpening with VISDEM using the corresponding mass of the pseudo-atomic model. The highest correlation (0.923) is obtained for a mass of 62 kDa.

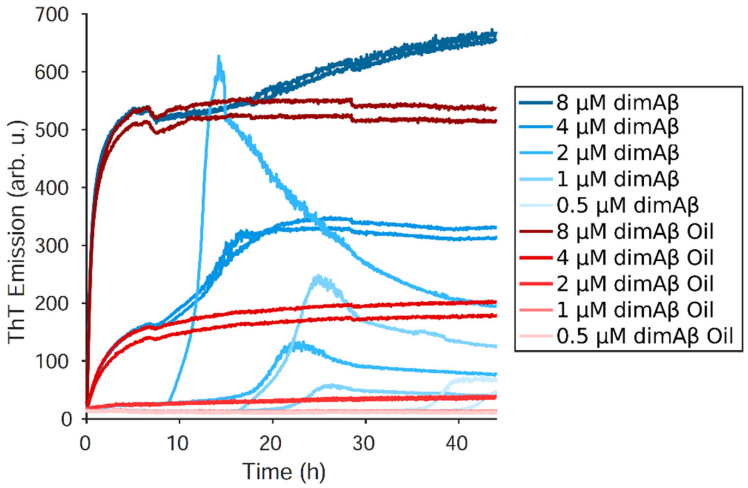

Supplementary Fig. 4 The air-water interface is crucial for fibril nucleation *in vitro*. Time courses of dimAβ assembly at pH 7.4 monitored by ThT fluorescence in a platereader. Half of the samples were covered by layering 10 µl of mineral oil on top of the aqueous solution. AβO formation was not impaired by mineral oil. Fibril nucleation, on the other hand, was retarded and not detectable during the whole timespan of the experiment.

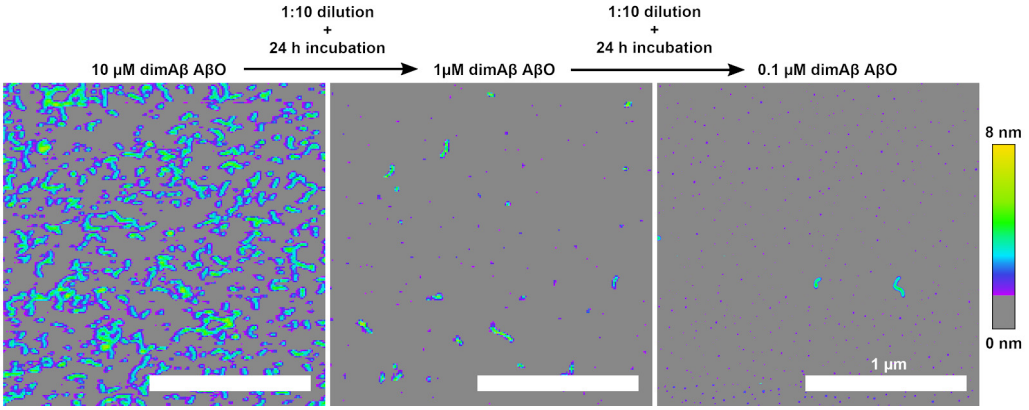

Supplementary Fig. 5 Long-term stability of diluted AβO. 10 µM dimAβ were quiescently incubated at 37°C, pH 7.4, for 72 h (left). Subsequently, the solution was diluted ten-fold to a dimAβ concentration of 1 µM and further quiescently incubated for 24 h at 37°C (middle). This solution was then further diluted ten-fold to a dimAβ concentration of 0.1 µM, which is far below the COC, and further incubated quiescently for 24 h at 37°C (right). Scalebar, 1 µm. *N*=1, between two and five micrographs were recorded for each condition.

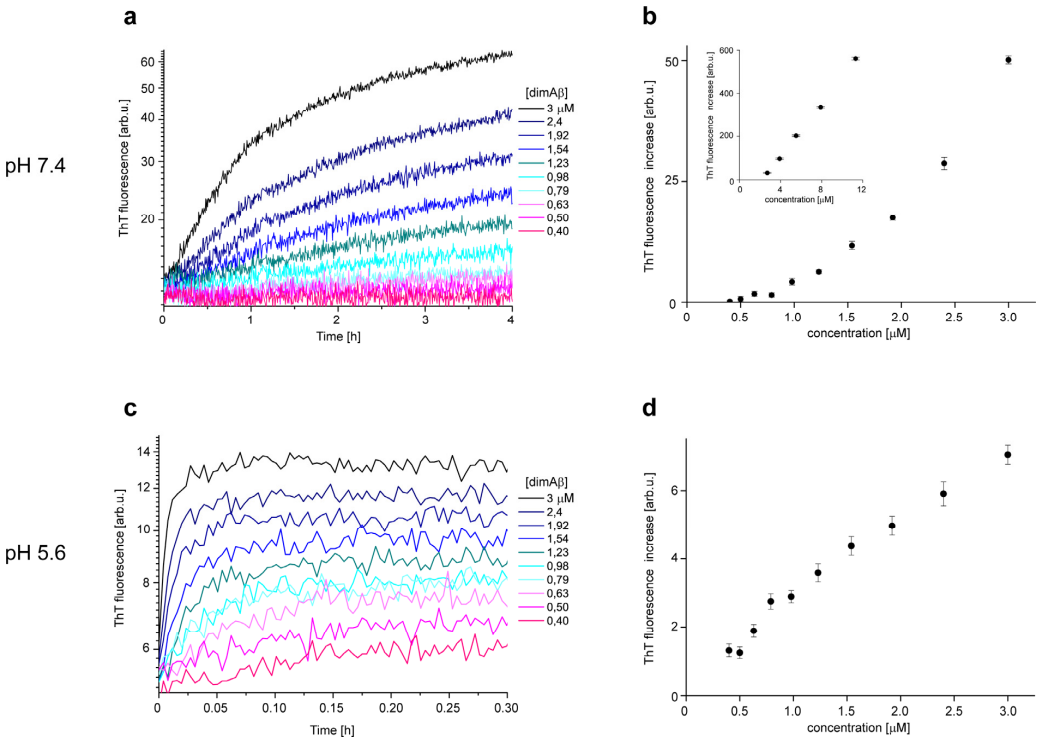

Supplementary Fig. 6 The critical concentration of AβO formation is reduced at acidic pH. Analysis of the AβO formation phase of dimAβ assembly at pH 7.4 (**a**, **b**) and pH 5.6 (**c**, **d**). **a**, **c** ThT fluorescence time traces at the indicated dimAβ concentrations. **b**, **d** The increase in ThT fluorescence intensity during the first 4 h (**b**) or 0.3 h (**d**) plotted against the dimAβ concentration. The inset in **b** shows data of a separate experiment spanning a range of higher concentrations. The data values in **b** and **d** are from single kinetic runs per concentration, with error bars representing the standard deviation of the final ten fluorescence readings in **a** and **c**. At pH 7.4, the intensity increase during the lag-free oligomerization phase scales linearly with protein concentration at dimAβ concentrations above ~2 μM (**b**, inset), whereas no lag-free oligomerization is detectable below ~0.5 μM, indicative of a COC of around 1 μM (**a**, **b**). At pH 5.6, however, there is no indication of disappearance of the oligomerization phase down to a concentration of 0.4 μM dimAβ (**c**, **d**). Due to the limited sensitivity of ThT at acidic pH it is not possible to reliably monitor oligomerization at lower concentrations and to determine the COC at this pH. Nevertheless, the COC at pH 5.6 is clearly lower than the COC at neutral pH, indicative of thermodynamic stabilization of AβOs at acidic pH.

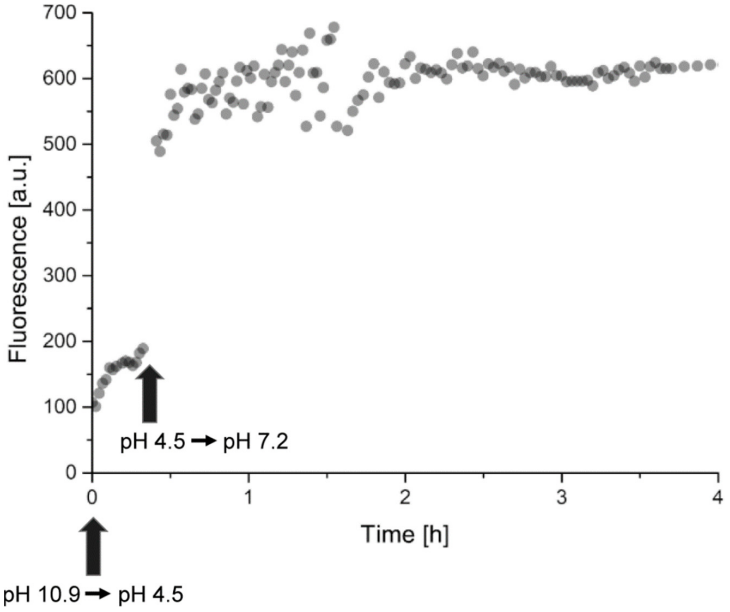

Supplementary Fig. 7 Stability of AβOs formed from Aβ42 at endo-lysosomal pH after shifting to neutral pH. ThT time course of AβO formation, initiated by pH adjustment from 10.9 to 4.5. Upon pH adjustment from pH 4.5 to pH 7.2 an immediate increase in fluorescence intensity is observed due to the pH sensitivity of ThT fluorescence. Apart from that, no other larger signal changes that would be expected in the case of disassembly of AβOs or replacement of AβOs by an alternative type of aggregate were observed.

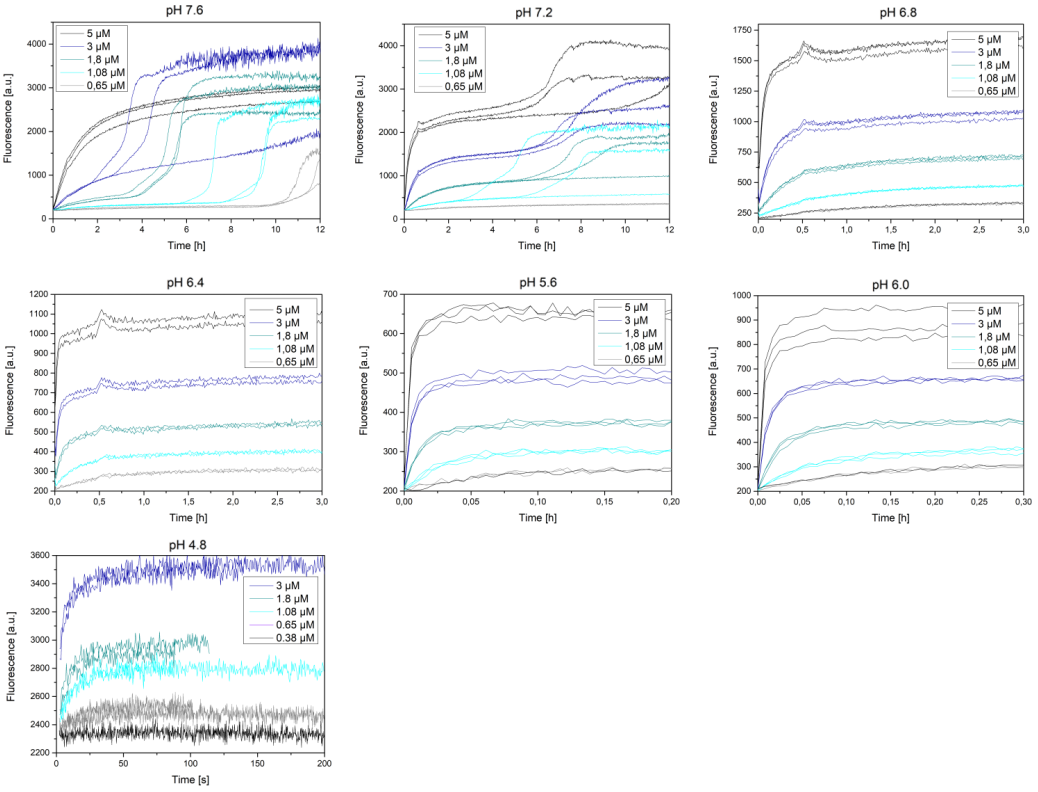

Supplementary Fig. 8 Replicate time traces from the dimAβ assembly experiment of Fig. 6.

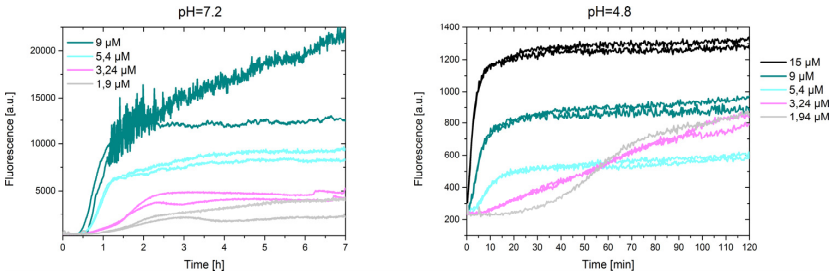

Supplementary Fig. 9 Replicate time traces from the Aβ42 assembly experiment of Fig. 7.

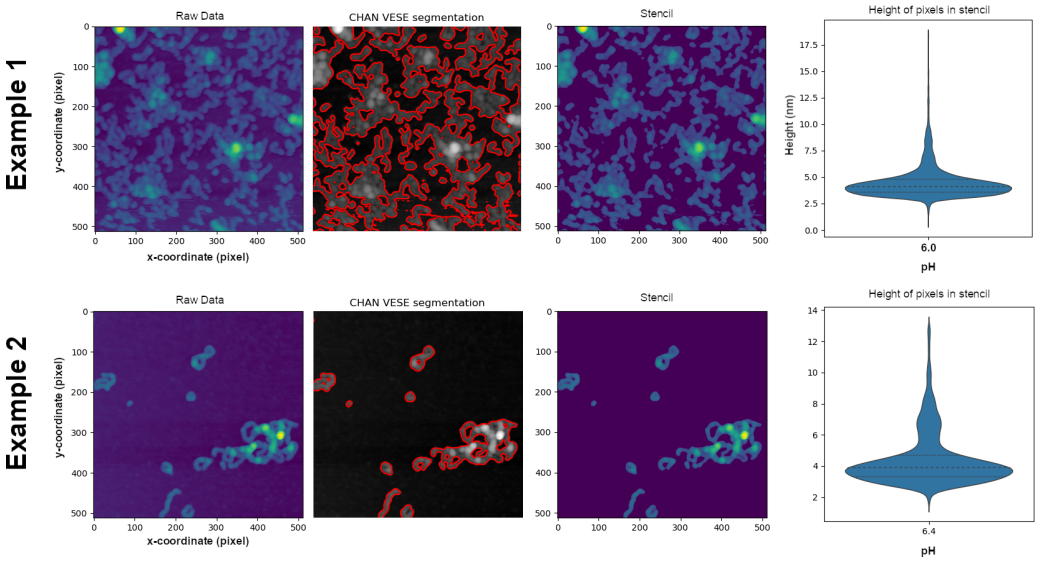

Supplementary Fig. 10 Examples of AFM image segmentation for height anaylsis. The Morphological Active Contours without Edges (MorphACWE) function 'morphological_chan_vese' of python's scikit-image module was used to distinguish and separate AβOs from background (typical settings were: iterations = 35; smooth = 1; lambda1 = 0.9; lambda2 = 0.89 to 0.895). Histographical height profiles of AβOs at different pH were determined as per pixel heights of the MorphACWE-isolated areas.

3. Results: PACMAN

3.1 Proteolytic Antigen Cleavage-Mediated AmplificatioN (PACMAN)

The method **P**roteolytic **A**ntigen **C**leavage-**M**ediated **A**mplificatio**N** (**PACMAN**) is a state-of-the-art take on proteolytic antibody engineering. It employs emulsion-based picoliter reactors, functionalized microbeads and *in vitro* transcription and translation (IVTT) to isolate antigen-specific proteolytic antibodies from combinatorial libraries. On a broader scale, beyond proteolytic antibodies, PACMAN may also serve as a platform to engineer proteases in general, by altering their specificities, processivities or chemical and environmental needs and susceptibilities. The concept of the PACMAN method is illustrated in Figure 3.1 and briefly described below.

First, microbeads are decorated with specifically designed target peptides and multiple copies of a template DNA which encodes one of the library members (e.g. from an antibody library or protease-derived mutagenesis library). To achive this, biotinylated target peptides are attached to streptavidin-functionalized microbeads. Streptavidin and biotin form the strongest non-covalent bond, known to date [290, 291], which is resistant to high temperatures, proteases and harsh solvent conditions. They are therefore perfectly suited to tightly and virtually irreversibly connect the aforementioned molecules to the microbeads. The target peptides are designed to contain the amino acid sequence of the target antigen or equivalently the amino acid sequence that shall be cleaved by the to-be engineered protease. The amino acid sequence is sandwiched between a spectrally distinct N-terminal and C-terminal fluorophor. For attachment to the streptavidin-coated microbeads, a biotin molecule is tethered to the N-terminus of the target peptide.

To achieve multivalent but monoclonal presentation of each library member on its own microbead, the genetic information of each library member is exclusively attached and replicated thousands of times onto individual microbeads via on-bead emulsion PCR (emPCR). Therefore, biotinylated primers are attached to the microbeads and a PCR is performed

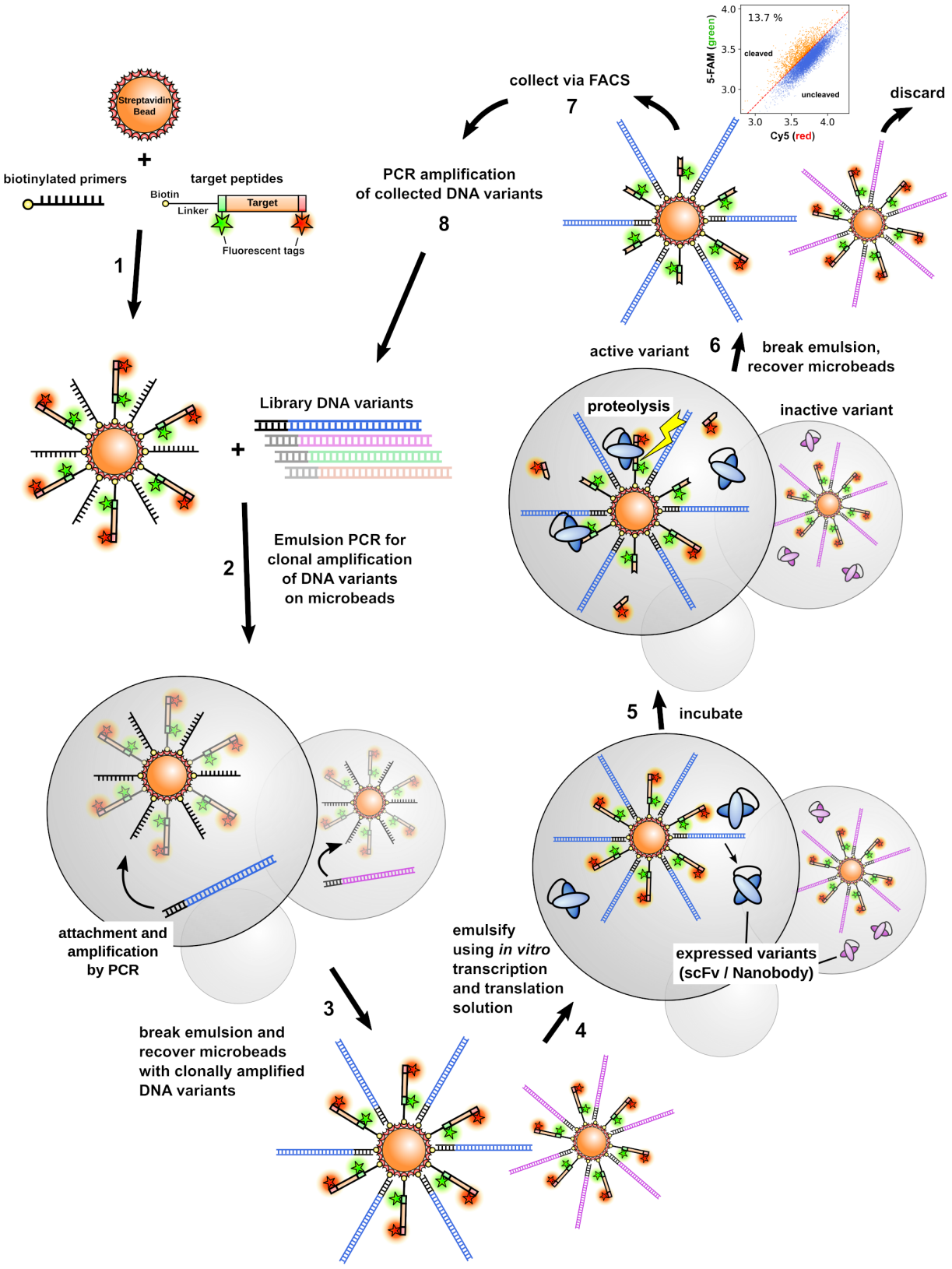

Figure 3.1: PACMAN scheme. Figure legend continued on the next page.

Figure 3.1: PACMAN scheme. Illustration of the principle of the PACMAN method. **1**, biotinylated forward primers are coupled to paramagnetic streptavidin-coated microbeads. Then, biotinylated target peptides harbouring the target antigen sequence between two different fluorophors (green and red) are added to and bound by the microbeads. **2**, microbeads coated with primers and peptides are mixed with library DNA variants and an on-bead emulsion PCR is performed to clonally amplify the library variants on individual microbeads. **3**, the emulsion is broken and the microbeads are collected and washed thoroughly to remove any unspecifically bound DNAs. **4**, microbeads are reemulsified in an *in vitro* transcription and translation solution. The library variants are expressed and confined within the same compartment as the encoding DNAs on the corresponding microbeads. **5**, the emulsion is incubated for several hours to allow sufficient expression of the variants and plenty of contact time with the target peptides. Active variants may proteolytically cleave the target sequences releasing the distal (red) fluorophors from the microbeads. **6**, the emulsion is broken, the microbeads are collected and thoroughly washed to remove the cut-off peptide fragments and fluorophors. **7**, microbeads are sorted by FACS, collecting the microbeads with a reduced distal (red) fluorophor signal. **8**, the DNA from the collected microbeads is amplified by PCR and used for subsequent selection cycles, maturation experiments or further analyses.

---

within an emulsion, which encapsulates individual microbeads together with a single template DNA molecule. During emPCR, each template is clonally amplified several thousand times and attached onto a microbead via the surface-attached primers.

Next, the microbeads are recovered and subsequently subjected to another emulsion, but this time, the aqueous phase contains an *in vitro* transcription and translation (IVTT) solution, which allows the transcription and translation of the microbead-attached DNA templates. A genotype-phenotype coupling is achieved by the *in vitro* compartmentalization (IVC) provided by the emulsion. Hence, expressed variants may only interact with the target peptides displayed on the surface of the same microbead that carries the corresponding template DNA. A proteolytically active library member can now cleave the target peptides, which are displayed on the surface of its microbead. By cleavage of the target peptides, the C-terminal fluorophors are released from the microbead. On the other hand, microbeads that are subjected to inactive library members remain unaltered.

Subsequently, microbeads with successfully cleaved target peptides may be recovered by Fluorescence-Activated Cell Sorting (FACS) according to their altered fluorescence profiles. Subsequently, the DNA from the recovered microbeads is reamplified by PCR and employed

in further PACMAN cycles or analyzed otherwise.

My aim designing PACMAN was to provide a selection method meeting a set of prerequisites to assure — by concept — only the isolation of antibodies with the best properties required to quickly advance into preclinical and clinical applications. These prerequisites included: 1) that the effective selection criterion of PACMAN should be the successfully executed cleavage of the antigen and not the stabilization of a transition-state of the proteolytic cleavage reaction (as described in section 1.5.3 using CRAAs by the Paul group). This is anticipated to limit mis-selections of antibodies that are proteolytically inactive, but feature nucleophilic properties. 2) during the whole selection process the antibodies should be untagged (i.e. not necessarily contain a His-tag, FLAG-tag, etc.) and uncoupled (i.e. not bound to phages or microbeads). This inflicts an additional selection pressure on the antibodies towards increased inherent solubility by elimination of artificial solubilizing or stabilizing cues. 3) the possibility to carefully adjust the inclusion or exclusion of chaperones and chaperonins, which act as a folding maschinery in the IVTT solution (e.g. GroEL/ES and DnaK). This may allow to provide a tuned selection environment favoring isolation of self-folding variants. 4) the method should provide means for a positive and a negative selection. This may, for example when PACMAN is applied to a mutagenesis library of a protease, allow the selection of a shift in the protease's specificity towards an altered cleavage sequence (e.g. to shift the sequence preference of a mutant TEV protease towards another amino acid instead of the original glycine/serine at the P1' position). On the other hand, it would provide means for targeted exclusion of specific antigens which may have presented undesired off-targets or it may be used to select for exclusive specificity towards a post-translationally modified antigen (e.g. phospho-Tau versus native Tau). This prerequisite may be provided by the use of two antinomic target peptides with distinct sets of fluorophors — one peptide providing a positive readout and the other peptide a negative readout in FACS.

3.2 Validation and optimization of the PACMAN method

Prior to antibody selections, the PACMAN method had to be validated and each step had to be optimized. For validation, the well-known Tobacco-Etch Virus (TEV) protease was utilized as a model protease. Ultimately, as validation experiment, template DNA featuring a TEV-protease expression cassette should be recovered from a mixture with excess DNA featuring an expression cassette encoding an irrelevant scFv. TEV-protease has a very similar size compared to scFvs with 27 kDa and 25–27 kDa, respectively. Therefore, TEV-protease

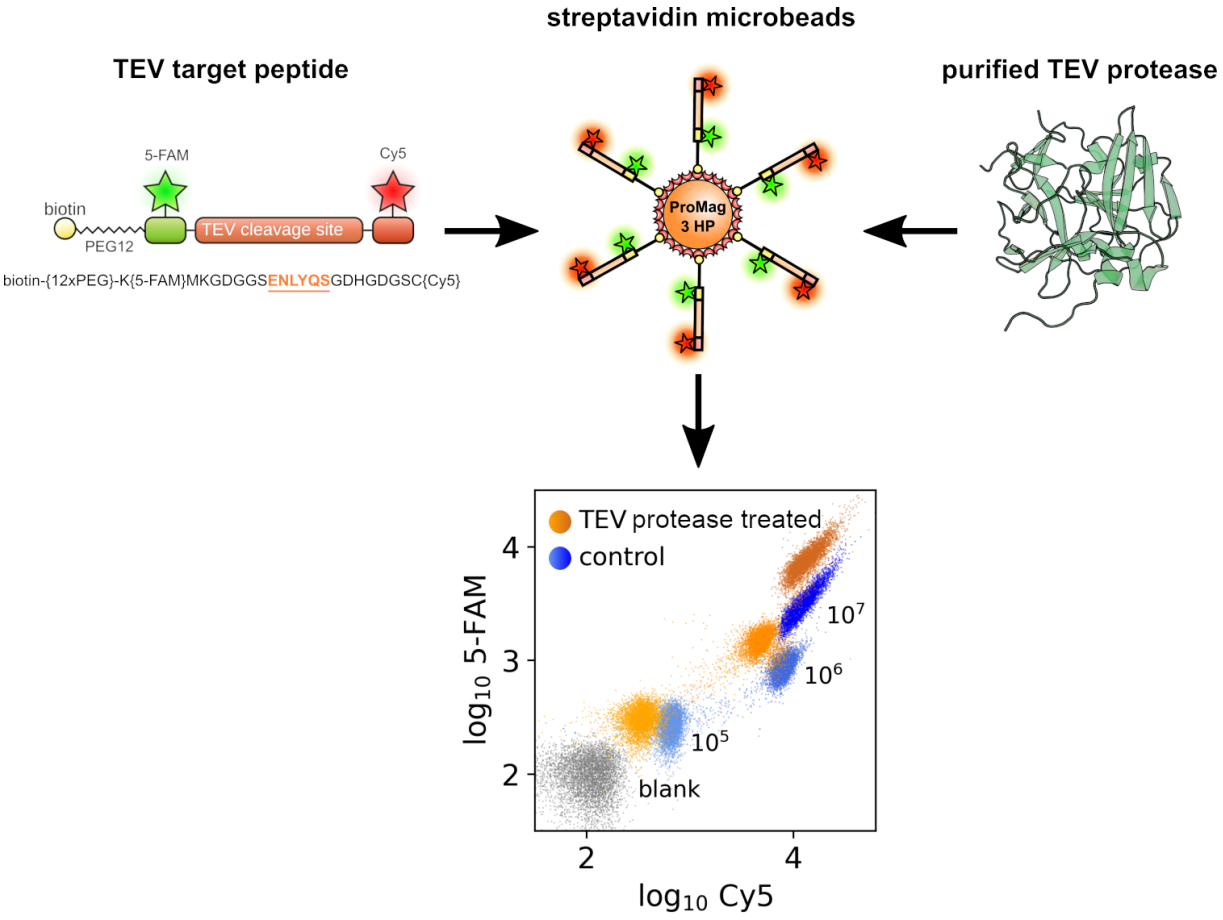

Figure 3.2: Optimization of the amount of TEV-target peptides per microbead. Promag HP 3 streptavidin microbeads were decorated with 10^5, 10^6 or 10^7 molecules of TEV-target peptide per microbead and subsequently subjected to 1 µg/ml purified TEV-protease over night at RT to assess the cleavability of the microbead-bound TEV-target peptides, which would lead to the release of the Cy5 fluorophor. The microbeads were analyzed by flow cytometry and the $\log_{10}$ of the fluorescence signals of 5-FAM and Cy5 are shown as scatter plot. Blank microbeads in grey, uncleaved control microbeads in blue hues and TEV-protease subjected microbeads in orange hues. The amount of TEV-target peptide molecules per microbead is annotated next to the corresponding adjacent microbead populations. TEV-protease model, pdb: 1Q31.

constituted a well-fitted model to assess the validity of the PACMAN concept and to probe and optimize each critical aspect of it.

3.2.1 Assessment of TEV-target peptide coupling to streptavidin-functionalized microbeads and subsequent accessibility by TEV-protease

A TEV-target peptide was designed featuring a TEV-cleavage site sandwiched between an N-terminal 5-FAM and a C-terminal Cy5 fluorophor. In addition, a biotin was linked to the N-terminus of the peptide to facilitate attachment to streptavidin-coated microbeads (see Figure 3.2). The peptide was synthesized by Pepscan.
To evaluate whether it was possible to bind TEV-target peptides to streptavidin-coated microbeads via streptavidin-biotin bond formation and to assess the optimal amount thereof per microbead, incremental amounts of TEV-target peptides were added to 3 µm Ø ProMag HP 3 streptavidin microbeads and analyzed by flow cytometry (see Figure 3.2). 10^5, 10^6 and 10^7 peptides/microbead were compared. Afterwards, purified TEV-protease was added to the microbeads and incubated over night to evaluate the accessibility of the TEV-target peptides by TEV-protease while the peptides were bound to microbeads in order to exclude that the proximity to the microbeads or local crowding effects might interfere with TEV-protease cleavage. As illustrated in Figure 3.2, TEV-target peptides were able to bind to ProMag 3 HP streptavidin microbeads and a concentration-dependent increase in 5-FAM and Cy5 fluorescence was detectable by flow cytometry. Furthermore, successful cleavage by purified TEV-protease was verified by detection of decreased Cy5 fluorescence and simultaneously increased 5-FAM fluorescence after TEV-protease treatment. The counter-intuitive simultaneous increase in 5-FAM fluorescence after TEV-protease treatment might be the result of abrogated Fluorescence Resonance Energy Transfer (FRET), as a result of Cy5 release from the peptides. 5-FAM and Cy5 represent a well-known FRET pair and were expected to exert FRET to some degree. Consequently, in the intact peptides, 5-FAM fluorescence was formally reduced. But after cleavage-mediated Cy5 release, 5-FAM fluorescence increased, as less energy was lost to Cy5 via FRET.

For subsequent experiments, 10^6 molecules/microbead of TEV-target peptides were used, as this concentration provided sufficient separation between TEV-protease-treated and untreated microbead populations while not unnecessarily consuming considerable amounts of the peptide.

3.2.2 TEV-protease produced by compartmentalized *in vitro* transcription and translation was able to cleave TEV-target peptides while maintaining genotype-phenotype coupling

Probably the most crucial and delicate step of PACMAN is the *in vitro* transcription and translation of each individual library member while its encoding DNA is attached to a microbead, while that is encapsulated in a picoliter-sized emulsion compartment. To evaluate the feasibility of this effort and to assess the lower limit of the necessary copies of the DNA coupled to each microbead to achieve sufficient expression by IVTT, the following assay was devised which aimed to emulate a PACMAN selection: ProMag HP 3 streptavidin microbeads were first decorated with 10^6 TEV-target peptides per microbead in a single batch, to guarantee equal starting conditions in terms of the initial fluorescence signal of the whole microbead population. The batch was then split into three aliquots and biotinylated DNA containing a TEV-protease expression cassette was added. The first aliquot contained a single molecule of biotinylated DNA per microbead, on average, the second aliquot contained one thousand biotinylated DNA molecules per microbead, on average, and the third aliquot was kept devoid of any DNA. The microbeads containing a single or one thousand DNA molecules/microbead were individually mixed one to ten with microbeads devoid of any DNA. A total of 10^6 microbeads of each mixture was subsequently subjected to an *in vitro* compartmentalization with PURExpress IVTT solution, supplemented with PURExpress disulfide bond enhancer (by New England Biolabs), DnaK mix (containing purified DnaK, DnaJ and GrpE, by Genefrontier) and GroE mix (containing purified GroEL and GroES, by Genefrontier) as aqueous phase and 2% FluoSurf as organic phase. The resultant emulsions were incubated at 37°C for four hours to allow TEV-protease expression and TEV-target peptide cleavage. The emulsions were broken using Fluorostop solution and microbeads were recovered, washed and analyzed using flow cytometry. As controls, to evaluate the effect of the encapsulation in terms of provision of a genotype-phenotype coupling, aliquots of the same microbead mixtures were subjected to IVTT, but without emulsification.

Microscopic analyses of the emulsions (see Figure 3.3 a) revealed an apparent mean diameter of 21.7 µm for microbead-bearing compartments (see Figure 3.3 b) and more than 80% of microbead-bearing compartments contained only a single microbead (see Figure 3.3 c), suggesting proper genotype-phenotype coupling might have been achieved by the IVC. To calculate the corresponding volumes of the compartments, their geometry induced by being squeezed between a microscopy slide and a cover slip during image acquisition had to be taken into account. As all microbeads appeared in the same focal plane, irrespective of their corresponding compartment diameters, compartments must have been tightly

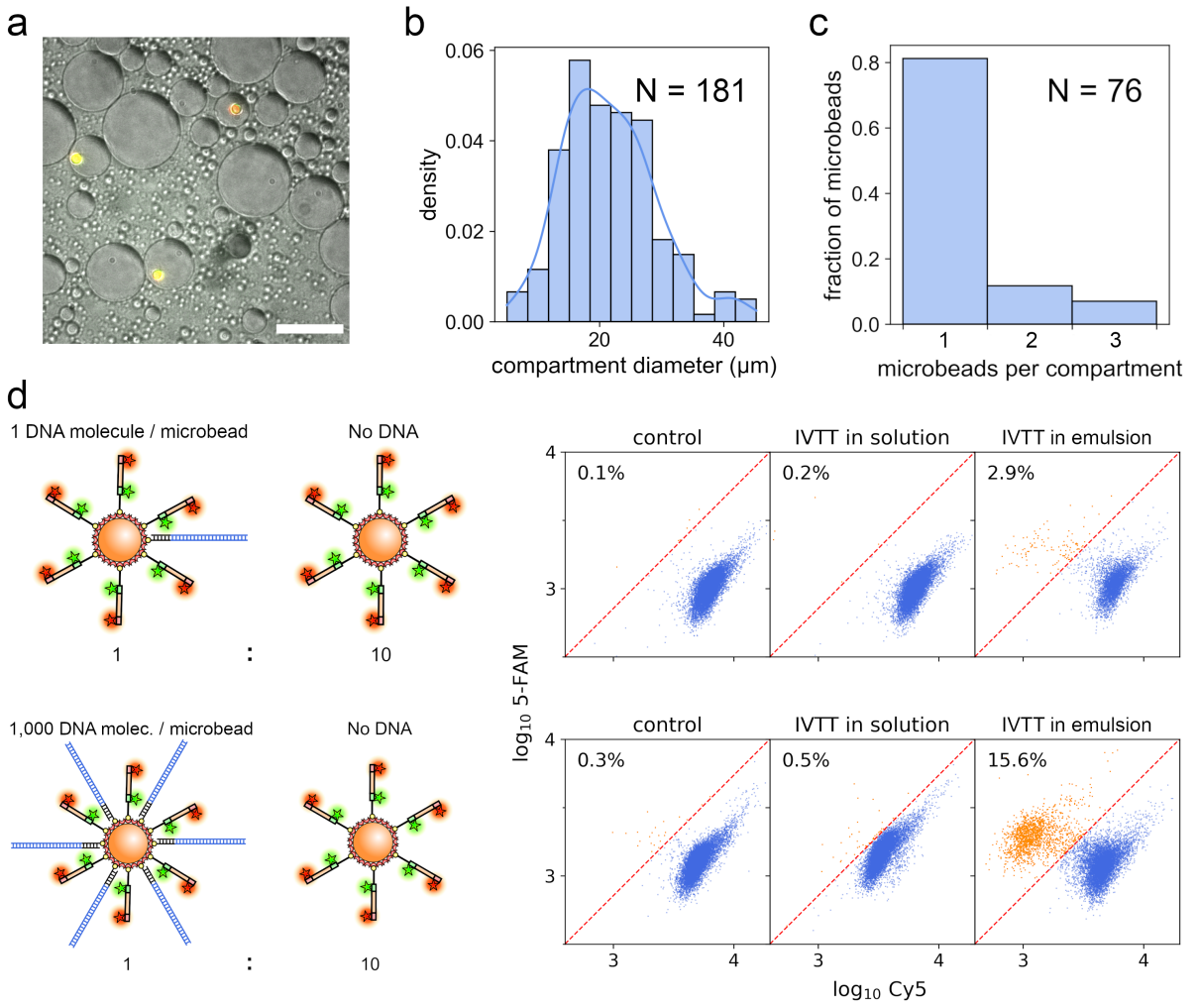

Figure 3.3: Compartmentalized *in vitro* transcription and translation of TEV-protease and TEV-target peptide cleavage. a, TIRF microscopy image of a FluoSurf IVTT emulsion containing microbeads decorated with 10^6 TEV-target peptides/microbead. Depicted is an overlay of the DIC-channel with the 5-FAM and Cy5 fluorescence channels. Scalebar, 25 µm. b, histogram analysis of the compartment diameters of microbead-bearing compartments. N = 181 compartments were included in the analysis. c, histogram of the fraction from total microbeads versus the number of microbeads contained in a given compartment. N = 76 compartments containing microbeads were analyzed. d, on the left, a scheme of the microbead composition used to gather the experimental data on the right is shown. On the right, scatter-plots of the flow cytometric analyses of microbeads from emulated PACMAN experiments are shown. 'control', contained microbeads that were not subjected to an emulsion nor IVTT. 'IVTT in solution' contained microbeads that were subjected to IVTT but without an emulsion. 'IVTT in emulsion', contained microbeads that were subjected to IVTT in emulsion, corresponding to an emulated PACMAN selection. The dashed red line was arbitrarily defined as a population boundary of microbeads with intact (lower right, blue dots) and cleaved (upper left, orange dots) TEV-target peptides. In the upper left corners, the percentage from total microbeads inside the region of microbeads with cleaved TEV-target peptides (orange dots) is given. Experiments in d were partially performed by Anne Pfitzer.

squeezed between the microscopy slide and the cover slip. Consequently, it was fair to assume a consistent layer thickness of 3 – 4 µm, limited only by the diameter of the microbeads. Thereby, the compartment volumes were estimated by calculating a cylindrical volume with an assumed height of 3 – 4 µm, rather than by calculating the more intuitive spherical volume using merely the apparent diameters of the droplet compartments. Cylindrical volumes yielded an average volume of 1.1 – 1.5 picoliter (pL), which corresponded to an estimated total of 1.2 – 1.6 x 10^7 compartments present in each IVC emulsion.

Flow cytometry data of these emulated PACMAN assays are shown in Figure 3.3 d. To easily appreciate differences in the microbead populations in the flow cytometry data, a population boundary (red diagonal dashed line) was arbitrarily defined, which separated the plots into areas containing microbeads with intact (lower right, blue dots) and microbeads with cleaved TEV-target peptides (upper left, orange dots) . The IVTT control sample without emulsification by IVC, containing a 1:10 mixture of microbeads harbouring a single molecule of TEV-protease-coding template DNA and without any DNA, respectively, presented identical fluorescence signals compared to untreated control microbeads. This suggested that TEV-protease expression attributable to the miniscule amount of TEV-protease-coding DNA present in the sample was insufficient to properly induce cleavage of a perceptible amount of TEV-target peptides. In comparison, the IVTT control sample without IVC, containing a 1:10 mixture of microbeads harbouring 1,000 molecules of TEV-protease-coding template DNA/microbead and microbeads without any DNA, respectively, presented a considerable shift of the whole microbead population towards the population boundary (towards the area of microbeads with cleaved TEV-target peptides). But as expected, without IVC the TEV-target peptides of all microbeads were indiscriminately cleaved to a similar extent, irrespective of whether the individual microbead was harbouring TEV protease-coding DNA or not. But as IVC was introduced by emulsification, a genotype-phenotype coupling was successfully established, evidenced by a disruptive separation of the microbeads into two populations with 15.6% of the microbeads falling into the area of microbeads with cleaved TEV-target peptides (orange dots) and the rest into the area of microbeads with intact TEV-target peptides (blue dots). Interestingly, slightly more than the anticipated 10% of microbeads were classified as microbeads with cleaved TEV-target peptides, which might be explained by occasionally having multiple microbeads encapsulated in a single compartment, while one of these microbeads harboured TEV-protease-coding DNA, resulting in additional, false positive signals due to coencapsulated microbeads that harbored no DNA. Unfortunately, this disruptive effect was not as prominent in the sample containing microbeads harbouring merely a single molecule of TEV-protease-coding DNA. Here, only 2.9% of the microbeads were classified as microbeads with cleaved TEV-target peptides, suggesting that a single DNA molecule might not be sufficient for robust expression in IVC IVTT.

The fact that a single molecule of template DNA/microbead appeared insufficient for IVC IVTT, but one thousand molecules were sufficient, was unfortunate, as consequently, to enable screening of divers libraries with PACMAN, an on-bead emulsion PCR was imperative to clonally amplify the DNA templates of each library member on individual microbeads prior to IVC IVTT. If that would have not been the case and a single DNA molecule would have been sufficient per microbead, biotinylated DNA templates could have simply been added to the microbeads in a simple batch coincubation — irrespective of the libraries complexity — to stochastically achieve monoclonal coverage of each microbead with a single DNA molecule without the detour presented by on-bead emPCR.

3.2.3 Optimization of on-bead emulsion polymerase chain reaction

On-bead emulsion PCR (emPCR) constitutes a method used for highly paralleled, clonal amplification and simultaneous attachment of millions of distinct DNA templates each monoclonally onto the surface of a microbead, while facilitating not only the attachment but also the amplification of each template DNA on the surface of the respective microbead. Eventually resulting in each microbead carrying hundreds to millions of clonal DNA copies of a distinct DNA template. This is especially handy, in applications that require display of distinct library members on individual microbeads, in case a single molecule of DNA is not enough for down-stream applications and hence clonal amplification is necessitated. In principle, on-bead emPCR is a PCR reaction in the presence of microbeads, which are decorated with one of the two primers while the whole reaction is compartmentalized into millions of picoliter-sized reaction droplets generated via water-in-oil emulsification. Included in the reaction is a carefully titrated amount of input DNA templates as to stochastically provide encapsulation of a single molecule of DNA together with a single microbead. During the PCR each DNA molecule is clonally amplified while concomitantly being attached to the microbead via its tethered primers.

Unfortuantely, on-bead emPCR is not a standardized, routine method, and hence not readily available. In fact, establishment and optimization of a viable protocol presented a major challenge of this project. Copious protocols have been published on this matter, but most of them had a prominent, inherent limitation rendering them inapt for application in PACMAN. Their amplification efficacies were promising for short DNA templates, but plummeted quickly with template lengths above 500 bp or were not evaluated for templates of longer lengths [259, 265, 292–297]. Unfortunately, the template DNA length of scFv antibody variants, as used in this study, is 1,000 – 1,100 bp, far exceeding the capabilities of the aforementioned protocols.

Few protocols claimed to have accomplished successful on-bead emPCR with DNA templates of ≥1,000 bp in length [258, 262, 265, 298]. But unfortunately, neither of these protocols could be readily reproduced nor adapted without considerable adjustments to be applicable for use in PACMAN. Therefore, meticulous effort was invested to establish an on-bead emPCR protocol complying to the needs of PACMAN.

My early, initial attempts at on-bead emPCR were performed with Abil EM 90-based emulsions, Phusion polymerase and 1 µm Ø ProMag streptavidin microbeads, but consistently failed to achieve any amplification of templates on microbeads (data not shown). Abil EM 90 is a broadly utilized surfactant in IVC experiments and reports exist about successful application thereof in on-bead emPCR experiments [265, 295, 297]. Unfortunately, all my attempts to reproduce these experiments were in vail. Therefore, an extensive literature review was conducted which hinted towards promising results by Diamante *et al.* and Mankowska *et al.* [258, 262], who applied HFE7500 as an organic solvent, a low-viscosity hydrofluoroether, and a fluorinated surfactant to prepare their emulsions. Both substances are probably most reknown for their use in microfluidic applications. Unfortunately, the particular surfactant used by Diamante *et al.* was not commercially available, but proprietary surfactant formulations in HFE7500 for microfluidic applications were commercially available and therefore lent themselves as a promising candidate to replace the Abil EM 90-based emulsions. Henceforth, all the following experiments were performed using 2% FluoSurf by Dolomite, unless stated otherwise. Furthermore, literature review suggested the use of larger microbeads with diameters of 3 µm and above might contribute to on-bead emPCR success [258, 259, 262, 296]. Accordingly, 3 µm Ø microbeads were used in the following experiments. The final insight from literature review was the apparent superiority of Titanium Taq polymerase-based on-bead emPCR formulations as opposed to other polymerases [258, 262, 296].
Reinforced by these insights, the protocols published by Diamante *et al.* [258] and Mankowska *et al.* [262] provided a valuable starting point for further optimization and were eventually adapted to the needs of PACMAN.

In a first instance, three different 3 µm Ø streptavidin-coated microbead products (Dynabeads M270, Dynabeads M280, ProMag HP 3) were compared in terms of their suitability for on-bead emPCR. Therefore, a short, 277 bp DNA fragment was used as a template DNA, which due to its short length, was anticipated to best assure on-bead emPCR success for an initial comparative assessent of the different microbead products. Emulsions were prepared with 2% FluoSurf as an oil-surfactant mixture and a Titanium Taq-based PCR formulation as aqueous component according to Diamante *et al.* [258]. Stable emulsions were quickly prepared with ease, due FluoSurf's simple preparation method via vortexing, which was

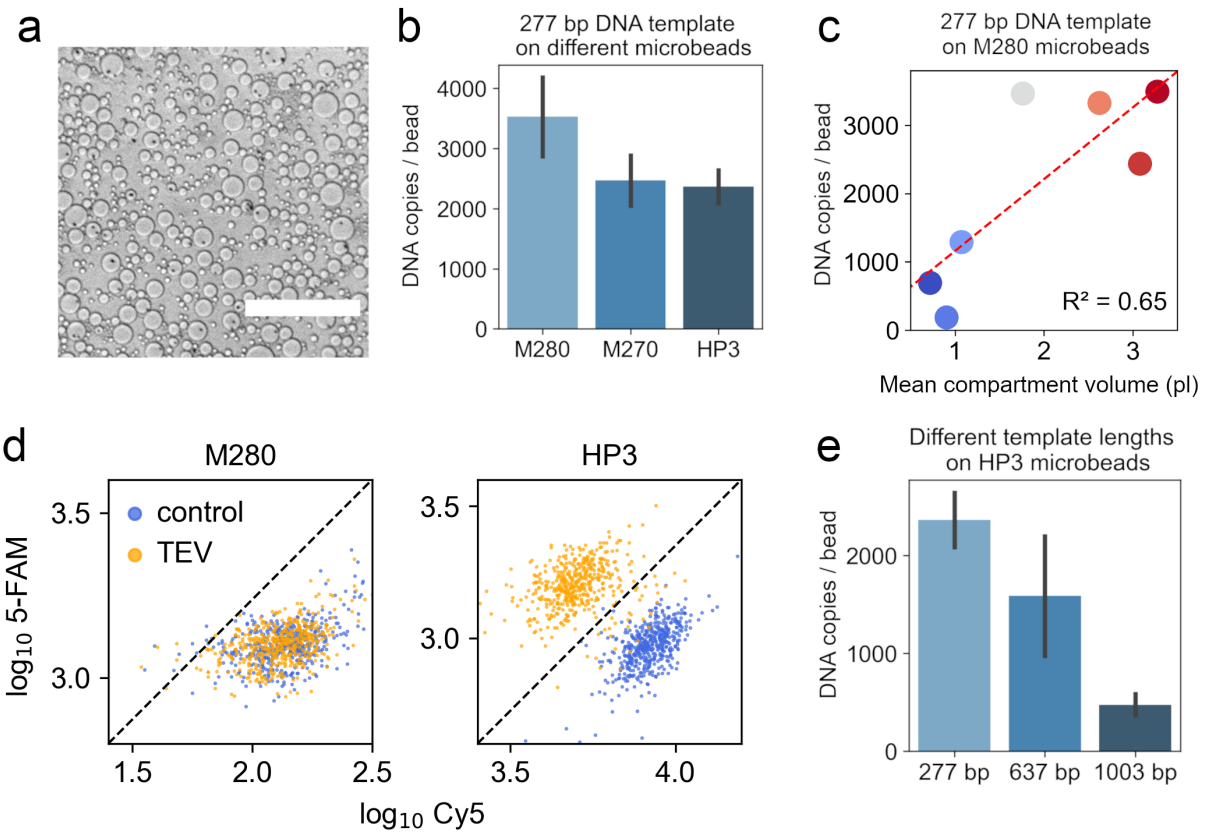

Figure 3.4: Evaluation of on-bead emulsion PCR parameters. a) representative DIC micrograph of an on-bead emPCR emulsion prepared with 3 µm Ø microbeads, Titanium Taq PCR mixture and 2% FluoSurf. Scalebar, 200 µm. b) comparison of the suitablility of different 3 µm Ø streptavidin-coated microbead products for use in on-bead emPCR (Dynabeads M270, Dynabeads M280 and ProMag 3 HP). qPCR analysis was performed to determine the DNA copies/microbead. On-bead emPCR was performed with 2.5x Titanium Taq polymerase in Titanium Taq buffer with 1 µM reverse primer. Microbeads were decorated with 1.2 x 10^5 biotinylated forward primers/microbead. A 277 bp DNA template was used as input template. 10^6 microbeads and $1.7x10^7$ molecules of template DNA were supplied to each reaction as suggested by Diamante *et al.* [258] c) Evaluation of the influence of the mean compartment sizes of the emulsions on the efficacies of the on-bead emPCR. The sizes of the emulsion compartments was varied by the use of different vortexers and speed settings for each reaction. M280 microbeads and a 277 bp input DNA template was used. d) Flowcytometric evaluation of the accessibility of microbead-bound TEV-target peptides by TEV-protease comparing Thermofisher's streptavidin-coated Dynabeads M280 and Bangs Laboratories ProMag HP 3 streptavidin microbeads. 10^6 TEV-target peptides were bound per microbead. Microbeads were treated with purified TEV-protease overnight and subsequently analyzed by flow cytometry. e) Evaluation of the effect of the template DNA length on the efficiency of on-bead emPCR. The DNA copies/microbead were determined by qPCR after on-bead emPCR.
qPCR was always performed in triplicates (n=3, mean±sd).

recommended for the product (see Figure 3.4 a). Mean compartment sizes of the emulsions could be slightly tweaked by varying the vortexer settings or changing the vortexer devices. Depending on the setup, it was possible to achieve mean compartment volumes between 0.7 – 3.3 pL, which corresponded to a total of 0.6 – 25 x 10^7 compartments per preparation. Intervariability of preparations with the same vortex setup was negligible.

In all initial experiments, 120,000 biotinylated primers ('b-TEG-TGS-Link-T7p For') were coupled per microbead prior to on-bead emPCR. On-bead emPCR was performed with Dynabeads M270, Dynabeads M280 and ProMag HP 3 microbeads and subsequently emPCR efficacies were analyzed by qPCR. After emPCR the microbeads underwent a rigorous washing procedure to remove any unspecifically bound DNAs. To faithfully determine emPCR efficacies after on-bead emPCR, it was necessary to be able to distinguish between DNA which was properly microbead-bound via streptavidin:biotin coupling and DNA which was either residually in solution or still unspecifically bound to the microbeads after the washing procedure. This distinction was readily accomplished by separating the microbeads from solution using a 0.2 µm PES syringe filter. This way, the bulk of the unspecifically bound DNA could be sheared off the microbeads by the filtering process and was then detectable in the eluate, while microbeads and properly streptavidin:biotin-bound DNA was retained by the filter. By comparing the DNA content of the original microbead suspension and the filtered eluate, on-bead emPCR efficacies could be faithfully derived and the wash protocols could be optimized. qPCR was always performed on a total of 1,000 microbeads per reaction, as determined via hemocytometer, and compared to the equivalent amount of the filtered eluate. Evaluation revealed a superior on-bead emPCR efficiency achieved with Dynabeads M280 with approximately 3.500 DNA copies/microbead (see Figure 3.4 b). Dynabeads M270 and Promag HP 3 microbeads proved slightly less efficient, both with approximately 2.500 DNA copies/microbead. Nevertheless, all three microbead products were ongoingly considered as potential candidates for on-bead emPCR optimization.

Using the Dynabeads M280, the influence of the mean IVC compartment volume on on-bead emPCR efficiency was evaluated. By adjusting the vortexer settings and the use of different vortexer devices, compartment volumes ranging from 0.7–3.3 pl, were prepared and on-bead emPCR efficacies were compared, revealing a positive correlation (R^2=0.65) between compartment volume and on-bead emPCR efficiency. Compartment volumes below 1.5 pl almost entirely diminished the efficiency and best results were achieved around the 3 pl volume mark, larger compartment volumes could unfortunately not be reliably prepared (see Figure 3.4 c). However, the larger, 3 pl compartments could be reproducibly prepared by 5 minutes of vortexing using the vortexer VV3 by VWR on strength setting 5 of 6 (see section 6.4.4 for further details)

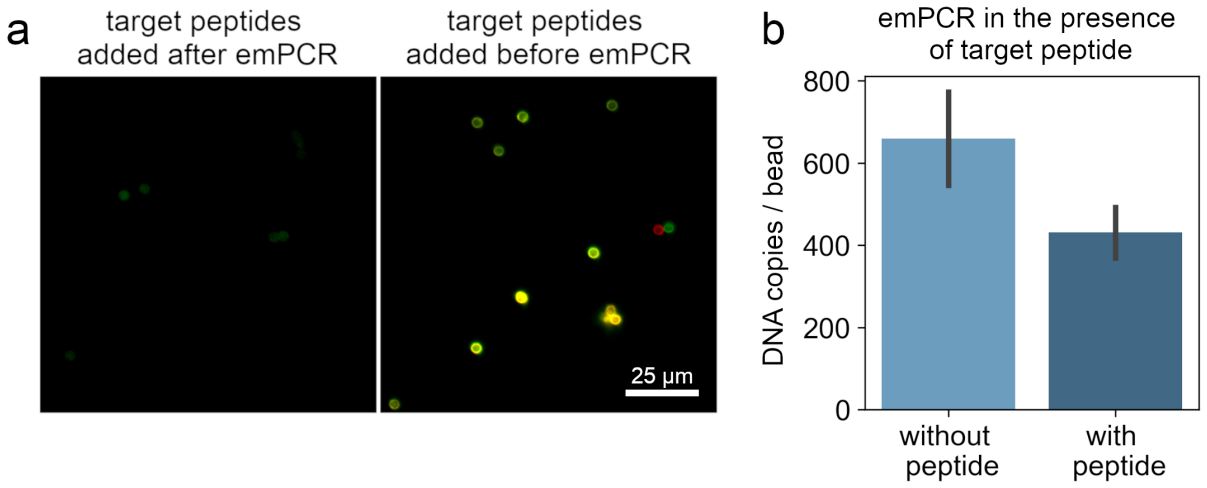

Figure 3.5: On-bead emPCR in the presence of TEV-target peptides. a) Evaluation of the binding capacity of apo-form streptavidin after on-bead emPCR. Left, micrograph of the merged FAM- and Cy5-channel of microbeads with TEV-target peptides added after on-bead emPCR. Right, microbeads with TEV-target peptides added prior to on-bead emPCR. b) qPCR evaluation of the achieved DNA copies/microbead after on-bead emPCR in the absence and presence of TEV-target peptides, which were bound to the microbeads prior to on-bead emPCR. TEV-protease-coding DNA (1,003 bp) was used as input templates for the on-bead emPCR.
qPCR was performed in triplicates (n=3, mean±sd).

Next, focusing on the accessibility of the TEV-target peptides by TEV-protease, while being bound to the different microbead products, revealed the surprising inability to execute cleavage, when the targets were bound to Dynabeads M280. Conversely, cleavage was readily achieved, when Promag HP 3 microbeads were used. Hence, the Dynabeads M280 were disqualified for use in PACMAN, as apparently, these microbeads protected the TEV-target peptides from access by TEV-protease (see Figure 3.4 d). Henceforth, all experiments were performed using Promag HP 3 microbeads only.

The most important factor yet to be evaluated, was to ensure that the current on-bead emPCR protocol allowed for the amplification of DNA templates with ≥1,000 bp in length, to enable the amplification of TEV-protease-encoding, as well as scFv-encoding templates. Hence, the amplification efficacies for larger templates were analyzed using a 637 bp nanobody-encoding template and the 1,003 bp TEV-protease-encoding template. As to be expected, the efficacies dropped considerably with increasing template lengths, but amplification was still achieved with the 1,003 bp TEV-protease-coding template with still approximately 500 DNA copies/microbead, which was anticipated to be sufficient for PACMAN (see Figure 3.4 e).

As a next step in preparation for PACMAN, it was initially intended to couple the biotinylated TEV-target peptides to the microbeads after on-bead emPCR, but conflicting with the original protocol by Diamante *et al.* [258], streptavidin in its ligand-free apo-form appeared to be susceptible to elevated temperatures leading to irreversible loss of its binding capacity as a consequence of the repeated heating cycles during emPCR (see Figure 3.5 a). As a consequence, microbeads were unable to bind TEV-target peptides after on-bead emPCR. Therefore, it was inevitably paramount to be able to bind the target peptides to the microbeads prior to on-bead emPCR and still achieve template amplification while also maintaining stability of the target peptides and especially their fluorophors.
Fortunately, the ligand-bound holo-form of streptavidin sustained the elevated temperatures during emPCR and also the fluorophors of the target peptides were unscathed by the process, as evidenced by prominent fluorescence intensities detected by fluorescence-microscopy after on-bead emPCR (see Figure 3.5 a). Subsequently, the influence of the presence of TEV-target peptides during on-bead emPCR was evaluated in terms of potential impairment of amplification efficacies (see Figure 3.5 b). Therefore, the DNA copies/microbead were compared between two on-bead emPCR preparations, one featuring microbeads decorated with 10^6 TEV-target peptide molecules/microbead in addition to the primers and the other without TEV-target peptides, otherwise the reaction conditions were identical. The presence of TEV-target peptides on the microbead surfaces turned out to negatively influence the on-bead emPCR efficiency, but fortunately, the efficiency was not entirely abrogated, but merely reduced by one-third of its efficiency achieved in the absence of TEV-target peptides. Nevertheless, this reduction in efficiency was not anticipated to interfere with the PACMAN process and optimization was optimistically continued.

Having established a viable protocol for on-bead emPCR, further effort was invested into the determination of the sweet-spot of the primer concentration coupled to the microbeads and furthermore, four polymerase formulations were compared: 2.5 X Titanium Taq in Titanium Taq buffer, 2.5 X Phusion polymerase in its HF-buffer, CloneAmp Hifi PCR premix and Q5 Hot Start High-Fidelity premix. At the same time, for each PCR formulation, three incremental concentrations of microbead-bound primers were compared: 10^5, 10^6 and 10^7 primers/microbead. Furthermore, for each condition four different DNA template lengths (277 bp, 637 bp, 1,003 bp and 2,164 bp) were compared in terms of the achievable DNA copies using on-bead emPCR. Finally, the stability of the emulsions after on-bead emPCR was evaluated (see Figure 3.6).
Of immediate notice, was the severe instability of the Phusion polymerase-based emPCR formulation. After emPCR, the emulsions were broken for the most part and a brownish film of released microbeads was found at the liquid-air interface and some were clumped together

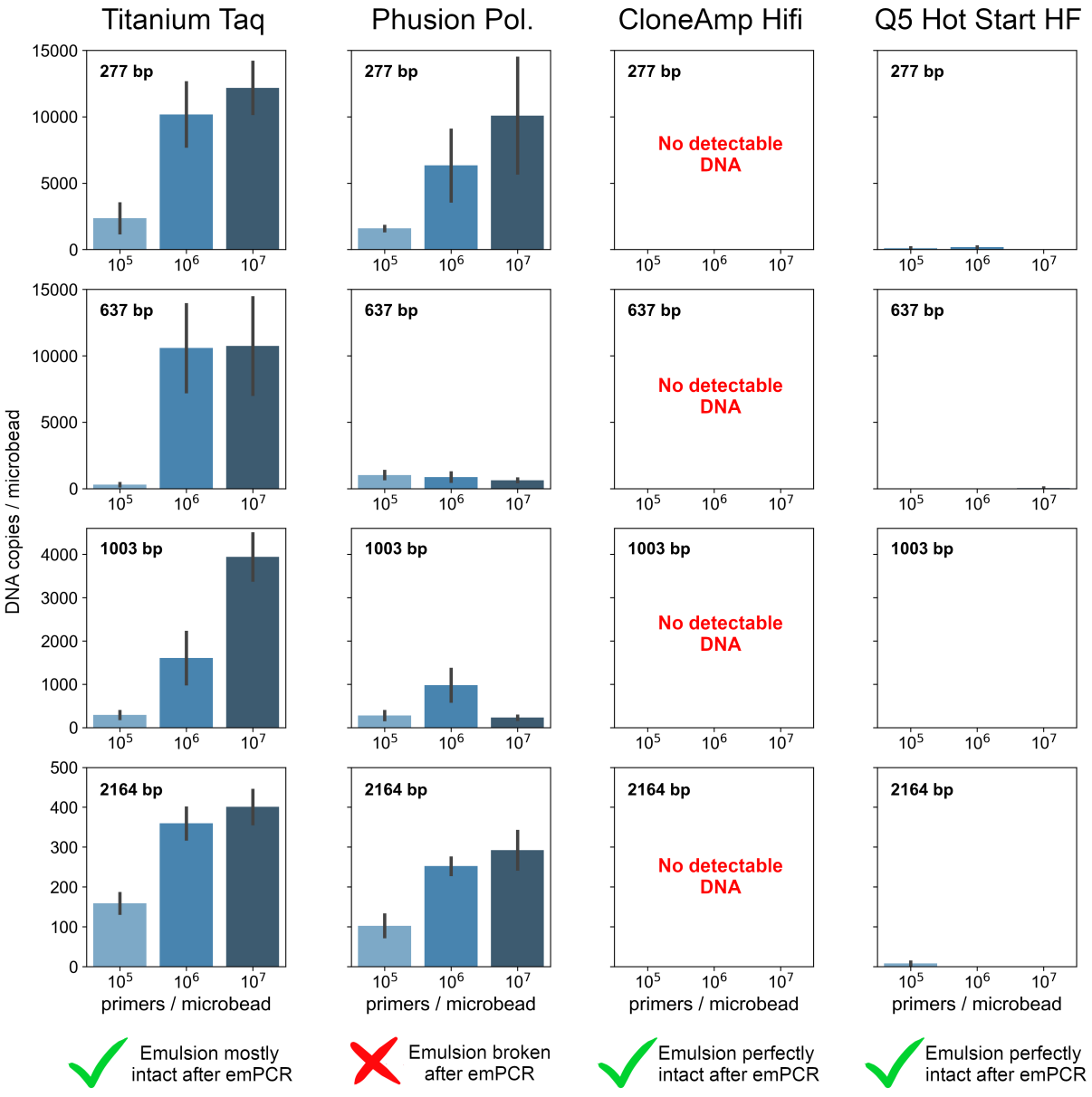

Figure 3.6: Effect of the microbead-bound primer concentration and DNA polymerase formulations on the on-bead emPCR efficiency. Figure legend continued on the next page.

Figure 3.6: Effect of the microbead-bound primer concentration and DNA polymerase formulations on on-bead emPCR efficiency. The on-bead emPCR efficacies were compared using 2.5 X Titanium Taq in Titanium Taq buffer, 2.5 X Phusion polymerase in HF-Buffer, CloneAmp Hifi premix and Q5 Hot Start High-Fidelity premix. For each condition, four different DNA templates were compared with nucleotide lengths as indicated in the upper left corner of the bar charts (277 bp, 637 bp, 1,003 bp and 2,164 bp). For each DNA template and polymerase formulation, on-bead emPCR was performed with microbeads harbouring 10^5, 10^6 and 10^7 primers/microbead. 1.7 x 10^7 molecules of input template DNA and 10^6 microbeads were used in each reaction. In addition, the stability of the emulsions after on-bead emPCR was evaluated and is indicated at the bottom of the columns.
qPCR was always performed in triplicates (n=3, mean±sd).

---

at the sides of the tube. Therefore, the determined DNA copies/microbead for the Phusion-based emPCR, as stated in Figure 3.6, have to be considered as irreliable, as compartmentalization was not provided throughout the emPCR. Conversely, the emPCR formulations based on the CloneAmp Hifi premix and Q5 Hot Start High-Fidelity premix presented astounding stability, unscathed by the PCR's temperature cycles. Furthermore, compartment volumes were on par to those of the Titanium Taq-based emPCR formulations. But unfortunately, no or barely any amplification of the DNA could be detected for the CloneAmp Hifi premix or the Q5 Hot Start High-Fidelity premix formulation. In all conditions, qPCR revealed either the total absence of any DNA or merely a miniscule amount of DNA.
The only viable formulation was based on the Titanium Taq product. In this case, the emulsions were mostly intact after PCR with but a negligible fraction of the microbeads escaping the emulsions. Here, increasing the amount of primers coupled to the microbeads, achieved dramatic increases in on-bead template amplification for all template lengths (see Figure 3.6, first column). For the shorter templates (277 bp and 637 bp), an amplification saturation was reached at around 10,000 DNA copies/microbead after on-bead emPCR, which was achieved by both 10^6 and 10^7 primers/microbead. The additional increase of primer concentration to 10^7 primers/microbead did not yield an additional increase in amplification in comparison to 10^6 primers/microbead. Furthermore, the larger DNA templates (1,003 bp and 2,164 bp) were also successfully amplified by on-bead emPCR based on the Titanium Taq product, albeit less efficiently. With the 1,003 bp template, an amplification of up to 4,000 copies/microbead was achieved using 10^7 primers/microbead. Unexpectedly, even the longest, 2,164 bp template was successfully amplified, albeit saturation was reached

at 400 copies/microbead. Nevertheless, this might still be sufficient for PACMAN, enabling introduction of library constructs approaching 70 kDa to future PACMAN selections.

In conclusion, considering the Titanium Taq-based on-bead emPCR, IVC compartment volumes and microbead-bound primer concentrations represented the most crucial parameters influencing on-bead emPCR success and efficiency. Tightly controlling the compartment volumes to larger volumes towards the vicinity of 3 pL, by adjusting vortexer settings, presented the best option for successful on-bead emPCR including DNA templates with up to 2,164 bp in length. The sweet-spot of primer concentration bound to microbeads was found to be 10^6 primers/microbead, efficacies did not benefit beyond that and amplification was saturated. Further increases in primer concentration might in contrast adversely induce sterical hindrance by crowding the microbead's surface, potentially impeding downstream applications.

3.2.4 Compartmentalized *in vitro* transcription and translation after on-bead emPCR

After on-bead emPCR, the successful amplification of templates was further confirmed by subsequent IVTT activity assays. Therefore, microbeads were decorated with TEV-target peptides and subsequently with DNA encoding a TEV-protease expression cassette was attached via on-bead emPCR, as described in the previous section. Subsequently, the microbeads were subjected to purified TEV-protease or IVC IVTT. In IVC IVTT, the microbead-attached TEV-protease-coding DNA was *in vitro* expressed in emulsions and incubated for 4 hours. Subsequently, the microbeads were harvested and analyzed by flow cytometry. IVC IVTT activity was compared between two emulsion formulations: One prepared with Abil EM 90 and the other with FluoSurf. As can be appreciated from Figure 3.7 a, in both IVC IVTT preparations, TEV-protease was successfully expressed as evidenced by cleavage of the microbead-bound TEV-target peptides, which was detected as a reduction of Cy5- and an increase of 5-FAM fluorescence across the whole microbead population as compared to control microbeads. Albeit, in both IVC IVTT preparations, the degree of TEV-target peptide cleavage was less efficient than that achieved by purified TEV-protease. IVC IVTT performed using Abil EM 90-based emulsions yielded slightly more efficient TEV-target cleavage as compared to FluoSurf-based IVC IVTT. Nevertheless, despite the slightly reduced TEV-protease activity achieved in FluoSurf-based IVC IVTT, it was still anticipated to be sufficient for the purpose of proving the feasibility of the PACMAN concept with TEV-protease as a model system. FluoSurf-based emulsions provided another benefit by reducing the amount of consumed IVTT solution, as merely 18 µl were used per emulsion preparation as compared to 50 µl in

Abil EM 90-based IVC IVTT. Albeit, it has to be noted, that a single FluoSurf-based IVC IVTT reaction could only accomodate for up to 10^6 microbeads, whereas a single Abil EM 90-based IVC IVTT reaction could accomodate for up to 4 x 10^6 microbeads. Therefore, for large-scale selections of antibodies, Abil-based IVC IVTT would be favored, as more microbeads could be used as input in relation to the consumed amount of IVTT solution.

In the afforementioned experiment, on-bead emPCR was performed with 1.7 x 10^7 molecules of template DNA per reaction (as suggested by Diamante *et al.* [258]). But, this concentration of DNA apparently saturated the emulsion droplets with template DNA, which was evident by the fact that virtually the whole microbead population appeared positive for TEV-protease-encoding DNA in IVC IVTT (as evidenced by the homogeneous reduction in Cy5 and increase in 5-FAM fluorescence throughout the entire microbead population after IVC IVTT, see Figure 3.7 a, orange populations). Consequently, assuming Poisson distribution probabilities, most microbeads must have been polyclonal, due to their emulsion compartment containing more than one DNA molecule. Hence, in a library screening experiment most microbeads would have displayed more than one library member under these conditions. Therefore, it was necessary to determine and evaluate the input DNA template concentration that would result in optimized monoclonality.

3.2.5 Assessment and optimization of monoclonality after on-bead emPCR

To be able to screen complex DNA libraries with PACMAN, it was necessary to ensure proper monoclonality of microbeads after on-bead emPCR to not contaminate the PACMAN selection output by having multiple library members presented on a single microbead. The DNA of library members is supplied to on-bead emPCR droplets in a Poisson distributed fashion, therefore the amount of input DNA used in on-bead emPCR had to be optimized to hit the probabilistic likelyhood in which single DNA occupation of droplets dominates. The empirical determination of the degree of monoclonality achieved using a specific amount of input DNA supplied to on-bead emPCR was performed by assessing the total fraction of microbeads, which were detected to excert TEV-protease activity in IVC IVTT experiments after on-bead emPCR as a function of the initially supplied amount of TEV-protease-encoding template DNA. Using the fraction of microbeads that evoked TEV-protease activity in IVC IVTT after on-bead emPCR (i.e. the fraction of microbeads which must have coincided with at least one molecule of TEV-protease-encoding DNA during on-bead emPCR), the percentage of microbeads that coincided with zero, one or more than one DNA templates during on-bead emPCR was derived using Poisson estimations. Using this workaround, the degree of monoclonality achieved by on-bead emPCR could be estimated simply from the subsequently

evoked activity by the microbeads. In general, according to evaluation of Poisson distributions (see Figure 3.7 b) a favorable degree of monoclonality is achieved when roughly two-thirds of the microbeads end up containing DNA after on-bead emPCR, which would derive to approximately 30% of microbeads being polyclonal, displaying more than one DNA template (i.e. they were encapsulated with more than one DNA template during on-bead emPCR), while 37% display exactly one DNA template and are therefore considered monoclonal (i.e. they were encapsulated with exactly one DNA template during on-bead emPCR)(see Figure 3.7 b). This distribution would be especially favorable for early PACMAN selection cycles, as it presents a sweet spot providing the largest total fraction of monoclonal microbeads. Nevertheless, for later selection cycles it would be beneficial to incrementally reduce the amount of input DNA templates to further reduce the fraction of polyclonal microbeads, albeit, consequently sacrificing on the total amount of microbeads that display any DNA.

To investigate the optimal amount of input DNA templates, three incremental amounts of DNA were evaluated as on-bead emPCR inputs and subsequently the microbeads were analyzed for TEV-protease activity evoked in IVC IVTT. 10^6 microbeads were used for each on-bead emPCR reaction and 1.7 x 10^7 (as reported by Diamante *et al.* [258]), 1.7 x 10^6 and 1.7 x 10^5 molecules of DNA containing a TEV-protease expression cassette were used as inputs (see Figure 3.7 c). An evaluation of the results using Poisson distributions to derive details on the achieved clonality are listed in Table 3.1.
With the amount of input DNA suggested by Diamante *et al.* [258], 1.7 x 10^7 molecules per reaction, the majority of microbeads (90.3%) subsequently evoked TEV-protease activity in IVC IVTT, which indicated an over-saturation of the IVC compartments with input DNA. In that case, most microbeads (67.7%) were estimated to have been polyclonal and merely 22.6% to have been monoclonal. For PACMAN selections, less input DNA would be favored to achieve the targeted two-thirds of microbeads obtaining DNA via on-bead emPCR. With 1.7 x 10^6 molecules of input DNA the fraction of microbeads that evoked TEV-protease activity in IVC IVTT was already below the two-thirds mark with 51.7%, which corresponded to 35.2% of the microbeads having been monoclonal and 16.5% having been polyclonal. Therefore, for the first few cycles of PACMAN selections, an amount of input DNA slightly above 1.7 x 10^6 would be desirable. Finally, 1.7 x 10^5 molecules of input DNA were evaluated which demarced the lower end of the evaluated input amounts. Here, merely a total of 13.7% of the microbeads evoked TEV-protease activity in IVC IVTT, but virtually all of the microbeads were monoclonal with a total of 12.7% and merely 1% polyclonal, but the rest did not harbor any DNA at all. This lower end of input DNA amount would represent a preferable amount in

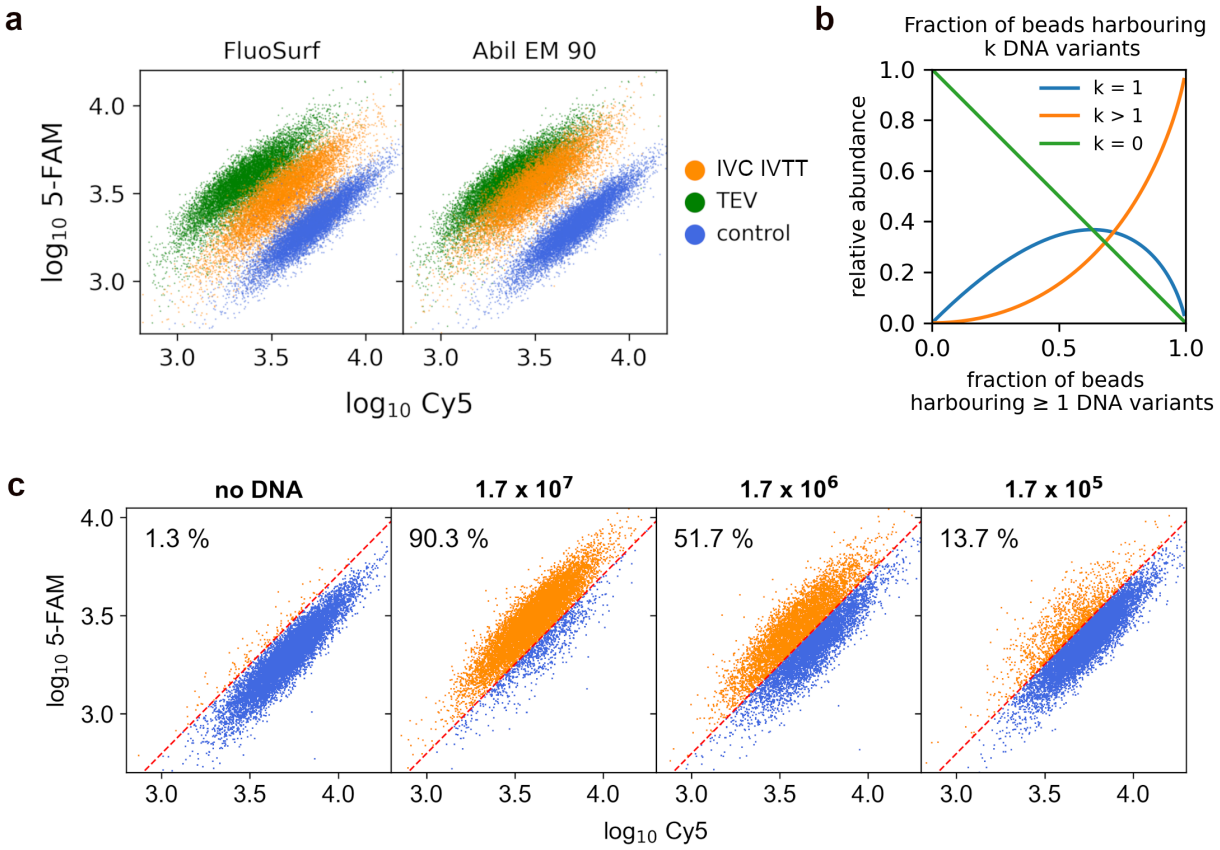

Figure 3.7: Activity-based evaluation of the degree of monoclonality after on-bead emPCR. a) flowcytometric analyses of microbeads after IVC IVTT after on-bead emPCR with template DNA containing a TEV-protease expression cassette. Microbeads were decorated with 10^6 TEV-target peptides/microbead in addition to the primers necessary for on-bead emPCR. TEV-protease activity evoked in IVC IVTT was compared in emulsions prepared with FluoSurf and Abil EM 90. As negative controls, microbeads without IVC IVTT treatment were analyzed and as positive controls microbeads were subjected to purified TEV-protease without IVC (labelled 'TEV'). b) Poisson equations describing the probabilistic likelihood of a microbead coinciding with 0, 1 or more than one library members as a function of the total microbeads coinciding with $\geq$ library members. c) On-bead emPCR was performed with different amounts of input DNA (amount stated above each dot plot) with microbeads harbouring 10^6 TEV-target peptides/microbead. Subsequently, microbeads were subjected to IVC IVTT using FluoSurf-based emulsions. Microbeads were analyzed via flow cytometry and results were plotted as dot plots. The percentage of microbeads with cleaved TEV-target peptides is given in the upper left corner (orange dots).

Table 3.1: Degrees of monoclonality and polyclonality achieved by on-bead emPCR depending on the amount of input DNA. Evaluation of the data from Figure 3.7 c using the Poisson distributions shown in Figure 3.7 b. Listed are always the fractions from the total of microbeads analyzed.

Molecules of input DNA	1.7×10^7	1.7×10^6	1.7×10^5
Fraction of TEV-protease-positive microbeads (microbeads that obtained more than zero DNA templates during on-bead emPCR)	0.903	0.517	0.137
Fraction of monoclonal microbeads	0.226	0.352	0.127
Fraction of polyclonal microbeads	0.677	0.165	0.010

late-stage PACMAN cycles, to assure monoclonality and suppress cross-contaminations by polyclonality in favor of stringency of the selection.

In literature, insights into on-bead emPCR efficacies and also monoclonality evaluations have often been obtained via staining of the microbead-bound DNA with DNA dyes or by annealing sequence-specific fluorescent oligonucleotide probes and subsequent analysis of DNA-bearing microbeads via flow cytometry [295–297]. Unfortunately, as opposed to the claims in literature, here it was not possible to determine the DNA load or monoclonality of microbeads after on-bead emPCR via staining of the generated DNA via DNA dyes (GelGreen, GelRed and SYBR green have been assessed without success) nor by annealing of site-specific fluorescently labeled oligonucleotide probes (PROBE-FITC-488-T7p, PROBE-ATTO490LS-T7TERM). It was possible, however, to stain defined ladder microbeads decorated with 10^2–10^6 biotinylated DNA molecules/microbead with DNA stains and subsequently detect correlating fluorescences via flow cytometry. Unfortunately, blank microbeads also adsorbed a considerable amount of the DNA stains leading to excessive background fluorescence. Furthermore, microbeads after on-bead emPCR always appeared homogeneously stained irrespective of the amount of applied input DNA. Under low input DNA conditions, only a fraction of the microbeads should have received DNA via on-bead emPCR while the majority should have remained blank and therefore unstained, but also here, all microbeads were homogeneously stained by the DNA dyes, suggesting that the microbeads were somehow chemically modified during the on-bead emPCR process leading to increased unspecific binding of the DNA stains. Consequently, a distinction of microbead populations was not possible, neither with DNA stains nor with fluorescent oligonucleotide probes (see Figure A.1). The situtation was even worse with fluorescent oligonucleotide probes, as not even a distinction between the microbeads of the clearly defined ladder standards was possible. Therefore, I do not recommend the use of these detection methods for assessment of

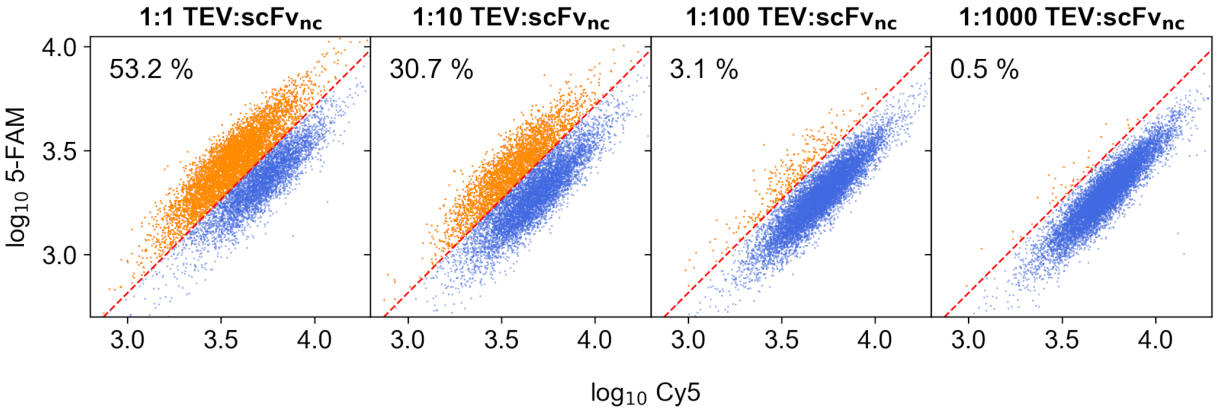

Figure 3.8: Emulated PACMAN selections with incremental dilutions of TEV-protease-encoding DNA with irrelevant DNA. Flowcytometric analyses of emulated PACMAN experiments with different ratios of TEV-protease:scFv$_{nc}$-encoding template DNAs. This experiment was intended to provide an impression of how a successful enrichment using PACMAN would present itself in flow cytometry.

DNA load or monoclonality when evaluating on-bead emPCR protocols.

3.2.6 Proof-of-principle of PACMAN

The proof-of-principle of PACMAN was obtained by recovering TEV-protease-encoding DNA from a dilute mixture with irrelevant DNA of similar nucleotide length (a random scFv, termed scFv$_{nc}$). First, to obtain a visual representation of how successful enrichments via PACMAN might appear in flow cytometry, different input DNA mixture ratios of active and inactive DNA variants were assessed in PACMAN experiments. PACMAN was performed with a 1:1, 1:10, 1:100 and a 1:1000 mixture of TEV-protease:scFv$_{nc}$-encoding template DNAs (see Figure 3.8). For these emulated PACMAN selection cycles, 10^6 microbeads were used for each reaction and they were decorated with 10^6 TEV-target peptides/microbead and on-bead emPCR was performed with 4 x 10^6 molecules of input template DNA from the indicated DNA mixtures. Subsequently, IVC IVTT was performed and microbeads were analyzed via flow cytometry.

As expected, the percentage of TEV-protease-positive microbeads, correlated with the ratio of the input DNA mixtures. In the 1:1 mixture 53.2% of the microbeads were classified as TEV-protease-positive and the percentage successively dropped to 0.5% for the 1:1000 mixture.

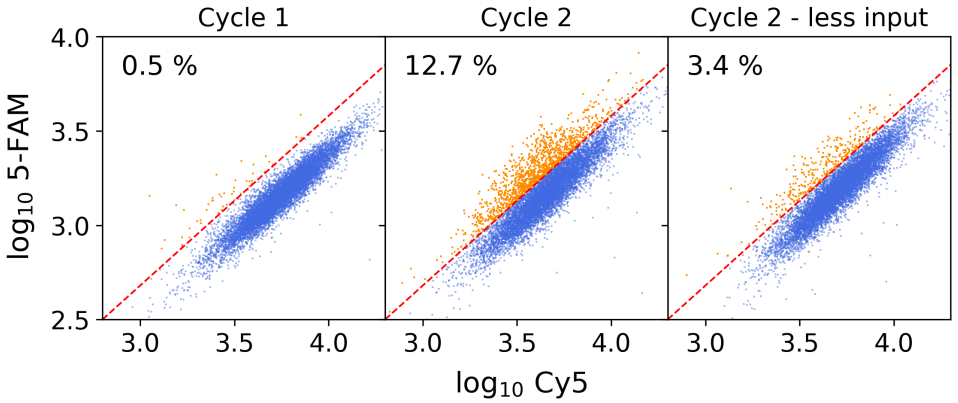

Input DNA DNA molecules per 10^6 beads	$4x10^6$	$4x10^6$	$1x10^6$
Sort gate	0.5%	1.5%	1.1%
Colonie PCR ratio of TEV to $scFv_{nc}$	12 to 36	42 to 11	98 to 0
Cumulative enrichment	333-fold	3,800-fold	≥98,000-fold

Figure 3.9: Recovery and amplification of TEV-protease-encoding DNA using PACMAN. In merely two cycles of PACMAN TEV-protease-encoding DNA was enriched at least 98,000-fold from an initial 1:1000 mixture of TEV-protease:$scFv_{nc}$-encoding DNA, respectively. The dot-plots show the FACS data of each PACMAN cycle and the bottom table lists the respective details and outcomes of each cycle.

Finally, the feasibility of the PACMAN method was verified by sequential enrichment of TEV-protease-encoding DNA via PACMAN from a dilute initial DNA mixture. Therefore, microbeads which were subjected to PACMAN with an initial 1:1000 TEV-protease:$scFv_{nc}$-encoding DNA mixture as input, were subsequently sorted via FACS (see Figure 3.9). A sort gate was defined to capture the upper most 0.5% of microbeads, which shifted towards the low-Cy5 and high-5-FAM fluorescence area (i.e. the area of microbeads with cleaved TEV-target peptides, which were thereby classified as TEV-protease-positive). 1,000 of these microbeads were collected and subsequently the microbead-attached DNA was reamplified by PCR. For a subsequent enrichment assessment, the reamplified DNA was subcloned into

pIgV plasmids and transformed into *E.coli*. Colony PCR with gene specific primers was applied to determine the TEV-protease:scFv$_{nc}$-encoding DNA ratios of the recovered DNA. After a single PACMAN selection cycle, the resulting ratio of TEV-protease:scFv$_{nc}$-encoding DNA was shifted from the initial 1:1000 to 1:3, which corresponded to a 333-fold enrichment of TEV-protease-encoding DNA (see Figure 3.9 first column).
The reamplified DNA from the first PACMAN cycle was further subjected to another PACMAN cycle. In comparison, it was evaluated whether an increase in stringency, by reducing the amount of input DNA, could increase the selection specificity and hence enhance the cumulative enrichment of TEV-protease-encoding DNA. In the less stringent second PACMAN cycle, again 4 x 10^6 molecules of DNA served as input for the on-bead emPCR, whereas in the more stringent second PACMAN cycle only 1 x 10^6 molecules were applied. After the second PACMAN cycles, the respective amplification of TEV-protease-coding DNA was again evaluated by colony PCR. With the less stringent setup, a cumulative enrichment of 3.800-fold was achieved (see Figure 3.9 second column). Interestingly, this was far surpassed by the more stringent setup which achieved a cumulative enrichment of at least 98,000-fold. In fact, not a single colony was found containing the negative scFv$_{nc}$-encoding DNA after the more stringent second PACMAN cycle (see Figure 3.9 third column).

With this, the proof-of-principle of PACMAN was demonstrated.

3.3 Proteolytic degradation of amyloids by polyclonal IgM isolated from human plasma

To assess the presence of natural proteolytic antibodies in human plasma and thereby evaluate the viability of my endeavor to isolate proteolytic, combinatorial single-chain anti-Aβ antibodies from the human antibody repertoire, polyclonal IgG- and IgM-class antibodies were isolated from human plasma. IgG-class antibodies were isolated via affinity chromatography with Protein A-conjugated agarose resin (see Figure 3.10 a) and IgM-class antibodies were isolated from the IgG-depleted plasma flow-through of the Protein A chromatography using a series of further chromatographies: Gravity flow with LigaTrap Human IgM resin (see Figure 3.10 b), size exclusion chromatography (SEC) using a Superdex 200 10/300 column (see Figure A.3) and finally by gravity flow with CaptureSelect Human IgM resin (see Figure 3.10 c).

According to Taguchi *et al.* [229], human IgG preparations excert little proteolytic activity, if any. But polyclonal IgM preparations were shown to excert prominent proteolytic

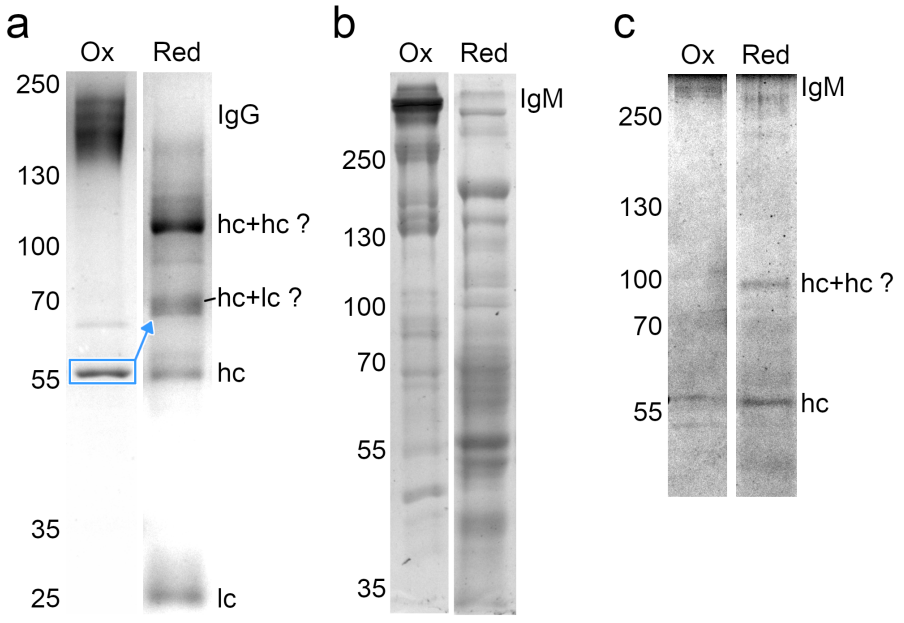

Figure 3.10: Purification of polyclonal IgG and IgM from human plasma. SDS-Page analyses of a) a representative Protein A purified IgG preparation. First lane, non-reduced (Ox), second lane reduced (Red). Three prominent bands were visible in the non-reduced sample between 130 and 250 kDa which were attributed to IgG1, IgG2 and IgG3. Another prominent band was visible at 57 kDa, which was attributed to human serum albumin (HSA) contamination. The apparent molecular weight of non-reduced HSA of approximately 57 kDa (blue square), shifted to 68 kDa upon reduction (blue arrow). In the reduced sample, IgG dissociated into individual light- and heavy-chains as well as partially reduced heavy- and light-chain complexes as well as dimeric heavy-chain complexes. b) Equivalent representation as in a), but for a representative IgM sample purified via gravity flow chromatography with LigaTrap Human IgM resin. As feed, the IgG-depleted flow-through of the gravity flow chromatography using Protein A-functionalized agarose resin was used. In the non-reduced sample (ox) prominent band clusters of IgM, dimeric Igs (IgA) and IgG1 IgG2 and IgG3 were detected, from top to bottom until 130 kDa. Below 130 kDa several bands of contaminating proteins were detected. In the reduced sample (Red) most of the bands attributed to IgM, IgA and IgG dissociated into their individual chains, albeit some residual bands were still detectable at the size of intact IgM, which might either represent insufficiently reduced IgM or some other high molecular weight contaminants. c) a representative IgM preparation after gravity flow with LigaTrap Human IgM resin followed by size exclusion chromatography with a Superdex 200 10/300 column and gravity flow with CaptureSelect Human IgM resin. In the non-reduced sample only IgM and residual HSA was detected. In the reduced sample, dissociated heavy-chains were detected, as well as a putative dimeric heavy-chain complex.

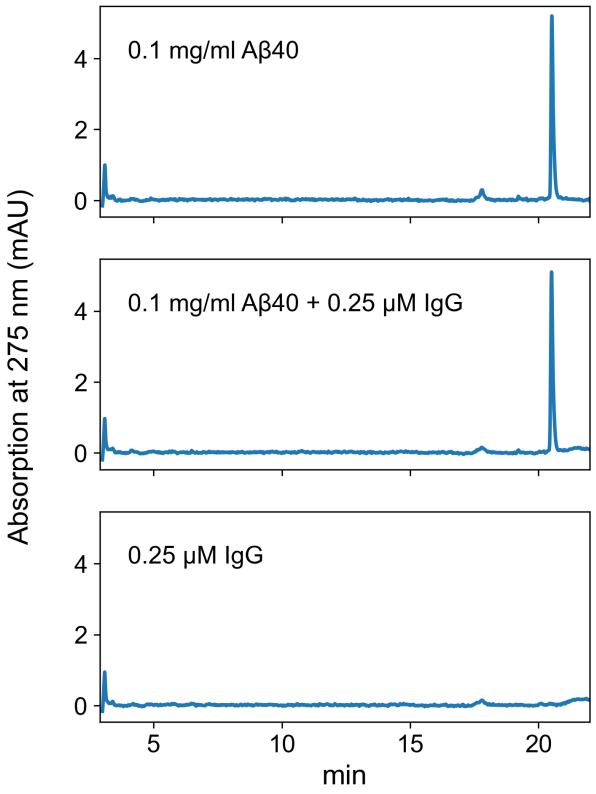

Figure 3.11: Proteolytic digestion of $A\beta_{40}$ by polyclonal IgG purified by gravity flow chromatography with Protein A-functionalized agarose resin. The tips of 0.5 ml low-bind reaction tubes were cut off and placed flush into 2 ml glass vials for HPLC so that it was still possible to seal the glass vials with septed screw caps. These reaction vessels were able to hold 50 µl reaction volumes. Samples contained 0.1 mg/ml $A\beta_{40}$ and 0.25 µM polyclonal IgG in a total volume of 50 µl in 1x PBS. Samples were incubated quiescently at 37°C for 96 hours. Afterwards, samples were analyzed by reverse-phase HPLC using a Zorbax 300SB-C8 4.6x250 mm column on a linear gradient of 0–80% ACN 0.1% TFA over 40 minutes. Digestion profiles of IgG preparations of four different donors presented identical chromatography profiles. One of these profiles is shown in the second panel. First panel, 0.1 mg/ml $A\beta_{40}$ control. Third panel, 0.25 µM polyclonal IgG control.

activity against Aβ. To confirm these findings, Protein A-purified IgG from plasma of four human donors was evaluated for their proteolytic activity against Aβ. Therefore, 0.1 mg/ml $A\beta_{40}$ was coincubated quiescently with 0.25 µM polyclonal IgG for 96 hours at 37°C. Proteolysis products were analyzed via reverse-phase HPLC (see Figure 3.11). But as expected, the peak profile of untreated $A\beta_{40}$ was identical to IgG-treated samples of all four donors, suggesting the absence of any proteolytic anti-Aβ activity excerted by IgG.

Confirmation of proteolytic anti-Aβ activity excerted by polyclonal IgM from human

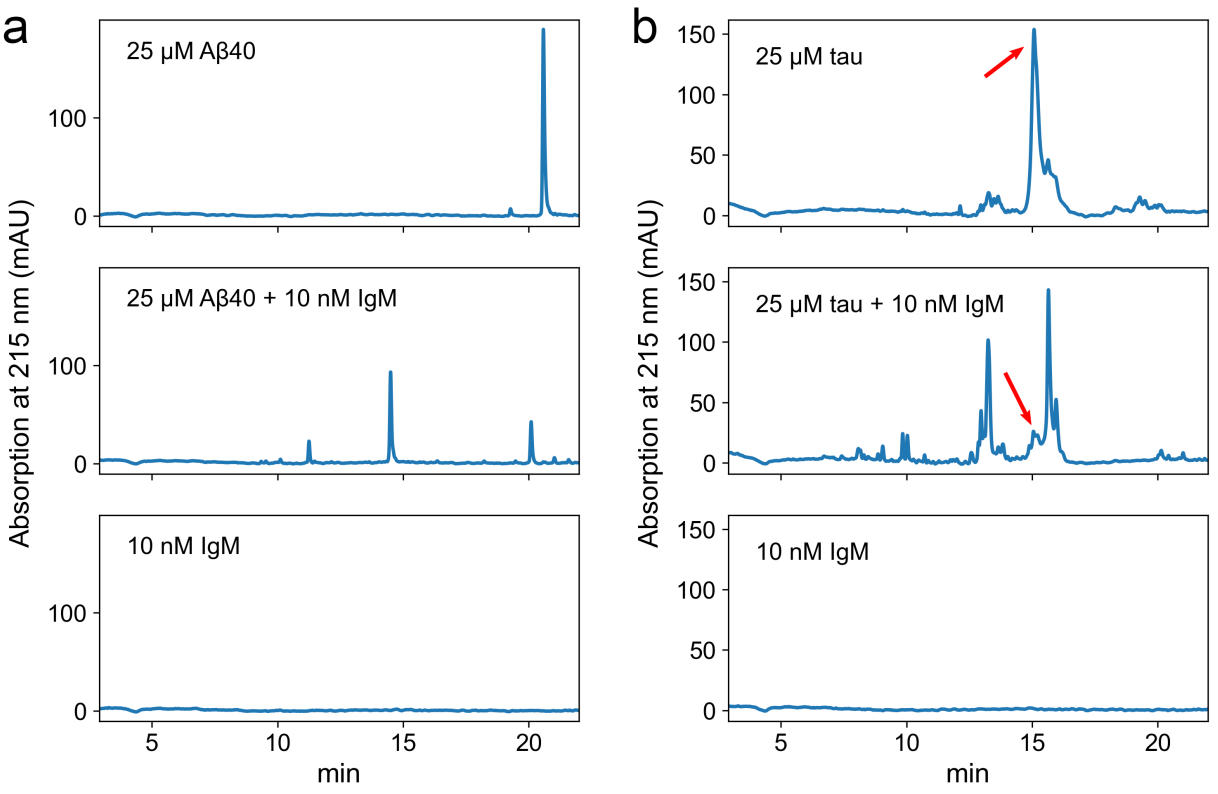

Figure 3.12: Proteolytic digestion of $A\beta_{40}$ and Tau protein by extensively purified polyclonal IgM. The tips of 0.5 ml low-bind reaction tubes were cut off and placed flush into 2 ml glass vials for HPLC so that it was still possible to seal the glass vials with septed screw caps. These reaction vessels were able to hold 50 µl reaction volumes. 25 µM $A\beta_{40}$ (a) as well as 25 µM Tau protein (b) were individually coincubated with 10 nM polyclonal IgM in 1x PBS. Additionally, as controls, 10 nM IgM alone and 25 µM $A\beta_{40}$ alone, as well as, 25 µM Tau protein alone were assessed. Samples were incubated quiescently at 37°C for 96 hours. Afterwards, samples were analyzed by reverse-phase HPLC using a Zorbax 300SB-C8 4.6x250 mm column on a linear gradient of 0–80% ACN 0.1% TFA over 40 minutes. The red arrows in b indicate the peaks of full-length 441 aa Tau protein.

plasma was initially impeded by persistent impurities in the IgM preparations. The IgG-depleted flow-through of the Protein A gravity flow chromatography was first subjected to another gravity flow chromatography using LigaTrap Human IgM resin, but SDS-Page analyses revealed a host of impurities (see Figure 3.10 b). Under non-reducing conditions, the most prominent bands at the very top of the gel were attributed to IgM. Another cluster of bands slightly above 250 kDa and three bands between 130–180 kDa were attributed to IgA and IgG (IgG1, IgG2 and IgG3), respectively. Apart from the Ig impurities a plethora of additional bands was found on the SDS-Page indicative for a poor specificity of the LigaTrap Human IgM resin. To further optimize the purity, a size exclusion chromatography (SEC) was performed using a Superdex 200 10/300 column (the SEC was performed by Anne Pfitzer).

Individually collected fractions were analyzed by SDS-Page (see Figure A.2). The first fraction, that contained protein (fraction 4), was picked for evaluation of proteolytic activity against Aβ, as the expected 900 kDa IgM antibodies would elute within the first fractions. In fact, the Superdex 200 10/300 column was admittedly not well suited for this preparation, as its separation range was maxed out at 600 kDa. Consequently, all proteins larger than 600 kDa eluted in the void volume including the IgM antibodies. Nevertheless, the proteolytic anti-Aβ activity of IgM from fraction 4 was assessed similarly to that of the IgG preparations. 0.1 mg/ml $A\beta_{40}$ was quiescently coincubated with 50 nM of the IgM from fraction 4 for 96 hours at 37°C. Reverse-phase HPLC analyses revealed degradation of $A\beta_{40}$, albeit a surprisingly early elution of the proteolytic products was detected, which was unfortunately suggestive for single amino acids or small di- or tripeptides. This was indicative for promiscuous aminopeptidase activity excerted by the IgM preparation and not the anticipated specific proteolytic anti-Aβ activity as proposed by literature [229], which would have generated distinct $A\beta_{1\text{-}16}$, $A\beta_{1\text{-}28}$ and $A\beta_{29\text{-}40}$ fragments.

As protease or peptidase contaminations were evident in the IgM preparations after LigaTrap followed by SEC, all size exclusion chromatography fractions that contained IgM, but no monovalent Igs (in the depicted example, fractions 4–12 as seen in Figure A.2) were combined and subjected to gravity flow chromatography with CatureSelect Human IgM resin. This resin promised to yield the most specific purification, as the resin was functionalized with anti-IgM antibodies. In the end, the entire purification procedure concluded in a major loss of total recovered IgM, but SDS-Page analyses of the final products suggested high purity (see Figure 3.10 c). To evaluate the proteolytic activity excerted against Aβ, 25 µM $A\beta_{40}$ was quiescently coincubated with 10 nM IgM for 96 hours at 37°C and cleavage products were analyzed via reverse-phase HPLC (see Figure 3.12 a). Finally, digestion profiles identical to those described by Taguchi *et al.* [229] were detected, suggesting that Aβ was successfully cleaved by highly pure polyclonal IgM. To the best of my abilities, these IgM preparations might cautiously be claimed to be sufficiently pure to address the broader question about the extent of proteolytic activity and specificities excerted by IgM antibodies against further amyloids and other proteins and peptides.

Out of curiosity, purified Tau protein, another amyloidogenic peptide associated with Alzheimer's Disease, was subjected to the highly purified polyclonal IgM to assess the possibility of the presence of proteolytic anti-Tau antibodies in the human antibody repertoire. Surprisingly, Tau was readily digested (see Figure 3.12 b). Several additional degradation products were detected in the IgM-treated Tau protein samples and full-length Tau was depleted. In future experiments, it would be interesting to evaluate the identity of these digestion products by LC-MS. Nevertheless, this finding might substantiate an unfolding opportunity, that

it might be possible to develop proteolyic combinatorial antibodies against a wider range of amyloid peptides beyond just Aβ.

In conclusion, IgM isolation was critically dependent on anti-IgM antibody-functionalized resin purification to ascertain purities and results equivalent to those provided by literature. Nevertheless, due to the persistent difficulties in IgM purification, it remains uncertain and leaves room for speculation, whether the observed proteolytic anti-Aβ and anti-Tau activity seen in the above mentioned experiments, as well as those described in literature, faithfully represent the action of IgM or whether some trace contaminations with other proteases or peptidases might still remain responsible.

3.4 Antibody libraries

Plenty of combinatorial antibody libraries are commercially available. Most of these in ready-to-use formats for phage display applications derived from a wide variety of species. Unfortunately, the availability of commercial, naive human antibody libraries is limited. Furthermore, the format of the available libraries is not readily suitable for IVTT experiments. Therefore, I sought out to develop naive human antibody libraries that comply to the needs of PACMAN and may provide an optimized foundation to allow the isolation of proteolytic antibodies against amyloid targets.

3.4.1 Considerations on the antibody formats included in the libraries

PACMAN is dependent on each library member being encoded in just a single DNA template and they may not exceed 2 kb in length. Combinatorial single-chain antibody formats have been thoroughly investigated with single-chain variable fragments (scFv) being the most reknown, which consist of a heavy- and a light-chain-derived Fv connected via a glycine-serine linker. Another well-known antibody format is the single-domain antibody (sdAb), also known as nanobody. These consist of a single heavy- or light-chain-derived Fv. Unfortunately, human-derived nanobodies are notoriously aggregation prone and just rarely soluble and functional. Nevertheless, in the field of proteolytic antibody research, reports about superior catalytic activity exhibited by human-derived nanobodies exist [230]. Furthermore, a non-physiological single-chain antibody consisting of two lambda light-chain Fvs has been isolated that by far exceeded the catalytic activity of IgM against Aβ [230]. Hence, for PACMAN, two antibody library formats appeared promising: First, an scFv library with deliberate inclusion of non-physiological $IgVL_2$ and $IgVH_2$ constructs alongside with the

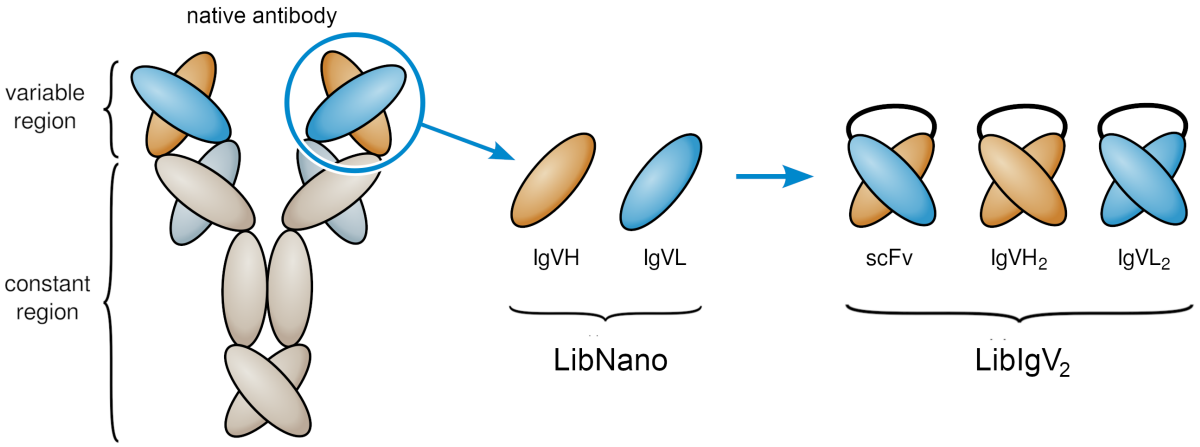

Figure 3.13: Antibody formats included in the antibody libraries. The antibody formats included in the antibody libraries LibNano and LibIgV_2 were derived from the variable regions (Fvs) of full-length antibodies of all classes (IgM, IgG, IgD, IgA, IgE). In the LibNano library, the Fvs of the heavy-chains (IgVH) and light-chains (IgVL) were included as single-domain antibodies (sdAbs), also called nanobodies, without further modification. In the LibIgV_2 library, Fvs were randomly conjoint via a $(G_4S)_4$ linker yielding physiological heterodimers (scFvs) and non-physiological homodimers ($IgVH_2$, $IgVL_2$)

usual scFv format. Second, a nanobody library that includes heavy- and light-chain-derived sdAbs. The conceptual derivation scheme of these two antibody formats can be reviewed in Figure 3.13.

Another benefit associated with the utilization of scFv and nanobody formats, as opposed to full-length antibodies, is the elimination of the proinflammatory aspect associated with their Fc domain, which has been linked to adverse effects in clinical studies (see Figure 1.4). Furthermore, the small size of scFvs and nanobodies facilitates elevated uptake across the BBB, which might later be further increased by attachment of cell-penetrating peptide sequences to the single-chain antibodies. Admittedly, an unfortunate disadvantage of scFvs and nanobodies is their short half-life in circulation, which might limit the duration of exposure of patients and thereby limit the effectiveness of any derived drug, albeit this aspect might later be addressed by pegylation or similar efforts to extent the half-life of the single-chain antibodies in the blood stream.

3.4.2 Assembly of the antibody libraries

In this study, two antibody libraries were derived from ten naive human buffy coats. A schematic overview of the library assembly process can be reviewed in Figure 3.14. Shortly, peripheral blood mononuclear cells (PBMCs) were harvested from buffy coats by Ficoll-paque

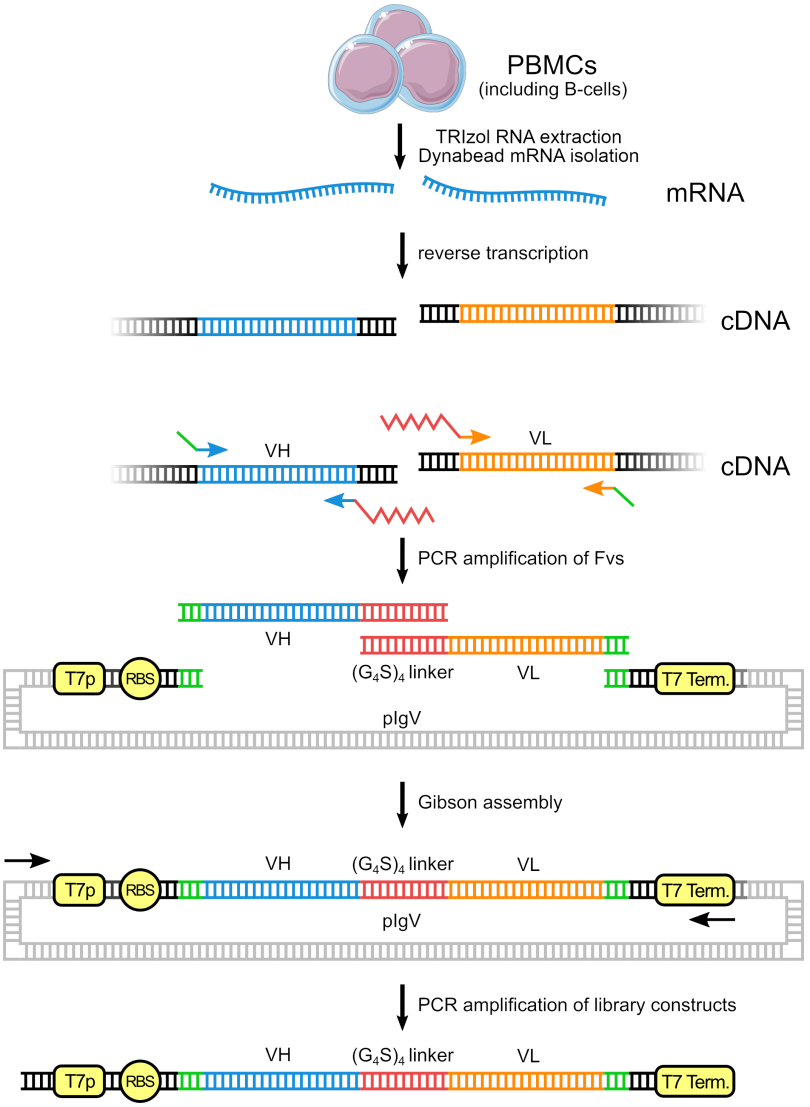

Figure 3.14: Cloning scheme of the antibody libraries. PBMCs were isolated from human blood donations using Ficoll-Paque density gradient centrifugation. PBMCs contain lymphocytes including mature B-cells, which express mature antibodies after somatic recombination. mRNA was isolated from PBMCs and converted to cDNA via reverse transcription. Using sequence specific primers, which included degenerate nucleotides, the Fvs of all antibody germline families were amplified. The primers further introduced overlaps with the pIgV plasmid or the necessary sequences for a $(G_4S)_4$ linker. Gibson assembly was used to join the homologous sequences of the Fv-amplicons and a linearized pIgV plasmid. Via introduction into the pIgV plasmid, a T7 promotor, a ribosome binding site and a T7 terminator were added, which was necessary for IVTT. Finally, the library was finalized into a format suitable for PACMAN via PCR with a forward primer that binds upstream of the T7 promoter and a reverse primer that includes the T7 terminator. T7p, T7 promotor, RBS, ribosome binding site, T7 Term., T7 terminator.
PBMC sprites were adapted from Servier Medical Art. Servier Medical Art by Servier is licensed under a Creative Commons Attribution 3.0 Unported License (https://creativecommons.org/licenses/by/3.0/).

Table 3.2: Fv amplification — primer groups and subgroups. The amplicons prepared with the ATG-V-Stop primer group encoded the Fvs, which were used to assemble the nanobody library: LibNano. The amplicons of the ATG-V-Link and Link-V-Stop primer group encoded the N-terminal and C-terminal Fvs, respectively, which were used to assemble the sinlge-chain dimeric Fv library: LibIgV_2. The subgroups (light grey) list the primers used for the amplification of each Fv family locus: heavy (VH), lambda (VL) and kappa (VK). In brackets, the optimized annealing temperatures of the primer combinations are stated that were used during the PCRs to amplify the Fv fragments.

ATG-V-Stop		**ATG-V-Link**		**Link-V-Stop**	
ATG-VH-Stop (65°C)		**ATG-VH-Link (65°C)**		**Link-VH-Stop (65°C)**	
fwd primers:	**rev primers:**	**fwd primers:**	**rev primers:**	**fwd primers:**	**rev primers:**
Vec-SalI-ATG-VH1/7-For	JH1_2_4_5-Vec-Rev	Vec-SalI-ATG-VH1/7-For	JH1_2_4_5-Rev-Link	Link-VH1/7-For	JH1_2_4_5-Vec-Rev
Vec-SalI-ATG-VH1-For	JH3_6-Vec-Rev	Vec-SalI-ATG-VH1-For	JH3_6-Rev-Link	Link-VH1-For	JH3_6-Vec-Rev
Vec-SalI-ATG-VH2-For		Vec-SalI-ATG-VH2-For		Link-VH2-For	
Vec-SalI-ATG-VH3_1-For		Vec-SalI-ATG-VH3_1-For		Link-VH3_1-For	
Vec-SalI-ATG-VH3_2-For		Vec-SalI-ATG-VH3_2-For		Link-VH3_2-For	
Vec-SalI-ATG-VH4_1-For		Vec-SalI-ATG-VH4_1-For		Link-VH4_1-For	
Vec-SalI-ATG-VH4_2-For		Vec-SalI-ATG-VH4_2-For		Link-VH4_2-For	
Vec-SalI-ATG-VH5-For		Vec-SalI-ATG-VH5-For		Link-VH5-For	
Vec-SalI-ATG-VH6-For		Vec-SalI-ATG-VH6-For		Link-VH6-For	
ATG-VL-Stop (60°C)		**ATG-VL-Link (60°C)**		**Link-VL-Stop (60°C)**	
fwd primers:	**rev primers:**	**fwd primers:**	**rev primers:**	**fwd primers:**	**rev primers:**
Vec-SalI-ATG-VL3-For	JL1-3-Vec-Rev	Vec-SalI-ATG-VL3-For	JL1-3-Rev-Link	Link-VL3-For	JL1-3-Vec-Rev
Vec-SalI-ATG-VL4ab-For	JL7-Vec-Rev	Vec-SalI-ATG-VL4ab-For	JL7-Rev-Link	Link-VL4ab-For	JL7-Vec-Rev
Vec-SalI-ATG-VL6-For		Vec-SalI-ATG-VL6-For		Link-VL6-For	
ATG-VL-Stop (65°C)		**ATG-VL-Link (65°C)**		**Link-VL-Stop (65°C)**	
fwd primers:	**rev primers:**	**fwd primers:**	**rev primers:**	**fwd primers:**	**rev primers:**
Vec-SalI-ATG-VL1-For	JL1-3-Vec-Rev	Vec-SalI-ATG-VL1-For	JL1-3-Rev-Link	Vec-SalI-ATG-VL1-For	JL1-3-Vec-Rev
Vec-SalI-ATG-VL2-For	JL7-Vec-Rev	Vec-SalI-ATG-VL2-For	JL7-Rev-Link	Vec-SalI-ATG-VL2-For	JL7-Vec-Rev
Vec-SalI-ATG-VL4c-For		Vec-SalI-ATG-VL4c-For		Vec-SalI-ATG-VL4c-For	
Vec-SalI-ATG-VL5-For		Vec-SalI-ATG-VL5-For		Vec-SalI-ATG-VL5-For	
Vec-SalI-ATG-VL7-For		Vec-SalI-ATG-VL7-For		Vec-SalI-ATG-VL7-For	
ATG-VK-Stop (62°C)		**ATG-VK-Link (62°C)**		**Link-VK-Stop (62°C)**	
fwd primers:	**rev primers:**	**fwd primers:**	**rev primers:**	**fwd primers:**	**rev primers:**
Vec-SalI-ATG-VK1-For	JK1-4-Vec-Rev	Vec-SalI-ATG-VK1-For	JK1-4-Rev-Link	Link-VK1-For	JK1-4-Vec-Rev
Vec-SalI-ATG-VK2-For	JK5-Vec-Rev	Vec-SalI-ATG-VK2-For	JK5-Rev-Link	Link-VK2-For	JK5-Vec-Rev
Vec-SalI-ATG-VK3-For		Vec-SalI-ATG-VK3-For		Link-VK3-For	
Vec-SalI-ATG-VK4-For		Vec-SalI-ATG-VK4-For		Link-VK4-For	
Vec-SalI-ATG-VK5-For		Vec-SalI-ATG-VK5-For		Link-VK5-For	
Vec-SalI-ATG-VK6-For		Vec-SalI-ATG-VK6-For		Link-VK6-For	

density gradient centrifugation. Subsequently, mRNA was isolated by total RNA extraction via Trizol method (see Figure A.4) and subsequent isolation of mRNA via Dynabead mRNA purification kit. Immediately afterwards, cDNA was synthesized from mRNA via SuperScript IV reverse transcription.

The variable regions of matured antibody sequences were amplified using specific primer sets that annealed to each V domain family and further introduced overhang sequences, which were necessary for assembly and subsequent ligation into the pIgV plasmid, that provided all further necessary sequence motifs for IVTT.

The primers were designed after meticulous evaluation of the V and J region exon nucleotide sequence alignments deposited into V BASE [299]. To include virtually all germline V families, up to three degenerate nucleotides were included in each primer (see Section 5.4.3).

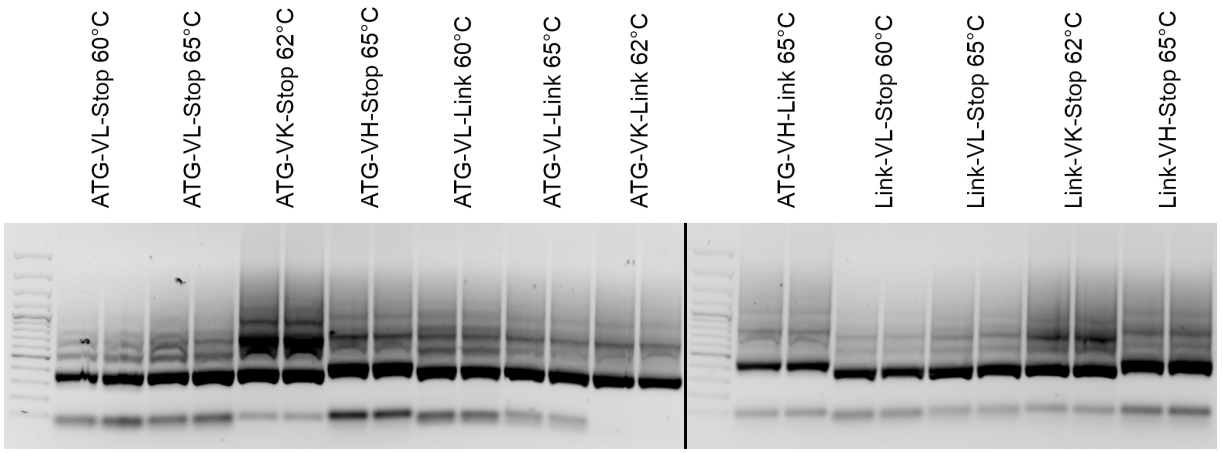

Figure 3.15: Amplification of Fvs. PCR amplification of all Fv variants from cDNA used to assemble the libraries LibNano and LibIgV$_2$. The PCRs were performed with individual primer mixtures for each subgroup as indicated in Table 3.2. The indicated temperatures denote the annealing temperature used during the PCR. The VL family fragments had to be split into two sets, as the respective primers achieved best amplifications at two different annealing temperatures (60°C and 65°C). The amplicons of interest ranged between 350 and 450 bp in length and were excised from the gel and purified for subsequent assembly into the library formats. Marker, GeneRuler 100 bp plus.

As can be seen in Figure 3.14, for the assembly of the library containing single-chain dimeric Fvs (LibIgV$_2$) each V domain family had to be amplified twice by PCR from cDNA: The first amplification, introduced a 5' pIgV plasmid overlap and start codon and a 3' sequence encoding parts of the $(G_4S)_4$ linker. Amplicons from that PCR encoded the N-terminal Fv of the IgV$_2$ antibodies. The second amplification, introduced a 5' sequence encoding the remaining part of the $(G_4S)_4$ linker and a 3' stop codon and pIgV plasmid overlap. These amplicons encoded the C-terminal Fv of the IgV$_2$ antibodies. All these motifs were introduced via extensions to the primers.

For the LibNano library, the V domain families were amplified with primers that introduced a 5' pIgV plasmid overlap and start codon and a 3' stop codon and 3' pIgV plasmid overlap. For each V domain family all primer combinations were evaluated individually by PCR and annealing temperatures were optimized (see Figure A.5). To amplify Fvs for library assembly, twelve PCR reactions were performed. One for each primer subgroup with an equimolar mixture of all forward and reverse primers of the respective subgroup and optimized annealing temperature during each PCR as listed in Table 3.2 (Subgroups and temperatures were: ATG-VH-Stop 65°C, ATG-VH-Link 65°C, Link-VH-Stop 65°C, ATG-VL-Stop 60°C, ATG-VL-Link 60°C, Link-VL-Stop 60°C, ATG-VL-Stop 65°C, ATG-VL-Link 65°C, Link-VL-Stop 65°C, ATG-VK-Stop 62°C, ATG-VK-Link 62°C, Link-VK-Stop 62°C). Amplicon quality was evaluated

by agarose gel electrophoresis (see Figure 3.15) and the corresponding bands of each subgroup were excised from the gel and DNA was recovered for subsequent library assemblies. The libraries were assembled via gibson assembly. Therefore, a linearized pIgV plasmid was generated by PCR and purified by gel elution. For the LibNano library, gibson assembly was performed with equimolar amounts of the Fv-amplicon subgroups of the ATG-V-Stop group. For the LibIgV_2 library, equimolar amounts of the Fv-amplicon subgroups of the ATG-V-Link and Link-V-Stop group were combined. For LibIgV_2, a three fragment gibson assembly was performed without preassembly of the IgV_2 before ligation into the pIgV plasmid.
As a final step, the gibson assembled libraries were reamplified by PCR into a linear format that included the T7 promotor, ribosome binding site and T7 terminator. The linearized libraries were subsequently used as input templates for PACMAN.
Anne Pfitzer performed a small-scale analysis of the quality of the generated LibIgV_2 library by transformation into *E.coli* and subsequent single-colony sequencing. The analysis revealed that eight out of ten clones contained properly assembled IgV_2 without any frameshifts or missing Fvs.
Unfortunately, large-scale analyses of the quality of both libraries and an estimation of their complexity via next-generation sequencing is still pending.

3.5 Attempts to isolate combinatorial proteolytic anti-Aβ antibodies

3.5.1 Synthesis of the Aβ-target peptide

The Aβ-target peptide was designed in alignment to the TEV-target peptide. The $Aβ_{40}$ sequence was intended to be encased by an N-terminal biotin and a FAM fluorophor and on the C-terminal side by an ATTO643 fluorophor. Initially, the peptide was commissioned to be synthesized by Thermofischer, but the synthesis failed twice and the order was abandoned. Consequently, I had to devise my own synthesis scheme (see Figure 3.16). For the synthesis, $Aβ_{40}$ with a C-terminal cysteine residue (termed $MAβ_{40}C$) was recombinantly expressed via coexpression with $Z_{Aβ3}$, which forms a soluble complex with Aβ and protects the *E.coli* cells from amyloid toxicity during expression. Purification of $MAβ_{40}C$ was performed as previously described for Aβ [300] by immobilization of the $MAβ_{40}C$:$Z_{Aβ3}$ complex on an IMAC column followed by subsequent elution with 8 M Urea to release $MAβ_{40}C$ from the complex. Next, $MAβ_{40}C$ was reduced with TCEP and RP-HPLC was performed to isolate monomeric $MAβ_{40}C$ and remove any residual $Z_{Aβ3}$ and other contaminants. Subsequently, ATTO643-maleimide

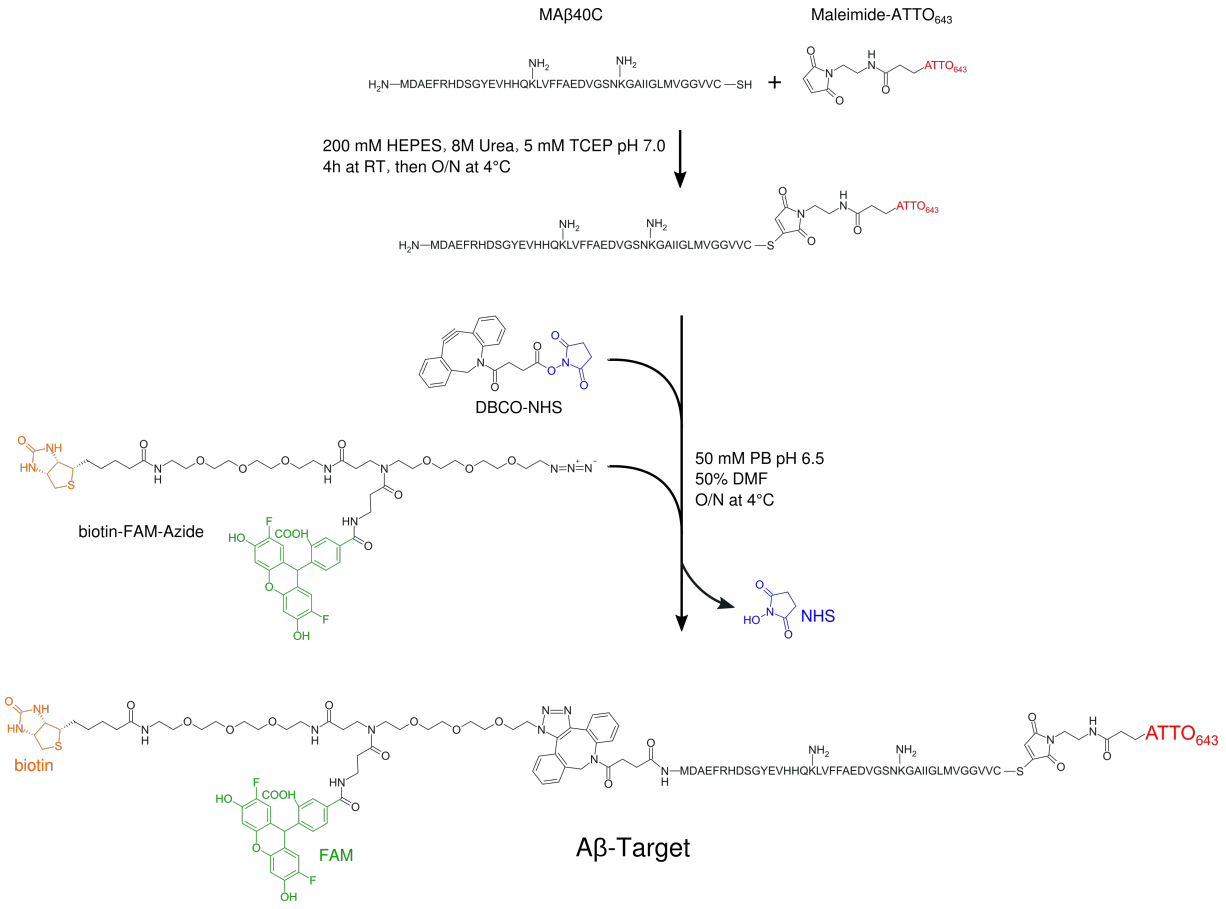

Figure 3.16: Scheme of the Aβ-target peptide synthesis. First, MAβ_{40}C was recombinantly expressed and purified. Maleimide-ATTO643 was conjugated to the C-terminal cysteine residue of MAβ_{40}C in the presence of 8 M Urea to keep MAβ_{40}C soluble and in the presence of 5 mM TCEP to keep MAβ_{40}C reduced and monomeric. The reaction was incubated for 4 hours at RT followed by an overnight incubation at 4°C. However, the incubation at 4°C should be avoided in the future, as it resulted in the formation of insoluble aggregates. MAβ_{40}C-ATTO643 was purified via RP-HPLC. Subsequently, the N-terminal 5-FAM and biotin moieties were attached by conjugation of a DBCO-NHS linker to the N-terminal amine group followed by attachment of a trifunctional biotin-FAM-azide compound to the DBCO moiety via copper-free click chemistry. The N-terminal amine of Aβ was favored over the ε-amines of both lysine residues in the DBCO-NHS crosslinking reaction by lowering the pH to 6.5 instead of the usually preferred pH of above 8 for NHS ester crosslinking, as the pKa of the N-terminal amine was lower than those of the ε-amines of the lysine residues. This reaction was performed in the presence of 50% DMF in an attempt to increase the solubility of MAβ_{40}C-ATTO643, but it was unfortunately still largely insoluble. In future attempts, the use of HFIP as a co-solvent should be evaluated to increase the solubility of MAβ_{40}C-ATTO643.

was attached to the C-terminal cysteine residue via succinimidyl thioether formation followed by purification via RP-HPLC. Finally, the biotin moiety and FAM fluorophor were attached in a two-step reaction by amine-reactive crosslinking of DBCO-NHS to the N-terminal amine group followed by copper-free click chemistry of a biotin-FAM-azide compound to the DBCO. A caveat of this reaction was that NHS was also able to react to the ε-amines of the lysine residues of the Aβ sequence. But, by maintaining a slightly acidic pH (pH 6.5) during the conjugation, NHS reactivity was biased towards crosslinking with the N-terminal amine instead of the ε-amines of the lysine residues which is usually favoured at a pH above 8. Hence, in a single batch reaction, NHS-DBCO was conjugated to the N-terminal amine of MAβ_{40}C-ATTO643 and in the same reaction the trifunctional biotin-FAM-azide compound was crosslinked via its azide-moiety to the DBCO by copper-free click chemistry. However, lysine reactivity was not be entirely abrogated, therefore the generated products of this reaction were stochastically comprised of a mixture in which most of the FAM-biotin-azide-DBCO-NHS was crosslinked to the N-terminal amine of MAβ_{40}C-ATTO643 while to a lesser degree some of the lysine residues were modified, which necessitated further purification of the distinct products via RP-HPLC followed by meticulous evaluation of their identities. Nevertheless, the exclusively N-terminally modified product was anticipated to be the most abundant product of this reaction.

Implementing my reaction scheme, the synthesis of MAβ_{40}C-ATTO643 was achieved without issue (data not shown). Subsequently, in the final synthesis reaction, several products were generated as anticipated. Four products were detected and isolated via RP-HPLC from the crude synthesis reaction (see Figure 3.17 a). Subsequently, the four distinct products were further evaluated for their identity. However, product 3 was the most abundant product, providing a first indication that it might have been the anticipated, exclusively N-terminally modified Aβ-target peptide.

For evaluation of the identity of the products, an aliquot of each product was digested with 0.01 X trypsin (Sigma) diluted in PBS for 16 hours at 37°C and the generated digestion fragments were analyzed via RP-HPLC. Trypsin has three potential cleavage sites within the Aβ sequence (R5, K16 and K28), while both lysines were also potential, undesired modification sites of FAM-biotin-azide-DBCO-NHS. Upon modification of a lysine residue, digestion via trypsin at that site was blocked. Evaluation of the digestion fragments that exhibited 643 nm and 488 nm absorption, i.e. the peptide fragments that contained a conjugated fluorophor, enabled the identification of the proper Aβ-target product. The correctly synthesized Aβ-target peptide product upon digestion was anticipated to yield the shortest digestion fragments that exhibit fluorescence, as all trypsin digestion sites would still have been susceptible to trypsin cleavage. Side products of the Aβ-target peptide synthesis that

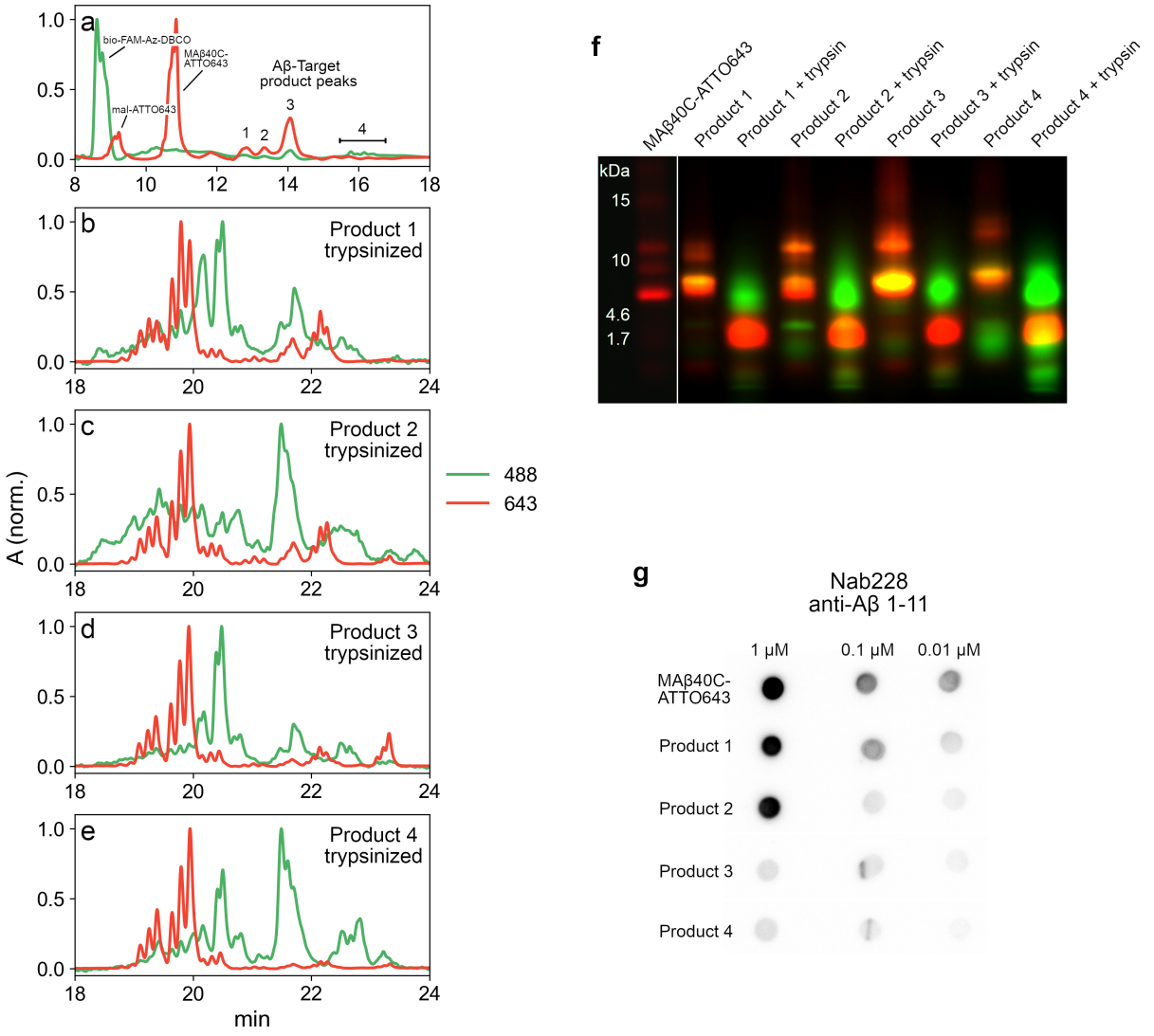

Figure 3.17: Investigations to identify the correctly synthesized Aβ-target peptide. a) RP-HPLC analysis of the crude conjugation reaction mixture in which DBCO-NHS and the trifunctional biotin-FAM-azide were crosslinked to MAβ_{40}C-ATTO643. 488 nm and 643 nm absorption data was normalized and identified peaks were labeled. Four putative Aβ-target peptide products were detected. b–e) Investigations into the product identities by trypsin digestion and subsequent analysis of the generated fragments via RP-HPLC. f) SDS-PAGE analysis of the putative Aβ-target peptide products and the corresponding fragments generated via trypsin digestion. The fluorescence of FAM and ATTO643 was detected and is shown in green and red, respectively. g) Dot-blot analysis of the putative Aβ-target products and detection with Nab228 antibody specific against the Aβ 1–11 epitope.

contained modified lysine residues, on the other hand, would have yielded longer fluorescent peptide fragments upon trypsin digestion.
The digestion fragments of all putative Aβ-target products were evaluated via RP-HPLC and results are shown in Figure 3.18 b–e. The longer a respective peptide fragment the later it tended to elute due to its higher hydrophobicity. The Aβ-target products 1 and 3 yielded trypsin digestion products inline with proper Aβ-target peptide identity, as they presented the earliest elution of their main digestion fragment exhibiting 488 nm absorption (at 20.5 minutes), which was expected to correspond to the N-terminal fragment containing the FAM-biotin-azide-DBCO-NHS modification at the N-terminal amine. Furthermore, both Aβ-target products, 1 and 3, presented another digestion fragment exhibiting 643 nm absorption, which eluted at 19.8 minutes that corresponded to the C-terminal fragment containing the ATTO643 fluorophor. Albeit, this latter peak was present in all four trypsin digested Aβ-target products. This suggested that the lysine residue at position 28 was likely unmodified in all four Aβ-target products, as modification of lysine 28 would have resulted in a delayed elution of the fragment exhibiting 643 nm absorption and would have furthermore simultaneously exhibited absorption at 488 nm, as the FAM-biotin-azide-DBCO-NHS moiety inevitably would have still been attached to the fragment.
The putative Aβ-target products 2 and 4, on the other hand, presented a delayed elution of the main digestion fragment exhibiting 488 nm absorption, which was suggestive for lysine modification at position 16.

To extend the analysis, all four putative Aβ-target peptide products and their corresponding trypsin digested fragments were analyzed by SDS-Page (see Figure 3.17 f). This analysis was unfortunately inconclusive beyond the fact that all Aβ-target peptide products contained FAM and ATTO643 fluorescence, while product 4 was likely modified at multiple positions with FAM-biotin-azide-DBCO-NHS, as evidenced by an increased FAM fluorescence in relation to its ATTO643 fluorescence.

As a final analysis, a dot-blot with all four Aβ-target peptide products was performed with subsequent detection using the anti-Aβ antibody Nab228, which detects the N-terminus of Aβ at epitope residues 1–11. I speculated that N-terminal modification of the Aβ-target peptide would obscure the N-terminus and thereby prevent antibody binding. And indeed, the Aβ-target peptide products 3 and 4 presented reduced antibody binding (see Figure 3.17 g). Consequently, Aβ-target peptide product 3 most likely corresponded to the proper Aβ-target, while product 4 corresponded to a double-labeled peptide (N-terminal and Lysine 16). Considering all analyses, product 2 most likely corresponded to a lysine 16 single-labeled peptide while product 1 still remains unresolved.

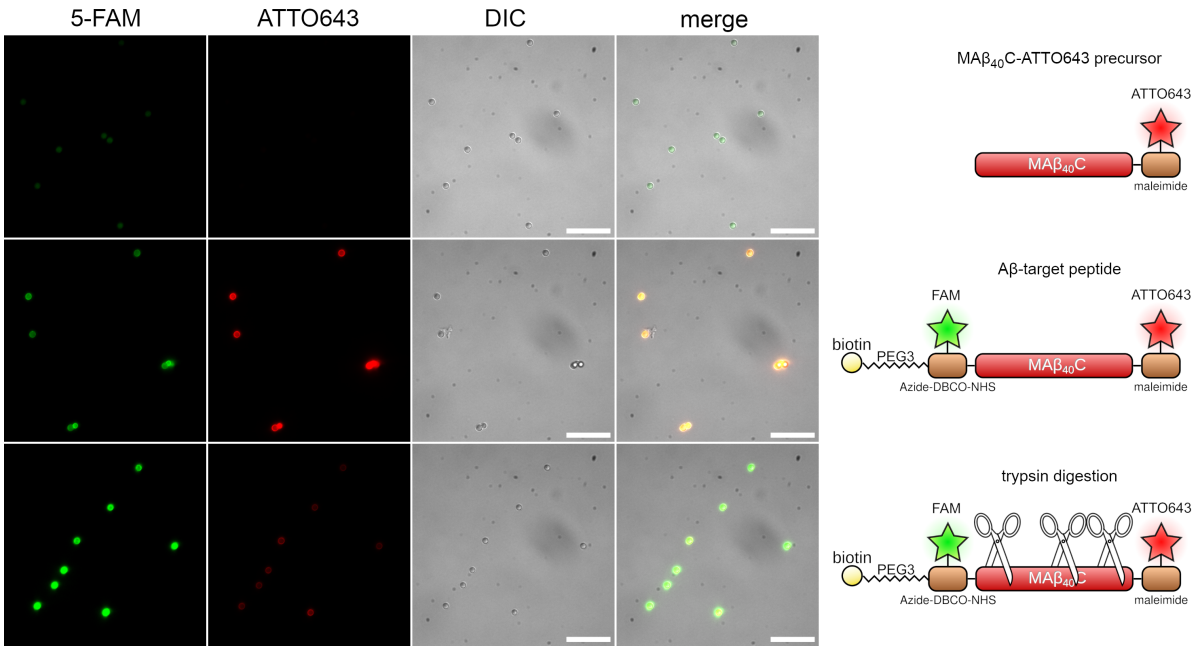

Figure 3.18: TIRF microscopy analysis of microbeads decorated with Aβ-target peptides. Promag HP 3 streptavidin microbeads were decorated with 10^6 Aβ-target peptides/microbead or 10^6 molecules/microbead of the precursor MAβ$_{40}$C-ATTO643 to evaluate whether the Aβ peptide without a biotin moiety would unspecifically bind to the microbeads. An aliquot of the Aβ-target peptide decorated microbeads was subjected to trypsin digestion with 0.01X trypsin overnight at 37°C.
Microscopy panels from left to right: 5-FAM fluorescence channel in green, ATTO643 fluorescence channel in red, DIC channel and merge. Top row, microbeads coincubated with MAβ$_{40}$C-ATTO643. Middle row, microbeads coincubated with the Aβ-target peptide. Bottom row, microbeads decorated with the Aβ-target peptide and subsequently subjected to trypsin digestion. Scalebar, 25 µm.

Beyond the here presented analyses, mass spectrometric analyses would have yielded definitive and conclusive evidence on the Aβ-target peptide products identities, but unfortunately mass spectrometry was not available to the institute and an on-demand service provided by the university was successively postponed indefinitely.

Ultimately, the final yield of the correct Aβ-target peptide product was 1.8 nmol, which was unfortunately an incredibly poor yield, nevertheless it was sufficient for a couple of PACMAN selections.

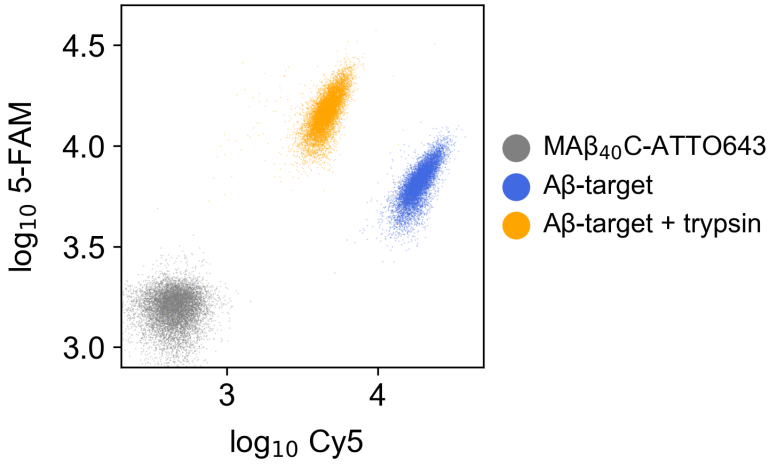

Figure 3.19: Flow cytometric analysis of microbeads decorated with Aβ-target peptides. The same microbeads as in Figure 3.18 were analyzed via flow cytometry to evaluate whether microbeads with cleaved Aβ-target peptides were spectrally sufficiently distinct from microbeads with intact Aβ-target peptides to allow for FACS sorting after PACMAN. The $\log_{10}$ of the 5-FAM and ATTO643 fluorescence signals are shown as scatter plot.

3.5.2 The Aβ-target peptide was able to bind to streptavidin-functionalized microbeads and remained accessible for trypsin digestion

It was evaluated whether the newly synthesized and verified Aβ-target peptide was able to bind to streptavidin-functionalized microbeads via streptavidin:biotin interaction. 10^6 molecules/microbead of the Aβ-target peptide were added to $5x10^7$ ProMag HP 3 streptavidin microbeads and incubated for 30 minutes at room temperature followed by an overnight incubation at 7°C at 1400 RPM in a thermomixer. As a control, to exclude that unspecific binding attributable to the sticky nature of Aβ might be responsible for attachment, the $MA\beta_{40}C$-ATTO643 precursor, which was devoid of any biotin moiety was added to a separate batch of microbeads at the same concentration. After peptide binding, microbeads were washed three times with breaking buffer with 30 minutes of incubation at room temperature at 1400 RPM, each, to wash off any unspecifically bound peptides. Subsequently, an aliquot of the microbeads decorated with Aβ-target peptides was subjected to an overnight digestion with 0.01X trypsin at 37°C to evaluate the accessibility of the cleavage-sites within the Aβ-target peptides in the microbead-bound state.

Microscopic analyses revealed, that the Aβ-target precursor, $MA\beta_{40}C$-ATTO643, was unable to bind to the microbeads (see Figure 3.18). Only residual autofluorescence of the microbeads in the 5-FAM channel was detected and none in the ATTO643 channel. On the

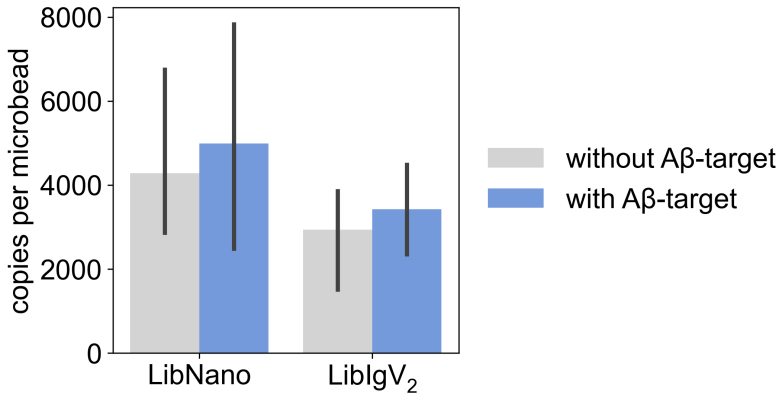

Figure 3.20: On-bead emPCR in the presence of Aβ-target peptides. On-bead emPCR was performed with both antibody libraries in comparison (LibNano and LibIgV$_2$) and in the presence and absence of Aβ-target peptides on the microbeads. 10^6 microbeads with 10^6 primers/microbead and 10^6 Aβ-target peptides/microbead or none were used for each on-bead emPCR reaction. 4x10^6 input DNA templates/reaction were used. Template lengths were 600–700 bp and 1,000–1,100 bp for LibNano and LibIgV$_2$, respectively.
The qPCR evaluation of the achieved DNA copies/microbead after on-bead emPCR is shown as bar chart. qPCR was performed in quadruplicates (n=4, mean±confidence interval of 95%).

other hand, microbeads that received the complete Aβ-target peptide presented vivid fluorescence in both the 5-FAM and ATTO643 channel. Furthermore, after trypsin treatment the ATTO643 signal was drastically diminished while the 5-FAM signal was increased, suggesting that successful cleavage and removal of the C-terminus together with the ATTO643 fluorophor was achieved.

The same microbeads were subsequently analyzed by flow cytometry which validated the results (see Figure 3.19). Furthermore, the populations of the microbeads with intact Aβ-target peptides were entirely separated from the microbeads with cleaved Aβ-target peptides, providing a perfect foundation for PACMAN selections of proteolytic single-chain anti-Aβ antibodies.

3.5.3 On-bead emulsion PCR in the presence of Aβ-target peptides attached on the microbead surface

It was evaluated whether the presence of the Aβ-target peptides on the surface of microbeads would result in a decreased efficiency of on-bead emPCR in terms of the achievable amount of DNA copies per microbead. Therefore, 10^6 biotinylated primers/microbead and 10^6 Aβ-target peptides/microbeads were attached to microbeads and subsequently on-bead

emPCR was performed. For comparison, microbeads that were devoid of Aβ-target peptides but contained the same amount of primers were subjected to on-bead emPCR. Furthermore, on-bead emPCR was performed with both antibody libraries in comparison — LibNano and LibIgV$_2$ — as input. qPCR analysis revealed no significant differences in the on-bead emPCR efficiency between Aβ-target peptide-decorated microbeads and microbeads that were devoid of Aβ-target peptides. The 600–700 bp long templates of the LibNano library achieved an average amplification of ∼4500 DNA copies/microbead, while the 1,000–1,100 bp long templates of the LibIgV$_2$ library achieved an amplification of ∼3,000 DNA copies/microbead (see Figure 3.20).

3.5.4 Expression of single-chain antibodies using *in vitro* transcription and translation reagent

To evaluate whether single-chain antibodies can be expressed with PURExpress *in vitro* transcription and translation reagent, the proteolytic antibody 2E6 reported by Taguchi *et al.* [230] was subcloned into the pIgV plasmid and subjected to IVTT containing PURExpress disulfide bond enhancer, which features DsbC and a proprietary blend of proteins and buffer components optimized for proper folding of proteins containing disulfide bridges. Furthermore, the IVTT reagent was further enhanced by addition of Genefrontier's GroE mixture and DnaK mixture, which have been shown to improve correctly folded antibody generation in IVTT [301–303]. 2E6 was readily expressed at 22°C, 30°C and 37°C, albeit expression was best achieved at 37°C (see Figure A.6 a). Expression was saturated after 2 hours of expression at 30°C and 37°C. Consequently, for PACMAN, 37°C was chosen as incubation temperature.

3.5.5 Failure to recapitulate proteolytic activity of antibodies 2E6 and 5D3 against Aβ

I performed multiple attempts to recapitulate the proteolytic activity of 2E6 and 5D3 against Aβ, as reported by Taguchi *et al.* [230]. Irrespective of the expression temperature and duration, as well as, the presence of PURExpress disulfide bond enhancer and Genefrontier's GroE and DnaK mixtures, no proteolytic activity of 2E6 was detected against Aβ (see Figure A.6 b). Zink ions were claimed to be necessary for 2E6 catalytic activity, but the inclusion of zink ions during the IVTT did not facilitate catalytic activity of 2E6. In an attempt to broaden the availability of metal ions during IVTT, a trace metal mixture (Trace Metal Mix A5 with Co from Millipore) was introduced to the IVTT reactions, but catalytic activity of 2E6 was equally

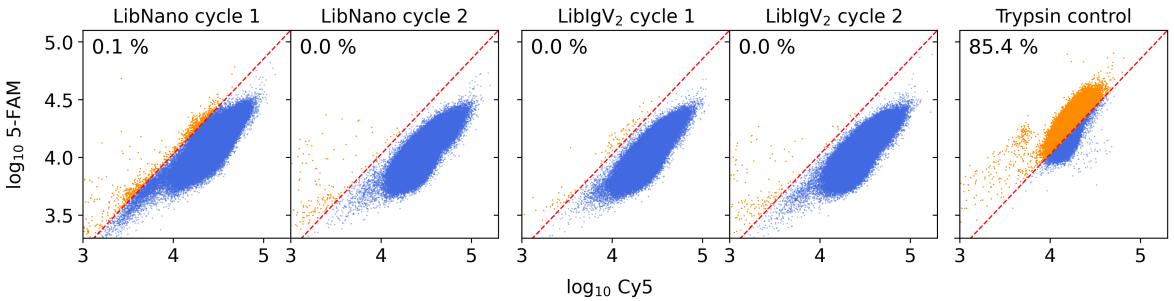

Figure 3.21: PACMAN selections of proteolytic anti-Aβ nanobodies and IgV_2 from combinatorial libraries. LibNano and $LibIgV_2$ were screened for proteolytic anti-Aβ antibodies via PACMAN. After PACMAN, microbeads were analyzed and sorted via FACS. In total, two consecutive PACMAN selection cycles were performed for each antibody library. The log_{10} of the 5-FAM and ATTO643 fluorescence intensities of the microbeads were plotted as dot-plots. Shown in the first two panels are the microbeads of PACMAN selection cycles one and two of LibNano and in the next two panels the outputs of PACMAN selection cycles one and two of $LibIgV_2$. The last panel shows a positive control of microbeads that were treated with trypsin to digest the peptides and hence remove the C-terminal ATTO643 fluorophors. The trypsin control indicates the best-case shift in fluorescence signal that could be expected for strongly active proteolytic anti-Aβ antibodies during PACMAN selections. The red dashed diagonal line indicates an arbitrarily set transition border used to delineate microbeads with cleaved Aβ-target peptides (orange dots) from microbeads with uncleaved Aβ-target peptides (blue dots). In the upper left corners of the dot-plot the percentages of microbeads falling into the area of microbeads with cleaved Aβ-target peptides is given.

absent (data not shown).

Similar efforts have been made for the antibody 5D3, but these were also shy of proteolytic activity.

As I was unable to recapitulate proteolytic activity of the two showcase proteolytic antibodies reported by Taguchi et al. [230], neither 2E6 nor 5D3 were available as positive controls for anti-Aβ PACMAN selections.

3.5.6 Unsuccessful PACMAN selections of proteolytic anti-Aβ antibodies from LibNano and $LibIgV_2$

A total of three PACMAN selections were performed for each antibody library and each selection consisted of two to three PACMAN cycles. The last attempt is exemplified below.

For each selection cycle 10^7 microbeads were subjected to PACMAN. Therefore, the microbeads were decorated with 10^6 Aβ-target peptides per microbead and 10^6 'b-TEG-TGS-Link-T7p For' primers per microbead. For the first selection cycles on-bead emPCR was

Table 3.3: Details on the exemplified PACMAN selections of proteolytic anti-Aβ antibodies from LibNano and LibIgV$_2$. Details on the PACMAN selections from LibNano and LibIgV$_2$ are listed. The amount of input DNA that was used for each 10^6 microbeads during the on-bead emPCRs of each selection cycle is listed. The total number of screened and sorted microbeads is indicated as well as the corresponding threshold percentage of the sort gate.

	LibNano		LibIgV$_2$	
	cycle 1	cycle 2	cycle 1	cycle 2
Input DNA DNA molecules per 10^6 microbeads	4x10^6	10^6	4x10^6	10^6
Total screened	2,540,004	2,105,912	2,018,257	2,113,888
Total sorted	12,325	15,473	62,812	14,341
Sort gate	0.5%	0.7%	3.1%	0.7%

performed with 4x10^6 molecules of input DNA templates for each 10^6 microbeads from either LibNano or LibIgV$_2$. After on-bead emPCR, microbeads were subjected to emulsification with IVTT reagent and were incubated for 3 days at 37°C to allow antibody expression and subsequent cleavage of Aβ-target peptides. Afterwards, microbeads were recovered from the emulsion and sorted via FACS isolating only the microbeads deviating the most towards the low-Cy5 high-FAM fluorescence area from the bulk of the microbead population (see Figure 3.21). A trypsin digested control microbead population was used as a gauge to estimate the fluorescence thresholds to single out microbeads with cleaved Aβ-target peptides. The percentage of the sorted microbeads from the total of screened microbeads is given in Table 3.3. Table 3.3 further contains details on the PACMAN selection cycles, such as the total amount of screened microbeads, the total amount of sorted microbeads and the amount of DNA template used as input for each selection. For each selection cycle at least 2 million microbeads were screened and at least 10,000 microbeads were collected.

In the given example in Figure 3.21 the first PACMAN cycle of LibNano and LibIgV$_2$ appeared to have contained a few microbeads that exhibited a fluorescence profile similar to that of the trypsin subjected control microbeads (orange dots in the same area as the main population of microbeads subjected trypsin digestion). This was especially prominent in selection cycle 1 of LibNano. But unfortunately, in selection cycle 2 of LibNano and LibIgV$_2$ this effect was not consolidated and virtually no microbeads were detected in the area in which microbeads with cleaved target peptides were expected, suggesting that proteolytic antibody selection was unsuccessful.

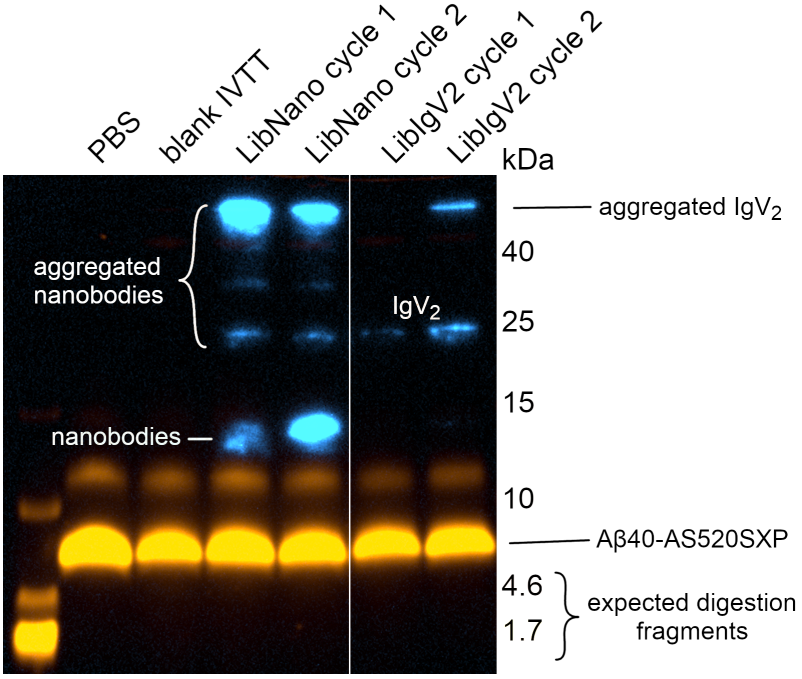

Figure 3.22: Assessment of enrichment of proteolytic anti-Aβ antibodies after PACMAN selections. The outputs of each PACMAN cycle was expressed in IVTT and examined for the presence of proteolytic activity against Aβ. 105 ng, 95 ng, 6.6 ng and 9.5 ng of the output DNA was used in 10 µl IVTT reactions from LibNano cycle 1, LibNano cycle 2, LibIgV$_2$ cycle 1 and LibIgV$_2$ cycle 2, respectively. The recoveries of the DNA from the LibIgV$_2$ selections were far less efficient than those from LibNano and therefore only a fraction of the DNA amount could be used in the latter IVTT reactions. After 4 hours of expression at 37°C the IVTT reactions were diluted 1:1 with Aβ$_{40}$-AbberiorStar520SXP in PBS to a final concentration of 10 µM. Samples were incubated at 37°C for 2 days to allow digestion of Aβ. Digestion products were evaluated on a 20% Tris-tricine SDS-PAGE and AbberiorStar520SXP fluorescence was recorded. Subsequently, a western-blot was performed using anti-cmyc detection antibodies to detect expression of the antibodies. AbberiorStar520SXP fluorescence is shown in orange, western-blot signal is overlayed in cyan. First lane, Spectra low-range prestained marker, second lane, Aβ$_{40}$-AbberiorStar520SXP control in PBS, third lane Aβ$_{40}$-AbberiorStar520SXP control in IVTT reagent without any DNA, lanes 4–7, LibNano cycle 1, LibNano cycle 2, LibIgV$_2$ cycle 1 and LibIgV$_2$ cycle 2, respectively.

To assess whether any proteolytic anti-Aβ antibodies were isolated and enriched from LibNano or LibIgV$_2$ after two successive cycles of PACMAN, the recovered DNA from each selection cycle was reamplified and subsequently *in vitro* expressed. The produced antibodies were evaluated for proteolytic activity against Aβ. 1 µM Aβ$_{40}$-AbberiorStar520SXP was subjected to the IVTT reactions after 4 hours of antibody expression. The digestion reactions were incubated for 24 hours at 37°C and subsequently analyzed using a 20% Tris-tricine SDS-PAGE gel to detect the presence of fluorescent digestion products (see Figure 3.22). Additionally, a western-blot using an anti-cmyc detection antibody was performed to detect

whether IVTT antibody production was successful.
The IVTT expression of antibodies has been successful for all selection outputs. Even the low concentrated DNA from the LibIgV$_2$ outputs was sufficient for detectable IgV$_2$ expression. The expressed nanobodies as well as IgV$_2$ exhibited a prominent aggregation tendency and cmyc-positive aggregates were visible in all samples. However, Aβ digestion was unfortunately not detected in any sample. All samples presented AbberiorStar520SXP fluorescence profiles identical to the PBS control. None of the samples presented any digestion fragments, as no additional fluorescences were detected below the Aβ$_{40}$-AbberiorStar520SXP band.

A total of three selections as presented above were executed and the results were indistinguishable from the one presented here. In total, more than six million microbeads were screened for LibNano and LibIgV$_2$, each. However, the results of all PACMAN selections and their subsequent analyses, unfortunately indicated that my attempts to isolate proteolytic anti-Aβ antibodies were unsuccessful.

4. Discussion & Conclusion

4.1 A sophisticated Aβ oligomer model

Biphasic Aβ aggregation kinetics and the formation of metastable AβO, which stitch together into bead-chain-like protofibrillar assemblies have previously been described [65, 279–283]. Oftentimes, these have been interpreted as on-pathway to rigid fibril formation or as representation of secondary nucleation events growing from the surfaces of rigid fibrils [283].
Using ThT aggregation kinetics together with our dimAβ-derived AβO model, I was able to discern an antagonistic role of metastable AβO on the nucleation and amplification processes of rigid Aβ fibrils and therefore I suggest the rejection of the nucleated conformational conversion (NCC) hypothesis [281], which states that metastable AβO convert into growth competent rigid fibril nuclei and that rigid fibrils grow by addition and conversion of metastable AβO onto the ends of growing fibrils. Contrary to that, our data suggest that metastable AβO exhibit an inhibitory effect on rigid fibril growth and amplification which exeeds beyond a mere competition for the Aβ monomer pool by actively suppressing secondary nucleation processes via binding to fibril surfaces and thereby blocking secondary nucleation sites. Goldsbury *et al.* [304] provided early evidence in agreement with our proposed off-pathway nature of AβO, by comparative morphological analyses of rigid Aβ fibril and protofibril preparations examined by AFM and mass-per-length analyses, which in agreement suggested that a direct conversion of oligomers and protofibrils into rigid fibrils was unlikely.
An extended debate on the on- and off-pathway nature of distinct amyloid oligomers was reviewed by Martin Muschol and Wolfgang Hoyer in Frontiers in Molecular Biosciences [305].

Beyond providing a tool for biophysical characterizations to obtain insights into Aβ aggregation kinetics and pathways, with dimAβ we provide a reliable and sophisticated AβO model which may serve as a toolkit to selectively study the pathophysiological implications specifically induced by AβO exposure. AβO derived from dimAβ are stable over time and over broad range of buffer compositions, including PBS and Dulbecco's Modified Eagle's Medium (DMEM), enabling cell culture and *in vivo* experiments in animal models while

ensuring morphological congruency of the AβO without further progression into fibrillar aggregates. Thereby, experiments can be reliably performed over extended periodes of time while providing specific AβO stimulation, which might aid in unraveling the specifics of AβO-induced insults in AD.

Albeit, there is one crucial caveat to bear in mind, it is still mostly unresolved whether our dimAβ-derived AβO model is structurally relevant in the sense of equivalently being present in the AD brain. Our current insights into their molecular morphologies are limited to comparisons of dimAβ-derived AβO to AβO formed *in vitro* by $Aβ_{40}$ and $Aβ_{42}$, which presented identical morphologies in AFM. Beyond that, unfortunately, a morphological comparison of dimAβ-derived AβO and *in vivo* AβO isolated from human AD brain homogenates is particularly challenging, as morphological data on patient-derived AβO are still concerningly sparce. On one hand, they are mostly limited to western blot analyses, density gradient centrifugations and dot blots with conformation-specific antibodies [40, 306], on the other hand, current AβO isolation methods involve harsh solvent conditions and consequently the morphological integrity of the obtained AβO remains questionable. Therefore, the available imaging data on patient-derived AβO are to be considered with appropriate caution. In attempts to image patient-derived AβO via electron microscopy by Esparza *et al.* [307], low and high molecular weight AβO-rich fractions have been isolated from AD brain homogenates via multiple centrifugations in the presence of detergents and high concentrations of sucrose followed by immunoprecipitation and elution via high pH. Likely, this procedure altered the molecular conformations and thereby the gross morphological appearence of the isolated AβO assemblies. Nevertheless, the AβO ultrastructures from this study consisted of multiple spheroid to ovoid subunits with sizes of 10–20 nm, which were in line with our AFM data of dimAβ-derived protofibrillar AβO substructures, which indicates that there might be some relevance to our dimAβ-derived AβO model.

To further close in on a conclusion on the putative presence of AβO in the AD brain, which exhibit conformational structures similar to those adopted by our dimAβ-derived AβO model, we currently aim to develop a conformationally sensitive antibody against dimAβ-derived AβO. These antibodies should not bind to monomeric or fibrillar Aβ and we aim to utilize this antibody to assess the presence of similar AβO structures in post-mortem AD brain slices and thereby confirm the relevance of our dimAβ-derived AβO model.

On another note, further AβO models exist, which enable the generation of similar AβO aggregates as derived from dimAβ, but these utilized substitutions of distinct amino acid positions with cysteine residues to generate Aβ dimers via disulfide bond formation [308, 309]. Multiple mutants — $Aβ_{42}$-A2C, $Aβ_{42}$-S8C and G_3C-Aβ ($Aβ_{42}$ followed by three glycine and a cysteine residue at its C-terminus) — formed AβO presenting similar morphologies as those

formed by dimAβ as discerned by AFM or TEM. Furthermore, in ThT experiments these mutant variants presented single exponential aggregation kinetics distinct from the sigmoidal kinetics observed in rigid fibril nucleation and growth. Rather, they were very similar to the kinetics observed during dimAβ-derived AβO formation in the initial phase of dimAβ's biphasic aggregation kinetics. In comparison to dimAβ, all these Aβ mutants presented less conformational freedom as evidenced by the fact that they were conformationally confined to the AβO state and were entirely restricted from accessing the fibrillar conformation space. Contrary to that, dimAβ-derived AβO were able to adopt fibrillar conformations under conditions of increased interaction with the water-air interphase via agitation by extended periods of shaking, suggesting that less sterical constriction was inflicted by the 20 aa long linker used to connect the two $Aβ_{40}$ subunits of dimAβ head-to-tail versus the dimerization via short disulfide bonds. Therefore, I dare to speculate that due to this increased conformational freedom, dimAβ-derived AβO might recapitulate a more faithful representation of native AβO — possibly including equivalent receptor-ligand interactions.
On that note, our initial results from primary mouse neurons subjected to dimAβ-derived AβO, revealed AβO binding to synaptic spines, reduction of spontaneous Ca^{2+} oscillations and AβO-induced tau missorting from the neurons' axons into their somato-dendritic compartments, which has similarly been observed for native AβO [63, 64]. Furthermore, the tau missorting effect was more prominent in neurons treated with dimAβ-derived AβO than with native $Aβ_{42}$-derived AβO, probably due to the metastable nature of dimAβ-derived AβO, which allowed exposure of the neurons for an extended period of time as opposed to the limited exposure window granted by native $Aβ_{42}$-derived AβO, which quickly progress into fibrils due to their transient nature [63, 64]. Here, we demonstrated that dimAβ-derived AβO faithfully induce robust expression of a disease-relevant phenotype in neurons. In this regard, dimAβ seems to provide an exquisite model to specifically study the effects of AβO over extended periods of time.

4.2 Consolidation of the Aβ oligomer hypothesis

Until just about a year ago, disbelieve in the amyloid cascade hypothesis grew in the AD community, as all Aβ-centric therapeutics consistently failed in clinical trials. Calls to rethink the causes of AD began to rise in the field, until aducanumab as the first Aβ-targeting drug, claimed to have finally alleviated symptom progression in a phase III study. Although this reimbued enthusiasm briefly faltered in the community due to uncovered inconsistencies revolving around aducanumab (see section 1.3.3.1), the latest success of lecanemab — an AβO-/protofibril-targeting antibody in another phase III study — seems to have ultimately

reconsolidated and finally confirmed the amyloid cascade hypothesis. By now, a staggering body of evidence specifically hints towards AβO as executive culprits in AD [34–40]. Lecanemab, as an AβO-/protofibril-targeting antibody, further supports and provides hard evidence in favor of this notion as it slowed down cognitive decline by 27% in AD patients treated with the highest dose of lecanemab compared to placebo. This further emphasizes the need for in-depth investigations into AβO biology to truly understand and finally intervene with AD development and progression.
On the other hand, the early center of scientific attention — Aβ fibrils and plaques — appear to slowly fade more into the background. Just recently, Blume et al. further stole the thunder of Aβ fibrils regarding their controversial disease relevance in a lead study [310]. They chronically stimulated the peroxisome proliferator-activated receptor γ (PPARγ) in transgenic $APP^{NL\text{-}G\text{-}F}$ mice via treatment with pioglitazone, which surprisingly led to a higher fibrillary composition of Aβ-plaques, while reducing AβO burden. This shift of AβO into a fibrillar conformation was furthermore protective on cognitive function in treated mice and promoted spatial learning and preserved synaptic density, suggesting that not the load of Aβ fibrils, but AβO correlates with symptom severity. This poor correlation of Aβ fibril/-plaque load with symptom severity has similarily been recognized in AD patients [311–314], suggesting that efforts in the development of Aβ fibril-targeting therapeutics might be a counterproductive endeavor.

Currently, the AD community seems more confident than ever before, that AβO represent a major — if not the most important — driver of AD pathology. A growing body of evidence attributes a negative impact on brain physiology to elevated levels of AβO. Conversely, to date, there have been no reports on an important role or critical dependency attributable to AβO in the physiology of the adult human. In contrast to that, Aβ monomers have been implicated in multiple physiological functions. They have been identified to act as anti-microbial [315–318] and anti-viral [319–321] peptides. Furthermore, physiological Aβ has been associated with neuroplasticity regulation [322–324], recovery from brain injury [325–328] and has been suggested to act as a sealant securing proper blood-brain-barrier integrity [329–331]. Albeit interestingly, in regards to AβO, a recent report may have finally attributed an essential physiological function to AβO during embryonic development. Bartley et al. [332] identified a transient physiological AβO expression during embryonic development of the chick retina which coincided with locally upregulated tau phosphorylation. In this context, AβO were suggested to act as a negative growth factor essential to proper retina development. Another report exists, that attributed a positive effect to picomolar concentrations of AβO on synaptic plasticity and memory formation in the hippocampus of mice, albeit elevated nanomolar concentrations were identified as detrimental

[333]. Beyond that, the AD field is set on the notion, that therapeutic removal of AβO in elderly humans will likely lead to beneficial effects on cognition in terms of AD development and progression. Concerns or expectations that AβO removal could lead to negative effects on healthy brain function are virtually nonexistent as currently no clinical or experimental evidence exists that would raise these concerns. But especially with these very nuanced speculations in mind, it will be necessary to obtain robust insights into AβO biology, especially in the physiological low picomolar concentration range, which is unfortunately exceedingly hard to probe due to the transient nature of native AβO, especially *in vitro*. Albeit this would be particularly important to uncover any potentially unforeseen dependencies or exigencies to the presence of AβO in healthy neurobiology.
This is where I hope that our dimAβ-derived AβO model might come in handy. With my latest publication [288] and the introduction of our dimAβ-derived AβO model, as a tool to study AβO biology, we assessed the scope of applicability of our model and moreover we aimed to shed light on the neuropathological implications associated with AβO and we further elucidated on a potential mechanism of *in vivo* AβO biogenesis, which is yet mostly unresolved. We examined the effect of pH on the generation of AβO using dimAβ and $Aβ_{42}$. For $Aβ_{42}$, at neutral pH, rigid fibril formation was generally favoured until a critical oligomer concentration of approximately 30 µM was exceeded, which gave rise to AβO formation. At pH 4.5, on the other hand, AβO readily formed at concentrations as low as 3 µM. Using dimAβ, we were able to estimate the extent of the acceleration of AβO formation in dependence of pH, revealing that AβO formation was accelerated ~8000-fold upon shifting of pH from 7.4 to 4.8. The endolysosomal system is known to naturally enrich Aβ to well above 2.5 µM [289] and furthermore provides an acidic pH in the range of 4.5–5.5, which is in line with the prerequisites for AβO formation. Supported by our data, we posit that the endolysosomal system might be a major contributor to AβO generation *in vivo*.
In support of our hypothesis on AβO biogenesis, Esbjörner *et al.* [334] observed Aβ aggregation in live-cell experiments via fluorescence lifetime microscopy and revealed that Aβ aggregation was indeed localized within endolysosomal compartments. Nevertheless, I acknowledge that our proposed mechanism of *in vivo* AβO generation is likely not the sole source of AβO in the AD brain, but complementary mechanisms are probably involved in the *in vivo* biogenesis of AβO, such as interactions with other amyloid proteins like TDP-43, which has been shown to promote AβO generation [335].

Another clue towards the operating principles of AβO was published in my reports in Chemical Science [128] and Angewandte Chemie [275]. Here, I reported on a remarkable mode of interaction of AβO with Aβ fibrils. AβO were found to bind to Aβ fibrils, but intriguingly, AβO arranged perpendicular to the fibril surface while only attaching with the tips of

their curvi-linear protofibril structure, like curly hair growing from a rigid rod. Beyond that, AβO exhibited an inhibitory effect on secondary nucleation of fibril growth by blocking nucleation sites on the surfaces of fibrils. As a potentially disease-relevant consequence, this retarding effect of AβO on fibril growth might secure AβO survival and extent the exposure duration of AD patients to toxic AβO by reducing secondary nucleation rates of fibrils and thereby decelerating AβO depletion.
The binding affinity of AβO towards Aβ fibrils might further support two opposing implications in regards to plaque involvement in AD, in which plaques might either serve as reservoirs of AβO, which could cause a chronic supply and release of toxic AβO in their vicinity or antithetically might support the implication that plaques act as sinks that burrow AβO into insoluble deposits and thereby alleviate their toxicity. Several groups reported on the presence of a toxic AβO halo surrounding plaques in post-mortem AD brains [336–340], which might favor the first assumption, but does not mutually exclude the sink hypothesis. Further investigations will be necessary to resolve this question.

As a closing remark on AβO, I hope that our dimAβ-derived AβO model might aid in the persuit to untangle the biology and pathophysiology of AβO in AD and to ultimately deduce novel strategies for therapeutic interventions. The elusive nature of native AβO currently limits our ability to derive tangible insights and to decipher their specific effects and insults in *in vitro*, cell culture and *in vivo* experiments as native AβO quickly transition into a conglomerate of distinct aggregate species muddying the experiments' readouts. Here, dimAβ-derived AβOs might prove useful as a substitute due to their metastable nature, which would allow investigations into the specific effects of AβO in temporally extended experiments, while consistently maintaining the AβO conformation. With a follow-up study, we hope to finally validate that dimAβ-derived AβO faithfully represent conformational aggregate species present in the AD brain. By developing a conformation-specific antibody using dimAβ-derived AβO as target antigen and monomeric and fibrillar Aβ as negative selections, the obtained antibodies should be able to specifically bind AβO, which are conformationally identical to dimAβ-derived AβO, but should not be able to bind Aβ monomers or fibrils. Utilizing this antibody as a probe, we should be able to prove or disprove the existence of dimAβ-derived AβO-like entities in the AD brian. If we could prove these conformational AβO species to be present in the AD brain, our dimAβ-derived AβO model would be affirmed as an invaluable tool to study the biology of AβO and might further aid in the development of novel AβO-centric therapeutics.

4.3 Controversial evidence on proteolytic anti-amyloid antibodies

To the best of my knowledge, this study provides the first independent replication of the results by the Paul group from 2008 [229], who first claimed to have detected natural proteolytic anti-Aβ IgM antibodies in human blood. Here, I present a replication of their results and further extent the picture by providing equivalent evidence for the existence of natural proteolytic anti-tau IgM. However, at the same time, I also have to distort the current picture of proteolytic antibodies by raising my suspicion that previous reports about their existence might have been premature, as other sources of error that might have explained the putative proteolytic activities seen in the experiments seem to have not been adequately excluded. Therefore, the detected proteolytic activities described here in this study as well as those reported in literature [228, 229] have to be appreciated with appropriate scepticism.
It has already been mentioned in earlier reports, that contaminations of the IgM preparations with residual proteases and peptidases was a major concern for misinterpretation in cleavage experiments and hence it had to be ensured that these contaminations were absent [229]. One attempt to achieve that, performed by the Paul group, was to wash the IgM using a denaturing gel filtration in 6 M guanidine hydrochloride in PBS. Thereby, any proteases complexed with the IgM were believed to dissociate and concomittantly be removed. After refolding of the eluted IgM via dialysis against PBS, the same proteolytic activity pattern against Aβ as before was recovered, albeit strongly reduced. This reduction in activity was attributed to insufficiently refolded IgM, but it was neglected that it might as well be the result of residual proteases still being carried over and the IgM being proteolytically inactive after all. Conversely, this experiment was claimed to prove that the catalytic activity was excerted by the IgM and not attributable to residual protease or peptidase contaminations. We were able to equivalently reproduce the afforementioned experiment (data not shown), however we are very hesitant to claim that this would be sufficient proof of purity and acknowledge that IgM-sized or particularly hard-to-remove proteases and peptidases can not be removed by this process and might still be responsible for the detected proteolytic activity. Afterall, miniscule trace contaminations could be sufficient to turn the tides in these experiments.

Upon hitherto extended investigations into proteolytic antibodies, I question that previous reports faithfully elaborated on the properties of proteolytic IgM and other classes of antibodies. Considering the following remarks, I doubt that the glorification of proteolytic antibodies was justified and I further question their existence entirely.

Our most recent data, acquired together with Anne Pfitzer and not shown in this work, suggest that the observed proteolytic activity excerted by IgM preparations highly depends on the coincidential stringency of the corresponding purification. Multiple preparations of IgM from the same plasma donation yielded deviating outcomes in terms of their proteolytic activity against Aβ. Some preparations recapitulated the proteolytic pattern against Aβ as reported by Taguchi *et al.* [229], while other preparations exhibited no activity at all and yet others presented an activity clearly originating from gross contamination with plasma peptidases/proteases. Intriguingly, IgM preparations which appeared to be exceedingly pure, as judged by SDS-PAGE analyses, exhibited no proteolytic activity at all. These results initially raised my suspicion that the putative proteolytic activity of IgM was yet insufficiently understood and might have been prematurely assigned to being an effect of the IgM and might, afterall, be attributed to some residual protease/peptidase contaminations.
Another blow to the proteolytic antibody theory comes from my consistent inability to reproduce any proteolytic activity of the monoclonal showcase single-chain antibodies 5D3 and 2E6, which have been selected against Aβ by Taguchi *et al.* [230] and have been claimed to excert proteolytic activity with outstanding specificity towards Aβ. Nevertheless, in my experiments, a plethora of attempts to reproduce these claims with distinct expression and purification procedures were all in vail (data not shown). I evaluated antibody production in *E.coli* via periplasmic expression, as originally reported by Taguchi *et al.* [230], but furthermore evaluated intracellular expression, as well as, media export via conjugation to outer membrane export signal peptides (PelB-5xD, OsmY and YebF). Intriguingly, expression and purification of the antibodies was successful in all evaluated cases, nevertheless, no proteolytic activity against Aβ was detected in any case. Furthermore, I evaluated production of 5D3 and 2E6 via IVTT, while investigating whether the inclusion of folding maschinery components in the form of GroEL/ES, DnaK/DnaJ/GrpE and DsbC might be crucial for activity or whether the inclusion of a trace metal mixture was necessary to obtain proteolytic activity (the metal mixture included zink and cobalt ions, which were claimed to be crucial for 2E6's functionality [230, 341]). Additionally, I evaluated the influence of the expression duration and temperature. Unfortunately, all attempts were shy of any proteolytic activity against Aβ, despite again, successful antibody production.
My inability to recapitulate any proteolytic activity exhibited by the recombinantly produced monoclonal single-chain antibodies, which were claimed to by far exceed the activity of polyclonal IgM preparations, represents another heavy nail in the coffin of proteolytic antibodies.

My last resort to restore the reputation of proteolytic antibodies was to isolate my own anti-Aβ single-chain proteolytic antibodies from combinatorial libraries via PACMAN. Unfortunately, these attempts joined the ranks of negative outcomes and no proteolytic antibodies

were obtained (more on that in the next section). Ultimately, by now, the expectation of proteolytic antibodies as a novel class of immuntherapeutics appears to be but a distant wistful idea and would require grand new and indubitable evidence from future investigations to reinstill their status or be laid to rest for good.

4.4 Selection of proteases and proteolytic antibodies via PACMAN — pitfalls and insights for future selections

The PACMAN method enables the isolation of sequence-specific proteases from complex libraries. PACMAN utilizes microbeads presenting the DNA of distinct library members encapsulated in bulk emulsions containing an *in vitro* transcription and translation system to express each library member in a droplet which acts as a discrete picoliter-sized reaction vessels. In addition to the DNA, the microbeads are decorated by attachment of complex target peptides, which contain the amino acid sequence that shall be cleaved by an active library member, but the N- and C-terminus of the target peptides are modified with two spectrally distinct fluorophors and a biotin-moiety at the very N-terminus for attachment to the microbeads (see Figure 3.1). During PACMAN, library members are expressed in confinement within the droplets which contain the corresponding microbead presenting their genetic information. During incubation, active library members cleave the target peptides, releasing the distal fluorophors from the microbead. Subsequently, microbeads with cleaved target peptides are isolated via FACS according to their altered fluorescence profiles and the DNA of active library members is thereby enriched.

The feasibility of PACMAN was successfully proven by enrichment of TEV-protease-encoding DNA from a dilute mixture with irrelevant DNA (see section 3.2.6). Within merely two PACMAN selection cycles, the irrelevant DNA was completely displaced by the active TEV-protease-encoding DNA, revealing the outstanding efficiency of the PACMAN method.

However, the intended use-case of PACMAN — the isolation of proteolytic antibodies from combinatorial libraries — was so far unsuccessful. In my attempts to isolate proteolytic antibodies, two combinatorial antibody libraries were derived from a total of ten buffy coat donations and screened for proteolytic anti-Aβ antibodies via PACMAN. The first library encoded nanobody formats of human heavy-chain and light-chain variable fragments. The second library encoded conventional scFv-formats as well as unnatural homodimeric IgV_2 consisting of two light-chain or two heavy-chain variable fragments tethered via a $(G_4S)_4$-linker. Both nanobodies and the unnatural homodimeric IgV_2 have previously been claimed

to excert superior proteolytic activities as opposed to other antibody formats [230].
The Aβ-target peptide necessary for the PACMAN selections was synthesized by recombinant expression and purification of an $A\beta_{40}$ variant which was modified by addition of a C-terminal cystein residue. Subsequently, the synthesis was concluded by consecutive modification of the C-terminal cysteine via thiol-reactive conjugation of a maleimide-ATTO643 compound and the N-terminus was modified via amine-reactive N-hydroxysuccinimide ester-mediated derivitization with an NHS-DBCO compound followed by copper-free click chemistry to attach a trifunctional azide-FAM-biotin compound to the DBCO moiety (see Figure 3.16). However, the Aβ-target peptide synthesis was accompanied by a crippling loss of reagents and products. Nevertheless, despite the dreading inefficiency, product was successfully synthesized with a sufficient yield for multiple PACMAN selections.
Unfortunately, all attempts to screen for proteolytic anti-Aβ antibodies via PACMAN were so far unsuccessful. The lack of success, however, was likely due to the absence of proteolytic antibodies in the human antibody repertoire and not due to a technical issue on the side of PACMAN. Nevertheless, it has to be granted that a few factors exist on the side of PACMAN that might have been responsible for the unsuccessful selections, which will be briefly discussed below:
The main caveat I recognize concerning my PACMAN selections was the very limited total number of screened antibody library members. A roughly aggregated total of six million microbeads for each antibody library was screened in my collective three selection attempts. This limits the potential maximum of screened antibody library members in the best-case scenario to six million distinct nanobodies and six million distinct IgV_2. Hence, if the prevalence of proteolytic activity in antibodies against Aβ is in the chance of one in a million, it was likely missed by my PACMAN selections. Therefore, my current attempts might have encompassed too few library members to ultimately conclude whether the isolation of proteolytic antibodies via PACMAN is a viable endeavor. To address these limitations it will be necessary to scale-up the processivity of PACMAN, escpecially by increasing the throughput of on-bead emPCR, which is currently the main limiting factor of throughput. Furthermore, the batch size of the Abil EM 90-based emulsions containing the *in vitro* transcription and translation reagent needs to be scaled up as well to accomodate for an increased number of microbeads.
However, with increasing concentrations of microbeads, their tendency to cluster increases. In my attempts to scale up PACMAN batch sizes, microbeads occasionally tended to cluster leading to horrendously large microbead clumps, comprised of hundreds to thousands of microbeads, ending up encapsulated in a single droplet, undermining the genotype-phenotype coupling necessary for PACMAN and displacing the IVTT reagent in the droplet.
Another issue that might be expected with PACMAN, is a limitation to its sensitivity in regards

to low turnover enzymatic activities. Bulk emulsion preparations are inherently heterogeneous in droplet sizes. Droplet sizes are distributed in a stochastic manner usually following a bell curve. However, these variations in reaction volume are also accompanied by variability in reaction efficiencies. Differences in reaction volume lead to random variability in on-bead emPCR efficiencies as well as in *in vitro* transcription and translation efficiencies and thereby, the specific readout of PACMAN becomes blurred. Thereby, low turnover enzymatic events, as in the case of proteolytic antibodies, might remain undetected in these indeterminate conditions. Another reason these low turnover events might have been missed in my PACMAN selections, was that approximately 1 million target peptides were coupled to each microbead, while the majority of these had to be cleaved to be confidently distinguished in FACS. However, this problem might be somewhat avoided by optimization of the target peptide concentration towards the lower limit of detectability in FACS.

In the future, it might be beneficial to continue the pursuit for proteolytic antibodies by taking advantage of microfuidics. Microfluidics could solve at least two of the limiting factors of PACMAN. Microfluidics provide incredibly even droplet sizes, on-chip manipulation and the possibility to sort droplets on the chip. Future selections might be attempted based on the show-case method developed by Price *et al.* [342] who used quenched substrate peptides and an *in vitro* transcription and translation reagent expressing a model protease in homodisperse microfluidic droplets. The generation of fluorescence after incubation was subsequently used as a readout for successfully cleaved substrate peptides. Combining this method with on-chip fluorescence activated droplet sorting (FADS) [269, 343] would allow for the omission of microbeads as solid carriers necessary for subsequent FACS sorting. Further extension of the workflow by an upstream droplet PCR could be used to increase the efficiency of the IVTT expression of each library member. Fallah-Araghi *et al.* [344] used droplet PCR to amplify the DNA of library members in droplets prior to IVTT, thereby obtaining droplets containing ~30,000 copies of the respective library member template DNA. Subsequently, these droplets were joined with droplets containing an IVTT reagent and substrate molecules to achieve efficient gene expression and substrate turnover.
Adopting these techniques for PACMAN would eliminate tedious and error-prone microbead handling and allow the solid detection of low-turnover enzymatic activity by elimination of heterogeneity in the droplet dimensions and hence reaction efficiencies. Albeit, these techniques require a specialized laboratory equipped with devices for microfluidic handling as well as sophisticated detection devices and computing for FADS. Therefore, applicability would currently be limited to a handful of laboratories, but as time progresses microfluidics will likely find their way into ordinary laboratories.

PACMAN as a platform for protease engineering

Despite the afforementioned shortcomings, PACMAN might find its value as an independent method in its own right. PACMAN could allow for the rapid development and implementation of adjustments to the substrate specificities of engineered proteases towards altered recognition sequences. By screening of mutagenesis libraries derived from known proteases and the use of target peptides which present the desired, altered recognition sequences, PACMAN could provide the necessary platform to quickly implement the desired adjustments to the proteases according to the operators' volition.
Thinking ahead, PACMAN might ultimately be used to provide a toolbox containing a set of highly specific proteases which can be used as precision tools for bioscience and bioengineering. I would like to lay the foundation of this toolbox by developing a modified TEV-protease that cleaves the signal sequence ENLYFQ|M instead of the native ENLYFQ|G/S, i.e exchanging the originally preferred glycine or serine residue at the P1' position of wildtype TEV-protease with a methionine residue.

If PACMAN is to be utilized on a grand scale, as it would be in the case of the provision of a toolbox containing multiple specialized proteases, the target peptide synthesis process would need to be optimized and streamlined. The current target peptide synthesis scheme was accompanied by a major loss of reagents and products due to insufficient solubilities in the reaction buffers. In future attempts, the inclusion of HFIP in the reaction buffers might enhance the solubility of the reagents.
Furthermore, the ease of achieving success with the required multiple peptide modifications could be ensured by a few considerations regarding the initial peptide sequence: Omitting cysteine and lysine residues in the target peptide sequences would drastically reduce the necessary post-modification clean up. A C-terminal cysteine residue is required for modification with one of the two fluorophors, therefore the inclusion of further cysteine residues in the target peptide sequence would necessitate downstream investigations and purifications to ensure the recovery of only those peptides with exclusive modification of the C-terminal cysteine residue. Likewise, inclusion of additional lysine residues should be avoided as they would introduce further amine groups, which would compete with N-terminal amine-reactive NHS modification, which is required for the conjugation of the trifunctional reagent that introduces the other fluorophor and the biotin moiety. Keeping these restrictions in mind while designing the target peptides would dramatically reduce post-synthesis labor.

4.5 In conclusion

This thesis provides novel insights into the behavior, pathophysiology and the origins of AβO *in vivo*. Furthermore, it provides dimAβ, a stable AβO model allowing temporally extended investigations into AβO without the risk of aggregation progression into fibrillar entities.
But, the main contribution of this thesis was PACMAN. A method that enables directed evolution of proteolytic enzymes. However, it was intended to be used for the isolation of proteolytic anti-Aβ antibodies from combinatorial libraries, which was unfortunately not achieved during this thesis. Nevertheless, both the establishment of the PACMAN method itself as well as the attempts to isolate proteolytic antibodies were overwhelmingly tedious as individual endeavors. They were high risk high reward ventures and sadly the ultimate goal of isolating proteolytic antibodies against Aβ was not achieved.
Nontheless, the PACMAN method was successfully established and might in the future enable the development of tailormade enzymes with narrowly defined proteolytic activities. Moreover, PACMAN is readily applicable in most laboratories posing only a low entrance barrier. The most restrictive requirement in terms of equipment is access to a FACS device. However, most universities nowadays offer FACS services as part of their core facilities. An entire PACMAN selection can easily be performed within a week liberating time for the more interesting downstream applications.

In the end, however, an unfortunate revelation of this thesis was sparked by my inability to reproduce the claimed catalytic activities of the reported proteolytic anti-Aβ single-chain antibodies 2E6 and 5D3 by the Paul group. Together with my lack of confidence regarding the putative proteolytic activities detected from isolated polyclonal IgM antibodies, due to the inherent difficulty to exclude residual contaminations with other plasma proteases in their preparations, it opens up room for speculations about proteolytic antibodies potentially being a misinterpretation of a fluke. Adding to that, the concern of insufficient purity was not applicable to the published showcase single-chain proteolytic antibodies 2E6 and 5D3 by the Paul group, which contrary to the IgM, were recombinantly produced and easily purified with confidence. The fact that these, however, did not exhibit any proteolytic activities against Aβ in my experiments, was therefore especially discouraging. Lastly, it all culminated with my inability to isolate any novel proteolytic antibodies via PACMAN which topped off my doubts regarding the existence of proteolytic antibodies.
Consequently, as a final conclusion, I raise my suspicion and constitute that proteolytic antibodies — as enticing as they might have appeared — might afterall remain but a myth.

5. Materials

5.1 Chemicals and reagents

2-propanol	Sigma-Aldrich
Abil EM90	Evonik
Acetic acid	Merck
Acetonitrile	VWR chemicals
Acrylamide/Bis Solution 40% (19:1)	Serva
Acrylamide Solution 40%	Fisher bioreagents
Adipic acid	Sigma-Aldrich, Merck
Agarose, my-Budget low-melt	Bio-budget
Ammonium persulfate (APS)	Roth
ATTO643-maleimide	ATTO-TEC
β-mercaptoethanol	Invitrogen
Bisacrylamide	Serva
Bromophenol blue	Riedel-de Haen
Coomassie Brilliant blue G 250	Sigma-aldrich, Merck
Chloroform	VWR NORMAPUR
Dibenzocyclooctin N-hydroxysuccinimide ester conjugate (DBCO-NHS)	Click Chemistry Tools
Diethylether	Honeywell, Riedel de Haen
Dithiothreitol (DTT)	Roth
N,N-Dimethylformamide, anhydrous, amine free, 99.9%	Thermo scientific
Dimethyl sulfoxide (DMSO)	Acros organics
dNTPs	Invitrogen
Ethylenediaminetetraacetic acid (EDTA)	Acros organics
Ethanol	Honeywell, Riedel de Haen
Ficoll-Paque PLUS	GE Healthcare

Fluorescein-biotin-azide	Click Chemistry Tools
Fluorostop	Dolomite
FluoSurf, 2%	Dolomite
GelRed	Biotum
GelGreen	Biotum
HCl	Honeywell, Fluka
HEPES, 4-(2-hydroxyethyl)-1-piperazineethanesulfonic acid, Pufferan	Roth
Imidazole, for buffer solutions	AppliChem
LB-Medium - Powder according to Lennox	AppliChem
Mineral oil	Sigma-Aldrich, Merck
NaCl	Applichem
NaOH	Fisher Scientific
Polyethylene glycol 6000 (PEG), Rotipuran Ph.Eur.	Roth
Phosphate buffered saline (PBS) tablets	Gibco, Thermo Fischer
Potassium phosphate, monobasic, KH_2PO_4	Fisher chemicals
Rotiphorese Gel 30 (37.5:1)	Roth
Sodium dodecyl sulfate	Merck
Sodium phosphate, dibasic, Na_2HPO_4	Honeywell, Fluka
Sodium phosphate, monobasic, NaH_2PO_4	Honeywell, Fluka
SYBR Green I DNA Dye (10,000 x)	Biozym
Tetramethylethylenediamine (TEMED)	Roth
Trace Metal Mix A5 with Co	Millipore
Tris(2-carboxyethyl)phosphine hydrochloride (TCEP)	TCI
N-Tris(hydroxymethyl)methylglycin (Tricine)	Serva
Trifluoroacetic acid (TFA)	Roth
Tris(hydroxymethyl)aminomethane (Tris), Trizma base	Sigma-Aldrich, Merck
Triton X-100	Thermo Scientific
Trypsin, 10X, EDTA Solution	Sigma Life Science
Xylene cyanol FF	Serva

5.1.1 Microbeads

Dynabeads M270 Streptavidin	Invitrogen
Dynabeads M280 Streptavidin	Invitrogen
ProMag HP 3 Streptavidin	Bangs Laboratories, Inc.

5.2 Enzymes, kits and antibodies

AceQ qPCR SYBR Green Master Mix	Vazyme
Anti-Myc tag antibody (ab9106), rabbit polyclonal	abcam
Goat Anti-Rabbit IgG H&L (HRP) (ab6721), goat polyclonal	abcam
DnaK mix	Genefrontier
Dynabeads mRNA Purification Kit	Invitrogen
GeneRuler 100 bp Plus DNA ladder	Thermo Scientific
GeneRuler 1 kb DNA ladder	Thermo Scientific
GroE mix	Genefrontier
NucleoSpin Gel and PCR Clean-up, Mini kit	Macherey-Nagel
PageRuler Plus Prestained Protein Ladder, 10 to 250 kDa	Thermo Scientific
Phusion High-Fidelity DNA Polymerase	New England Biolabs
Protein A conjugated to agarose beads	made in-house
Proteinase K	New England Biolabs
PURExpress *In Vitro* Protein Synthesis Kit	New England Biolabs
QIAshredder	QIAGEN
RNase inhibitor, murine	New England Biolabs
Spectra Multicolor Low Range Protein Ladder	Thermo Scientific
Superscript IV First-Strand Synthesis System	Invitrogen
SuperSignal West Pico Plus	Thermo Scientific
T5 exonuclease	made in-house
Taq DNA Ligase	made in-house
TEV protease	made in-house
Titanium Taq DNA Polymerase	Takara Bio

TRIzol reagent	Invitrogen
Ultrapure BSA	Invitrogen

5.3 Buffers and solutions

PBS was either prepared using PBS tablets according to the manufacturer's instructions to prepare a 1x solution or it was prepared as a 10x stock solution as follows and diluted to a 1x solution with H_2O as needed:

10x PBS	1.37 M NaCl 100 mM Na_2HPO_4 18 mM KH_2PO_4 27 mM KCl pH 7.4 (adjusted with HCl)
10x Tris-tricine SDS-Page anode buffer (diluted to 1x with H_2O prior to use)	2 M Tris pH 8.9 (titrated with HCl)
10x Tris-tricine SDS-Page kathode buffer (diluted to 1x with H_2O prior to use)	1 M Tris 1 M tricine 1% SDS pH was not adjusted
10x TGS (diluted to 1x with H_2O prior to use)	250 mM Tris 1.92 M glycine 1% SDS pH 8.8
1x TBS-T	20 mM Tris 150 mM NaCl 0.1% Tween-20 pH 7.5 (titrated with HCl)

4x Laemmli loading buffer	250 mM Tris 8% SDS 40% glycerol 50 mM DTT (omitted in non-reducing buffer) 0.002% bromophenol blue (omitted in colorless buffer) pH 6.8 (titrate with HCl)
Colloidal coomassie blue staining solution	0.02% Coomassie brilliant blue G250 5% aluminium sulfate 10% ethanol 2% orthophosphoric acid
6x DNA loading dye	5 ml glycerol 25 mg bromophenol blue 25 mg Xylene cyanol FF ad 10 ml with 10 mM Tris 1 mM EDTA pH 8.2
50x TAE-buffer (diluted to 1x with H_2O prior to use)	2 M Tris 1 M acetic acid 50 mM EDTA pH 8.5 (should not be adjusted)
TE-buffer	10 mM Tris 1 mM EDTA pH 8.0
Breaking buffer	10 mM Tris 100 mM NaCl 1% Triton X-100 1% SDS pH 8.0

Bind and wash buffer	20 mM Tris 1 M NaCl 1 mM EDTA 0.05% Triton X-100 pH 7.5
5x isothermal Gibson buffer	25% PEG-8000 500 mM Tris-HCl pH 7.5 50 mM $MgCl_2$ 50 mM DTT 5 mM NAD 1 mM of each of the four dNTPs (dATP, dCTP, dGTP, dTTP)
1.33x Gibson master mix	50 µl 5x Isothermal Gibson Buffer 0.625 µl in-house Taq DNA ligase (1600 U/µl) 0.5 µl in-house T5 exonuclease (2 U/µl) 3.1 µl Phusion polymerase (2 U/µl) 133.3 µl Milli-Q H_2O

5.3.1 Solutions used in emulsification and *in vitro* transcription translation (IVTT)

Mineral oil Abil EM90 surfactant mix	2% Abil EM90 0.05% Triton X-100 in mineral oil

PURExpress *in vitro* transcription translation mix (for 50 µl, as used in Abil EM90 emulsions)	20 µl Solution A (PURExpress kit, NEB) 15 µl Solution B (PURExpress kit, NEB) 0.5 µl RNAse inhibitor, murine (NEB) 2 µl PURExpress disulfide bond enhancer 1 (NEB) 2 µl PURExpress disulfide bond enhancer 2 (NEB) 2 µl DnaK enzyme (Genefrontier) 0.66 µl GroE enzyme (Genefrontier) 1.33 µl GroE dilution buffer (Genefrontier) 1 µl UltraPure BSA (Invitrogen) 2.5 µl 10 % Triton X-100 0.5 µl diluted Trace Metal Mix A5 with Co (diluted 1:100 in H_2O) 2 µl Milli-Q H_2O
PURExpress *in vitro* transcription translation mix (for 18 µl, as used in FluoSurf emulsions)	7.2 µl Solution A (PURExpress kit, NEB) 5.4 µl Solution B (PURExpress kit, NEB) 0.18 µl RNAse inhibitor, murine (NEB) 0.72 µl PURExpress disulfide bond enhancer 1 (NEB) 0.72 µl PURExpress disulfide bond enhancer 2 (NEB) 0.72 µl DnaK enzyme (Genefrontier) 0.24 µl GroE enzyme (Genefrontier) 0.48 µl GroE dilution buffer (Genefrontier) 0.36 µl UltraPure BSA (Invitrogen) 0.9 µl 10 % Triton X-100 0.18 µl diluted Trace Metal Mix A5 with Co (diluted 1:100 in H_2O) 0.72 µl Milli-Q H_2O

PURExpress solutions were usually scaled up according to the amount of samples that needed to be prepared. Recipes above list ingredients for a single emulsion reaction.

5.4 Primers

5.4.1 Primers specific for the pIgV plasmid (5’ to 3’)

Link-T7p For	AAGTGCTAGTGGTGCTAGCC
b-TEG-TGS-Link-T7p For	[biotin][TEG]TGTGTGTGTGTGTGTGTGTGTGTGAAGTGCTAGTGGTGCTAGCC
No-extension-T7-Term Rev	CAAAAAACCCCTCAAGACCCG
Vector Amplification For	GGTGCAGCAGAGCAGAAA
Vector Amplification Rev	CATGTCGACTCTCCTTCTTAAA
PROBE-FITC-488-T7p	[FITC]CCCTATAGTGAGTCGTATTA
PROBE-ATTO490LS-T7TERM	[ATTO490LS]CAAAAAACCCCTCAAGACCCG

5.4.2 Primer specific for the TEV sequence

qPCR TEV For	ATGAATCGTCGTCGCCGTC

5.4.3 Primers for the amplification of the antibody Fv repertoire from cDNA

Primers for the amplification of VH families (5’ to 3’):

These forward primers all introduce an overlap sequence to the 5’-UTR of the pIgV plasmid, a start codon and they contain the complementary sequence of the respective, indicated VH antibody family sequences (bold).

Vec-SalI-ATG-VH1/7-For	AGGAGAGTCGACATGGCC**CARRTSCAGCTGGTRCARTCTGG**
Vec-SalI-ATG-VH1-For	AGGAGAGTCGACATGGCC**SAGGTBCAGCTGGTGCAGTCTGG**
Vec-SalI-ATG-VH2-For	AGGAGAGTCGACATGGCC**CAGRTCACCTTGAAGGAGTCTGG**
Vec-SalI-ATG-VH3_1-For	AGGAGAGTCGACATGGCC**SARGTGCAGCTGGTGGAGTCTGG**
Vec-SalI-ATG-VH3_2-For	AGGAGAGTCGACATGGCC**GAGGTGCAGCTGKTGGAGWCYSG**
Vec-SalI-ATG-VH4_1-For	AGGAGAGTCGACATGGCC**CAGGTGCAGCTGCAGGAGTCGGG**
Vec-SalI-ATG-VH4_2-For	AGGAGAGTCGACATGGCC**CAGSTGCAGCTRCAGSAGTSSGG**
Vec-SalI-ATG-VH5-For	AGGAGAGTCGACATGGCC**GARGTGCAGCTGGTGCAGTCTGG**
Vec-SalI-ATG-VH6-For	AGGAGAGTCGACATGGCC**CAGGTACAGCTGCAGCAGTCAGG**

These forward primers all introduce part of the $(G_4S)_4$ linker sequence and they contain the complementary sequence of the respective, indicated VH family sequences (bold).

Link-VH1/7-For	AGCGGCGGCGGCGGCTCTGGTGGTGGTGGATCC**CARRTSCAGCTGGTRCARTCTGG**
Link-VH1-For	AGCGGCGGCGGCGGCTCTGGTGGTGGTGGATCC**SAGGTBCAGCTGGTGCAGTCTGG**
Link-VH2-For	AGCGGCGGCGGCGGCTCTGGTGGTGGTGGATCC**CAGRTCACCTTGAAGGAGTCTGG**
Link-VH3_1-For	AGCGGCGGCGGCGGCTCTGGTGGTGGTGGATCC**SARGTGCAGCTGGTGGAGTCTGG**
Link-VH3_2-For	AGCGGCGGCGGCGGCTCTGGTGGTGGTGGATCC**GAGGTGCAGCTGKTGGAGWCYSG**
Link-VH4_1-For	AGCGGCGGCGGCGGCTCTGGTGGTGGTGGATCC**CAGGTGCAGCTGCAGGAGTCGGG**
Link-VH4_2-For	AGCGGCGGCGGCGGCTCTGGTGGTGGTGGATCC**CAGSTGCAGCTRCAGSAGTSSGG**
Link-VH5-For	AGCGGCGGCGGCGGCTCTGGTGGTGGTGGATCC**GARGTGCAGCTGGTGCAGTCTGG**
Link-VH6-For	AGCGGCGGCGGCGGCTCTGGTGGTGGTGGATCC**CAGGTACAGCTGCAGCAGTCAGG**

These reverse primers are complementary to the sequences of the respective, indicated JH antibody family sequences (bold) and introduce a stop codon followed by an overlapping sequence with the 3'-UTR of the pIgV plasmid.

JH1_2_4_5-Vec-Rev	CTGCTCTGCTGCACC**TGAGGAGACRGTGACCAGGGTKCC**
JH3_6-Vec-Rev	CTGCTCTGCTGCACC**TGARGAGACGGTGACCRKKGTCCC**

These reverse primers are complementary to the sequences of the respective, indicated JH antibody family sequences (bold) and introduce part of the $(G_4S)_4$linker sequence.

JH1_2_4_5-Rev-Link	ACCAGAGCCGCCGCCGCCGCTACCACCACCACC**TGAGGAGACRGTGACCAGGGTKCC**
JH3_6-Rev-Link	ACCAGAGCCGCCGCCGCCGCTACCACCACCACC**TGARGAGACGGTGACCRKKGTCCC**

Primers for the amplification of VK families (5’ to 3’):

These forward primers all introduce an overlap sequence to the 5’-UTR of the pIgV plasmid, a start codon and they contain the complementary sequence of the respective, indicated VK antibody family sequences (bold).

Vec-SalI-ATG-VK1-For	AGGAGAGTCGACATGGCC**GMCATCCRGWTGACCCAGTCTCC**
Vec-SalI-ATG-VK2-For	AGGAGAGTCGACATGGCC**GATRTTGTGATGACYCAGWCTCC**
Vec-SalI-ATG-VK3-For	AGGAGAGTCGACATGGCC**GAAATWGTGWTGACRCAGTCTCC**
Vec-SalI-ATG-VK4-For	AGGAGAGTCGACATGGCC**GACATCGTGATGACCCAGTCTCC**
Vec-SalI-ATG-VK5-For	AGGAGAGTCGACATGGCC**GAAACGACACTCACGCAGTCTCC**
Vec-SalI-ATG-VK6-For	AGGAGAGTCGACATGGCC**GAWRTTGTGMTGACWCAGTCTCC**

These forward primers all introduce part of the $(G_4S)_4$ linker sequence and they contain the complementary sequence of the respective, indicated VK family sequences (bold).

Link-VK1-For	AGCGGCGGCGGCGGCTCTGGTGGTGGTGGATCC**GMCATCCRGWTGACCCAGTCTCC**
Link-VK2-For	AGCGGCGGCGGCGGCTCTGGTGGTGGTGGATCC**GATRTTGTGATGACYCAGWCTCC**
Link-VK3-For	AGCGGCGGCGGCGGCTCTGGTGGTGGTGGATCC**GAAATWGTGWTGACRCAGTCTCC**
Link-VK4-For	AGCGGCGGCGGCGGCTCTGGTGGTGGTGGATCC**GACATCGTGATGACCCAGTCTCC**
Link-VK5-For	AGCGGCGGCGGCGGCTCTGGTGGTGGTGGATCC**GAAACGACACTCACGCAGTCTCC**
Link-VK6-For	AGCGGCGGCGGCGGCTCTGGTGGTGGTGGATCC**GAWRTTGTGMTGACWCAGTCTCC**

These reverse primers are complementary to the sequences of the respective, indicated JK antibody family sequences (bold) and introduce a stop codon followed by an overlapping sequence with the 3'-UTR of the pIgV plasmid.

JK1-4-Vec-Rev	CTGCTCTGCTGCACC**TTTGATHTCCASYTTGGTCCC**
JK5-Vec-Rev	CTGCTCTGCTGCACC**TTTAATCTCCAGTCGTGTCCC**

These reverse primers are complementary to the sequences of the respective, indicated JK antibody family sequences (bold) and introduce part of the $(G_4S)_4$linker sequence.

JK1-4-Rev-Link	A C C A G A G C C G C C G C C G C C G C T A C C A C C A C C A C C **TTTGATHTCCASYTTGGTCCC**
JK5-Rev-Link	ACCAGAGCCGCCGCCGCCGCTACCACCACCACC**TGARGATTTAATCTCCAGTCGTGTCCCGACGGTGACCRKKGTCCC**

Primers for the amplification of VL families (5' to 3'):

These forward primers all introduce an overlap sequence to the 5'-UTR of the pIgV plasmid, a start codon and they contain the complementary sequence of the respective, indicated VL antibody family sequences (bold).

Vec-SalI-ATG-VL1-For	AGGAGAGTCGACATGGCC**CAGTCTGTGYTGACKCAGCC**
Vec-SalI-ATG-VL2-For	AGGAGAGTCGACATGGCC**CAGTCTGCCCTGACTCAGCC**
Vec-SalI-ATG-VL3-For	AGGAGAGTCGACATGGCC**TCCTMTGAGCTGACWCAG**
Vec-SalI-ATG-VL4ab-For	AGGAGAGTCGACATGGCC**CAGCYTGTGCTGACTCAATC**
Vec-SalI-ATG-VL4c-For	AGGAGAGTCGACATGGCC**CTGCCTGTGCTGACTCAGCC**
Vec-SalI-ATG-VL5-For	AGGAGAGTCGACATGGCC**CAGSCTGTGCTGACYCAGCC**
Vec-SalI-ATG-VL6-For	AGGAGAGTCGACATGGCC**AATTTTATGCTGACTCAGCCC**
Vec-SalI-ATG-VL7-For	AGGAGAGTCGACATGGCC**CAGRCTGTGGTGACTCAGGAGCCCTC**

These forward primers all introduce part of the $(G_4S)_4$ linker sequence and they contain the complementary sequence of the respective, indicated VL family sequences (bold).

Link-VL1-For	AGCGGCGGCGGCGGCTCTGGTGGTGGTGGATCC**CAGTCTGTGYTGACKCAGCC**
Link-VL2-For	AGCGGCGGCGGCGGCTCTGGTGGTGGTGGATCC**CAGTCTGCCCTGACTCAGCC**
Link-VL3-For	AGCGGCGGCGGCGGCTCTGGTGGTGGTGGATCC**TCCTMTGAGCTGACWCAG**
Link-VL4ab-For	AGCGGCGGCGGCGGCTCTGGTGGTGGTGGATCC**CAGCYTGTGCTGACTCAATC**
Link-VL4c-For	AGCGGCGGCGGCGGCTCTGGTGGTGGTGGATCC**CTGCCTGTGCTGACTCAGCC**
Link-VL5-For	AGCGGCGGCGGCGGCTCTGGTGGTGGTGGATCC**CAGSCTGTGCTGACYCAGCC**
Link-VL6-For	AGCGGCGGCGGCGGCTCTGGTGGTGGTGGATCC**AATTTTATGCTGACTCAGCCC**
Link-VL7-For	AGCGGCGGCGGCGGCTCTGGTGGTGGTGGATCC**CAGRCTGTGGTGACTCAGGAGCCCTC**

These reverse primers are complementary to the sequences of the respective, indicated JL antibody family sequences (bold) and introduce a stop codon followed by an overlapping sequence with the 3'-UTR of the pIgV plasmid.

JL1-3-Vec-Rev	CTGCTCTGCTGCACC**TAGGACGGTSASCTTGGTCCC**
JL7-Vec-Rev	CTGCTCTGCTGCACC**GAGGACGGTCAGCTGGGTGCC**

These reverse primers are complementary to the sequences of the respective, indicated JL antibody family sequences (bold) and introduce part of the $(G_4S)_4$ linker sequence.

JL1-3-Rev-Link	ACCAGAGCCGCCGCCGCCGCTACCACCACCACC**TAGGACGGTSASCTTGGTCCC**

JL7-Rev-Link	ACCAGAGCCGCCGCCGCCGCTACCACCACCACC**GAGGACGGTCAGCTGGGTGCC**

5.5 Plasmids

The pIgV plasmid was derived from the plasmid contained in the PURExpress kit encoding the DHFR control. DHFR was removed and a cloning-site was added containing the restriction sites SalI and NotI. These restriction sites were chosen as they are not present in antibody germline DNA sequences, as stated by V BASE. Furthermore, a c-myc tag was added, which would be in-frame and C-terminal to the antibody sequences which can be inserted using Gibson cloning technique.

The pIgV TEV plasmid was prepared by inserting the TEV protease sequence into the pIgV plasmid using Gibson cloning technique. The TEV sequence was obtained from a plasmid used in-house to produce TEV protease for recombinant protein production. The TEV sequence inserted into the pIgV plasmid contained an N-terminal TEV cleavage site, which was a remainder from the source plasmid, which originally contained an MBP-(TEV cleavage site)-TEV fusion protein. The TEV sequence further contained a C-terminal 5xR-tag that aimed to increase solubility.

pIgV

AAAAATAAACAAATAGGGGTTCCGCGCACATTTCCCCGAAAAGTGCTAGTGGTGCTAGCCCC
GCGAAATTAATACGACTCACTATAGGGTCTAGAAATAATTTTGTTTAACTTTAAGAAGGAGAG
TCGACATGGGTGCAGCAGAGCAGAAATTGATTTCTGAGGAAGATTTGTAGTGAGCGGCCGC
GCTAGCGGTCCCGGGGGATCGATCCGGCTGCTAACAAAGCCCGAAAGGAAGCTGAGTTGG
CTGCTGCCACCGCTGAGCAATAACTAGCATAACCCCTTGGGGCCTCTAAACGGGTCTTGAG
GGGTTTTTTGCTGAAAGGAGGAACTATATCCGGAAGCTTGGCACTGGCCGACCGGGGTCGA
GCACTGACTCGCTGCGCTCGGTCGTTCGGCTGCGGCGAGCGGTATCAGCTCACTCAAAGGC
GGTAATACGGTTATCCACAGAATCAGGGGATAACGCAGGAAAGAACATGTGAGCAAAAGGC
CAGCAAAAGGCCAGGAACCGTAAAAAGGCCGCGTTGCTGGCGTTTTTCCATAGGCTCCGCC
CCCCTGACGAGCATCACAAAAATCGACGCTCAAGTCAGAGGTGGCGAAACCCGACAGGACT
ATAAAGATACCAGGCGTTTCCCCCTGGAAGCTCCCTCGTGCGCTCTCCTGTTCCGACCCTGC
CGCTTACCGGATACCTGTCCGCCTTTCTCCCTTCGGGAAGCGTGGCGCTTTCTCATAGCTCA
CGCTGTAGGTATCTCAGTTCGGTGTAGGTCGTTCGCTCCAAGCTGGGCTGTGTGCACGAAC
CCCCCGTTCAGCCCGACCGCTGCGCCTTATCCGGTAACTATCGTCTTGAGTCCAACCCGCTA
AGACACGACTTATCGCCACTGGCAGCAGCCACTGGTAACAGGATTAGCAGAGCGAGGTATG
TAGGCGGTGCTACAGAGTTCTTGAAGTGGTGGCCTAACTACGGCTACACTAGAAGAACAGT
ATTTGGTATCTGCGCTCTGCTGAAGCCAGTTACCTTCGGAAAAAGAGTTGGTAGCTCTTGAT
CCGGCAAACAAACCATCGCTGGTAGCGGTGGTTTTTTTGTTTGCAAGCAGCAGATTACGCGC
AGAAAAAAAGGATCTCAAGAAGATCCTTTGATCTTTTCTACGGGGTCTGACGCTCAGTGGAA
CGAAAACTCACAGATCCGGGATTTTGGTCATGAGATTATCAAAAAGGATCTTCACCTAGATC
CTTTTAAATTAAAAATGAAGTTTTAAATCAATCTAAAGTATATATGAGTAAACTTGGTCTGACA
GTTACCAATGCTTAATCAGTGAGGCACCTATCTCAGCGATCTGTCTATTTCGTTCATCCATAG
TTGCCTGACTCCCCGTCGTGTAGATAACTACGATACGGGAGGGCTTACCATCTGGCCCCAG
TGCTGCAATGATACCGCGAGACCCACGCTCACCGGCTCCAGATTTATCAGCAATAAACCAGC
CAGCCGGAAGGGCCGAGCGCAGAAGTGGTCCTGCAACTTTATCCGCCTCCATCCAGTCTAT
TAATTGTTGCCGGGAAGCTAGAGTAAGTAGTTCGCCAGTTAATAGTTTGCGCAACGTTGTTG
CCATTGCTACAGGCATCGTGGTGTCACGCTCGTCGTTTGGTATGGCTTCATTCAGCTCCGGT
TCCCAACGATCAAGGCGAGTTACATGATCCCCCATGTTGTGCAAAAAAGCGGTTAGCTCCTT
CGGTCCTCCGATCGTTGTCAGAAGTAAGTTGGCCGCAGTGTTATCACTCATGGTTATGGCAG
CACTGCATAATTCTCTTACTGTCATGCCATCCGTAAGATGCTTTTCTGTGACTGGTGAGTACT
CAACCAAGTCATTCTGAGAATAGTGTATGCGGCGACCGAGTTGCTCTTGCCCGGCGTCAATA
CGGGATAATACCGCGCCACATAGCAGAACTTTAAAAGTGCTCATCATTGGAAAACGTTCTTC
GGGGCGAAAACTCTCAAGGATCTTACCGCTGTTGAGATCCAGTTCGATGTAACCCACTCGTG
CACCCAACTGATCTTCAGCATCTTTTACTTTCACCAGCGTTTCTGGGTGAGCAAAAACAGGA
AGGCAAAATGCCGCAAAAAAGGGAATAAGGGCGACACGGAAATGTTGAATACTCATACTCT
TCCTTTTTCAATATTATTGAAGCATTTATCAGGGTTATTGTCTCATGAGCGGATACATATTTGA
ATGTATTTAG

pIgV TEV

AATAGGGGTTCCGCGCACATTTCCCCGAAAAGTGCTAGTGGTGCTAGCCCCGCGAAATTAATACGACTC
ACTATAGGGTCTAGAAATAATTTTGTTTAACTTTAAGAAGGAGAGTCGACATGGAAAATCTTTATTTTCAA
GGTCATCATCATCATCATCATCATGGAGAAAGCTTGTTTAAGGGGCCGCGTGATTACAACCCGATATCGA
GCACCATTTGTCATTTGACGAATGAATCTGATGGGCACACAACATCGTTGTATGGTATTGGATTTGGTCC
CTTCATCATTACAAACAAGCACTTGTTTAGAAGAAATAATGGAACACTGTTGGTCCAATCACTACATGGTG
TATTCAAGGTCAAGAACACCACGACTTTGCAACAACACCTCATTGATGGGAGGGACATGATAATTATTCG
CATGCCTAAGGATTTCCCACCATTTCCTCAAAAGCTGAAATTTAGAGAGCCACAAAGGGAAGAGCGCATA
TGTCTTGTGACAACCAACTTCCAAACTAAGAGCATGTCTAGCATGGTGTCAGACACTAGTTGCACATTCC
CTTCATCTGATGGCATATTCTGGAAGCATTGGATTCAAACCAAGGATGGGCAGTGTGGCAGTCCATTAGT
ATCAACTAGAGATGGGTTCATTGTTGGTATACACTCAGCATCGAATTTCACCAACACAAACAATTATTTCA
CAAGCGTGCCGAAAAACTTCATGGAATTGTTGACAAATCAGGAGGCGCAGCAGTGGGTTAGTGGTTGGC
GATTAAATGCTGACTCAGTATTGTGGGGGGGCCATAAAGTTTTCATGGTGAAACCTGAAGAGCCTTTTCA
GCCAGTTAAGGAAGCGACTCAACTCATGAATCGTCGTCGCCGTCGCTAATAAGCGGCCGCGCTAGCGGT
CCCGGGGGATCGATCCGGCTGCTAACAAAGCCCGAAAGGAAGCTGAGTTGGCTGCTGCCACCGCTGAG
CAATAACTAGCATAACCCCTTGGGGCCTCTAAACGGGTCTTGAGGGGTTTTTTGCTGAAAGGAGGAACT
ATATCCGGAAGCTTGGCACTGGCCGACCGGGGTCGAGCACTGACTCGCTGCGCTCGGTCGTTCGGCTG
CGGCGAGCGGTATCAGCTCACTCAAAGGCGGTAATACGGTTATCCACAGAATCAGGGGATAACGCAGG
AAAGAACATGTGAGCAAAAGGCCAGCAAAAGGCCAGGAACCGTAAAAAGGCCGCGTTGCTGGCGTTTT
TCCATAGGCTCCGCCCCCCTGACGAGCATCACAAAAATCGACGCTCAAGTCAGAGGTGGCGAAACCCGA
CAGGACTATAAAGATACCAGGCGTTTCCCCCTGGAAGCTCCCTCGTGCGCTCTCCTGTTCCGACCCTGC
CGCTTACCGGATACCTGTCCGCCTTTCTCCCTTCGGGAAGCGTGGCGCTTTCTCATAGCTCACGCTGTAG
GTATCTCAGTTCGGTGTAGGTCGTTCGCTCCAAGCTGGGCTGTGTGCACGAACCCCCCGTTCAGCCCGA
CCGCTGCGCCTTATCCGGTAACTATCGTCTTGAGTCCAACCCGCTAAGACACGACTTATCGCCACTGGCA
GCAGCCACTGGTAACAGGATTAGCAGAGCGAGGTATGTAGGCGGTGCTACAGAGTTCTTGAAGTGGTG
GCCTAACTACGGCTACACTAGAAGAACAGTATTTGGTATCTGCGCTCTGCTGAAGCCAGTTACCTTCGGA
AAAAGAGTTGGTAGCTCTTGATCCGGCAAACAAACCATCGCTGGTAGCGGTGGTTTTTTTGTTTGCAAGC
AGCAGATTACGCGCAGAAAAAAAGGATCTCAAGAAGATCCTTTGATCTTTTCTACGGGGTCTGACGCTCA
GTGGAACGAAAACTCACAGATCCGGGATTTTGGTCATGAGATTATCAAAAAGGATCTTCACCTAGATCCT
TTTAAATTAAAAATGAAGTTTTAAATCAATCTAAAGTATATATGAGTAAACTTGGTCTGACAGTTACCAATG
CTTAATCAGTGAGGCACCTATCTCAGCGATCTGTCTATTTCGTTCATCCATAGTTGCCTGACTCCCCGTCG
TGTAGATAACTACGATACGGGAGGGCTTACCATCTGGCCCCAGTGCTGCAATGATACCGCGAGACCCAC
GCTCACCGGCTCCAGATTTATCAGCAATAAACCAGCCAGCCGGAAGGGCCGAGCGCAGAAGTGGTCCT
GCAACTTTATCCGCCTCCATCCAGTCTATTAATTGTTGCCGGGAAGCTAGAGTAAGTAGTTCGCCAGTTA
ATAGTTTGCGCAACGTTGTTGCCATTGCTACAGGCATCGTGGTGTCACGCTCGTCGTTTGGTATGGCTTC
ATTCAGCTCCGGTTCCCAACGATCAAGGCGAGTTACATGATCCCCCATGTTGTGCAAAAAAGCGGTTAGC
TCCTTCGGTCCTCCGATCGTTGTCAGAAGTAAGTTGGCCGCAGTGTTATCACTCATGGTTATGGCAGCAC
TGCATAATTCTCTTACTGTCATGCCATCCGTAAGATGCTTTTCTGTGACTGGTGAGTACTCAACCAAGTCA
TTCTGAGAATAGTGTATGCGGCGACCGAGTTGCTCTTGCCCGGCGTCAATACGGGATAATACCGCGCCA
CATAGCAGAACTTTAAAAGTGCTCATCATTGGAAAACGTTCTTCGGGGCGAAAACTCTCAAGGATCTTAC
CGCTGTTGAGATCCAGTTCGATGTAACCCACTCGTGCACCCAACTGATCTTCAGCATCTTTTACTTTCACC
AGCGTTTCTGGGTGAGCAAAAACAGGAAGGCAAAATGCCGCAAAAAAGGGAATAAGGGCGACACGGAA
ATGTTGAATACTCATACTCTTCCTTTTTCAATATTATTGAAGCATTTATCAGGGTTATTGTCTCATGAGCGG
ATACATATTTGAATGTATTTAGAAAAATAAACA

5.6 Peptides

TEV-target

[biotin][PEG12]K(5FAM)MKGDGGSENLYFQSGDHG DGSC(Cy5) 4179.9 Da	Pepscan

5.7 Devices

0.1–2.5 µl pipette Research	Eppendorf
2–20 µl pipette Research plus	Eppendorf
20–200 µl pipette Research plus	Eppendorf
100–1000 µl pipette Research plus	Eppendorf
Centrifuge 5425 R	Eppendorf
Cell Disruptor	Constant Systems LTD
CLARIOstar	BMG Labtech
CytoFLEX S	Beckman Coulter
CytoFLEX SRT	Beckman Coulter
FACSCanto II	BD Biosciences
FACSAria III	BD Biosciences
G:Box, gel documentation system	Syngene
Gel Doc XR System	BIO-RAD
HPLC-Chromatograph, 1260 Infinity	Agilent Technologies
HPLC-Column, Zorbax 300SB-C8, 4.6 x 250 mm	Agilent Technologies
MagnaRack Magnetic Separation Rack	Invitrogen
Mastercycler epgradient S	Eppendorf
Microwave MW7873	Severin
Mini-Centrifuge	Fisherbrand
Mini-PROTEAN Tetra Vertical Electrophoresis Cell	BIO-RAD

Mini-Sub Cell GT	BIO-RAD
NanoDrop 2000 spectrophotometer	Thermo scientific, PEQLAB
NGC Discover System	BIO-RAD
PerfectBlue Gelsystem, Maxi M	VWR
Power Source power supply, 300V	VWR
QS High Precision Cell, 10mm light path, centre 15	Hellma Analytics
qTower^3 G, qPCR cycler	Analytik Jena
Sonicator bath SONOREX RK100H	Bandelin
Spectrophotometer V-650	Jasco
Sub-Cell GT Gel Caster	BIO-RAD
ThermoMixer C	Eppendorf
Trans-Blot Turbo, Transfer system	BIO-RAD
TruBlu Blue Light Transilluminator	Edvotek
VV3 vortexer	VWR

5.7.1 The iTrapR: A magnetic microstirrer with ice water bath functionality

The iTrapR (details shown in Figure 5.1) was designed to accomodate for precise, speed-controlled magnetic stirring while optimally clamping 2 ml Agilent glass vials to the middle of the microstirrer rotors. Furthermore, the iTrapR provides the opportunity to simultaneously cool samples in an ice water bath. The iTrapR provides four independently controlled microstirrers and ice water baths. Speeds may be set individually from 0 – 2100 RPM and are monitored using a photoelectric speedometer. Timers can be set individually for each microstirrer and they automatically stop the rotation of the respective microstirrer when they counted down to zero. I designed the iTrapR using Blender3D and it was mostly 3D printed. It is controlled using an Arduino Mega 2560 REV3. Build details and programs are beyond the scope of this thesis, but the interested reader may send a request in case further details are desired.

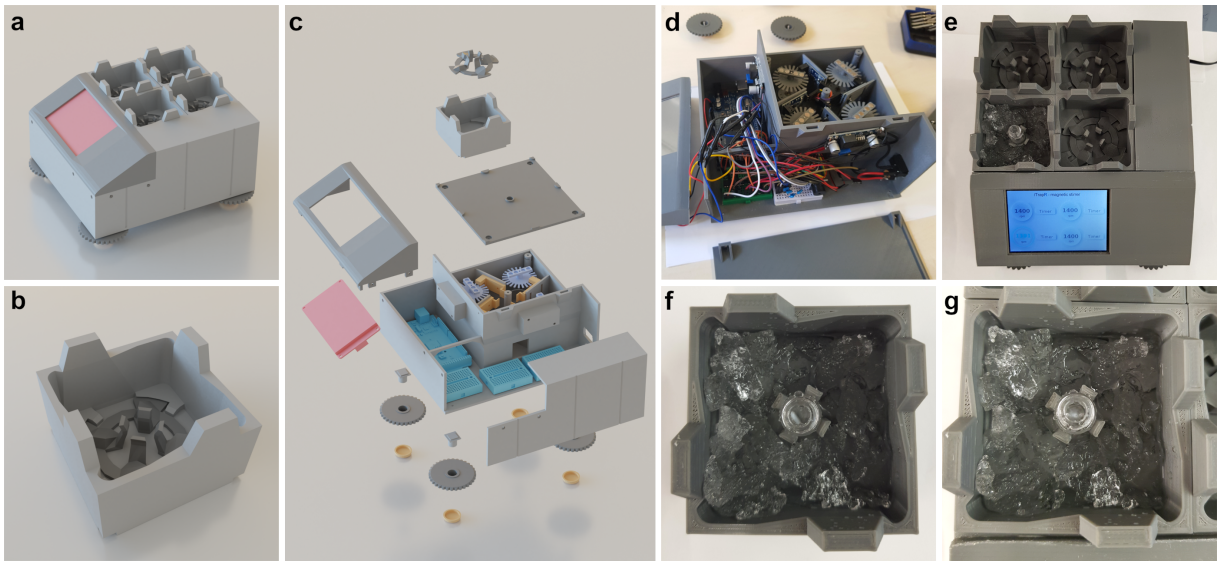

Figure 5.1: The iTrapR: A magnetic microstirrer with ice water baths. a) assembled 3D rendering of the iTrapR. b) 3D rendering of an ice water bath with the clamp to hold the 2 ml Agilent glass vials. c) an exploded 3D rendering of the iTrapR showing the internal design of the device. d) the internal setup and wiring of an iTrapR prototype assembly. e) assembled and running iTrapR prototype. f) ice water bath filled with water and ice while clamping a 2 ml Agilent glass vial. The 2x7 mm microstirbar can be seen in the vial. g) ice water bath from e) was inserted into a slot of the iTrapR and the spinning microstirbar can be appreciated.

5.8 Consumables

8-Lid chain, flat	Sarstedt
Acrodisc Syringe Filter with Supor Membrane - 0.2 µm, 13 mm	Pall corporation
Amersham Hybond P 0.2 PVDF membrane	Cytiva
Amersham Protran 0.2 µm NC, blotting membrane	GE Healthcare
Amicon Ultra Centrifugal Filters, 15 ml	Merck
Assay Plate 3881, 96-well Half Area, No Lid, Non-Binding Surface, Black with Clear Bottom, Polystyrene	Corning
Blotting Paper, 703	VWR

Cover slip, glass, 24 x 60 mm	Menzel-Gläser
Cover slip, glass, 22 x 22 mm	Menzel-Gläser
Filter tips 2.5 µl, Biosphere plus	Sarstedt
Filter tips 20 µl, Biosphere plus	Sarstedt
Filter tips 200 µl, Biosphere plus	Sarstedt
Glass vial, screw, 2 ml, ambr, WrtOn	Agilent Technologies
Glass vial insert, 250 µl pulled point glass	Agilent Technologies
Glass vial blue screw caps & septa	Agilent Technologies
Multiply-Pro cup 0.2ml, PP, PCR tubes	Sarstedt
Multiply-µStrip cup 0.2ml, white, PCR tubes	Sarstedt
PCR Film, adhesive	Eppendorf
Protein LoBind Tube 0.5 ml	Eppendorf
Protein LoBind Tube 1.5 ml	Eppendorf
Quality Pipette Tips 100-1000 µl	Sarstedt
SealPlate film	Sigma-aldrich
SafeSeal tube 1.5 ml, PP	Sarstedt
SafeSeal micro tube 2 ml, PP	Sarstedt
Tube 15 ml, 120 x 17 mm, PP	Sarstedt
Tube 50 ml, 114 x 28 mm, PP	Sarstedt
twin.tec PCR Plate 96, semi-skirted, blue	Eppendorf

6. Methods

6.1 General molecular biology methods

6.1.1 Analysis of DNA via agarose gel electrophoresis

Usually, a 1% agarose gel was prepared by dissolving 0.5 g agarose in 50 ml 1x TAE buffer and melting the agarose by heating in a microwave with intermittened shaking. The molten agarose was cooled down in a water bath until the flask could be barely touched by hands. 3 µl 10,000x GelRed DNA staining solution was added and mixed in. The agarose was poured into an agarose tray clamped into a gel caster and the appropriate combs were inserted. The gel polymerized while cooling to RT for 30 minutes. The tray was removed from the gel caster and placed into the electrophoresis chamber filled with 1x TAE buffer. DNA samples were mixed with 6x DNA loading buffer and filled into the wells. DNA was separated by length by applying 120 V for 1 hour.
DNA was illuminated using UV light and imaged using a G:Box gel documentation system.

6.1.2 Extraction of DNA from agarose gel

After electrophoresis, a desired DNA band was excised from the agarose gel using a scalpel, while being illuminated using a TruBlu Blue Light Transilluminator to visualize the DNA. The band of interest was excised and DNA was extracted using the NucleoSpin Gel and PCR Clean-up Mini kit according to the manual. DNA was eluted using 20–30 µl 5 mM Tris pH 8.5 (supplied in the kit), but in deviation to the manual, the sample was incubated in a Thermomixer at 65°C at 800 RPM for 5 minutes prior to elution, which increased the total yield.

6.1.3 Determination of nucleic acid concentration

Concentration of nucleic acids was determined using a NanoDrop 2000 photospectrometer. 1.5 µl of the nucleic acid solution was applied on the sample pedestal and measured using the appropriate device settings for RNA or DNA. A spectrum was measured and the concentration determined using optical density (O.D.) at 260 nm wavelength. An O.D. of 1 corresponds to 40 µg/ml RNA or 50 µg/ml DNA. Purity was assessed by the ratio between the O.D. at 260 nm and 280 nm. A 260/280 ratio of ∼1.8 was considered pure for DNA and ∼2.0 for RNA.

6.1.4 Determination of protein concentration

Protein concentration was determined using UV-Vis spectroscopy using the Spectrophotometer V-650 (Jasco) with QS High Precision Cell cuvettes (Hellma Analytics). The device utilizes a split beam setup allowing simultaneous measurement of a sample and its blank. Spectra were recorded in the wavelength range of 210–340 nm with a scan speed of 400 nm/min and a bandwidth of 1.0 nm in continuous scan mode. 80–100 µl of an appropriately diluted protein sample was pipetted into a cuvette and the respective blank buffer control into another cuvette. Both cuvettes were inserted into the device into the respective sample and blank slots. After measurement, the absorption at 280 nm was corrected by substracting the absorption at 340 nm and was then used to calculate the concentration of the protein sample using the lambert-beer equation: $A = {}_{280nm} \cdot d \cdot c$. The extinction coefficient (ε) at 280 nm for IgG (MW 150–180 kDa) was 210,000 $M^{-1}cm^{-1}$ and for IgM (MW 900 kDa) was 1,062,000 $M^{-1}cm^{-1}$.

6.1.5 Protein analysis by sodium dodecyl sulfate polyacrylamide gel electrophoresis (SDS-PAGE)

Analyses of proteins by their molecular weight was performed using SDS-PAGE. SDS-PAGE gels were composed of a stacking and a resolving gel. Depending on the molecular weight of the protein of interest a Tris-glycine gel or a Tris-tricine gel was

Table 6.1: Composition of 8% tris-glycine gels — amount sufficient for **2 gels**

	resolving gel	**stacking gel**
1.5 M Tris-HCl, pH 8.8	2.5 ml	-
0.5 M Tris-HCl, pH 6.8	-	1.5 ml
Rotiphorese Gel 30 (37.5:1)	2.6 ml	830 µl
Milli-Q H_2O	4.7 ml	2.8 ml
10% SDS	100 µl	50 µl
TEMED	10 µl	10 µl
10% APS	100 µl	50 µl

Table 6.2: Composition of 20% tris-tricine gels — amount sufficient for **4 gels**

	resolving gel	**stacking gel**
3 M Tris-HCl, 0.3% SDS, pH 8.45	10 ml	4.2 ml
34.3% acrylamide, 1.1% bisacrylamide	17 ml	2 ml
Glycerol	3.2 ml	-
Milli-Q H_2O	2.3 ml	2.8 ml
TEMED	50 µl	50 µl
10% APS	100 µl	100 µl

used for larger (> 40 kDa) or smaller (< 40 kDa) proteins, respectively. Tris-glycine gels were usually 8% and Tris-tricine gels were 20% polyacrylamide gels. Stacking gels contained 5 % polyacrylamide.

The SDS-PAGE's glass plates were assembled in the casting device according to the manufacturer's instructions. The polyacrylamide resolving gel was prepared first. All components were mixed and APS was added as the last ingredient, starting the polymerization process. While still liquid, the solution was pipetted into the 0.75 mm opening between the two glass slides until filled $\sim$1.5 cm to the top. The rest of the chamber was filled with isopropanol. This ensured a flat polymerization of the interphase. After the resolving gel was fully polymerized, isopropanol was removed

and the stacking gel, while still liquid, was layered on top. The appropriate comb was inserted into the opening. After polymerization was completed the casted SDS-PAGE gels were either used at the same day or stored wrapped in wet paper towels for up to one week at 4°C.

SDS-PAGE gels were placed into a Mini-PROTEAN electrophoresis chamber. For Tris-glycine gels, 1x TBS buffer was filled into the cathode and anode chamber. For Tris-tricine gels, 1x Tris-tricine kathode buffer was filled into the kathode chamber and 1x Tris-tricine anode buffer was filled into the anode chamber (buffer compositions listed in section 5.3).

Protein samples were prepared by mixing with 4x laemmli loading buffer to a 1x solution (e.g. 2.5 µl 4x laemmli loading buffer with 7.5 µl protein sample). Samples were heated to 95°C for 5 minutes, unless stated otherwise, and then loaded into the wells of the SDS-PAGE gel. Additionally, the appropriate prestained protein marker was loaded into a free well. Samples were separated by applying a fixed current of 30 mA per gel for 1–4 hours until either the bromophenol blue stain left the gel at the bottom or in case the colorless laemmli loading buffer was used, until the prestained protein marker traveled a satisfactory distance.

The chamber was disassembled and the gel removed from the glass sandwich. Subsequently, the gel was further either used in western blot analysis or for immediate detection of fluorescent proteins *in situ* using a Gel Doc XR System or stained using colloidal coomassie blue solution. Therefore, the gel was placed in a plastic tray and covered with the colloidal coomassie blue solution and incubated overnight with agitation. If necessary, the gel was destained with 2% acetic acid, 10% ethanol while a paper tissue was added into the tray to capture released stains. The gel was agitated until the destaining was satisfactory. The gel was rinsed three times with H_2O and images were recorded on a Gel Doc XR System.

6.1.6 Western blot analysis

After SDS-PAGE, the gel was removed from the glass cassette and washed multiple times with H_2O and subsequently the stacking gel was separated from the resolving gel and discarded. A 0.2 µm PVDF membrane was cut to the size of the resolving

gel and activated in 100% ethanol for a few minutes. Six sheets of western blot paper were cut to the same size as the membrane and soaked in 1x TGS buffer. The western blot sandwich was assembled by placing three sheets of soaked, but not dripping wet, western blot paper into a chamber of the semi-dry Trans-Blot Turbo transfer system. The activated PVDF membrane was removed from the ethanol, quickly rinsed in 1x TGS and added ontop of the western blot paper. The resolving gel was carefully placed and aligned ontop of the PVDF membrane and the remaining three soaked, but not dripping, western blot paper sheets were placed ontop. Bubbles were removed with a western blot roller. Excess liquid around the western blot sandwich was removed with a tissue. The chamber was closed and placed into the transfer device. The transfer was performed using the standard program of the device. Afterwards, the chamber was disassembled and the membrane was carefully removed from the sandwich. The membrane was placed into a 50 ml conical tube and the entire subsequent treatment was performed in the tube. The membrane was blocked with 5 % skimmed milk in 1x TBS-T. The tube was placed on a tube roller mixer for 30 minutes. The primary antibody was usually diluted 1:1000 in 5% skimmed milk in a total volume of 5 ml. The skimmed milk solution used for blocking was removed from the tube and the 5 ml primary antibody solution was added. The primary antibody was either incubated for 1 hour at room temperature on a tube roller mixer or overnight at 4°C. Afterwards, the membrane was washed 5x with 1x TBS-T for 5 minutes on a tube roller mixer. The HRP-conjugated secondary antibody was usually diluted 1:5000 in 5% skimmed milk in a total volume of 5 ml. The wash liquid was discarded from the tube containing the membrane and the secondary antibody solution was added. The secondary antibody was incubated for 30 minutes to 1 hour at room temperature on a tube roller mixer. Subsequently, the membrane was again washed 5x with 1x TBS-T with 5 minutes of incubation each.

Western blot was developed using SuperSignal West Pico Plus according to the manual and recorded using a Gel Doc XR System.

6.2 Antibody library preparation

The following sections describe the methods involved in the antibody library preparations.

6.2.1 Isolation of peripheral blood mononuclear cells (PBMC)

In this study, buffy coat samples from human donors were processed. Processing of human buffy coat samples was approved by the ethics committee of the Heinrich-Heine University Düsseldorf (Study-No.: 6144R — ”Erstellung einer Antikörperbibliothek für die therapeutische Grundlagenforschung”). PBMCs were isolated from human buffy coats using the ficoll-paque density gradient centrifugation technique. Therefore, 25 ml of the buffy coat was diluted with 25 ml 1x PBS, 2 mM EDTA, pH 7.2. 15 ml ficoll-paque was placed into a 50 ml conical tube and 35 ml of the diluted buffy coat was carefully layered on top of the ficoll-paque layer. After centrifugation at 400 x g for 40 minutes at 20°C in a swing-out rotor with brakes turned to the lowest setting of the centrifuge, the PBMC layer was transferred to a fresh 50 ml conical tube using pasteur pipettes. The cells were washed by filling the tube with 1x PBS, 2 mM EDTA, pH 7.2 and centrifugation at 300 x g for 10 minutes at 20°C. To remove contaminating platelets, the PBMCs were washed two more times by filling the tube with 1x PBS, 2 mM EDTA, pH 7.2 and centrifugation at 200 x g for 15 minutes at 20°C. Subsequently, the cells were resuspended in 5 ml 1x PBS, 2 mM EDTA, pH7.2 and counted using a hemocytometer after trypan blue staining.
Staining was performed by mixing 50 µl of the cell suspension with 50 µl 0.4% trypan blue solution. 10 µl of the stained cells were applied onto the hemocytometer slide and cells were counted according to the manufacturer’s instructions and calculations.
Subsequently, the cells were aliquoted into 2 ml tubes at 1–2x10^7 cells per tube. The cells were pelleted by brief centrifugation at 1000 x g for 1 minute at RT. The supernatant was removed and the cells resuspended and lysed in 1 ml TRIzol. Lysed samples were stored at -20°C for up to 6 months without any apparent loss of quality in the RNA.

6.2.2 mRNA isolation

First, total RNA was isolated from the PBMCs by TRIzol extraction. Therefore, cells lysed in TRIzol were subjected to further mechanical homogenization using QIAshredder columns. Lysates were transferred to QIAshredder columns and homogenized by centrifugation at 16.100 x g at RT for 2 minutes.
Total RNA was isolated according to the instructions of the TRIzol manufacturer. Briefly, 0.2 ml chloroform was added per 1 ml of TRIzol reagent used for lysis. Samples were incubated for 2–3 minutes and subsequently centrifuged at 12,000 x g for 15 minutes at 4°C. The upper, colorless, aqueous layer was transferred to a new tube, while avoiding disturbance of the interphase. 0.5 ml isopropanol was added to the aqueous phase per 1 ml of initial TRIzol reagent used. Samples were incubated for 10 minutes at RT followed by centrifugation at 12,000 x g for 10 minutes at 4°C. RNA formed a pellet and the supernatant was removed using a micropipette. The pellet was resuspended in 1 ml 75% ethanol per 1 ml of initial TRIzol reagent used. Samples were vortexed briefly and then centrifuged at 7.500 x g for 5 minutes at 4°C. The supernatant was removed using a micropipette and the RNA was dried under a sterile bench for approx. 30 minutes. RNA was resuspended in 20 µl RNAse-free Milli-Q H_2O and placed on ice immediately. The total yield was typically between 25 and 50 µg as determined by Nanodrop sprectrometry.
RNA quality control was performed by separating 2 µl of the total RNA with 2 µl 6x DNA loading dye and 6 µl RNAse-free Milli-Q H_2O on a 1 % agarose gel.
Isolation of mRNA from total RNA was performed using the Dynabeads mRNA Purification kit immediately after total RNA isolation. Depending on the total RNA yield, the amount of Dynabeads used for isolation was adjusted (200 µl Dynabead solution for 75 µg total RNA). Dynabeads were washed by magnetic separation with 100 µl Binding Buffer (supplied in the kit). Total RNA was adjusted by dilution with RNAse-free Milli-Q H_2O to a total volume of 100 µl and incubated at 65°C for 2 minutes. A 1:1 ratio of Binding Buffer to sample volume was recommended by the manufacturer. Diluted total RNA was added to the Dynabeads and were incubated while shaking at 800 RPM for 5 minutes at RT. Subsequently, Dynabeads were washed twice with 200 µl Washing Buffer B (supplied in the kit). Dynabeads were resuspended in 20

µl 10 mM Tris-HCl pH 7.5 and heated to 65°C for 2 minutes to elute the mRNA and were immediately placed into a magnet rack. The eluted mRNA was transferred to a new tube, concentration was determined using a Nanodrop spectrometer and then immediately used for cDNA synthesis.

6.2.3 Generation of cDNA

Synthesis of cDNA from mRNA was performed separately for each donor using the SuperScript IV First-Strand Synthesis System according to the manufacturer's instructions. Briefly, for each mRNA preparation 1 µl 50 µM oligo $d(T)_{20}$ primer, 1 µl 10 mM dNTPs and 11 µl mRNA (but only up to 500 ng total, if it would have been exceeded the rest was instead substituted by DEPC-treated water – all preparations contained between 170–500 ng) were mixed and incubated at 65°C for 5 minutes and then incubated on ice for 1 minute. Subsequently, 4 µl 5x SSIV Buffer, 1 µl 100 mM DTT, 1 µl RNaseOUT Recombinant RNase Inhibitor and 1 µl SuperScript IV Reverse Transcriptase (200 U/µl) were added and mixed. Samples were incubated at 50°C for 10 minutes followed by 10 minutes at 80°C. Finally, 1 µl RNase H was added and incubated at 37°C for 20 minutes.
As storage in the SuperScript mixture lead to premature degradation of the cDNA, it was purified using the NucleoSpin Gel and PCR Clean-up kit for long-term storage. Finally, the concentration of the cDNA was determined by spectroscopy using a Nanodrop 2000 photospectrometer.

6.2.4 Antibody Fv amplification from cDNA

For Fv amplification from cDNA, PCRs were performed with an equimolar mixture of the cDNA preparations of all ten donors as input. Twelve PCRs were performed, one for each primer subgroup, as listed in Table 3.2. The composition and temperature profiles of the PCRs are listed in Tables 6.3 and 6.4, respectively. Annealing temperatures were optimized for each primer subgroup and are indicated in Table 3.2.
After PCR, the DNA was resolved on a 1% agarose gel and the corresponding bands of the Fv-amplicons were excised from the gel and eluted using NucleoSpin Gel and PCR Clean-up kit.

Table 6.3: PCR composition used in the generation of Fv-amplicons using CloneAmp HiFi PCR premix.

Component	Volume
2x CloneAmp HiFi PCR Premix	25 µl
Primer Subgroup Mix [10 µM]	2.5 µl
Primer Subgroup Mix [10 µM]	2.5 µl
cDNA mix (10% of the total PCR volume)	5 µl
Milli-Q H_2O	15 µl

Table 6.4: PCR temperature profile used in the generation of Fv-amplicons for library preparation.

Temperature	Time	Cycles
94°C	2 min	
94°C	1 min	|
60°C or 62°C or 65°C	1 min	35x
72°C	2 min	|
72°C	10 min	
15°C	hold	

6.2.5 Preparation of linear pIgV plasmid

Linear pIgV plasmid for Gibson assembly was generated by PCR as described in Table 6.5 using the temperature profile in Table 6.6. After PCR the DNA was resolved on a 1% agarose gel and the corresponding band of the linearized pIgV plasmid (2234 bp) was excised. Subsequently, the linear plasmid was purified and eluted from the gel via NucleoSpin Gel and PCR Clean-up kit and concentration was determined by photospectrometry.

6.2.6 Gibson assembly of antibody libraries

An in-house made 1.33x Gibson assembly mixture (see Section 5.3) was used to introduce the Fv-amplicons into the pIgV plasmid. Gibson assembly facilitates the

Table 6.5: PCR composition used in the generation of linear pIgV plasmid for library preparation using CloneAmp HiFi PCR premix.

Component	**Volume**
2x CloneAmp HiFi PCR Premix	25 µl
Primer [10 µM] — Vector Amplification For	2.5 µl
Primer [10 µM] — Vector Amplification Rev	2.5 µl
Template DNA — pIgV plasmid	1 µl (50-500 pg/µl)
Milli-Q H_2O	19 µl

Table 6.6: PCR temperature profile used in the generation of linear pIgV plasmid for library preparation.

Temperature	**Time**	**Cycles**
98°C	2 min	
98°C	30 s	|
57°C	30 s	35x
72°C	2 min	|
72°C	5 min	
15°C	hold	

conjunction of multiple DNA-fragments via homologous sequences (15–80 bp) at the end of the fragments. DNA fragments with the respective homologous ends were mixed 1:3 with the 1.33x Gibson assembly mixture (e.g. 5 µl DNA-fragments and 15 µl 1.33x Gibson assembly mixture) and incubated for 1 hour at 50°C to facilitate enzymatic assembly.

Assembly of LibNano. 100 ng of each Fv-amplicon encoding Nanobodies (ATG-VL60-Stop, ATG-VL65-Stop, ATG-VK62-Stop and ATG-VH65-Stop) were mixed with 1 µg linearized pIgV plasmid in a total volume of 41.5 µl. 124.5 µl 1.33x Gibson assembly mixture was added to the DNA and subsequently incubated at 50°C for 1 hour.

Assembly of LibIgV$_2$. 100 ng of each Fv-amplicon encoding half of an IgV$_2$ (ATG-VL60-Link, ATG-VL65-Link, ATG-VK62-Link, ATG-VH65-Link, Link-VL60-Stop, Link-VL65-Stop, Link-VK62-Stop and Link-VH65-Stop) were mixed with 1 µg linearized pIgV plasmid in a total volume of 53 µl. 161 µl 1.33x Gibson assembly mixture was added to the DNA and subsequently incubated at 50°C for 1 hour.

Subsequently, the DNA was resolved on a 1% agarose gel and the band corresponding to the assembled product was excised, eluted via NucleoSpin Gel and PCR Clean-up kit and used for the preparation of linear input DNA for PACMAN (see Section 6.4.2).

6.3 Methods utilized to isolate and study polyclonal antibodies from human plasma

The plasma supernatants of the Ficoll-Paque density gradient centrifugations used to isolate PBMCs from donor buffy coats were scavenged to furhter purify polyclonal IgG and IgM to assess the presence of specific proteolytic activity as a mechanism of action of adaptive immunity.

6.3.1 Isolation of IgG antibodies from human plasma

Polyclonal IgG was isolated from human plasma using Protein A-functionalized agarose resin. Therefore, plasma was buffered by a 1:10 addition of 10x PBS. Two milliliter of Protein A-functionalized agarose slurry was transferred to a gravity flow column and equilibrated with 10 CV 1x PBS. Most of the liquid was removed and a stopper was placed onto the tip of the column to stop the flow. 2 ml of the buffered plasma was added to the column and incubated for 10 minutes with intermittened shaking. The column was washed with 10 CV 1x PBS and the flow through was collected as IgG-depleted plasma, which was subsequently used for IgM isolation. IgG was acid eluted using 10 ml 0.1 M glycine pH 3.5. Immediately afterwards, 1 ml 1 M tris pH 8.0 was added to the collection flask to adjust the pH. The neutralized eluate was transferred to a 50 kDa MWCO Amicon Ultra Centrifugal Filter and buffer was

exchanged twice with 1x PBS by centrifugation at 4,000 x g. Samples were filtered using a 0.2 µm PES syringe filter. Concentration of IgG was determined via UV-Vis spectroscopy and lambert-beer equation using $\varepsilon_{280\,nm}$ = 210,000 $M^{-1}cm^{-1}$.

6.3.2 Isolation of IgM antibodies from human plasma

Polyclonal IgM was isolated from IgG-depleted human plasma which was a byproduct of IgG isolation. 1 ml LigaTrap human IgM resin slurry was transferred to a gravity flow column and equillibrated with 10 CV 10 mg/ml adipic acid, 800 mM NaCl, pH 5.8. The IgG-depleted plasma was diluted 1:4 with 50 mg/ml adipic acid, 4.0 M NaCl, pH 5.8 and added to the column. The sample was incubated on the column for 10 minutes with intermittened shaking. Resin was washed with 20 CV 10 mg/ml adipic acid, 800 mM NaCl, pH 5.8 and subsequently eluted with 10 ml 0.1 M sodium acetate, pH 4.0. The eluate was neutralized with 12% 3.0 M tris-base, pH 11.1. The neutralized eluate was transferred to a 50 kDa MWCO Amicon Ultra Centrifugal Filter and buffer was exchanged twice with 1x PBS by centrifugation at 4,000 x g.
IgM was further purified by size exclusion chromatography using a Superdex 200 10/300 column on an NGC Discover System for liquid chromatography. The column was equillibrated with 1x PBS and samples were loaded onto the column. IgM eluted in the void volume peak, which was collected and transferred to a 50 kDa MWCO Amicon Ultra Centrifugal Filter to increase the concentration by centrifugation at 4,000 x g.
As a final purification step, CaptureSelect human IgM resin was used to further purify the IgM with high specificity. 1 ml CaptureSelect human IgM resin slurry was transferred to a gravity flow column and equillibrated with 10 CV 1x PBS. IgM samples were added to the resin and incubated for 10 minutes with intermittened shaking. Column was washed with 20 CV 1x PBS and IgM was eluted with 10 ml 0.1 M glycine pH 3.5. The eluate was immediately neutralized with 1 ml 1 M tris pH 8.0. The neutralized eluate was transferred to a 50 kDa MWCO Amicon Ultra Centrifugal Filter and buffer was exchanged twice with 1x PBS by centrifugation at 4,000 x g. Samples were filtered using a 0.2 µm PES syringe filter. Concentration of IgM

was determined via UV-Vis spectroscopy and lambert-beer equation using $\varepsilon_{280\,nm}$ = 1,062,000 $M^{-1}cm^{-1}$.

6.3.3 Evaluation of proteolytic antigen cleavage by antibodies

Proteolytic activity of polyclonal IgG and IgM was assessed by coincubation with amyloid peptides and subsequent analysis via reverse-phase HPLC. Therefore, the tips of 0.5 ml low-bind reaction tubes were cut off and placed flush into 2 ml Agilent glass vials for HPLC so that it was still possible to seal the glass vials with septed screw caps. These reaction vessels were able to hold 50 µl reaction volume and were used to coincubate the Igs with amyloid peptides. Typically, 25 µM of the respective amyloid peptide and 10 nM of polyclonal IgM or 0.25 µM of polyclonal IgG in a total volume of 50 µl in 1x PBS were incubated quiescently at 37°C for 96 hours.

6.3.4 High-Pressure Liquid Chromatography analysis

Amyloid proteolysis products generated by the proteolytic activity of Igs were analyzed by reverse-phase high-pressure liquid chromatography (RP-HPLC) on a 1260 Infinity HPLC-Chromatograph by Agilent Technologies using a Zorbax 300SB-C8 4.6 x 250 mm column applying a linear gradient of 0–80% ACN 0.1% TFA over 40 minutes. 20 µl samples were injected using the autosampler of the HPLC device. Data analysis was performed using python version 3.8 and matplotlib version 3.3.0. Chromatogram data was baseline corrected by substraction of a 7^{th}-order polynomial fit.

6.4 Methods related to PACMAN

6.4.1 Synthesis of the Aβ-target peptide

$MA\beta_{40}C$ was recombinantly produced by coexpression of $MA\beta_{40}C$ and $Z_{A\beta3}$ as previously described for the production of Aβ and dimAβ [128, 300]. Both $MA\beta_{40}C$ and $Z_{A\beta3}$ were encoded on the bacterial expression vector pACYCDuet-1 (Novagen) which was designed for bicistronic expression. $MA\beta_{40}C$ was inserted into the first

multiple cloning site (MCS) and $Z_{A\beta3}$, as a His-tagged $(His)_6$-$Z_{A\beta3}$ variant, was cloned into the second MCS of the vector. BL21(DE3) *E.coli* cells were transformed with the plasmid and overnight precultures were prepared in 50 ml LB medium with 100 µg/ml carbenicillin. The next day, 2 litre LB medium with 100 µg/ml carbenicillin were inoculated with 40 ml of the preculture. Cells were grown to an O.D. of 0.6 for approximately 3 hours at 37°C and subsequently expression was induced by adding 1 mM IPTG followed by further incubation at 37°C for 4 hours. Cells were harvested by centrifugation and stored at -20°C.

For purification of $MA\beta_{40}C$, cell pellets were resuspended in 50 mM sodium phosphate, 300 mM NaCl, 20 mM imidazole pH 8 supplemented with EDTA-free protease inhibitor tablets, as recommended by the manufacturer. Cells were lysed via cell disruptor at 2.9 kbar and cell debris was removed via centrifugation at 18,000 RPM at 4°C for 40 minutes. The $MA\beta_{40}C$:$Z_{A\beta3}$ complex was captured by IMAC on a HisTrap 5 ml excel column and $MA\beta_{40}C$ was eluted via denaturation of the complex with 8 M Urea in 20 mM sodium phosphate pH 7. To remove residual $Z_{A\beta3}$, the eluate was first reduced by supplementing 5 mM TCEP and subsequently separated via RP-HPLC on a semi-preparative Zorbax 300SB-C8 RP-HPLC column (9.4 mm × 250 mm) connected to an Agilent 1260 Infinity system with UV detection at 214 nm and 275 nm. Monomeric $MA\beta_{40}C$ was eluted on a gradient of 12.5% to 45% acetonitrile in water with 0.1% (v/v) trifluoroacetic acid over 15 minutes at 80°C. The eluate was lyophilized and powdered $MA\beta_{40}C$ was stored at RT.

$MA\beta_{40}C$-ATTO643 was synthesized via maleimide conjugation to the C-terminal cysteine residue via succinimidyl thioether formation. 1 mg maleimide-ATTO643 was dissolved in 100 µl DMF and 1 mg $MA\beta_{40}C$ was dissolved in 600 µl 8 M Urea 20 mM sodium phosphate pH 7.0 supplemented with 5 mM TCEP. 33 µl maleimide-ATTO643 was added to the $MA\beta_{40}C$ solution and incubated for 4 hours at room temperature followed by an overnight incubation at 4°C on a tube roller. In hintsight, the overnight incubation was detrimental to the synthesis as most of the product aggregated and was impossible to redissolve. Nevertheless, the $MA\beta_{40}C$-ATTO643 product was purified via RP-HPLC by elution on a gradient of 25% to 45% acetonitrile in water with 0.1% (v/v) trifluoroacetic acid over 15 minutes at 80°C while detecting the absorption at 643 nm. The $MA\beta_{40}C$-ATTO643 product peak was collected

and lyophillized. Aliquots were prepared by dissolving in HFIP and lyophilization in appropriate aliquot sizes.

20 nmol MAβ_{40}C-ATTO643 was dissolved in 500 µl 50% DMF, 50% 50 mM sodium phosphate pH 6.5. The DMF was intended to increase the solubility of MAβ_{40}C-ATTO643, as it was virtually insoluble in aquaeous solutions. However, even with the addition of DMF and heating to 80°C only partial dissolution was achieved (for future syntheses the use of HFIP as cosolvent should be evaluated). To the MAβ_{40}C-ATTO643 solution 1.6 µl 62.5 mM NHS-DBCO (25 mg in 1 ml DMF), for a 5-fold excess, and 26 µl 9 mM biotin-FAM-azide (1 mg in 100 µl DMF), for a 10-fold excess, was added and incubated overnight at 4°C on a tube roller. Final purification was performed via RP-HPLC. Products were eluted on a gradient of 25% to 45% acetonitrile in water with 0.1% (v/v) trifluoroacetic acid over 15 minutes at 80°C while detecting the absorption at 488 nm and 643 nm. All putative product peaks that simultaneously absorbed at 488 nm and 643 nm were collected and lyophillized. Aliquots were prepared by dissolving in HFIP and lyophilization in appropriate aliquot sizes. Subsequently, the products were stored at -80°C. Final product concentration was determined by dissolving one aliquot in PBS and subsequent UV-Vis spectroscopy. The absorption at 643 nm was measured and the lambert-beer equation was used to calculate the concentration with an $\varepsilon_{643\,\mathrm{nm}}$ = 150,000 $M^{-1}cm^{-1}$.

6.4.2 Preparation of input-DNA for PACMAN

Input-DNA for PACMAN needed to contain a T7 promoter with a short 5'UTR before the promotor sequence, a ribosome binding site (RBS), the sequence encoding the protein of interest (starting with an ATG and stopping with a stop-codon) followed by a 3'-UTR which ends with a T7 terminator sequence. These were the prerequisites for application in IVTT. Therefore, input-DNA was prepared using the primers "No-extension-T7-Term Rev" and "Link-T7p For". As template, the gene of interest or library was subcloned into the pIgV plasmid providing the promotor and terminator regions. Input-DNA was either prepared using Phusion polymerase, as described in Table 6.7 or CloneAmp HiFi PCR premix, as described in Table 6.8. A temperature profile as shown in Table 6.9 was used.

Table 6.7: PCR composition used in the preparation of input-DNA using Phusion polymerase.

Component	**Volume (single template)**	**Volume (library as template)**
5x HF-Buffer	10 µl	10 µl
dNTPs [10 mM each]	1 µl	1 µl
Primer [10 µM] – Link-T7p For	2.5 µl	2.5 µl
Primer [10 µM] – No-extension-T7-Term Rev	2.5 µl	2.5 µl
DMSO	1.5 µl	1.5 µl
Template DNA	1 µl (50-500 pg/µl)	5 µl (up to 100 ng/µl)
Milli-Q H_2O	31 µl	26 µl
Phusion polymerase	0.5 µl	0.5 µl

Table 6.8: PCR composition used in the preparation of input-DNA using CloneAmp HiFi PCR premix.

Component	**Volume (single template)**	**Volume (library as template)**
2x CloneAmp HiFi PCR Premix	25 µl	25 µl
Primer [10 µM] – Link-T7p For	2.5 µl	2.5 µl
Primer [10 µM] – No-extension-T7-Term Rev	2.5 µl	2.5 µl
Template DNA	1 µl (50-500 pg/µl)	5 µl (up to 100 ng/µl)
Milli-Q H_2O	19 µl	15 µl

Table 6.9: PCR temperature profile used in the preparation of input-DNA for PACMAN.

Temperature	**Time**	**Cycles**
98°C	2 min	
98°C	30 s	|
58°C	30 s	35x or 25x for libraries
72°C	1 min	|
72°C	5 min	
15°C	hold	

After PCR, the products were separated on a 1% agarose gel, excised and eluted from the gel. The concentration was determined and subsequently used in PACMAN selections.

6.4.3 Coupling of biotinylated primers and target peptides to streptavidin-coated microbeads

Usually, 5x10^7 ProMag HP3 streptavidin microbeads were used. Microbeads were washed three times with 200 µl bind and wash buffer and resuspended in 50 µl bind and wash buffer. Typically, 120,000 or 10^6 biotinylated primers were coupled per microbead. Therefore, 1 µl or 8.3 µl (10 µM) ”b-TEG-TGS-Link-T7p For” primer was added, respectively, quickly vortexed to evenly disperse the primers and microbeads in solution. Microbeads were incubated at 1400 RPM at RT for 30 minutes. The peptide was aliquoted by dissolving in Hexafluoroisopropanol (HFIP), splitting into aliquots of appropriate size and subsequent lyophilization. Aliquots were prepared as 0.9 nmol aliquots for the Aβ-target peptide and 1.66 nmol aliquots for the TEV-target peptide.
Usually 10^6 peptide molecules were coupled per microbead. In case of the Aβ-target peptide, an aliquot was dissolved in 100 µl 1x PBS and sonicated until no precipitate was visible. 9.2 µl of that solution was added to the microbeads (10^6 peptides/microbead) and incubated overnight at 1400 RPM 7°C. The rest of the Aβ-target peptide aliquot was stored at -80°C and used for several months. In case of the TEV-target peptide, an aliquot was dissolved in 500 µl 1x PBS and 25 µl of that solution was added to the microbead suspension (10^6 peptides/microbead) and incubated overnight at 1400 RPM 7°C. The rest of the TEV-target aliquot was stored at -80°C and used for several months. Afterwards, the microbeads were washed three times with 200 µl breaking buffer using a magnetic rack and then incubated overnight at 1400 RPM 7°C. Microbeads were washed three times with 200 µl bind and wash buffer and subsequently resuspended in 100 µl bind and wash buffer supplemented with 0.1% sodium azide (NaN_3) and stored at 4°C for several months.

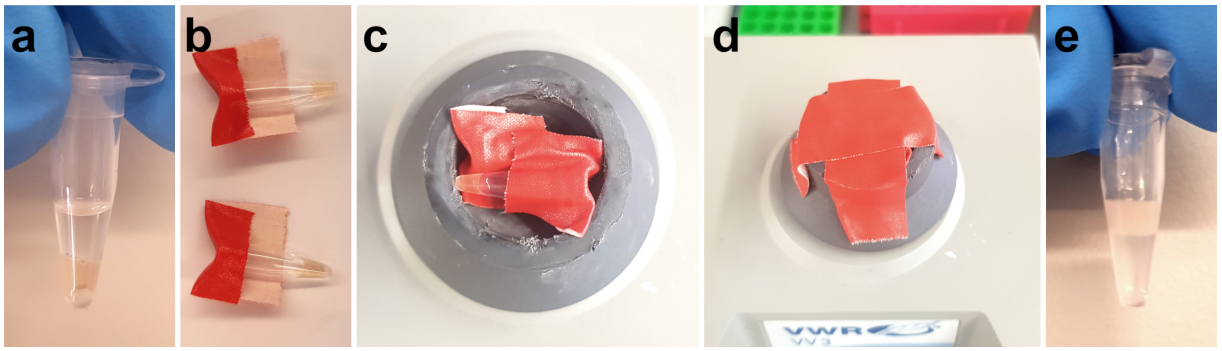

Figure 6.1: Preparation of FluoSurf-based emulsions. FluoSurf-based emulsions were prepared in 200 µl PCR tubes. After the aqueous and organic phase were added to the tube (a), lids were closed and wrapped with fabric tape (b). Up to two tubes were placed horizontally into the rubber opening of the VWR VV3 vortexer (c). The opening was closed using fabric tape (d). Emulsions were formed by vortexing at speed setting 5 of 6 for 5 minutes. The successfully prepared emulsion floated on top (e).

6.4.4 On-bead emulsion PCR (emPCR)

10^6 (unless stated otherwise) ProMag HP3 streptavidin microbeads decorated with 120,000 (unless stated otherwise) biotinylated primers (b-TEG-TGS-Link-T7p For) per microbead and 10^6 (unless stated otherwise) biotinylated target peptides (TEV-target or Aβ-target) per microbead were used. The PCR was based on Titanium Taq polymerase and the emulsion was based on FluoSurf.
Microbeads were washed three times with 100 µl Milli-Q H_2O and resuspended at a concentration of 500,000 microbeads/µl in Milli-Q H_2O. The PCR was prepared as shown in Table 6.10. Unless stated otherwise, 4x10^6 molecules of input DNA were used per emulsion.

The total volume of the PCR mixture was 18 µl. To prepare the emulsion, the PCR mixture was quickly vortexed or sonicated in a sonicator bath to resuspend the microbeads, subsequently 54 µl 2% FluoSurf was added to the PCR mixture in a 200 µl PCR tube. The PCR tube was vortexed for 5 minutes at RT using a VWR VV3 vortexer on speed setting 5 of 6 (detailed sample placement depicted in Figure 6.1). PCR was performed according to the temperature profile shown in Table 6.11.

After PCR, the emulsion was broken and microbeads were recovered. Therefore,

Table 6.10: PCR composition used in on-bead emPCR.

Component	**Volume**
10x Titanium Taq buffer	1.8 µl
dNTPs [10 mM each]	0.45 µl
Primer [10 µM] – No-extension-T7-Term Rev	1.8 µl
Milli-Q H_2O	10.05 µl
Microbeads in Milli-Q H_2O	2 µl
Template DNA (4 x 10^6 molecules/µl)	1 µl
Titanium Taq polymerase	0.9 µl

the emulsion was transferred to a fresh 0.5 ml low-bind reaction tube and the PCR tube was rinsed with 200 µl breaking buffer which was also transferred to the 0.5 ml reaction tube. 60 µl Fluoro-Stop was added and the tube was shaken by hand to break the emulsion. The aqueous and organic phases were separated either by placing the tube in a rack and settling by gravity or by quick spin-down in a mini centrifuge. The upper phase contained the aqueous phase with the microbeads which was transferred to a fresh 1.5 ml reaction tube. To ensure complete microbead recovery, a small amount of the organic phase was transferred as well. The reaction tube was placed into a magnetic rack and microbeads were separated from the liquid. The whole liquid was removed and microbeads were washed three times with

Table 6.11: PCR temperature profile used in on-bead emPCR.

Temperature	**Time**	**Cycles**
94°C	2 min	
94°C	30 s	|
48°C	30 s	30x
72°C	2-4 min	|
72°C	5 min	
45°C	5 min	
25°C	20 min	
15°C	hold	

200 µl breaking buffer and incubated overnight at 7°C at 1400 RPM, subsequently the microbeads were washed three times with 200 µl bind and wash buffer and incubated overnight at 7°C at 1400 RPM. Finally, the microbeads were washed three times with 200 µl TE buffer.
Nevertheless, the wash protocol had to always be evaluated depending on the current experiment. Depending on the used microbead product, the presence of target peptides and the amount of contaminating soluble DNA, the wash protocols had to be adjusted. Residual DNA was usually best removed by successive washings with TE buffer, but in the presence of target peptides a more intensive wash protocol including repeated breaking buffer and bind and wash buffer washing steps was favored.

Afterwards, microbeads were stored in bind and wash buffer supplemented with 0.1% NaN_3 at 4°C until further use.

6.4.5 Determination of the amount of DNA copies bound to microbeads by qPCR

The efficiency of on-bead emPCR was evaluated using qPCR by determining the number of DNA copies per microbead. After on-bead emPCR, after the intensive wash protocol, microbeads were again washed three times with 100 µl Milli-Q H_2O. 50 µl of the microbead suspension was diluted with 250 µl Milli-Q H_2O. The microbead concentration was determined using a Neubauer enhanced cytometer according to the manufacturer's instructions. Subsequently, the sample was further diluted to obtain 250 microbeads/µl in a total volume of 300 µl Milli-Q H_2O. As a control, whether the wash protocol was sufficient to remove unspecifically bound DNA from the microbeads, approximately half of the volume of the microbead suspension was filtered through a 0.2 µm syringe filter to remove all microbeads. Thereby, residual unspecifically bound DNA was washed off the microbeads and eluted, but the microbeads were caught in the filter. Always both, the microbead suspension and the filtered eluate, were analyzed by qPCR. In case almost no DNA was detected in the filtered eluate, microbeads were considered sufficiently washed. Then

Table 6.12: qPCR composition.

Component	**Volume**
2x AceQ qPCR SYBR Green Master Mix	5 µl
Primer [10 µM] – qPCR TEV For or Vector Amplification For	0.2 µl
Primer [10 µM] – No-extension-T7-Term Rev	0.2 µl
Microbeads (1000/reaction) or filtered eluate	4 µl
Milli-Q H_2O	0.6 µl

Table 6.13: qPCR temperature profile.

Temperature	**Time**	**Cycles**
95°C	30 s	
95°C	10 s	40x
60°C	30 s	|
melt	15 s	

the emPCR efficiency could be confidently evaluated by qPCR on the microbead sample.

The qPCR mixture was assembled as listed in Table 6.12. All samples were measured in three to four replicates. For samples containing TEV DNA, the forward primer ”qPCR TEV For” was used, otherwise the forward primer ”Vector Amplification For” was used. The PCR temperature profile shown in Table 6.13 was used. Ct values for each sample were measured using a qTower^3 G (Analytik Jena) qPCR device.

To calculate the number of copies per microbead, a standard curve was prepared using microbeads harbouring 10, 100, 1,000, 10,000 and 100,000 biotinylated molecules of the respective DNA per microbead.
Biotinylated DNA was prepared as described in section 6.4.2, but instead of the primer ”Link-T7p For”, the biotinylated primer ”b-TEG-TGS-Link-T7p For” was used in the PCR.
To prepare each microbead standard, 10^6 ProMag HP 3 streptavidin microbeads were

washed three times with 100 µl bind and wash buffer. 10, 100, 1,000, 10,000 or 100,000 biotinylated DNA molecules/microbead were added to the microbeads and incubated overnight at 7°C at 1400 RPM. The microbeads were washed three times with 100 µl breaking buffer and incubated overnight at 7°C, 1400 RPM. Microbeads were further washed three times with 100 µl bind and wash buffer and incubated overnight at 7°C, 1400 RPM. Subsequently, microbeads were washed three times with 100 µl TE buffer. qPCR was performed in triplicates as described above.
To calculate the standard curve, the $\log_{10}$ of the DNA copies/microbead of each standard sample was plotted against its respective Ct-value and a linear regression was performed. The qPCR efficiency (E) was calculated using the slope of the linear regression: $E = 10^{-1/slope}$. Using the intercept (I) of the linear regression and the qPCR efficiency (E) the average number of DNA copies per microbead of the on-bead emPCR samples was calculated using: $N = E^{I-Ct}$.

6.4.6 *in vitro* transcription and translation in emulsion

The Abil EM 90-based protocol was preferred when at least 4 x 10^6 beads were used in a PACMAN selection. The Abil-based emulsion consumed more IVTT solution (50 µl) in a single preparation as compared to the FluoSurf-based emulsion (18 µl), but accomodated for more microbeads in relation to the amount of used IVTT solution. The Abil-based method was therefore preferred especially in early selection cycles, as more variants could be screened in a single preparation. In later selection cycles and in method-optimization experiments, FluoSurf was preferred as IVTT solution could be conserved and FluoSurf provided a considerably superior ease of handling.

Abil EM 90-based protocol

An Abil EM 90-based IVTT emulsion could accomodate for up to 5x10^6 microbeads in a single preparation. Unless stated otherwise, 5x10^6 microbeads, after on-bead emPCR, were used. Microbeads were washed twice with 100 µl 1x PBS and twice with 100 µl 1x PBS, 1 mg/ml UltraPure BSA using a magnetic rack. Afterwards, microbeads were separated using the magnetic stand and the whole aqueous solution was removed. Microbeads were resuspended in 50 µl PURExpress IVTT solution (5.3.1). From this point, the IVTT/microbead mixture was kept on ice.

500 µl mineral oil Abil EM90 surfactant mixture was freshly prepared and placed in a 2 ml Agilent glass vial with a 2x7 mm microstirbar. The glass vial was placed into a slot of the iTrapR containing crushed ice and water. The RPM was set to 1200 and a timer was set to 10 minutes.

The microbead IVTT mixture was pipetted up and down to nicely disperse the microbeads. The timer was started and the microbead IVTT mixture was slowly added to the stirring and chilled mineral oil Abil EM 90 surfactant mixture in aliquots of 10 µl, one aliquot per minute. As the microbeads decorated with target peptides tended to cluster and aggregate in the IVTT solution, the microbead/IVTT mixture was sonicated in a sonicator bath right before taking each aliquot, to disperse the microbeads. After the whole aqueous phase was added, the emulsion continued to stir for 5 minutes until the timer ran out and automatically turned off the stirring.

The emulsion was removed from the glass vial using a pipette and transferred to a 1.5 ml reaction tube. The emulsion was incubated quiescently at 37°C for 4 hours or up to 5 days. During incubation time, variants were expressed and cleavage of target peptides took place.

To break the emulsion and to recover the microbeads after incubation, the emulsion was centrifuged at 16,100 x g for 15 minutes at RT (important!). The supernatant oil phase was removed thoroughly to leave as little residual oil as possible. 200 µl breaking buffer was added and the emulsion pellet was disrupted by pipetting up and down. 1 ml diethylether was added and vortexed. The aqueous and the organic phase were separated by brief centrifugation using a mini centrifuge. The upper diethylether phase was discarded. Usually, one diethylether extraction was sufficient for microbead recovery, but if necessary, the diethylether extraction was repeated. Microbeads were separated using a magnetic rack and the whole liquid was removed. Microbeads were washed with 200 µl breaking buffer, resuspended in 100 µl breaking buffer and transferred to a fresh 1.5 ml reaction vessel. Microbeads were washed two more times with 100 µl breaking buffer and then incubated in a refrigerated thermomixer at 1400 RPM at 7°C overnight. Microbeads were washed again three times with 100 µl breaking buffer and then five times with 100 µl 1x PBS. Subsequently, microbeads were sorted or analyzed using FACS or flow cytometry, respectively.

FluoSurf-based protocol

A FluoSurf-based IVTT emulsion may accomodate for a max of 10^6 microbeads in a single preparation. Unless stated otherwise, 10^6 microbeads, after on-bead emPCR, were used. Microbeads were washed twice with 100 µl 1x PBS and twice with 100 µl 1x PBS, 1 mg/ml UltraPure BSA using a magnetic rack. Afterwards, microbeads were separated using the magnetic stand and the whole aqueous solution was removed. Microbeads were resuspended in 18 µl PURExpress IVTT solution (5.3.1) in a 200 µl PCR tube. The emulsion was prepared by adding 54 µl 2% FluoSurf and vortexing for 5 minutes at RT using a VWR VV3 vortexer on speed setting 5 of 6 (detailed sample placement depicted in Figure 6.1). The emulsion was incubated quiescently at 37°C for 4 hours, unless stated otherwise. During the incubation time, variants were expressed and cleavage of target peptides took place.
After incubation, the emulsion was broken and microbeads were recovered. Therefore, the emulsion was transferred to a fresh 0.5 ml low-bind reaction tube, the PCR tube was rinsed with 200 µl breaking buffer, which was then also transferred to the 0.5 ml reaction tube. 60 µl Fluoro-Stop was added and the tube was shaken by hand to break the emulsion. The aqueous and organic phases were separated either by placing the tube in a rack and settling by gravity or by quick spin-down in a mini centrifuge. The upper phase contained the aqueous phase together with the microbeads which was transferred to a fresh 1.5 ml reaction tube. To ensure complete microbead recovery, a small amount of the organic phase was transferred as well. The reaction tube was placed into a magnetic rack and microbeads were separated from the liquid. The whole liquid was removed and microbeads were washed three times with 100 µl breaking buffer and then incubated in a refrigerated thermomixer at 1400 RPM at 7°C overnight. Microbeads were washed again three times with 100 µl breaking buffer and then five times with 100 µl 1x PBS. Subsequently, microbeads were sorted or analyzed using FACS or flow cytometry, respectively.

6.4.7 Flow cytometer analysis of microbeads

Flow cytometer analysis was performed using a BD FACSCanto II or a Beckman Coulter CytoFLEX S device. Microbeads were appropriately diluted with 1x PBS in a 5 ml

flow cytometry tube. Usually, 50 µl microbead suspension (∼500,000 microbeads) was diluted with 500 µl 1x PBS.
The acquisition setup was the same for both devices. Single microbeads were gated using the forward scatter (FSC) and side scatter (SSC) channels in linear scale, additionally the fluorescence channels of FITC and APC were recorded. Usually, 10,000 single microbead events were recorded. Subsequent data analysis of the fluorescence signals was performed using python version 3.8, FlowCal version 1.3.0 and matplotlib version 3.3.0.

6.4.8 Fluorescence-activated cell sorting (FACS) of microbeads

Fluorescence-activated cell sorting was performed using a BD FACS ARIA III or a Beckman Coulter CytoFLEX SRT device. Microbeads were appropriately diluted with 1x PBS in a 5 ml flow cytometry tube. Usually, the whole microbead suspension was diluted to a total volume of 500 µl with 1x PBS.
The acquisition and gating setup was the same for both devices. Single microbeads were gated using the forward scatter (FSC) and side scatter (SSC) channel in linear scale. The fluorescence channels FITC and APC were used to evaluate the cleavage status of the microbead-bound target peptides. A sort gate and the sort mode was set as described in the results section and microbeads were collected directly into 96-well plates, which were later used for PCR amplification of the DNA bound to the microbeads. Subsequent data analysis of the fluorescence signals was performed using python version 3.8, FlowCal version 1.3.0 and matplotlib version 3.3.0.

6.4.9 Reamplification of DNA from sorted microbeads

DNA bound to sorted microbeads was reamplified by PCR. PCR was performed using Phusion polymerase in the initial experiments used to prove the principle of PACMAN via recovery of TEV-protease-coding DNA. In the experiments to isolate antibodies from libraries, the microbead-bound DNA was reamplified using Hifi CloneAmp PCR premix, as the recovery using Phusion polymerase was unsatisfactory. In the initial experiments, the PCR was set up according to Table 6.14. The approximate volume

Table 6.14: PCR composition used for reamplification of DNA from sorted microbeads. x is the estimated volume of the sorted microbeads.

Component	**Volume**
5x HF-Buffer	10 µl
dNTPs [10 mM each]	1 µl
Primer [10 µM] – Link-T7p For	2.5 µl
Primer [10 µM] – No-extension-T7-Term Rev	2.5 µl
DMSO	1.5 µl
Milli-Q H_2O	32–x µl
Phusion polymerase	0.5 µl

Table 6.15: PCR composition used for reamplification of DNA from sorted microbeads using CloneAmp PCR premix.

Component	**Volume**
2x CloneAmp HiFi PCR Premix	25 µl
Primer [10 µM] – Link-T7p For	2.5 µl
Primer [10 µM] – No-extension-T7-Term Rev	2.5 µl
1x PBS	20 µl

of the collected microbeads was estimated using a micropipette. The PCR temperature profile of Table 6.9 was used.

For sorts that yielded more than 5 µl of sample, as was the case for the screenings of the antibody libraries, the microbeads were separated from the liquid using a 96-well magnetic separator rack and the whole liquid was removed. The FACS solution has an inhibitory effect on the PCR and had to be removed prior to PCR if volumes exeeded 5 µl. In these cases, the PCR composition from Table 6.15 was used. The separated microbeads in the 96-well plate were resuspended in the 50 µl PCR reaction mix and mixed well. The PCR was subsequently performed according to the temperature profile in Table 6.9.

The products of the PCR were separated using a 1% agarose gel and the band corresponding to the size of the anticipated products were excised and eluted.

A. Supplementary Data

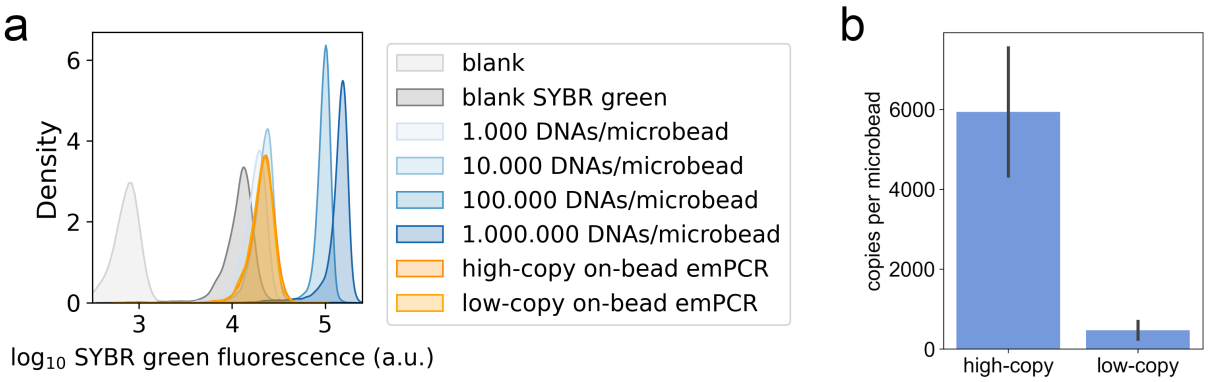

Figure A.1: DNA stains do not provide a sufficient readout for monoclonality assessments of microbeads after on-bead emPCR. a, flowcytometric analysis of microbeads stained with SYBR green DNA stain after on-bead emPCR. In light grey, unstained control ProMag HP 3 streptavidin microbeads. In dark grey, SYBR green stained control microbeads, which show a strong background adsorption of the DNA stain. In blue hues, microbeads decorated with different amounts of biotinylated DNA/microbead were stained with SYBR green and a trend in the fluorescence intensity correlating with the amount of DNA was evident. Two on-bead emPCR reactions were performed with a high and low amount of input DNAs. In the SYBR green staining the two microbead populations are not discernible. b, the microbeads from the same two on-bead emPCR reactions as in a) were analyzed by qPCR revealing the remarkable difference in the DNA load.

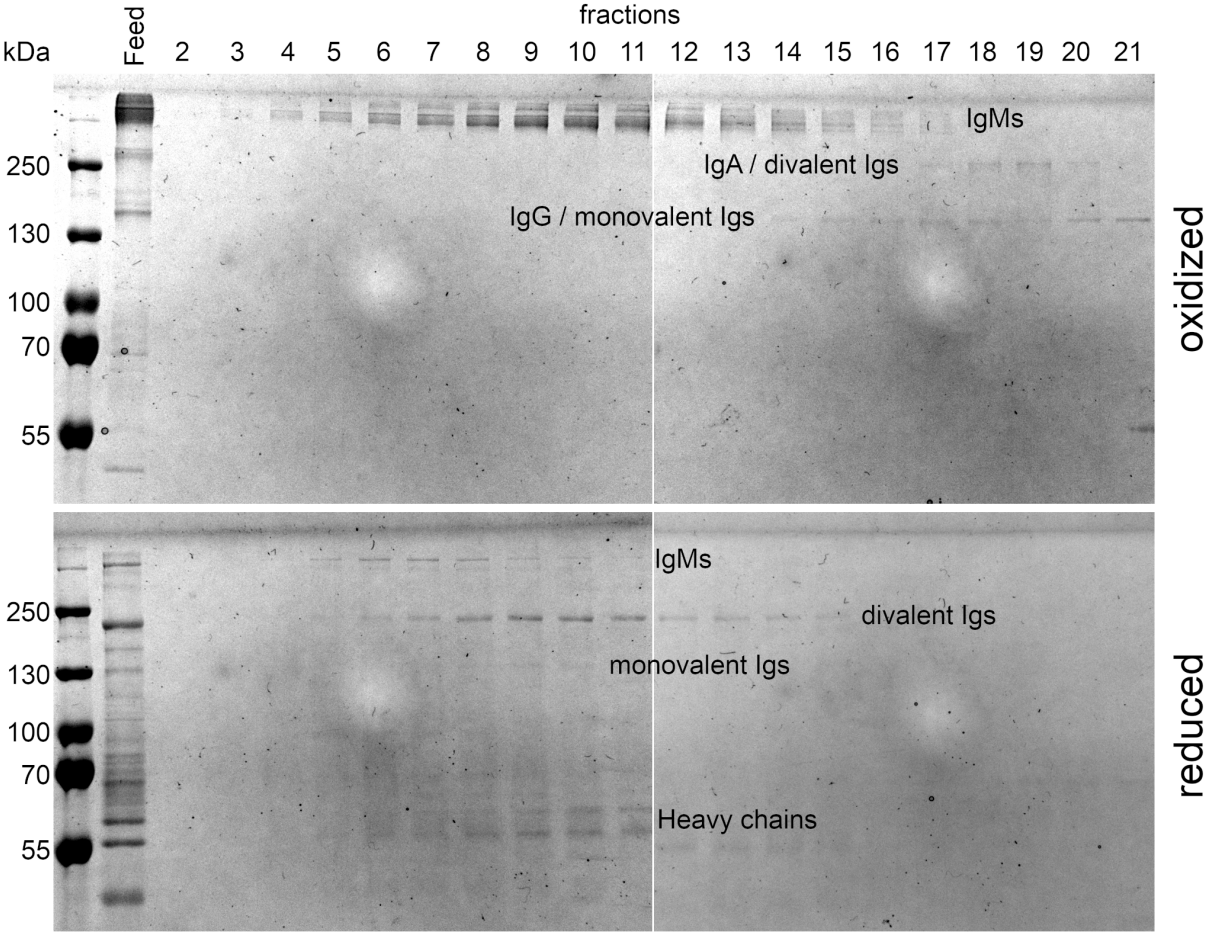

Figure A.2: Purification of polyclonal human IgM by size exclusion chromatograhy. IgG-depleted human plasma was subjected to gravity flow with LigaTrap human IgM resin. The IgM-rich eluate was further purified by size exclusion chromatography using a Superdex 200 10/300 column. The individual elution fractions were separated on an 8% glycine SDS-Page gel. On the upper stitched gel the fractions were not reduced and on the lower stitched gel the samples were reduced. Marker, PageRuler Plus prestained. Feed, the IgM-rich LigaTrap eluate, which was used as feed for the size exclusion chromatography.

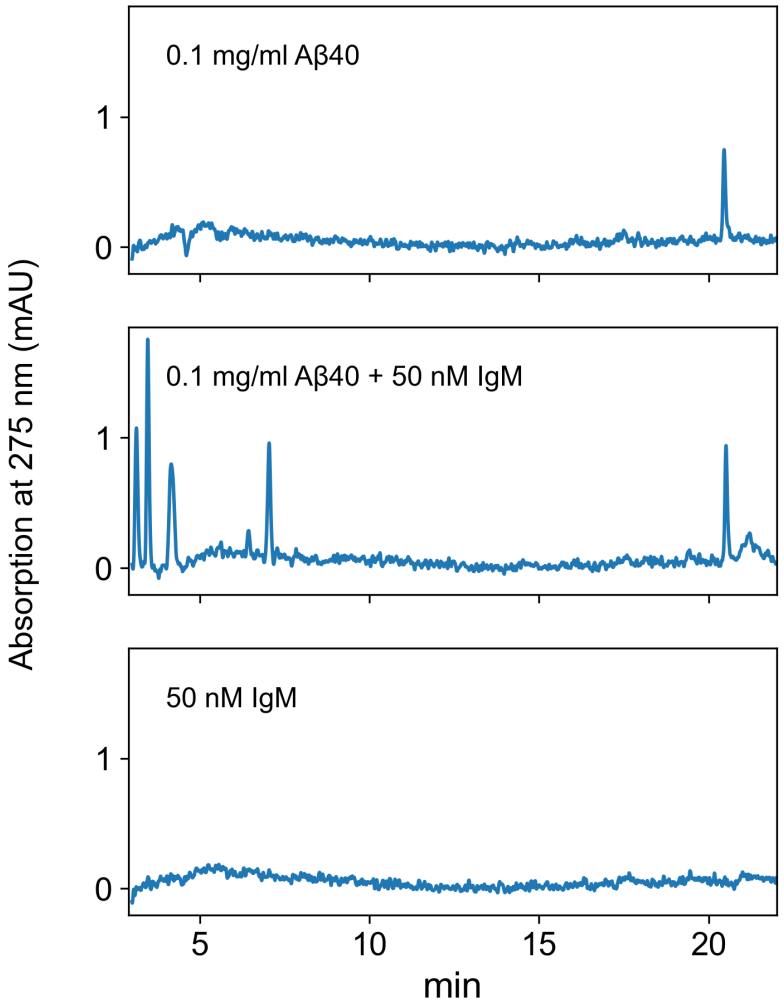

Figure A.3: Digestion of $A\beta_{40}$ by polyclonal IgM purified from IgG-depleted human plasma by LigaTrap Human IgM gravity flow chromatography and subsequent Superdex 200 10/300 chromatography. To isolate polyclonal IgM from human plasma, it was first subjected to to gravity flow chromatography with Protein A-resin for IgG-depletion. The flow-through was collected and further subjected to gravity flow chromatography with LigaTrap Human IgM resin which was claimed to preferentially bind human IgM, but with residual affinity towards the other Ig-classes. Afterwards, the IgM-rich eluate was further purified by size exclusion chromatography using a Superdex 200 10/300 column (see FigureA.2). The eluted fraction 4 was used to perform the depicted $A\beta_{40}$ digestion. 100 µg/ml $A\beta_{40}$ was coincubated quiescently with 50 nM polyclonal IgM from fraction 4 for 96 hours at 37°C. Samples were analyzed by reverse-phase HPLC using a Zorbax 300SB-C8 4.6x250 mm column with a linear gradient of 0–80% ACN 0.1% TFA over 40 minutes. Sample incubation in this experiment was performed in conical HPLC glass vial insets and not in low-bind tubes, which resulted in some loss of full-length $A\beta_{40}$ by binding to the glass walls. Therefore, the peak height of $A\beta_{40}$ in the HPLC chromatogramm does not reliably represent the $A\beta_{40}$ concentration in the samples. The important information from this experiment is the presence of early elution peaks at 275 nm within the first seven minutes, which are indicative for single amino acids and small di- to oligo peptides.

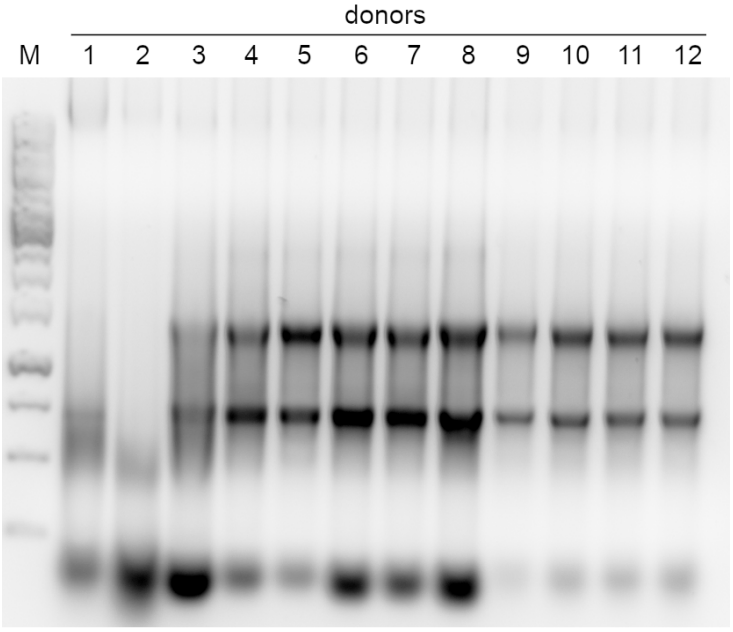

Figure A.4: Quality control of total RNA extractions from human PBMCs from twelve donors. Total RNA was isolated via Trizol extraction. Afterwards, total RNA was analyzed by 1% agarose gel electrophoresis. Prominent rRNA bands were visible in donor samples 3–12 indicative for a purification with limited degradation by Rnases. Samples 1 and 2 unfortunately showed RNA degradation and were therefore excluded from library preparation. Marker, GeneRuler 1 kb DNA ladder.

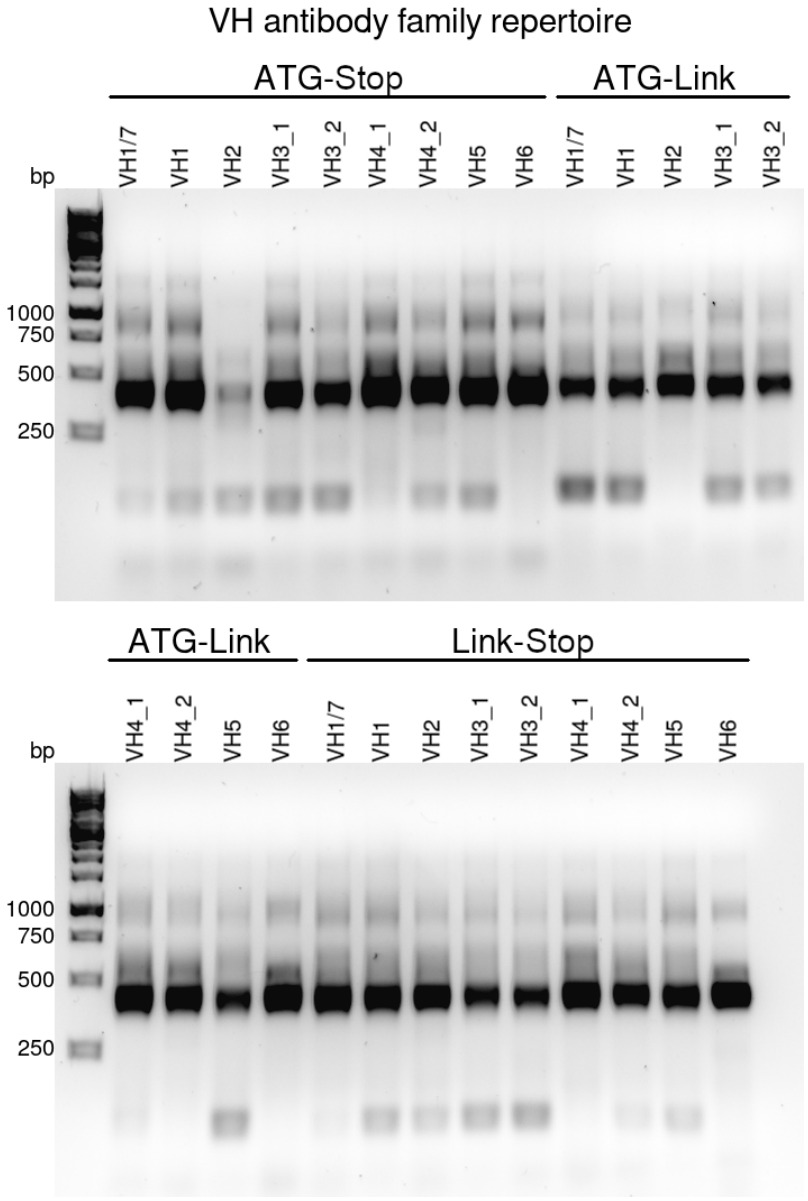

Figure A.5: PCR amplification of the VH antibody family repertoire. All necessary primer combinations used to amplify the VH antibody family repertoire from cDNA were examined by PCR. All forward primers which introduce either a 5' plasmid overlap with a start-codon or a linker to the VH fragment were evaluated individually for each VH family. All reverse primers which introduce either a stop-codon with a 3' plasmid overlap were combined before PCR, as well as all reverse primers that introduce a linker were combined before PCR. An optimized annealing temperature was previously determined (65°C) and here evaluated for all primer combinations. Marker, GeneRuler 1 kb DNA ladder.
The same effort was invested into the evaluation of optimized annealing temperatures for the amplification of the VL and VK antibody family repertoire by Stefanie Williams during her Bachelor thesis.

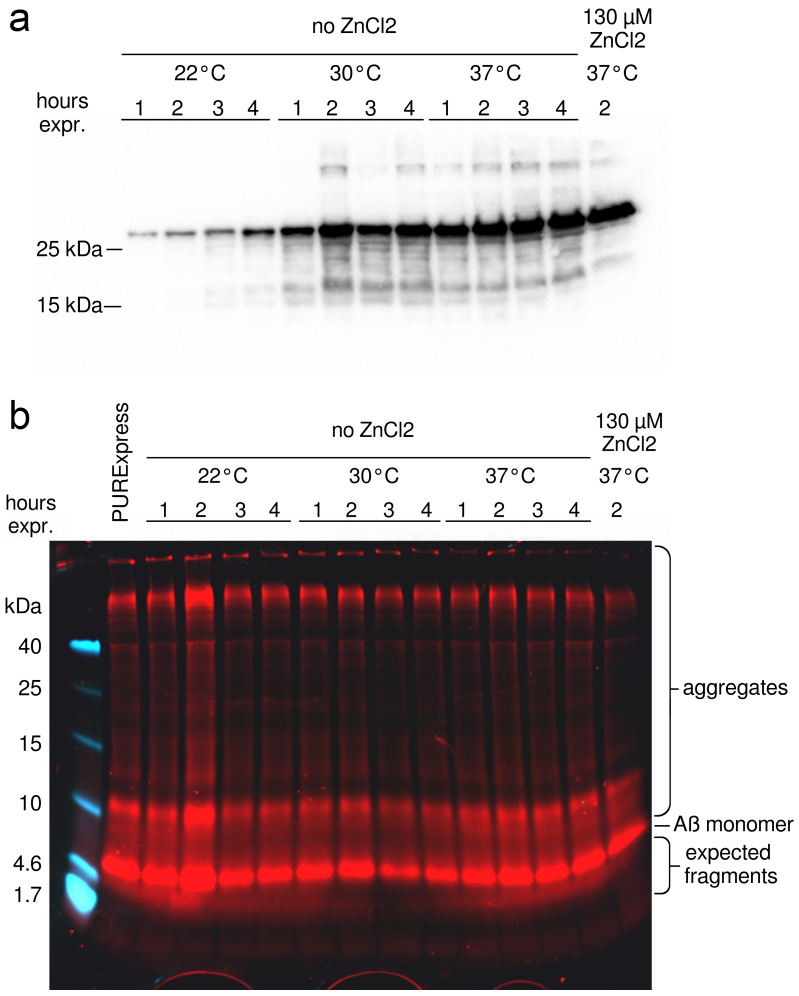

Figure A.6: Evaluation of PURExpress IVTT parameters to express $IgVL_2$ 2E6 and attempts to cleave Aβ. a, $IgVL_2$ 2E6 [230] was subcloned into the pIgV plasmid to introduce a T7 promotor and a T7 terminator necessary for IVTT via PURExpress. 250 ng plasmid was used for each 25 µl of IVTT reaction volume. The expression temperature and duration was optimized to express $IgVL_2$ 2E6 using PURExpress IVTT solution. Expression was performed at 22°C, 30°C and 37°C for 1–4 hours. The sample in the last lane was substituted with 130 µM $ZnCl_2$, as zink ions were claimed to be crucial for 2E6 activity according to Taguchi et al. [230]. Expression products were analyzed on a 20% tris-tricine SDS-Page and by subsequent western-blot analysis using rabbit anti-cmyc primary antibody and goat anti-rabbit HRP-conjugated secondary antibody. The $IgVL_2$ 2E6 band at 27kDa was most prominent after 4 hours of expression at 37°C. This suggested that IVTT expression of single-chain antibody fragments should be best performed at 37°C for 4 hours. b, attempts to cleave Aβ with the IVTT expressed 2E6 antibodies. 2 µl of the IVTT reaction mixtures were mixed with 1 µl 10 µM HiLyte555-$Aβ_{42}$ and 8 µl PBS and incubated for 2 days at 37°C. The sample in the first lane contained the PURExpress reagent without any DNA (negative control). Reaction products were separated on a 20% Tris-tricine SDS-PAGE gel and HiLyte555 fluorescence was recorded. Unfortunately, no cleavage products were detected in any condition.

B. Author contributions

1. Filip Hasecke †, Tatiana Miti †, Carlos Perez, Jeremy Barton, Daniel Schölzel, Lothar Gremer, Clara S. R. Grüning, Garrett Matthews, Georg Meisl, Tuomas P. J. Knowles, Dieter Willbold, Philipp Neudecker, Henrike Heise, Ghanim Ullah, Wolfgang Hoyer and Martin Muschol — **Origin of metastable oligomers and their effects on amyloid fibril self-assembly.** Chem. Sci., 2018

   I designed and performed all experiments and analyses related to dimAβ and Aβ. I contributed to the writing of the manuscript and the formulation of responses to revisions.

2. Filip Hasecke †, Chamani Niyangoda †, Gustavo Borjas, Jianjun Pan, Garrett Matthews, Martin Muschol and Wolfgang Hoyer — **Protofibril–Fibril Interactions Inhibit Amyloid Fibril Assembly by Obstructing Secondary Nucleation.** Angew. Chem. Int. Ed., 2021

   I designed and performed all experiments and analyses related to dimAβ and Aβ, except for the data in Figure 1 D–G. I designed all illustrations. All data in the supplementary information was generated by me. I contributed to the writing of the manuscript and the formulation of responses to revisions.

3. Marie P. Schützmann †, Filip Hasecke †, Sarah Bachmann †, Mara Zielinski, Sebastian Hänsch, Gunnar F. Schröder, Hans Zempel and Wolfgang Hoyer — **Endo-lysosomal Aβ concentration and pH trigger formation of Aβ oligomers that potently induce Tau missorting.** Nat Commun, 2021

   I performed the experiments in figures 1 b,c and f, figure 5, supplementary figure 4, 5 and 10. I analyzed the data in figure 6 i–p, figure 7 c–h and figure 8. I designed and illustrated the schemes in figure 1 a and 9 and rendered all AFM data and composed the figures in the maintext except for figures 2–4. I

contributed to the writing of the manuscript and the formulation of responses to revisions.

† Equal contributions, joint first authors.

References

[1] Fabrizio Chiti and Christopher M. Dobson. **Protein Misfolding, Amyloid Formation, and Human Disease: A Summary of Progress Over the Last Decade**. *Annual Review of Biochemistry*, 86(1):27–68, 2017.

[2] Maria M. Picken. **The Pathology of Amyloidosis in Classification: A Review**. *Acta Haematologica*, 143(4):322–334, 2020.

[3] Alois Alzheimer. **Über einen eigenartigen schweren Erkrankungsprozeß der Hirnrinde**. *Neurologisches Centralblatt*, pages 1129–36, 1906.

[4] Daniel P. Perl. **Neuropathology of Alzheimer's Disease**. *Mount Sinai Journal of Medicine: A Journal of Translational and Personalized Medicine*, 77(1):32–42, 2010.

[5] Michael A. DeTure and Dennis W. Dickson. **The neuropathological diagnosis of Alzheimer's disease**. *Molecular Neurodegeneration*, 14(1):32, December 2019.

[6] Hrishikesh Kaza, Manas R Barik, Mamatha M Reddy, Ruchi Mittal, and Sujata Das. **Gelatinous drop-like corneal dystrophy: a review**. *British Journal of Ophthalmology*, 101(1):10–15, January 2017.

[7] R. J. Krane, R. C. Klugo, and C. A. Olsson. **Seminal vesicle amyloidosis**. *Urology*, 2(1):70–72, July 1973.

[8] Reinhold P. Linke, Reinhild Joswig, Charles L. Murphy, Shuching Wang, Hui Zhou, Ulrich Gross, Christoph Rocken, Per Westermark, Deborah T. Weiss, and Alan Solomon. **Senile seminal vesicle amyloid is derived from semenogelin I**. *Journal of Laboratory and Clinical Medicine*, 145(4):187–193, April 2005.

[9] Asuman Argon, Adnan Sımşır, Banu Sarsik, Burçin Tuna, Kutsal Yörükoğlu, Gülen Gül Nıflıoğlu, and Sait Sen. **Amyloidosis of seminal vesicles; incidence and pathologic characteristics**. *Turk Patoloji Dergisi*, 28(1):44–48, 2012.

[10] Zichu Yang, Alexander Laird, Ashley Monaghan, Morag Seywright, Imran Ahmad, and Hing Y Leung. **Incidental seminal vesicle amyloidosis observed in diagnostic prostate biopsies—are routine investigations for systemic amyloidosis warranted?** *Asian Journal of Andrology*, 15(1):149–151, January 2013.

[11] B. M. Singh, D. M. Jackson, R. Wills, J. Davies, and P. H. Wise. **Delayed diagnosis in non-insulin dependent diabetes mellitus.** *BMJ : British Medical Journal*, 304(6835):1154–1155, May 1992.

[12] D. Himanshu, Wahid Ali, and Mohd Wamique. **Type 2 diabetes mellitus: pathogenesis and genetic diagnosis**. *Journal of Diabetes & Metabolic Disorders*, 19(2):1959–1966, December 2020.

[13] Claire Webster. **What is dementia, why make a diagnosis and what are the current roadblocks?** *World Alzheimer Report 2021*, page 7, 2021.

[14] Emma Nichols, Jaimie D Steinmetz, Stein Emil Vollset, Kai Fukutaki, Julian Chalek, Foad Abd-Allah, Amir Abdoli, Ahmed Abualhasan, Eman Abu-Gharbieh, Tayyaba Tayyaba Akram, Hanadi Al Hamad, Fares Alahdab, Fahad Mashhour Alanezi, Vahid Alipour, Sami Almustanyir, Hubert Amu, Iman Ansari, Jalal Arabloo, Tahira Ashraf, Thomas Astell-Burt, Getinet Ayano, Jose L

Ayuso-Mateos, Atif Amin Baig, Anthony Barnett, Amadou Barrow, Bernhard T Baune, Yannick Béjot, Woldesellassie M Mequanint Bezabhe, Yihienew Mequanint Bezabih, Akshaya Srikanth Bhagavathula, Sonu Bhaskar, Krittika Bhattacharyya, Ali Bijani, Atanu Biswas, Srinivasa Rao Bolla, Archith Boloor, Carol Brayne, Hermann Brenner, Katrin Burkart, Richard A Burns, Luis Alberto Cámera, Chao Cao, Felix Carvalho, Luis F S Castro-de Araujo, Ferrán Catalá-López, Ester Cerin, Prachi P Chavan, Nicolas Cherbuin, Dinh-Toi Chu, Vera Marisa Costa, Rosa A S Couto, Omid Dadras, Xiaochen Dai, Lalit Dandona, Rakhi Dandona, Vanessa De la Cruz-Góngora, Deepak Dhamnetiya, Diana Dias da Silva, Daniel Diaz, Abdel Douiri, David Edvardsson, Michael Ekholuenetale, Iman El Sayed, Shaimaa I El-Jaafary, Khalil Eskandari, Sharareh Eskandarieh, Saman Esmaeilnejad, Jawad Fares, Andre Faro, Umar Farooque, Valery L Feigin, Xiaoqi Feng, Seyed-Mohammad Fereshtehnejad, Eduarda Fernandes, Pietro Ferrara, Irina Filip, Howard Fillit, Florian Fischer, Shilpa Gaidhane, Lucia Galluzzo, Ahmad Ghashghaee, Nermin Ghith, Alessandro Gialluisi, Syed Amir Gilani, Ionela-Roxana Glavan, Elena V Gnedovskaya, Mahaveer Golechha, Rajeev Gupta, Veer Bala Gupta, Vivek Kumar Gupta, Mohammad Rifat Haider, Brian J Hall, Samer Hamidi, Asif Hanif, Graeme J Hankey, Shafiul Haque, Risky Kusuma Hartono, Ahmed I Hasaballah, M Tasdik Hasan, Amr Hassan, Simon I Hay, Khezar Hayat, Mohamed I Hegazy, Golnaz Heidari, Reza Heidari-Soureshjani, Claudiu Herteliu, Mowafa Househ, Rabia Hussain, Bing-Fang Hwang, Licia Iacoviello, Ivo Iavicoli, Olayinka Stephen Ilesanmi, Irena M Ilic, Milena D Ilic, Seyed Sina Naghibi Irvani, Hiroyasu Iso, Masao Iwagami, Roxana Jabbarinejad, Louis Jacob, Vardhmaan Jain, Sathish Kumar Jayapal, Ranil Jayawardena, Ravi Prakash Jha, Jost B Jonas, Nitin Joseph, Rizwan Kalani, Amit Kandel, Himal Kandel, André Karch, Ayele Semachew Kasa, Gizat M Kassie, Pedram Keshavarz, Moien AB Khan, Mahalaqua Nazli Khatib, Tawfik Ahmed Muthafer Khoja, Jagdish Khubchandani, Min Seo Kim, Yun Jin Kim, Adnan Kisa, Sezer Kisa, Mika Kivimäki, Walter J Koroshetz, Ai Koyanagi, G Anil Kumar, Manasi Kumar, Hassan Mehmood Lak, Matilde Leonardi, Bingyu Li, Stephen S Lim, Xuefeng Liu, Yuewei Liu, Giancarlo Logroscino, Stefan Lorkowski, Giancarlo Lucchetti, Ricardo Lutzky Saute, Francesca Giulia Magnani, Ahmad Azam Malik, João Massano, Man Mohan Mehndiratta, Ritesh G Menezes, Atte Meretoja, Bahram Mohajer, Norlinah Mohamed Ibrahim, Yousef Mohammad, Arif Mohammed, Ali H Mokdad, Stefania Mondello, Mohammad Ali Ali Moni, Md Moniruzzaman, Tilahun Belete Mossie, Gabriele Nagel, Muhammad Naveed, Vinod C Nayak, Sandhya Neupane Kandel, Trang Huyen Nguyen, Bogdan Oancea, Nikita Otstavnov, Stanislav S Otstavnov, Mayowa O Owolabi, Songhomitra Panda-Jonas, Fatemeh Pashazadeh Kan, Maja Pasovic, Urvish K Patel, Mona Pathak, Mario F P Peres, Arokiasamy Perianayagam, Carrie B Peterson, Michael R Phillips, Marina Pinheiro, Michael A Piradov, Constance Dimity Pond, Michele H Potashman, Faheem Hyder Pottoo, Sergio I Prada, Amir Radfar, Alberto Raggi, Fakher Rahim, Mosiur Rahman, Pradhum Ram, Priyanga Ranasinghe, David Laith Rawaf, Salman Rawaf, Nima Rezaei, Aziz Rezapour, Stephen R Robinson, Michele Romoli, Gholamreza Roshandel, Ramesh Sahathevan, Amirhossein Sahebkar, Mohammad Ali Sahraian, Brijesh Sathian, Davide Sattin, Monika Sawhney, Mete Saylan, Silvia Schiavolin, Allen Seylani, Feng Sha, Masood Ali Shaikh, Ks Shaji, Mohammed Shannawaz, Jeevan K Shetty, Mika Shigematsu, Jae Il Shin, Rahman Shiri, Diego Augusto Santos Silva, João Pedro Silva, Renata Silva, Jasvinder A Singh, Valentin Yurievich Skryabin, Anna Aleksandrovna Skryabina, Amanda E Smith, Sergey Soshnikov, Emma Elizabeth Spurlock, Dan J Stein, Jing Sun, Rafael Tabarés-Seisdedos, Bhaskar Thakur, Binod Timalsina, Marcos Roberto Tovani-Palone, Bach Xuan Tran, Gebiyaw Wudie Tsegaye, Sahel Valadan Tahbaz, Pascual R Valdez, Narayanaswamy Venketasubramanian, Vasily Vlassov, Giang Thu Vu, Linh Gia Vu, Yuan-Pang Wang, Anders Wimo, Andrea Sylvia Winkler, Lalit Yadav, Seyed Hossein Yahyazadeh Jabbari, Kazumasa Yamagishi, Lin Yang, Yuichiro Yano, Naohiro Yonemoto, Chuanhua Yu, Ismaeel Yunusa, Siddhesh Zadey, Mikhail Sergeevich Zastrozhin, Anasthasia Zastrozhina, Zhi-Jiang Zhang, Christopher J L Murray, and Theo Vos. **Estimation of the global prevalence of dementia in 2019 and forecasted prevalence in 2050: an analysis for the Global Burden of Disease Study 2019**. *The Lancet Public Health*, 7(2):e105–e125, February 2022.

[15] Carole Deyts, Gopal Thinakaran, and Angèle T. Parent. **APP Receptor? To Be or Not To Be**. *Trends in Pharmacological Sciences*, 37(5):390–411, May 2016.

[16] Mark P. Mattson. **Pathways towards and away from Alzheimer's disease**. *Nature*, 430 (7000):631–639, August 2004.

[17] Geert Van Gassen, Wim Annaert, and Christine Van Broeckhoven. **Binding Partners of Alzheimer's Disease Proteins: Are They Physiologically Relevant?** *Neurobiology of Disease*, 7(3):135–151, June 2000.

[18] Heather C. Rice, Daniel de Malmazet, An Schreurs, Samuel Frere, Inge Van Molle, Alexander N. Volkov, Eline Creemers, Irena Vertkin, Julie Nys, Fanomezana M. Ranaivoson, Davide Comoletti, Jeffrey N. Savas, Han Remaut, Detlef Balschun, Keimpe D. Wierda, Inna Slutsky, Karl Farrow, Bart De Strooper, and Joris de Wit. **Secreted amyloid-β precursor protein functions as a GABABR1a ligand to modulate synaptic transmission**. *Science*, 363(6423):eaao4827, January 2019.

[19] R. Vassar, B. D. Bennett, S. Babu-Khan, S. Kahn, E. A. Mendiaz, P. Denis, D. B. Teplow, S. Ross, P. Amarante, R. Loeloff, Y. Luo, S. Fisher, J. Fuller, S. Edenson, J. Lile, M. A. Jarosinski, A. L. Biere, E. Curran, T. Burgess, J. C. Louis, F. Collins, J. Treanor, G. Rogers, and M. Citron. **Beta-secretase cleavage of Alzheimer's amyloid precursor protein by the transmembrane aspartic protease BACE**. *Science (New York, N.Y.)*, 286(5440):735–741, October 1999.

[20] J. P. Greenfield, J. Tsai, G. K. Gouras, B. Hai, G. Thinakaran, F. Checler, S. S. Sisodia, P. Greengard, and H. Xu. **Endoplasmic reticulum and trans-Golgi network generate distinct populations of Alzheimer beta-amyloid peptides**. *Proceedings of the National Academy of Sciences of the United States of America*, 96(2):742–747, January 1999.

[21] C. Nordstedt, G.L. Caporaso, J. Thyberg, S.E. Gandy, and P. Greengard. **Identification of the Alzheimer beta/A4 amyloid precursor protein in clathrin-coated vesicles purified from PC12 cells.** *Journal of Biological Chemistry*, 268(1):608–612, January 1993.

[22] G. L. Caporaso, K. Takei, S. E. Gandy, M. Matteoli, O. Mundigl, P. Greengard, and P. De Camilli. **Morphologic and biochemical analysis of the intracellular trafficking of the Alzheimer beta/A4 amyloid precursor protein**. *The Journal of Neuroscience: The Official Journal of the Society for Neuroscience*, 14(5 Pt 2):3122–3138, May 1994.

[23] Kwasi G. Mawuenyega, Tom Kasten, Wendy Sigurdson, and Randall J. Bateman. **Amyloid-beta Isoform Metabolism Quantitation by Stable Isotope Labeled Kinetics**. *Analytical biochemistry*, 440(1):56–62, September 2013.

[24] John Hardy and Dennis J. Selkoe. **The Amyloid Hypothesis of Alzheimer's Disease: Progress and Problems on the Road to Therapeutics**. *Science*, 297(5580):353–356, July 2002.

[25] Sonia Ciudad, Eduard Puig, Thomas Botzanowski, Moeen Meigooni, Andres S. Arango, Jimmy Do, Maxim Mayzel, Mariam Bayoumi, Stéphane Chaignepain, Giovanni Maglia, Sarah Cianferani, Vladislav Orekhov, Emad Tajkhorshid, Benjamin Bardiaux, and Natàlia Carulla. **Aβ(1-42) tetramer and octamer structures reveal edge conductivity pores as a mechanism for membrane damage**. *Nature Communications*, 11(1):3014, June 2020.

[26] Jinming Wu, Thorsten B. Blum, Daniel P Farrell, Frank DiMaio, Jan Pieter Abrahams, and Jinghui Luo. **Cryo-electron Microscopy Imaging of Alzheimer's Amyloid-beta 42 Oligomer Displayed on a Functionally and Structurally Relevant Scaffold**. *Angewandte Chemie International Edition*, 60(34):18680–18687, 2021.

[27] Leonid Breydo, Dmitry Kurouski, Suhail Rasool, Saskia Milton, Jessica W. Wu, Vladimir N. Uversky, Igor K. Lednev, and Charles G. Glabe. **Structural differences between amyloid beta oligomers**. *Biochemical and Biophysical Research Communications*, 477(4):700–705, September 2016.

[28] Dennis J Selkoe and John Hardy. **The amyloid hypothesis of Alzheimer's disease at 25 years**. *EMBO Molecular Medicine*, 8(6):595–608, June 2016.

[29] Marius Kollmer, William Close, Leonie Funk, Jay Rasmussen, Aref Bsoul, Angelika Schierhorn, Matthias Schmidt, Christina J. Sigurdson, Mathias Jucker, and Marcus Fändrich. **Cryo-EM structure and polymorphism of Aβ amyloid fibrils purified from Alzheimer's brain tissue**. *Nature Communications*, 10(1):4760, December 2019.

[30] Lothar Gremer, Daniel Schölzel, Carla Schenk, Elke Reinartz, Jörg Labahn, Raimond B. G. Ravelli, Markus Tusche, Carmen Lopez-Iglesias, Wolfgang Hoyer, Henrike Heise, Dieter Willbold, and Gunnar F. Schröder. **Fibril structure of amyloid-β(1-42) by cryo-electron microscopy**. *Science (New York, N.Y.)*, 358(6359):116–119, October 2017.

[31] Ganesh M. Shankar, Shaomin Li, Tapan H. Mehta, Amaya Garcia-Munoz, Nina E. Shepardson, Imelda Smith, Francesca M. Brett, Michael A. Farrell, Michael J. Rowan, Cynthia A. Lemere, Ciaran M. Regan, Dominic M. Walsh, Bernardo L. Sabatini, and Dennis J. Selkoe. **Amyloid-β protein dimers isolated directly from Alzheimer's brains impair synaptic plasticity and memory**. *Nature Medicine*, 14(8):837–842, August 2008.

[32] Richard A. Armstrong. **The molecular biology of senile plaques and neurofibrillary tangles in Alzheimer's disease**. *Folia Neuropathologica*, 47(4):289–99, December 2009.

[33] M. Mahafuzur Rahman and Christofer Lendel. **Extracellular protein components of amyloid plaques and their roles in Alzheimer's disease pathology**. *Molecular Neurodegeneration*, 16(1):59, August 2021.

[34] T. Oda, G. M. Pasinetti, H. H. Osterburg, C. Anderson, S. A. Johnson, and C. E. Finch. **Purification and Characterization of Brain Clusterin**. *Biochemical and Biophysical Research Communications*, 204(3):1131–1136, November 1994.

[35] Suman De, David C. Wirthensohn, Patrick Flagmeier, Craig Hughes, Francesco A. Aprile, Francesco S. Ruggeri, Daniel R. Whiten, Derya Emin, Zengjie Xia, Juan A. Varela, Pietro Sormanni, Franziska Kundel, Tuomas P. J. Knowles, Christopher M. Dobson, Clare Bryant, Michele Vendruscolo, and David Klenerman. **Different soluble aggregates of Aβ42 can give rise to cellular toxicity through different mechanisms**. *Nature Communications*, 10(1):1541, December 2019.

[36] Meenakshi Verma, Abhishek Vats, and Vibha Taneja. **Toxic species in amyloid disorders: Oligomers or mature fibrils**. *Annals of Indian Academy of Neurology*, 18(2):138–145, 2015.

[37] Minako Hoshi, Michio Sato, Shinichiro Matsumoto, Akihiko Noguchi, Kaori Yasutake, Natsuko Yoshida, and Kazuki Sato. **Spherical aggregates of β-amyloid (amylospheroid) show high neurotoxicity and activate tau protein kinase I/glycogen synthase kinase-3β**. *Proceedings of the National Academy of Sciences*, 100(11):6370–6375, May 2003.

[38] Karie N. Dahlgren, Arlene M. Manelli, W. Blaine Stine, Lorinda K. Baker, Grant A. Krafft, and Mary Jo LaDu. **Oligomeric and Fibrillar Species of Amyloid-β Peptides Differentially Affect Neuronal Viability** *. *Journal of Biological Chemistry*, 277(35):32046–32053, August 2002.

[39] M. P. Lambert, A. K. Barlow, B. A. Chromy, C. Edwards, R. Freed, M. Liosatos, T. E. Morgan, I. Rozovsky, B. Trommer, K. L. Viola, P. Wals, C. Zhang, C. E. Finch, G. A. Krafft, and W. L. Klein. **Diffusible, nonfibrillar ligands derived from Abeta1-42 are potent central nervous system neurotoxins**. *Proceedings of the National Academy of Sciences of the United States of America*, 95(11):6448–6453, May 1998.

[40] Rakez Kayed, Elizabeth Head, Jennifer L. Thompson, Theresa M. McIntire, Saskia C. Milton, Carl W. Cotman, and Charles G. Glabe. **Common structure of soluble amyloid oligomers implies common mechanism of pathogenesis**. *Science (New York, N.Y.)*, 300(5618):486–489, April 2003.

[41] Hyoung-Gon Lee, Gemma Casadesus, Xiongwei Zhu, Atsushi Takeda, George Perry, and Mark A. Smith. **Challenging the amyloid cascade hypothesis: senile plaques and amyloid-beta as protective adaptations to Alzheimer disease**. *Annals of the New York Academy of Sciences*, 1019:1–4, June 2004.

[42] Renee C. Gaspar, Stephanie A. Villarreal, Nicole Bowles, Robert W. Hepler, Joseph G. Joyce, and Paul J. Shughrue. **Oligomers of β-amyloid are sequestered into and seed new plaques in the brains of an AD mouse model**. *Experimental Neurology*, 223(2):394–400, June 2010.

[43] Erika N. Cline, Maíra Assunção Bicca, Kirsten L. Viola, and William L. Klein. **The Amyloid-β Oligomer Hypothesis: Beginning of the Third Decade**. *Journal of Alzheimer's disease: JAD*, 64(s1):S567–S610, 2018.

[44] Heledd H. Jarosz-Griffiths, Elizabeth Noble, Jo V. Rushworth, and Nigel M. Hooper. **Amyloid-β Receptors: The Good, the Bad, and the Prion Protein**. *The Journal of Biological Chemistry*, 291(7):3174–3183, February 2016.

[45] Nadine S. Rösener, Lothar Gremer, Elke Reinartz, Anna König, Oleksandr Brener, Henrike Heise, Wolfgang Hoyer, Philipp Neudecker, and Dieter Willbold. **A d-enantiomeric peptide interferes with heteroassociation of amyloid-β oligomers and prion protein**. *The Journal of Biological Chemistry*, 293(41):15748–15764, October 2018.

[46] Ladan Amin and David A. Harris. **Aβ receptors specifically recognize molecular features displayed by fibril ends and neurotoxic oligomers**. *Nature Communications*, 12(1):3451, June 2021.

[47] Senthilkumar Sivanesan, Aaron Tan, and Jayakumar Rajadas. **Pathogenesis of Abeta oligomers in synaptic failure**. *Current Alzheimer Research*, 10(3):316–323, March 2013.

[48] Marianne Renner, Pascale N. Lacor, Pauline T. Velasco, Jian Xu, Anis Contractor, William L. Klein, and Antoine Triller. **Deleterious effects of amyloid beta oligomers acting as an extracellular scaffold for mGluR5**. *Neuron*, 66(5):739–754, June 2010.

[49] Pascale N. Lacor, Maria C. Buniel, Paul W. Furlow, Antonio Sanz Clemente, Pauline T. Velasco, Margaret Wood, Kirsten L. Viola, and William L. Klein. **Aβ Oligomer-Induced Aberrations in Synapse Composition, Shape, and Density Provide a Molecular Basis for Loss of Connectivity in Alzheimer's Disease**. *Journal of Neuroscience*, 27(4):796–807, January 2007.

[50] D. M. Hartley, D. M. Walsh, C. P. Ye, T. Diehl, S. Vasquez, P. M. Vassilev, D. B. Teplow, and D. J. Selkoe. **Protofibrillar intermediates of amyloid beta-protein induce acute electrophysiological changes and progressive neurotoxicity in cortical neurons**. *The Journal of Neuroscience: The Official Journal of the Society for Neuroscience*, 19(20):8876–8884, October 1999.

[51] Igor Klyubin, Dominic M. Walsh, William K. Cullen, Julia V. Fadeeva, Roger Anwyl, Dennis J. Selkoe, and Michael J. Rowan. **Soluble Arctic amyloid beta protein inhibits hippocampal long-term potentiation in vivo**. *The European Journal of Neuroscience*, 19(10):2839–2846, May 2004.

[52] A. M. Klein, N. W. Kowall, and R. J. Ferrante. **Neurotoxicity and oxidative damage of beta amyloid 1-42 versus beta amyloid 1-40 in the mouse cerebral cortex**. *Annals of the New York Academy of Sciences*, 893:314–320, 1999.

[53] Fernanda G. De Felice, Pauline T. Velasco, Mary P. Lambert, Kirsten Viola, Sara J. Fernandez, Sergio T. Ferreira, and William L. Klein. **Abeta oligomers induce neuronal oxidative stress through an N-methyl-D-aspartate receptor-dependent mechanism that is blocked by the Alzheimer drug memantine**. *The Journal of Biological Chemistry*, 282(15):11590–11601, April 2007.

[54] Taro Yasumoto, Yusaku Takamura, Mayumi Tsuji, Takahiro Watanabe-Nakayama, Keiko Imamura, Haruhisa Inoue, Shiro Nakamura, Tomio Inoue, Atsushi Kimura, Satoshi Yano, Hisao Nishijo, Yuji Kiuchi, David B. Teplow, and Kenjiro Ono. **High molecular weight amyloid β1-42 oligomers induce neurotoxicity via plasma membrane damage**. *The FASEB Journal*, 33(8):9220–9234, 2019.

[55] Tomohiro Umeda, Takami Tomiyama, Naomi Sakama, Saya Tanaka, Mary P. Lambert, William L. Klein, and Hiroshi Mori. **Intraneuronal amyloid β oligomers cause cell death via endoplasmic reticulum stress, endosomal/lysosomal leakage, and mitochondrial dysfunction in vivo**. *Journal of Neuroscience Research*, 89(7):1031–1042, July 2011.

[56] Takami Tomiyama, Shogo Matsuyama, Hiroyuki Iso, Tomohiro Umeda, Hiroshi Takuma, Kiyouhisa Ohnishi, Kenichi Ishibashi, Rie Teraoka, Naomi Sakama, Takenari Yamashita, Kazuchika Nishitsuji, Kazuhiro Ito, Hiroyuki Shimada, Mary P. Lambert, William L. Klein, and Hiroshi Mori. **A mouse model of amyloid beta oligomers: their contribution to synaptic alteration, abnormal tau phosphorylation, glial activation, and neuronal loss in vivo**. *The Journal of Neuroscience: The Official Journal of the Society for Neuroscience*, 30(14):4845–4856, April 2010.

[57] Rola Ismail, Peter Parbo, Lasse Stensvig Madsen, Allan K. Hansen, Kim V. Hansen, Jeppe L. Schaldemose, Pernille L. Kjeldsen, Morten G. Stokholm, Hanne Gottrup, Simon F. Eskildsen, and David J. Brooks. **The relationships between neuroinflammation, beta-amyloid and tau deposition in Alzheimer's disease: a longitudinal PET study**. *Journal of Neuroinflammation*, 17(1):151, May 2020.

[58] Jeffrey M. Craft, D. Martin Watterson, and Linda J. Van Eldik. **Human amyloid beta-induced neuroinflammation is an early event in neurodegeneration**. *Glia*, 53(5):484–490, April 2006.

[59] Jefferson W. Kinney, Shane M. Bemiller, Andrew S. Murtishaw, Amanda M. Leisgang, Arnold M. Salazar, and Bruce T. Lamb. **Inflammation as a central mechanism in Alzheimer's disease**. *Alzheimer's & Dementia: Translational Research & Clinical Interventions*, 4:575–590, January 2018.

[60] Myles R. Minter, Juliet M. Taylor, and Peter J. Crack. **The contribution of neuroinflammation to amyloid toxicity in Alzheimer's disease**. *Journal of Neurochemistry*, 136(3):457–474, 2016.

[61] Hans Zempel and Eckhard Mandelkow. **Lost after translation: missorting of Tau protein and consequences for Alzheimer disease**. *Trends in Neurosciences*, 37(12):721–732, December 2014.

[62] Fernanda G. De Felice, Diana Wu, Mary P. Lambert, Sara J. Fernandez, Pauline T. Velasco, Pascale N. Lacor, Eileen H. Bigio, Jasna Jerecic, Paul J. Acton, Paul J. Shughrue, Elizabeth Chen-Dodson, Gene G. Kinney, and William L. Klein. **Alzheimer's disease-type neuronal tau hyperphosphorylation induced by Aβ oligomers**. *Neurobiology of aging*, 29(9):1334–1347, September 2008.

[63] Hans Zempel, Julia Luedtke, Yatender Kumar, Jacek Biernat, Hana Dawson, Eckhard Mandelkow, and Eva-Maria Mandelkow. **Amyloid-β oligomers induce synaptic damage via Tau-dependent microtubule severing by TTLL6 and spastin**. *The EMBO journal*, 32(22): 2920–2937, November 2013.

[64] Hans Zempel, Edda Thies, Eckhard Mandelkow, and Eva-Maria Mandelkow. **Abeta oligomers cause localized Ca(2+) elevation, missorting of endogenous Tau into dendrites, Tau phosphorylation, and destruction of microtubules and spines**. *The Journal of Neuroscience: The Official Journal of the Society for Neuroscience*, 30(36):11938–11950, September 2010.

[65] M. P. Lambert, A. K. Barlow, B. A. Chromy, C. Edwards, R. Freed, M. Liosatos, T. E. Morgan, I. Rozovsky, B. Trommer, K. L. Viola, P. Wals, C. Zhang, C. E. Finch, G. A. Krafft, and W. L. Klein. **Diffusible, nonfibrillar ligands derived from Abeta1-42 are potent central nervous system neurotoxins**. *Proceedings of the National Academy of Sciences of the United States of America*, 95(11):6448–6453, May 1998.

[66] Pascale N. Lacor, Maria C. Buniel, Paul W. Furlow, Antonio Sanz Clemente, Pauline T. Velasco, Margaret Wood, Kirsten L. Viola, and William L. Klein. **Abeta oligomer-induced aberrations in synapse composition, shape, and density provide a molecular basis for loss of connectivity in Alzheimer's disease**. *The Journal of Neuroscience: The Official Journal of the Society for Neuroscience*, 27(4):796–807, January 2007.

[67] Leticia Forny-Germano, Natalia M. Lyra e Silva, André F. Batista, Jordano Brito-Moreira, Matthias Gralle, Susan E. Boehnke, Brian C. Coe, Ann Lablans, Suelen A. Marques, Ana Maria B. Martinez, William L. Klein, Jean-Christophe Houzel, Sergio T. Ferreira, Douglas P. Munoz, and Fernanda G. De Felice. **Alzheimer's disease-like pathology induced by amyloid-β oligomers in nonhuman primates**. *The Journal of Neuroscience: The Official Journal of the Society for Neuroscience*, 34(41):13629–13643, October 2014.

[68] John A. Hardy and Gerald A. Higgins. **Alzheimer's Disease: The Amyloid Cascade Hypothesis**. *Science*, 256(5054):184–185, April 1992.

[69] Jeffrey Cummings, Garam Lee, Kate Zhong, Jorge Fonseca, and Kazem Taghva. **Alzheimer's disease drug development pipeline: 2021**. *Alzheimer's & Dementia: Translational Research & Clinical Interventions*, 7(1):e12179, 2021.

[70] Shih-Ya Hung and Wen-Mei Fu. **Drug candidates in clinical trials for Alzheimer's disease**. *Journal of Biomedical Science*, 24(1):47, December 2017.

[71] Robert Vassar. **BACE1 inhibitor drugs in clinical trials for Alzheimer's disease**. *Alzheimer's Research & Therapy*, 6(9):89, December 2014.

[72] Justyna Godyń, Jakub Jończyk, Dawid Panek, and Barbara Malawska. **Therapeutic strategies for Alzheimer's disease in clinical trials**. *Pharmacological Reports*, 68(1):127–138, February 2016.

[73] Takeshi Tabira. **Immunization therapy for Alzheimer disease: a comprehensive review of active immunization strategies**. *The Tohoku Journal of Experimental Medicine*, 220(2): 95–106, February 2010.

[74] Li-Kai Huang, Shu-Ping Chao, and Chaur-Jong Hu. **Clinical trials of new drugs for Alzheimer disease**. *Journal of Biomedical Science*, 27:18, January 2020.

[75] Angela Tian Hui Kwan, Saman Arfaie, Joseph Therriault, Pedro Rosa-Neto, and Serge Gauthier. **Lessons Learnt from the Second Generation of Anti-Amyloid Monoclonal Antibodies Clinical Trials**. *Dementia and Geriatric Cognitive Disorders*, 49(4):334–348, 2020.

[76] Jing Zhao, Xinyue Liu, Weiming Xia, Yingkai Zhang, and Chunyu Wang. **Targeting Amyloidogenic Processing of APP in Alzheimer's Disease**. *Frontiers in Molecular Neuroscience*, 13, 2020.

[77] Masihuz Zaman, Asra Nasir Khan, Wahiduzzaman, Syed Mohammad Zakariya, and Rizwan Hasan Khan. **Protein misfolding, aggregation and mechanism of amyloid cytotoxicity: An overview and therapeutic strategies to inhibit aggregation**. *International Journal of Biological Macromolecules*, 134:1022–1037, August 2019.

[78] Sofia Giorgetti, Claudio Greco, Paolo Tortora, and Francesco Antonio Aprile. **Targeting Amyloid Aggregation: An Overview of Strategies and Mechanisms**. *International Journal of Molecular Sciences*, 19(9):2677, September 2018.

[79] F. Re, C. Airoldi, C. Zona, M. Masserini, B. La Ferla, N. Quattrocchi, and F. Nicotra. **Beta Amyloid Aggregation Inhibitors: Small Molecules as Candidate Drugs for Therapy of Alzheimer's Disease**. *Current Medicinal Chemistry*, 17(27):2990–3006, September 2010.

[80] Paul A. Novick, Dahabada H. Lopes, Kim M. Branson, Alexandra Esteras-Chopo, Isabella A. Graef, Gal Bitan, and Vijay S. Pande. **Design of β-Amyloid Aggregation Inhibitors from a Predicted Structural Motif**. *Journal of Medicinal Chemistry*, 55(7):3002–3010, April 2012.

[81] Safura Jokar, Saeedeh Khazaei, Hossein Behnammanesh, Amir Shamloo, Mostafa Erfani, Davood Beiki, and Omid Bavi. **Recent advances in the design and applications of amyloid-β peptide aggregation inhibitors for Alzheimer's disease therapy**. *Biophysical Reviews*, 11(6):901–925, December 2019.

[82] Yuan Luo, Sheetal Vali, Suya Sun, Xuesong Chen, Xia Liang, Tatiana Drozhzhina, Elena Popugaeva, and Ilya Bezprozvanny. **Aβ42-Binding Peptoids as Amyloid Aggregation Inhibitors and Detection Ligands**. *ACS Chemical Neuroscience*, 4(6):952–962, June 2013.

[83] P. Talaga. **beta-Amyloid Aggregation Inhibitors for the Treatment of Alzheimer Disease Dream or Reality?** *Mini Reviews in Medicinal Chemistry*, 1(2):175–186, July 2001.

[84] Jing Zhao, Xinyue Liu, Weiming Xia, Yingkai Zhang, and Chunyu Wang. **Targeting Amyloidogenic Processing of APP in Alzheimer's Disease**. *Frontiers in Molecular Neuroscience*, 13, 2020.

[85] Arun K. Ghosh, Dongwoo Shin, Debbie Downs, Gerald Koelsch, Xinli Lin, Jacques Ermolieff, and Jordan Tang. **Design of Potent Inhibitors for Human Brain Memapsin 2 (β-Secretase)**. *Journal of the American Chemical Society*, 122(14):3522–3523, April 2000.

[86] Kelly Willemijn Menting and Jurgen A. H. R. Claassen. **β-secretase inhibitor; a promising novel therapeutic drug in Alzheimer's disease**. *Frontiers in Aging Neuroscience*, 6, 2014.

[87] Matthew E. Kennedy, Andrew W. Stamford, Xia Chen, Kathleen Cox, Jared N. Cumming, Marissa F. Dockendorf, Michael Egan, Larry Ereshefsky, Robert A. Hodgson, Lynn A. Hyde, Stanford Jhee, Huub J. Kleijn, Reshma Kuvelkar, Wei Li, Britta A. Mattson, Hong Mei, John Palcza, Jack D. Scott, Michael Tanen, Matthew D. Troyer, Jack L. Tseng, Julie A. Stone, Eric M. Parker, and Mark S. Forman. **The BACE1 inhibitor verubecestat (MK-8931) reduces CNS β-amyloid in animal models and in Alzheimer's disease patients**. *Science Translational Medicine*, 8 (363):363ra150, November 2016.

[88] Patrick C. May, Brian A. Willis, Stephen L. Lowe, Robert A. Dean, Scott A. Monk, Patrick J. Cocke, James E. Audia, Leonard N. Boggs, Anthony R. Borders, Richard A. Brier, David O. Calligaro, Theresa A. Day, Larry Ereshefsky, Jon A. Erickson, Hykop Gevorkyan, Celedon R. Gonzales, Douglas E. James, Stanford S. Jhee, Steven F. Komjathy, Linglin Li, Terry D. Lindstrom, Brian M. Mathes, Ferenc Martényi, Scott M. Sheehan, Stephanie L. Stout, David E. Timm, Grant M. Vaught, Brian M. Watson, Leonard L. Winneroski, Zhixiang Yang, and Dustin J. Mergott. **The potent BACE1 inhibitor LY2886721 elicits robust central Aβ pharmacodynamic responses in mice, dogs, and humans**. *The Journal of Neuroscience: The Official Journal of the Society for Neuroscience*, 35(3):1199–1210, January 2015.

[89] Fredrik Jeppsson, Susanna Eketjäll, Juliette Janson, Sofia Karlström, Susanne Gustavsson, Lise-Lotte Olsson, Ann-Cathrine Radesäter, Bart Ploeger, Gvido Cebers, Karin Kolmodin, Britt-Marie Swahn, Stefan von Berg, Tjerk Bueters, and Johanna Fälting. **Discovery of AZD3839, a Potent and Selective BACE1 Inhibitor Clinical Candidate for the Treatment of Alzheimer Disease***. *Journal of Biological Chemistry*, 287(49):41245–41257, November 2012.

[90] Maarten Timmers, Bianca Van Broeck, Steven Ramael, John Slemmon, Katja De Waepenaert, Alberto Russu, Jennifer Bogert, Hans Stieltjes, Leslie M. Shaw, Sebastiaan Engelborghs, Dieder Moechars, Marc Mercken, Enchi Liu, Vikash Sinha, John Kemp, Luc Van Nueten, Luc Tritsmans, and Johannes Rolf Streffer. **Profiling the dynamics of CSF and plasma Aβ reduction after treatment with JNJ-54861911, a potent oral BACE inhibitor**. *Alzheimer's & Dementia (New York, N. Y.)*, 2(3):202–212, September 2016.

[91] J. R. Sims, K. J. Selzler, A. M. Downing, B. A. Willis, C. D. Aluise, J. Zimmer, S. Bragg, S. Andersen, M. Ayan-Oshodi, E. Liffick, J. Eads, A. M. Wessels, S. Monk, J. Schumi, and J. Mullen. **Development Review of the BACE1 Inhibitor Lanabecestat (AZD3293/LY3314814)**. *The Journal of Prevention of Alzheimer's Disease*, 4(4):247–254, 2017.

[92] Kei Sakamoto, Shunji Matsuki, Kyoko Matsuguma, Tatsuya Yoshihara, Naoki Uchida, Fumihiko Azuma, Muir Russell, Glen Hughes, Samantha Budd Haeberlein, Robert C. Alexander, Susanna Eketjäll, and Alan R. Kugler. **BACE1 Inhibitor Lanabecestat (AZD3293) in a Phase 1 Study of Healthy Japanese Subjects: Pharmacokinetics and Effects on Plasma and Cerebrospinal Fluid Aβ Peptides**. *Journal of Clinical Pharmacology*, 57(11):1460–1471, November 2017.

[93] Vladimir Volloch and Sophia Rits. **Results of Beta Secretase-Inhibitor Clinical Trials Support Amyloid Precursor Protein-Independent Generation of Beta Amyloid in Sporadic Alzheimer's Disease**. *Medical Sciences*, 6(2):45, June 2018.

[94] **Another BACE inhibitor fails in phase III trials**. June 2018. URL https://www.clinicaltrialsarena.com/comment/another-bace-inhibitor-fails-phase-iii-trials/. Accessed on 2022-04-02.

[95] Michael F. Egan, James Kost, Pierre N. Tariot, Paul S. Aisen, Jeffrey L. Cummings, Bruno Vellas, Cyrille Sur, Yuki Mukai, Tiffini Voss, Christine Furtek, Erin Mahoney, Lyn Harper Mozley, Rik Vandenberghe, Yi Mo, and David Michelson. **Randomized Trial of Verubecestat for Mild-to-Moderate Alzheimer's Disease**. *New England Journal of Medicine*, 378(18):1691–1703, May 2018.

[96] David Henley, Nandini Raghavan, Reisa Sperling, Paul Aisen, Rema Raman, and Gary Romano. **Preliminary Results of a Trial of Atabecestat in Preclinical Alzheimer's Disease**. *New England Journal of Medicine*, 380(15):1483–1485, April 2019.

[97] Michael F. Egan, James Kost, Tiffini Voss, Yuki Mukai, Paul S. Aisen, Jeffrey L. Cummings, Pierre N. Tariot, Bruno Vellas, Christopher H. van Dyck, Merce Boada, Ying Zhang, Wen Li, Christine Furtek, Erin Mahoney, Lyn Harper Mozley, Yi Mo, Cyrille Sur, and David Michelson. **Randomized Trial of Verubecestat for Prodromal Alzheimer's Disease**. *New England Journal of Medicine*, 380(15):1408–1420, April 2019.

[98] Rachelle S. Doody, Rema Raman, Martin Farlow, Takeshi Iwatsubo, Bruno Vellas, Steven Joffe, Karl Kieburtz, Feng He, Xiaoying Sun, Ronald G. Thomas, Paul S. Aisen, Alzheimer's Disease Cooperative Study Steering Committee, Eric Siemers, Gopalan Sethuraman, Richard Mohs, and Semagacestat Study Group. **A phase 3 trial of semagacestat for treatment of Alzheimer's disease**. *The New England Journal of Medicine*, 369(4):341–350, July 2013.

[99] David B. Henley, Karen L. Sundell, Gopalan Sethuraman, Sherie A. Dowsett, and Patrick C. May. **Safety profile of semagacestat, a gamma-secretase inhibitor: IDENTITY trial findings**. *Current Medical Research and Opinion*, 30(10):2021–2032, October 2014.

[100] Annakaisa Haapasalo and Dora M. Kovacs. **The many substrates of presenilin/γ-secretase**. *Journal of Alzheimer's disease: JAD*, 25(1):3–28, 2011.

[101] Nathalie Jurisch-Yaksi, Ragna Sannerud, and Wim Annaert. **A fast growing spectrum of biological functions of γ-secretase in development and disease**. *Biochimica Et Biophysica Acta*, 1828(12):2815–2827, December 2013.

[102] Chihiro Sato, Guojun Zhao, and Ma. Xenia G. Ilagan. **An Overview of Notch Signaling in Adult Tissue Renewal and Maintenance**. *Current Alzheimer research*, 9(2):227–240, February 2012.

[103] Corinne E. Augelli-Szafran, Han-Xun Wei, Dai Lu, Jing Zhang, Yongli Gu, Ting Yang, Pamela Osenkowski, Wenjuan Ye, and Michael S Wolfe. **Discovery of Notch-Sparing γ-Secretase Inhibitors**. *Current Alzheimer research*, 7(3):207–209, May 2010.

[104] Todd E. Golde, Edward H. Koo, Kevin M. Felsenstein, Barbara A. Osborne, and Lucio Miele. **γ-Secretase inhibitors and modulators**. *Biochimica et Biophysica Acta (BBA) - Biomembranes*, 1828(12):2898–2907, December 2013.

[105] Jing Zhang, Dai Lu, Han-Xun Wei, Yongli Gu, Dennis J. Selkoe, Michael S. Wolfe, and Corinne E. Augelli-Szafran. **Part 3: Notch-sparing γ-secretase inhibitors: SAR studies of 2-substituted aminopyridopyrimidinones**. *Bioorganic & Medicinal Chemistry Letters*, 26(9): 2138–2141, May 2016.

[106] Kathryn Rogers, Kevin M. Felsenstein, Lori Hrdlicka, Zhiming Tu, Faris Albayya, Winnie Lee, Sarah Hopp, Mary-Jo Miller, Darcie Spaulding, Zhiyong Yang, Hilliary Hodgdon, Scott Nolan, Melody Wen, Don Costa, Jean-Francois Blain, Emily Freeman, Bart De Strooper, Veerle Vulsteke, Louise Scrocchi, Henrik Zetterberg, Erik Portelius, Birgit Hutter-Paier, Daniel Havas, Michael Ahlijanian, Dorothy Flood, Liza Leventhal, Gideon Shapiro, Holger Patzke, Richard Chesworth, and Gerhard Koenig. **Modulation of γ-secretase by EVP-0015962 reduces amyloid deposition and behavioral deficits in Tg2576 mice**. *Molecular Neurodegeneration*, 7:61, December 2012.

[107] FORUM Pharmaceuticals Inc. **Safety, Tolerability, Pharmacokinetics, and Effects of EVP-0962 on Cerebral Spinal Fluid Amyloid Concentrations in Healthy Subjects and in Subjects With Mild Cognitive Impairment or Early Alzheimer's Disease**. Clinical trial registration NCT01661673, clinicaltrials.gov, January 2014. URL https://clinicaltrials.gov/ct2/show/NCT01661673. Accessed on 2022-04-03.

[108] Hillel Grossman, George Marzloff, Xiaodong Luo, Derek LeRoith, Mary Sano, and Giulio Pasinetti. **P1-279: NIC5-15 as a treatment for Alzheimer's: Safety, pharmacokinetics and clinical variables**. *Alzheimer's & Dementia*, 5(4S_Part_9):P259–P259, 2009.

[109] Humanetics Corporation. **A Single Site, Randomized, Double-blind, Placebo Controlled Trial of NIC5-15 in Subjects With Alzheimer's Disease**. Clinical trial registration NCT01928420, clinicaltrials.gov, October 2016. URL https://clinicaltrials.gov/ct2/show/NCT01928420. Accessed on 2022-04-03.

[110] Bart De Strooper. **Lessons from a Failed γ-Secretase Alzheimer Trial**. *Cell*, 159(4):721–726, November 2014.

[111] Janine Kutzsche, Dagmar Jürgens, Antje Willuweit, Knut Adermann, Carola Fuchs, Stefanie Simons, Manfred Windisch, Michael Hümpel, Wolfgang Rossberg, Michael Wolzt, and Dieter Willbold. **Safety and pharmacokinetics of the orally available antiprionic compound PRI-002: A single and multiple ascending dose phase I study**. *Alzheimer's & Dementia (New York, N. Y.)*, 6(1):e12001, 2020.

[112] Fusheng Yang, Giselle P. Lim, Aynun N. Begum, Oliver J. Ubeda, Mychica R. Simmons, Surendra S. Ambegaokar, Pingping P. Chen, Rakez Kayed, Charles G. Glabe, Sally A. Frautschy, and Gregory M. Cole. **Curcumin Inhibits Formation of Amyloid β Oligomers and Fibrils, Binds Plaques, and Reduces Amyloid in Vivo***. *Journal of Biological Chemistry*, 280(7):5892–5901, February 2005.

[113] John A. Hey, Jeremy Y. Yu, Mark Versavel, Susan Abushakra, Petr Kocis, Aidan Power, Paul L. Kaplan, John Amedio, and Martin Tolar. **Clinical Pharmacokinetics and Safety of ALZ-801, a Novel Prodrug of Tramiprosate in Development for the Treatment of Alzheimer's Disease**. *Clinical Pharmacokinetics*, 57(3):315–333, March 2018.

[114] Martin Tolar, Susan Abushakra, John A. Hey, Anton Porsteinsson, and Marwan Sabbagh. **Aducanumab, gantenerumab, BAN2401, and ALZ-801—the first wave of amyloid-targeting drugs for Alzheimer's disease with potential for near term approval**. *Alzheimer's Research & Therapy*, 12(1):95, August 2020.

[115] Ryan Limbocker, Silvia Errico, Denise Barbut, Tuomas P. J. Knowles, Michele Vendruscolo, Fabrizio Chiti, and Michael Zasloff. **Squalamine and trodusquemine: two natural products for neurodegenerative diseases, from physical chemistry to the clinic**. *Natural Product Reports*, 2022.

[116] Johnny Habchi, Paolo Arosio, Michele Perni, Ana Rita Costa, Maho Yagi-Utsumi, Priyanka Joshi, Sean Chia, Samuel I. A. Cohen, Martin B. D. Müller, Sara Linse, Ellen A. A. Nollen, Christopher M. Dobson, Tuomas P. J. Knowles, and Michele Vendruscolo. **An anticancer drug suppresses the primary nucleation reaction that initiates the production of the toxic Aβ42 aggregates linked with Alzheimer's disease**. *Science Advances*, 2(2):e1501244, February 2016.

[117] Ziao Fu, Darryl Aucoin, Mahiuddin Ahmed, Martine Ziliox, William E. Van Nostrand, and Steven O. Smith. **Capping of aβ42 oligomers by small molecule inhibitors**. *Biochemistry*, 53(50):7893–7903, December 2014.

[118] Francesco A. Aprile, Pietro Sormanni, Michele Perni, Paolo Arosio, Sara Linse, Tuomas P. J. Knowles, Christopher M. Dobson, and Michele Vendruscolo. **Selective targeting of primary and secondary nucleation pathways in Aβ42 aggregation using a rational antibody scanning method**. *Science Advances*, 3(6):e1700488, June 2017.

[119] Kazuma Murakami, Takuya Yoshioka, Shiori Horii, Mizuho Hanaki, Satohiro Midorikawa, Shinji Taniwaki, Hiroki Gunji, Ken-ichi Akagi, Taiji Kawase, Kenji Hirose, and Kazuhiro Irie. **Role of the carboxy groups of triterpenoids in their inhibition of the nucleation of amyloid β42 required for forming toxic oligomers**. *Chemical Communications*, 54(49):6272–6275, June 2018.

[120] Rashik Ahmed, Bryan VanSchouwen, Naeimeh Jafari, Xiaodan Ni, Joaquin Ortega, and Giuseppe Melacini. **Molecular Mechanism for the (-)-Epigallocatechin Gallate-Induced Toxic to Nontoxic Remodeling of Aβ Oligomers**. *Journal of the American Chemical Society*, 139(39):13720–13734, October 2017.

[121] Paul Matthew Seidler, David R. Boyer, Kevin A. Murray, Tianxiao P. Yang, Megan Bentzel, Michael R. Sawaya, Gregory Rosenberg, Duilio Cascio, Christopher Kazu Williams, Kathy L. Newell, Bernardino Ghetti, Michael A. DeTure, Dennis W. Dickson, Harry V. Vinters, and David S. Eisenberg. **Structure-based inhibitors halt prion-like seeding by Alzheimer's disease–and tauopathy–derived brain tissue samples**. *Journal of Biological Chemistry*, 294(44): 16451–16464, November 2019.

[122] Phetcharat Boonruamkaew, Pennapa Chonpathompikunlert, Long Binh Vong, Sho Sakaue, Yasushi Tomidokoro, Kazuhiro Ishii, Akira Tamaoka, and Yukio Nagasaki. **Chronic treatment with a smart antioxidative nanoparticle for inhibition of amyloid plaque propagation in Tg2576 mouse model of Alzheimer's disease**. *Scientific Reports*, 7(1):3785, June 2017.

[123] Georg Meisl, Julius B. Kirkegaard, Paolo Arosio, Thomas C. T. Michaels, Michele Vendruscolo, Christopher M. Dobson, Sara Linse, and Tuomas P. J. Knowles. **Molecular mechanisms of protein aggregation from global fitting of kinetic models**. *Nature Protocols*, 11(2):252–272, February 2016.

[124] Sara Linse. **Mechanism of amyloid protein aggregation and the role of inhibitors**. *Pure and Applied Chemistry*, 91(2):211–229, February 2019.

[125] Samuel I. A. Cohen, Sara Linse, Leila M. Luheshi, Erik Hellstrand, Duncan A. White, Luke Rajah, Daniel E. Otzen, Michele Vendruscolo, Christopher M. Dobson, and Tuomas P. J. Knowles. **Proliferation of amyloid-β42 aggregates occurs through a secondary nucleation mechanism**. *Proceedings of the National Academy of Sciences*, 110(24):9758–9763, June 2013.

[126] Samuel I. A. Cohen, Paolo Arosio, Jenny Presto, Firoz Roshan Kurudenkandy, Henrik Biverstål, Lisa Dolfe, Christopher Dunning, Xiaoting Yang, Birgitta Frohm, Michele Vendruscolo, Jan Johansson, Christopher M. Dobson, André Fisahn, Tuomas P. J. Knowles, and Sara Linse. **A molecular chaperone breaks the catalytic cycle that generates toxic Aβ oligomers**. *Nature Structural & Molecular Biology*, 22(3):207–213, March 2015.

[127] Mattias Törnquist, Thomas C. T. Michaels, Kalyani Sanagavarapu, Xiaoting Yang, Georg Meisl, Samuel I. A. Cohen, Tuomas P. J. Knowles, and Sara Linse. **Secondary nucleation in amyloid formation**. *Chemical Communications*, 54(63):8667–8684, August 2018.

[128] Filip Hasecke, Tatiana Miti, Carlos Perez, Jeremy Barton, Daniel Schölzel, Lothar Gremer, Clara S. R. Grüning, Garrett Matthews, Georg Meisl, Tuomas P. J. Knowles, Dieter Willbold, Philipp Neudecker, Henrike Heise, Ghanim Ullah, Wolfgang Hoyer, and Martin Muschol. **Origin of metastable oligomers and their effects on amyloid fibril self-assembly**. *Chemical Science*, 9(27):5937–5948, July 2018.

[129] Filip Hasecke, Chamani Niyangoda, Gustavo Borjas, Jianjun Pan, Garrett Matthews, Martin Muschol, and Wolfgang Hoyer. **Protofibril-Fibril Interactions Inhibit Amyloid Fibril Assembly by Obstructing Secondary Nucleation**. *Angewandte Chemie International Edition*, n/a(n/a).

[130] Katiuscia Pagano, Simona Tomaselli, Henriette Molinari, and Laura Ragona. **Natural Compounds as Inhibitors of Aβ Peptide Aggregation: Chemical Requirements and Molecular Mechanisms**. *Frontiers in Neuroscience*, 14, 2020.

[131] Sofia Giorgetti, Claudio Greco, Paolo Tortora, and Francesco Antonio Aprile. **Targeting Amyloid Aggregation: An Overview of Strategies and Mechanisms**. *International Journal of Molecular Sciences*, 19(9):2677, September 2018.

[132] P. Hemachandra Reddy, Maria Manczak, Xiangling Yin, Mary Catherine Grady, Andrew Mitchell, Sahil Tonk, Chandra Sekhar Kuruva, Jasvinder Singh Bhatti, Ramesh Kandimalla, Murali Vijayan, Subodh Kumar, Rui Wang, Jangampalli Adi Pradeepkiran, Gilbert Ogunmokun, Kavya Thamarai, Kandi Quesada, Annette Boles, and Arubala P Reddy. **Protective Effects of Indian Spice Curcumin Against Amyloid Beta in Alzheimer's Disease**. *Journal of Alzheimer's disease : JAD*, 61(3):843–866, 2018.

[133] John M. Ringman, Sally A. Frautschy, Edmond Teng, Aynun N. Begum, Jenny Bardens, Maryam Beigi, Karen H. Gylys, Vladimir Badmaev, Dennis D. Heath, Liana G. Apostolova, Verna Porter, Zeba Vanek, Gad A. Marshall, Gerhard Hellemann, Catherine Sugar, Donna L. Masterman, Thomas J. Montine, Jeffrey L. Cummings, and Greg M. Cole. **Oral curcumin for Alzheimer's disease: tolerability and efficacy in a 24-week randomized, double blind, placebo-controlled study**. *Alzheimer's Research & Therapy*, 4(5):43, 2012.

[134] R. Scott Turner, Ronald G. Thomas, Suzanne Craft, Christopher H. van Dyck, Jacobo Mintzer, Brigid A. Reynolds, James B. Brewer, Robert A. Rissman, Rema Raman, and Paul S. Aisen. **A randomized, double-blind, placebo-controlled trial of resveratrol for Alzheimer disease**. *Neurology*, 85(16):1383–1391, October 2015.

[135] Friedemann Paul. **Sunphenon EGCg (Epigallocatechin-Gallate) in the Early Stage of Alzheimer´s Disease**. Clinical trial registration NCT00951834, clinicaltrials.gov, July 2021. URL https://clinicaltrials.gov/ct2/show/NCT00951834. Accessed on 2022-04-03.

[136] L. Lannfelt, N. R. Relkin, and E. R. Siemers. **Amyloid-ß-directed immunotherapy for Alzheimer's disease**. *Journal of Internal Medicine*, 275(3):284–295, 2014.

[137] M.B. Usman, S. Bhardwaj, S. Roychoudhury, D. Kumar, A. Alexiou, P. Kumar, R.K. Ambasta, P. Prasher, S. Shukla, V. Upadhye, F.A. Khan, R. Awasthi, M.D. Shastri, S.K. Singh, G. Gupta, D.K. Chellappan, K. Dua, S.K. Jha, J. Ruokolainen, K.K. Kesari, S. Ojha, and N.K. Jha. **Immunotherapy for Alzheimer's Disease: Current Scenario and Future Perspectives**. *The Journal Of Prevention of Alzheimer's Disease*, pages 1–18, 2021.

[138] **Randomized Safety, Tolerability and Pilot Efficacy of AN-1792 in Alzheimer's Disease**. URL https://clinicaltrials.gov/ct2/show/NCT00021723. Accessed on 2022-04-06.

[139] J.-M. Orgogozo, S. Gilman, J.-F. Dartigues, B. Laurent, M. Puel, L. C. Kirby, P. Jouanny, B. Dubois, L. Eisner, S. Flitman, B. F. Michel, M. Boada, A. Frank, and C. Hock. **Subacute meningoencephalitis in a subset of patients with AD after Abeta42 immunization**. *Neurology*, 61 (1):46–54, July 2003.

[140] S. Gilman, M. Koller, R. S. Black, L. Jenkins, S. G. Griffith, N. C. Fox, L. Eisner, L. Kirby, M. Boada Rovira, F. Forette, J.-M. Orgogozo, and AN1792(QS-21)-201 Study Team. **Clinical effects of Abeta immunization (AN1792) in patients with AD in an interrupted trial**. *Neurology*, 64(9):1553–1562, May 2005.

[141] Heii Arai, Hideo Suzuki, and Tamotsu Yoshiyama. **Vanutide cridificar and the QS-21 adjuvant in Japanese subjects with mild to moderate Alzheimer's disease: results from two phase 2 studies**. *Current Alzheimer Research*, 12(3):242–254, 2015.

[142] Florence Pasquier, Carl Sadowsky, Ann Holstein, Ghislaine Le Prince Leterme, Yahong Peng, Nicholas Jackson, Nick C. Fox, Nzeera Ketter, Enchi Liu, J. Michael Ryan, and ACC-001 (QS-21) Study Team. **Two Phase 2 Multiple Ascending-Dose Studies of Vanutide Cridificar (ACC-001) and QS-21 Adjuvant in Mild-to-Moderate Alzheimer's Disease**. *Journal of Alzheimer's disease: JAD*, 51(4):1131–1143, 2016.

[143] Michael Hull, Carl Sadowsky, Heii Arai, Ghislaine Le Prince Leterme, Ann Holstein, Kevin Booth, Yahong Peng, Tamotsu Yoshiyama, Hideo Suzuki, Nzeera Ketter, Enchi Liu, and J. Michael Ryan. **Long-Term Extensions of Randomized Vaccination Trials of ACC-001 and QS-21 in Mild to Moderate Alzheimer's Disease**. *Current Alzheimer Research*, 14(7):696–708, 2017.

[144] A. Schneeberger, M. Mandler, O. Otava, W. Zauner, F. Mattner, and W. Schmidt. **Development of AFFITOPE vaccines for Alzheimer's disease (AD) — From concept to clinical testing**. *JNHA - The Journal of Nutrition, Health and Aging*, 13(3):264–267, March 2009.

[145] Achim Schneeberger, Markus Mandler, Frank Mattner, and Walter Schmidt. **AFFITOME® technology in neurodegenerative diseases: The doubling advantage**. *Human Vaccines*, 6 (11):948–952, November 2010.

[146] Affiris AG. **Randomized, Controlled, Parallel Group, Patient-blinded, Single-center Phase I Pilot Study to Assess Tolerability and Safety of Repeated s.c. Administration of a Single-dose of Affitope AD01 Applied With or Without Adjuvant to Patients With Mild to Moderate Alzheimer's Disease**. Clinical trial registration NCT00495417, clinicaltrials.gov, October 2010. URL https://clinicaltrials.gov/ct2/show/NCT00495417. Accessed on 2022-04-04.

[147] Affiris AG. **Phase Ib Follow-up Study to Evaluate Long-term Safety and Tolerability of Immunization With AFFITOPE AD01 Applied During AFFiRiS 001**. Clinical trial registration NCT00711139, clinicaltrials.gov, May 2010. URL https://clinicaltrials.gov/ct2/show/NCT00711139. Accessed on 2022-04-04.

[148] A. Schneeberger, S. Hendrix, M. Mandler, N. Ellison, V. Bürger, M. Brunner, L. Frölich, N. Mimica, J. Hort, M. Rainer, D. Imarhiagbe, A. Kurz, O. Peters, H.-J. Gertz, L. Tierney, F. Mattner, W. Schmidt, and B. Dubois. **Results from a Phase II Study to Assess the Clinical and Immunological Activity of AFFITOPE® AD02 in Patients with Early Alzheimer's Disease**. *The Journal of Prevention of Alzheimer's Disease*, 2(2):103–114, 2015.

[149] M. Vukicevic, E. Fiorini, S. Siegert, R. Carpintero, M. Rincon-Restrepo, P. Lopez-Deber, N. Piot, M. Ayer, I. Rentero, C. Babolin, S. Bravo-Veyrat, V. Giriens, C. Morici, M. Beuzelin, A. Gesbert, S. Rivot, S. Depretti, P. Donati, J. Streffer, A. Pfeifer, and M. H. Kosco-Vilbois. **An amyloid beta vaccine that safely drives immunity to a key pathological species in Alzheimer's disease: pyroglutamate amyloid beta**. *Brain Communications*, 4(1):fcac022, February 2022.

[150] AC Immune SA. **A Phase Ib Multi-Center, Double-Blind, Randomized, Placebo-Controlled Dose Escalation Study of the Safety, Tolerability and Immunogenicity of ACI-24 in Adults With Down Syndrome**. Clinical trial registration NCT02738450, clinicaltrials.gov, September 2021. URL https://clinicaltrials.gov/ct2/show/NCT02738450. Accessed on 2022-04-04.

[151] AC Immune SA. **A Phase 2 Double-blind, Randomized, Placebo-controlled Study to Assess the Safety, Tolerability and Target Engagement of ACI-24 in Adults With Down Syndrome**. Clinical trial registration NCT04373616, clinicaltrials.gov, October 2021. URL https://clinicaltrials.gov/ct2/show/NCT04373616. Accessed on 2022-04-04.

[152] Rik Vandenberghe, Marie-Emmanuelle Riviere, Angelika Caputo, Judit Sovago, R. Paul Maguire, Martin Farlow, Giovanni Marotta, Raquel Sanchez-Valle, Philip Scheltens, J. Michael Ryan, and Ana Graf. **Active Aβ immunotherapy CAD106 in Alzheimer's disease: A phase 2b study**. *Alzheimer's & Dementia : Translational Research & Clinical Interventions*, 3(1):10–22, December 2016.

[153] Cristina Lopez Lopez, Pierre N. Tariot, Angelika Caputo, Jessica B. Langbaum, Fonda Liu, Marie-Emmanuelle Riviere, Carolyn Langlois, Marie-Laure Rouzade-Dominguez, Martin Zalesak, Suzanne Hendrix, Ronald G. Thomas, Vissia Viglietta, Rob Lenz, J. Michael Ryan, Ana Graf, and Eric M. Reiman. **The Alzheimer's Prevention Initiative Generation Program: Study design of two randomized controlled trials for individuals at risk for clinical onset of Alzheimer's disease**. *Alzheimer's & Dementia (New York, N. Y.)*, 5:216–227, 2019.

[154] Hayk Davtyan, Anahit Ghochikyan, Irina Petrushina, Armine Hovakimyan, Arpine Davtyan, Anna Poghosyan, Annette M. Marleau, Nina Movsesyan, Anatoly Kiyatkin, Suhail Rasool, Anna Kirstine Larsen, Peter Juul Madsen, Karen Malene Wegener, Dorte Kornerup Ditlevsen, David H. Cribbs, Lars Ostergaard Pedersen, and Michael G. Agadjanyan. **Immunogenicity, Efficacy, Safety, and Mechanism of Action of Epitope Vaccine (Lu AF20513) for Alzheimer's Disease: Prelude to a Clinical Trial**. *The Journal of Neuroscience*, 33(11):4923–4934, March 2013.

[155] H. Lundbeck A/S. **Interventional, Open-label, Multiple-immunisation Study of the Immunogenicity, Pharmacodynamics and Safety of Lu AF20513 in Patients With Mild Alzheimer's Disease or Mild Cognitive Impairment Due to Alzheimer's Disease**. Clinical trial registration NCT03819699, clinicaltrials.gov, February 2020. URL https://clinicaltrials.gov/ct2/show/NCT03819699. Accessed on 2022-04-04.

[156] Chang Yi Wang, Pei-Ning Wang, Ming-Jang Chiu, Connie L. Finstad, Feng Lin, Shugene Lynn, Yuan-Hung Tai, Xin De Fang, Kesheng Zhao, Chung-Ho Hung, Yiting Tseng, Wen-Jiun Peng, Jason Wang, Chih-Chieh Yu, Be-Sheng Kuo, and Paul A. Frohna. **UB-311, a novel UBITh® amyloid β peptide vaccine for mild Alzheimer's disease**. *Alzheimer's & Dementia (New York, N. Y.)*, 3(2):262–272, June 2017.

[157] United Neuroscience Ltd. **A Randomized, Double-blind, Placebo-controlled, 3-arm Parallel-group, Multicenter, Phase IIa Study to Evaluate the Safety, Tolerability, Immunogenicity, and Efficacy of UBITh® AD Immunotherapeutic Vaccine (UB-311) in Patients With Mild Alzheimer's Disease**. Clinical trial registration NCT02551809, clinicaltrials.gov, March 2020. URL https://clinicaltrials.gov/ct2/show/NCT02551809. Accessed on 2022-04-04.

[158] Merck Sharp & Dohme Corp. **A Double-Blind, Randomized, Placebo-Controlled, Dose Escalating Study to Evaluate the Safety, Tolerability, and Immunogenicity of V950 Formulated on Aluminum-Containing Adjuvant With or Without ISCOMATRIX™ in Patients With Alzheimer Disease**. Clinical trial registration NCT00464334, clinicaltrials.gov, September 2015. URL https://clinicaltrials.gov/ct2/show/NCT00464334. Accessed on 2022-04-04.

[159] Yan Zhang and Daniel H. S. Lee. **Sink hypothesis and therapeutic strategies for attenuating Abeta levels**. *The Neuroscientist: A Review Journal Bringing Neurobiology, Neurology and Psychiatry*, 17(2):163–173, April 2011.

[160] Biljana Georgievska, Susanne Gustavsson, Johan Lundkvist, Jan Neelissen, Susanna Eketjäll, Veronica Ramberg, Tjerk Bueters, Karin Agerman, Anders Juréus, Samuel Svensson, Stefan Berg, Johanna Fälting, and Urban Lendahl. **Revisiting the peripheral sink hypothesis: Inhibiting BACE1 activity in the periphery does not alter $\upbeta$-amyloid levels in the CNS**. *Journal of Neurochemistry*, 132(4):477–486, 2015.

[161] Julie A. Stone, Eric Parker, Huub Jan Kleijn, Mark Forman, Michael Egan, Malcolm Rowland, and William Potter. **Is the Peripheral Sink Hypothesis Physiologically Feasible? Evidence from Model-Based Assessment of the Amyloid Pathway**. *Alzheimer's & Dementia*, 12 (7S_Part_9):P443–P443, 2016.

[162] Manuel Menendez-Gonzalez, Huber S. Padilla-Zambrano, Gabriel Alvarez, Estibaliz Capetillo-Zarate, Cristina Tomas-Zapico, and Agustin Costa. **Targeting Beta-Amyloid at the CSF: A New Therapeutic Strategy in Alzheimer's Disease**. *Frontiers in Aging Neuroscience*, 10, 2018.

[163] Victor M. Pulgar. **Transcytosis to Cross the Blood Brain Barrier, New Advancements and Challenges**. *Frontiers in Neuroscience*, 12, 2019.

[164] Donna M. Wilcock, Sanjay K. Munireddy, Arnon Rosenthal, Kenneth E. Ugen, Marcia N. Gordon, and Dave Morgan. **Microglial activation facilitates Abeta plaque removal following intracranial anti-Abeta antibody administration**. *Neurobiology of Disease*, 15(1):11–20, February 2004.

[165] Dave Morgan. **The role of microglia in antibody-mediated clearance of amyloid-beta from the brain**. *CNS & neurological disorders drug targets*, 8(1):7–15, March 2009.

[166] Maike Gold, David Mengel, Stephan Röskam, Richard Dodel, and Jan-Philipp Bach. **Mechanisms of action of naturally occurring antibodies against β-amyloid on microglia**. *Journal of Neuroinflammation*, 10(1):795, January 2013.

[167] Kristi Henjum, Vibeke Årskog, Charlotte B. Jendresen, Tormod Fladby, Reidun Torp, and Lars N. G. Nilsson. **Analyzing microglial-associated Aβ in Alzheimer's disease transgenic mice with a novel mid-domain Aβ-antibody**. *Scientific Reports*, 10(1):10590, June 2020.

[168] Vanessa Laversenne, Sameer Nazeeruddin, Emma C. Källstig, Philippe Colin, Christel Voize, and Bernard L. Schneider. **Anti-Aβ antibodies bound to neuritic plaques enhance microglia activity and mitigate tau pathology**. *Acta Neuropathologica Communications*, 8(1):198, November 2020.

[169] Ronald S. Black, Reisa A. Sperling, Beth Safirstein, Ruth N. Motter, Allan Pallay, Alice Nichols, and Michael Grundman. **A single ascending dose study of bapineuzumab in patients with Alzheimer disease**. *Alzheimer Disease and Associated Disorders*, 24(2):198–203, June 2010.

[170] Reisa Sperling, Stephen Salloway, David J. Brooks, Donatella Tampieri, Jerome Barakos, Nick C. Fox, Murray Raskind, Marwan Sabbagh, Lawrence S. Honig, Anton P. Porsteinsson, Ivan Lieberburg, H. Michael Arrighi, Kristen A. Morris, Yuan Lu, Enchi Liu, Keith M. Gregg, Robert H. Brashear, Gene G. Kinney, Ronald Black, and Michael Grundman. **Amyloid-related imaging abnormalities (ARIA) in Alzheimer's disease patients treated with bapineuzumab: A retrospective analysis**. *Lancet neurology*, 11(3):241–249, March 2012.

[171] Stephen Salloway, Reisa Sperling, Nick C. Fox, Kaj Blennow, William Klunk, Murray Raskind, Marwan Sabbagh, Lawrence S. Honig, Anton P. Porsteinsson, Steven Ferris, Marcel Reichert, Nzeera Ketter, Bijan Nejadnik, Volkmar Guenzler, Maja Miloslavsky, Daniel Wang, Yuan Lu, Julia Lull, Iulia Cristina Tudor, Enchi Liu, Michael Grundman, Eric Yuen, Ronald Black, and H. Robert Brashear. **Two Phase 3 Trials of Bapineuzumab in Mild-to-Moderate Alzheimer's Disease**. *New England Journal of Medicine*, 370(4):322–333, January 2014.

[172] Abdelrahman Ibrahim Abushouk, Ahmed Elmaraezy, Amro Aglan, Reham Salama, Samar Fouda, Rana Fouda, and Ammar M. AlSafadi. **Bapineuzumab for mild to moderate Alzheimer's disease: a meta-analysis of randomized controlled trials**. *BMC Neurology*, 17(1):66, April 2017.

[173] Pfizer. **A Phase 2 Multicenter, Randomized, Double Blind, Placebo-Controlled Study Of The Safety, Tolerability, And Pharmacokinetics Of Multiple Doses Of PF-04360365 In Patients With Mild To Moderate Alzheimer's Disease**. Clinical trial registration NCT00722046, clinicaltrials.gov, April 2016. URL https://clinicaltrials.gov/ct2/show/NCT00722046. Accessed on 2022-04-14.

[174] Jaren W. Landen, Niels Andreasen, Carol L. Cronenberger, Pamela F. Schwartz, Anne Börjesson-Hanson, Henrik Östlund, Catherine A. Sattler, Brendon Binneman, and Martin M. Bednar. **Ponezumab in mild-to-moderate Alzheimer's disease: Randomized phase II PET-PIB study**. *Alzheimer's & Dementia : Translational Research & Clinical Interventions*, 3(3):393–401, June 2017.

[175] Claire Leurent, James A. Goodman, Yao Zhang, Ping He, Jonathan R. Polimeni, Mahmut Edip Gurol, Monica Lindsay, Linda Frattura, Usharbudh Shivraj Sohur, Anand Viswanathan, Martin M. Bednar, Eric E. Smith, Ponezumab Trial Study Group, and Steven M. Greenberg. **Immunotherapy with ponezumab for probable cerebral amyloid angiopathy**. *Annals of Clinical and Translational Neurology*, 6(4):795–806, April 2019.

[176] Rachelle S. Doody, Ronald G. Thomas, Martin Farlow, Takeshi Iwatsubo, Bruno Vellas, Steven Joffe, Karl Kieburtz, Rema Raman, Xiaoying Sun, Paul S. Aisen, Eric Siemers, Hong Liu-Seifert, and Richard Mohs. **Phase 3 Trials of Solanezumab for Mild-to-Moderate Alzheimer's Disease**. *New England Journal of Medicine*, 370(4):311–321, January 2014.

[177] Eric R. Siemers, Karen L. Sundell, Christopher Carlson, Michael Case, Gopalan Sethuraman, Hong Liu-Seifert, Sherie A. Dowsett, Michael J. Pontecorvo, Robert A. Dean, and Ronald Demattos. **Phase 3 solanezumab trials: Secondary outcomes in mild Alzheimer's disease patients**. *Alzheimer's & Dementia: The Journal of the Alzheimer's Association*, 12(2):110–120, February 2016.

[178] Lawrence S. Honig, Bruno Vellas, Michael Woodward, Mercè Boada, Roger Bullock, Michael Borrie, Klaus Hager, Niels Andreasen, Elio Scarpini, Hong Liu-Seifert, Michael Case, Robert A. Dean, Ann Hake, Karen Sundell, Vicki Poole Hoffmann, Christopher Carlson, Rashna Khanna, Mark Mintun, Ronald DeMattos, Katherine J. Selzler, and Eric Siemers. **Trial of Solanezumab for Mild Dementia Due to Alzheimer's Disease**. *The New England Journal of Medicine*, 378(4):321–330, January 2018.

[179] Jeffrey L. Cummings, Sharon Cohen, Christopher H. van Dyck, Mark Brody, Craig Curtis, William Cho, Michael Ward, Michel Friesenhahn, Christina Rabe, Flavia Brunstein, Angelica Quartino, Lee A. Honigberg, Reina N. Fuji, David Clayton, Deborah Mortensen, Carole Ho, and Robert Paul. **ABBY: A phase 2 randomized trial of crenezumab in mild to moderate Alzheimer disease**. *Neurology*, 90(21):e1889–e1897, May 2018.

[180] Ting Yang, Yifan Dang, Beth Ostaszewski, David Mengel, Verena Steffen, Christina Rabe, Tobias Bittner, Dominic M. Walsh, and Dennis J. Selkoe. **Target engagement in an alzheimer trial: Crenezumab lowers amyloid β oligomers in cerebrospinal fluid**. *Annals of Neurology*, 86 (2):215–224, August 2019.

[181] Kenta Yoshida, Anita Moein, Tobias Bittner, Susanne Ostrowitzki, Helen Lin, Lee Honigberg, Jin Y. Jin, and Angelica Quartino. **Pharmacokinetics and pharmacodynamic effect of crenezumab on plasma and cerebrospinal fluid beta-amyloid in patients with mild-to-moderate Alzheimer's disease**. *Alzheimer's Research & Therapy*, 12(1):16, January 2020.

[182] Heather Guthrie, Lawrence S. Honig, Helen Lin, Kaycee M. Sink, Kathleen Blondeau, Angelica Quartino, Michael Dolton, Montserrat Carrasco-Triguero, Qinshu Lian, Tobias Bittner, David Clayton, Jillian Smith, and Susanne Ostrowitzki. **Safety, Tolerability, and Pharmacokinetics of Crenezumab in Patients with Mild-to-Moderate Alzheimer's Disease Treated with Escalating Doses for up to 133 Weeks**. *Journal of Alzheimer's Disease*, 76(3):967–979.

[183] Eli Lilly and Company. **Assessment of Safety, Tolerability, and Efficacy of Donanemab in Early Symptomatic Alzheimer's Disease**. Clinical trial registration NCT04437511, clinicaltrials.gov, April 2022. URL https://clinicaltrials.gov/ct2/show/NCT04437511. Accessed on 2022-04-14.

[184] Stephen Loucian Lowe, Brian A. Willis, Anne Hawdon, Fanni Natanegara, Laiyi Chua, Joanne Foster, Sergey Shcherbinin, Paul Ardayfio, and John R. Sims. **Donanemab (LY3002813) dose-escalation study in Alzheimer's disease**. *Alzheimer's & Dementia: Translational Research & Clinical Interventions*, 7(1):e12112, 2021.

[185] Susanne Ostrowitzki, Robert A. Lasser, Ernest Dorflinger, Philip Scheltens, Frederik Barkhof, Tania Nikolcheva, Elizabeth Ashford, Sylvie Retout, Carsten Hofmann, Paul Delmar, Gregory Klein, Mirjana Andjelkovic, Bruno Dubois, Mercè Boada, Kaj Blennow, Luca Santarelli, Paulo Fontoura, and SCarlet RoAD Investigators. **A phase III randomized trial of gantenerumab in prodromal Alzheimer's disease**. *Alzheimer's Research & Therapy*, 9(1):95, December 2017.

[186] Gregory Klein, Paul Delmar, Nicola Voyle, Sunita Rehal, Carsten Hofmann, Danielle Abi-Saab, Mirjana Andjelkovic, Smiljana Ristic, Guoqiao Wang, Randall Bateman, Geoffrey A. Kerchner, Monika Baudler, Paulo Fontoura, and Rachelle Doody. **Gantenerumab reduces amyloid-β plaques in patients with prodromal to moderate Alzheimer's disease: a PET substudy interim analysis**. *Alzheimer's Research & Therapy*, 11(1):101, December 2019.

[187] Stephen Salloway, Martin Farlow, Eric McDade, David B. Clifford, Guoqiao Wang, Jorge J. Llibre-Guerra, Janice M. Hitchcock, Susan L. Mills, Anna M. Santacruz, Andrew J. Aschenbrenner, Jason Hassenstab, Tammie L. S. Benzinger, Brian A. Gordon, Anne M. Fagan, Kelley A. Coalier, Carlos Cruchaga, Alison A. Goate, Richard J. Perrin, Chengjie Xiong, Yan Li, John C. Morris, B. Joy Snider, Catherine Mummery, G. Mustafa Surti, Didier Hannequin, David Wallon, Sarah B. Berman, James J. Lah, Ivonne Z. Jimenez-Velazquez, Erik D. Roberson, Christopher H. van Dyck, Lawrence S. Honig, Raquel Sánchez-Valle, William S. Brooks, Serge Gauthier, Douglas R. Galasko, Colin L. Masters, Jared R. Brosch, Ging-Yuek Robin Hsiung, Suman Jayadev, Maité Formaglio, Mario Masellis, Roger Clarnette, Jérémie Pariente, Bruno Dubois, Florence Pasquier, Clifford R. Jack, Robert Koeppe, Peter J. Snyder, Paul S. Aisen, Ronald G. Thomas, Scott M. Berry, Barbara A. Wendelberger, Scott W. Andersen, Karen C. Holdridge, Mark A. Mintun, Roy Yaari, John R. Sims, Monika Baudler, Paul Delmar, Rachelle S. Doody, Paulo Fontoura, Caroline Giacobino, Geoffrey A. Kerchner, and Randall J. Bateman. **A trial of gantenerumab or solanezumab in dominantly inherited Alzheimer's disease**. *Nature Medicine*, 27(7):1187–1196, July 2021.

[188] Jeff Sevigny, Ping Chiao, Thierry Bussière, Paul H. Weinreb, Leslie Williams, Marcel Maier, Robert Dunstan, Stephen Salloway, Tianle Chen, Yan Ling, John O'Gorman, Fang Qian, Mahin Arastu, Mingwei Li, Sowmya Chollate, Melanie S. Brennan, Omar Quintero-Monzon, Robert H. Scannevin, H. Moore Arnold, Thomas Engber, Kenneth Rhodes, James Ferrero, Yaming Hang, Alvydas Mikulskis, Jan Grimm, Christoph Hock, Roger M. Nitsch, and Alfred Sandrock. **The antibody aducanumab reduces Aβ plaques in Alzheimer's disease**. *Nature*, 537(7618): 50–56, September 2016.

[189] Rajesh R Tampi, Brent P Forester, and Marc Agronin. **Aducanumab: evidence from clinical trial data and controversies**. *Drugs in Context*, 10:2021–7–3, October 2021.

[190] David S. Knopman, David T. Jones, and Michael D. Greicius. **Failure to demonstrate efficacy of aducanumab: An analysis of the EMERGE and ENGAGE trials as reported by Biogen, December 2019**. *Alzheimer's & Dementia*, 17(4):696–701, 2021.

[191] Jeffrey Cummings, Paul Aisen, Cynthia Lemere, Alireza Atri, Marwan Sabbagh, and Stephen Salloway. **Aducanumab produced a clinically meaningful benefit in association with amyloid lowering**. *Alzheimer's Research & Therapy*, 13(1):98, May 2021.

[192] Chad J. Swanson, Yong Zhang, Shobha Dhadda, Jinping Wang, June Kaplow, Robert Y. K. Lai, Lars Lannfelt, Heather Bradley, Martin Rabe, Akihiko Koyama, Larisa Reyderman, Donald A. Berry, Scott Berry, Robert Gordon, Lynn D. Kramer, and Jeffrey L. Cummings. **A randomized, double-blind, phase 2b proof-of-concept clinical trial in early Alzheimer's disease with lecanemab, an anti-Aβ protofibril antibody**. *Alzheimer's Research & Therapy*, 13(1): 80, April 2021.

[193] Eisai Inc. **A Placebo-Controlled, Double-Blind, Parallel-Group, 18-Month Study With an Open-Label Extension Phase to Confirm Safety and Efficacy of BAN2401 in Subjects With Early Alzheimer's Disease**. Clinical trial registration NCT03887455, clinicaltrials.gov, October 2021. URL https://clinicaltrials.gov/ct2/show/NCT03887455. Accessed on 2022-04-14.

[194] Christopher H. van Dyck, Chad J. Swanson, Paul Aisen, Randall J. Bateman, Christopher Chen, Michelle Gee, Michio Kanekiyo, David Li, Larisa Reyderman, Sharon Cohen, Lutz Froelich, Sadao Katayama, Marwan Sabbagh, Bruno Vellas, David Watson, Shobha Dhadda, Michael Irizarry, Lynn D. Kramer, and Takeshi Iwatsubo. **Lecanemab in Early Alzheimer's Disease**. *New England Journal of Medicine*, 0(0):null, November 2022.

[195] Yu-Hui Liu, Brian Giunta, Hua-Dong Zhou, Jun Tan, and Yan-Jiang Wang. **Immunotherapy for Alzheimer disease: the challenge of adverse effects**. *Nature Reviews. Neurology*, 8(8): 465–469, August 2012.

[196] Christopher H. van Dyck. **Anti-Amyloid-β Monoclonal Antibodies for Alzheimer's Disease: Pitfalls and Promise**. *Biological Psychiatry*, 83(4):311–319, February 2018.

[197] Margaret M. Racke, Laura I. Boone, Deena L. Hepburn, Maia Parsadainian, Matthew T. Bryan, Daniel K. Ness, Kathy S. Piroozi, William H. Jordan, Donna D. Brown, Wherly P. Hoffman, David M. Holtzman, Kelly R. Bales, Bruce D. Gitter, Patrick C. May, Steven M. Paul, and Ronald B. DeMattos. **Exacerbation of cerebral amyloid angiopathy-associated microhemorrhage in amyloid precursor protein transgenic mice by immunotherapy is dependent on antibody recognition of deposited forms of amyloid beta**. *The Journal of Neuroscience: The Official Journal of the Society for Neuroscience*, 25(3):629–636, January 2005.

[198] Yannick Chantran, Jean Capron, Sonia Alamowitch, and Pierre Aucouturier. **Anti-Aβ Antibodies and Cerebral Amyloid Angiopathy Complications**. *Frontiers in Immunology*, 10, 2019.

[199] Roy O. Weller and James A. Nicoll. **Cerebral amyloid angiopathy: pathogenesis and effects on the ageing and Alzheimer brain**. *Neurological Research*, 25(6):611–616, September 2003.

[200] Steven M. Greenberg, Brian J. Bacskai, Mar Hernandez-Guillamon, Jeremy Pruzin, Reisa Sperling, and Susanne J. van Veluw. **Cerebral amyloid angiopathy and Alzheimer disease — one peptide, two pathways**. *Nature Reviews Neurology*, 16(1):30–42, January 2020.

[201] Yu-Hui Liu, Xian-Le Bu, Chun-Rong Liang, Ye-Ran Wang, Tao Zhang, Shu-Sheng Jiao, Fan Zeng, Xiu-Qing Yao, Hua-Dong Zhou, Juan Deng, and Yan-Jiang Wang. **An N-terminal antibody promotes the transformation of amyloid fibrils into oligomers and enhances the neurotoxicity of amyloid-beta: the dust-raising effect**. *Journal of Neuroinflammation*, 12(1): 153, August 2015.

[202] Irene H. Cheng, Kimberly Scearce-Levie, Justin Legleiter, Jorge J. Palop, Hilary Gerstein, Nga Bien-Ly, Jukka Puolivaöli, Sylvain Lesné, Karen H. Ashe, Paul J. Muchowski, and Lennart Mucke. **Accelerating Amyloid-β Fibrillization Reduces Oligomer Levels and Functional Deficits in Alzheimer Disease Mouse Models***. *Journal of Biological Chemistry*, 282(33): 23818–23828, August 2007.

[203] Irina Petrushina, Anahit Ghochikyan, Mikayel Mktrichyan, Gregory Mamikonyan, Nina Movsesyan, Hayk Davtyan, Archita Patel, Elizabeth Head, David H. Cribbs, and Michael G. Agadjanyan. **Alzheimer's disease peptide epitope vaccine reduces insoluble but not soluble/oligomeric Abeta species in amyloid precursor protein transgenic mice**. *The Journal of Neuroscience: The Official Journal of the Society for Neuroscience*, 27(46):12721–12731, November 2007.

[204] Alexandra J. Mably, Wen Liu, Jessica M. Mc Donald, Jean-Cosme Dodart, Frédérique Bard, Cynthia A. Lemere, Brian O'Nuallain, and Dominic M. Walsh. **Anti-Aβ antibodies incapable of reducing cerebral Aβ oligomers fail to attenuate spatial reference memory deficits in J20 mice**. *Neurobiology of Disease*, 82:372–384, October 2015.

[205] N. C. Fox, R. S. Black, S. Gilman, M. N. Rossor, S. G. Griffith, L. Jenkins, M. Koller, and AN1792(QS-21)-201 Study. **Effects of Abeta immunization (AN1792) on MRI measures of cerebral volume in Alzheimer disease**. *Neurology*, 64(9):1563–1572, May 2005.

[206] Juan Deng, Huayan Hou, Brian Giunta, Takashi Mori, Yan-Jiang Wang, Frank Fernandez, Sascha Weggen, Wataru Araki, Demian Obregon, and Jun Tan. **Autoreactive-Aβ antibodies promote APP β-secretase processing**. *Journal of Neurochemistry*, 120(5):732–740, March 2012.

[207] S. Li, J. Deng, H. Hou, J. Tian, B. Giunta, Y. Wang, D. Sawmiller, A. Smith, P. R. Sanberg, D. Obregon, T. Mori, and J. Tan. **Specific antibody binding to the APP672–699 region shifts APP processing from α- to β-cleavage**. *Cell Death & Disease*, 5(8):e1374–e1374, August 2014.

[208] Joseph W. Arndt, Fang Qian, Benjamin A. Smith, Chao Quan, Krishna Praneeth Kilambi, Martin W. Bush, Thomas Walz, R. Blake Pepinsky, Thierry Bussière, Stefan Hamann, Thomas O. Cameron, and Paul H. Weinreb. **Structural and kinetic basis for the selectivity of aducanumab for aggregated forms of amyloid-β**. *Scientific Reports*, 8(1):6412, April 2018.

[209] Jun Zhao, Ruth Nussinov, and Buyong Ma. **Antigen binding allosterically promotes Fc receptor recognition**. *mAbs*, 11(1):58–74, October 2018.

[210] Nicolas S. Merle, Sarah Elizabeth Church, Veronique Fremeaux-Bacchi, and Lubka T. Roumenina. **Complement System Part I – Molecular Mechanisms of Activation and Regulation**. *Frontiers in Immunology*, 6, 2015.

[211] Benjamin S Goldberg and Margaret E Ackerman. **Antibody-mediated complement activation in pathology and protection**. *Immunology & Cell Biology*, 98(4):305–317, 2020.

[212] McKenzie Prillaman. **Heralded Alzheimer's drug works — but safety concerns loom**. *Nature*, November 2022.

[213] McKenzie Prillaman. **Alzheimer's drug slows mental decline in trial — but is it a breakthrough?** *Nature*, 610(7930):15–16, September 2022.

[214] Stephen Salloway, Spyros Chalkias, Frederik Barkhof, Patrick Burkett, Jerome Barakos, Derk Purcell, Joyce Suhy, Fiona Forrestal, Ying Tian, Kimberly Umans, Guanfang Wang, Priya Singhal, Samantha Budd Haeberlein, and Karen Smirnakis. **Amyloid-Related Imaging Abnormalities in 2 Phase 3 Studies Evaluating Aducanumab in Patients With Early Alzheimer Disease**. *JAMA Neurology*, 79(1):13–21, January 2022.

[215] Pam Belluck and Rebecca Robbins. **Three F.D.A. Advisers Resign Over Agency's Approval of Alzheimer's Drug**. *The New York Times*, June 2021.

[216] **Flurry of Investigations Besets Aducanumab | ALZFORUM**. URL https://www.alzforum.org/news/conference-coverage/flurry-investigations-besets-aducanumab. Accessed on 2022-04-04.

[217] Dominika Pietrzak, **Aduhelm: an overiview of what's happened so far**. July 2021. URL https://remapconsulting.com/aduhelm-the-story-so-far/. Accessed on 2022-04-04.

[218] Pam Belluck, Sheila Kaplan, and Rebecca Robbins. **How an Unproven Alzheimer's Drug Got Approved**. *The New York Times*, July 2021.

[219] EMA, **Meeting highlights from the Committee for Medicinal Products Human Use (CHMP) 13-16 December 2021**. December 2021. URL https://www.ema.europa.eu/en/news/meeting-highlights-committee-medicinal-products-human-use-chmp-13-16-december-2021. Accessed on 2022-04-04.

[220] **Pfizer drops out of dementia drug race | Alzheimer's Society**. URL https://www.alzheimers.org.uk/research/care-and-cure-research-magazine/pfizer-dementia-drug. Accessed on 2022-04-17.

[221] Sudhir Paul, Deanna J. Volle, Carol M. Beach, Donald R. Johnson, Michael J. Powell, and Richard J. Massey. **Catalytic Hydrolysis of Vasoactive Intestinal Peptide by Human Autoantibody**. *Science*, 244(4909):1158–1162, 1989.

[222] Hiroaki Taguchi, Stephanie Planque, Yasuhiro Nishiyama, Paul Szabo, Marc E. Weksler, Robert P. Friedland, and Sudhir Paul. **Catalytic antibodies to amyloid-$\upbeta$ peptide in defense against Alzheimer disease**. *Autoimmunity Reviews*, 7(5):391–397, May 2008.

[223] Sudhir Paul, Stephanie Planque, and Yasuhiro Nishiyama. **Beneficial Catalytic Immunity to Aβ Peptide**. *Rejuvenation Research*, 13(2-3):179–187, April 2010.

[224] L. Li, S. Paul, S. Tyutyulkova, M. D. Kazatchkine, and S. Kaveri. **Catalytic activity of anti-thyroglobulin antibodies**. *Journal of Immunology (Baltimore, Md.: 1950)*, 154(7):3328–3332, April 1995.

[225] S. Lacroix-Desmazes, A. Moreau, null Sooryanarayana, C. Bonnemain, N. Stieltjes, A. Pashov, Y. Sultan, J. Hoebeke, M. D. Kazatchkine, and S. V. Kaveri. **Catalytic activity of antibodies against factor VIII in patients with hemophilia A**. *Nature Medicine*, 5(9):1044–1047, September 1999.

[226] P. Thiagarajan, R. Dannenbring, K. Matsuura, A. Tramontano, G. Gololobov, and S. Paul. **Monoclonal antibody light chain with prothrombinase activity**. *Biochemistry*, 39(21):6459–6465, May 2000.

[227] K. Matsuura and H. Sinohara. **Catalytic cleavage of vasopressin by human Bence Jones proteins at the arginylglycinamide bond**. *Biological Chemistry*, 377(9):587–589, September 1996.

[228] Stephanie A. Planque, Yasuhiro Nishiyama, Mariko Hara, Sari Sonoda, Sarah K. Murphy, Kenji Watanabe, Yukie Mitsuda, Eric L. Brown, Richard J. Massey, Stanley R. Primmer, Brian O'Nuallain, and Sudhir Paul. **Physiological IgM class catalytic antibodies selective for transthyretin amyloid**. *The Journal of Biological Chemistry*, 289(19):13243–13258, May 2014.

[229] Hiroaki Taguchi, Stephanie Planque, Yasuhiro Nishiyama, Jindrich Symersky, Stephane Boivin, Paul Szabo, Robert P. Friedland, Paul A. Ramsland, Allen B. Edmundson, Marc E. Weksler, and Sudhir Paul. **Autoantibody-catalyzed hydrolysis of amyloid beta peptide**. *The Journal of Biological Chemistry*, 283(8):4714–4722, February 2008.

[230] Hiroaki Taguchi, Stephanie Planque, Gopal Sapparapu, Stephane Boivin, Mariko Hara, Yasuhiro Nishiyama, and Sudhir Paul. **Exceptional Amyloid β Peptide Hydrolyzing Activity of Nonphysiological Immunoglobulin Variable Domain Scaffolds**. *The Journal of Biological Chemistry*, 283(52):36724–36733, December 2008.

[231] D C Parker. **T Cell-Dependent B Cell Activation**. *Annual Review of Immunology*, 11(1): 331–360, 1993.

[232] N Baumgarth. **A two-phase model of B-cell activation**. *Immunological reviews*, 176:171–180, August 2000.

[233] Stephanie Planque, Yogesh Bangale, Xiao-Tong Song, Sangeeta Karle, Hiroaki Taguchi, Brian Poindexter, Roger Bick, Allen Edmundson, Yasuhiro Nishiyama, and Sudhir Paul. **Ontogeny of proteolytic immunity: IgM serine proteases**. *The Journal of Biological Chemistry*, 279(14): 14024–14032, April 2004.

[234] Yogesh Bangale, Sangeeta Karle, Stephanie Planque, Yong-Xin Zhou, Hiroaki Taguchi, Yasuhiro Nishiyama, Lan Li, Ravishankar Kalaga, and Sudhir Paul. **VIPase autoantibodies in Fas-defective mice and patients with autoimmune disease**. *The FASEB Journal*, 17(6):628–635, 2003.

[235] A. Tramontano, G. Gololobov, and S. Paul. **Proteolytic Antibodies: Origins, Selection and Induction**. *Catalytic Antibodies*, 77:1–17, 2000.

[236] Thomas Fehr, Hussein Y. Naim, Martin F. Bachmann, Adrian F. Ochsenbein, Pius Spielhofer, Etienne Bucher, Hans Hengartner, Martin A. Billeter, and Rolf M. Zinkernagel. **T-cell independent IgM and enduring protective IgG antibodies induced by chimeric measles viruses**. *Nature Medicine*, 4(8):945–948, August 1998.

[237] **B-cell activation by T-cell-independent type 2 antigens as an integral part of the humoral immune response to pathogenic microorganisms**. *Immunological Reviews*, 176 (1):154–170, 2000.

[238] Sudhir Paul, Sangeeta Karle, Stephanie Planque, Hiroaki Taguchi, Maria Salas, Yasuhiro Nishiyama, Beverly Handy, Robert Hunter, Allen Edmundson, and Carl Hanson. **Naturally Occurring Proteolytic Antibodies: SELECTIVE IMMUNOGLOBULIN M-CATALYZED HYDROLYSIS OF HIV gp120***. *Journal of Biological Chemistry*, 279(38):39611–39619, September 2004.

[239] Sudhir Paul, Stephanie Planque, and Yasuhiro Nishiyama. **Immunological Origin and Functional Properties of Catalytic Autoantibodies to Amyloid β Peptide**. *Journal of Clinical Immunology*, 30(1):43–49, May 2010.

[240] Andrea Cerutti. **The regulation of IgA class switching**. *Nature Reviews Immunology*, 8(6): 421–434, June 2008.

[241] Yukie Mitsuda, Stephanie Planque, Mariko Hara, Robert Kyle, Hiroaki Taguchi, Yasuhiro Nishiyama, and Sudhir Paul. **Naturally occurring catalytic antibodies: evidence for preferred development of the catalytic function in IgA class antibodies**. *Molecular Biotechnology*, 36(2):113–122, June 2007.

[242] Stephanie Planque, Yukie Mitsuda, Hiroaki Taguchi, Maria Salas, Mary-Kate Morris, Yasuhiro Nishiyama, Robert Kyle, Pablo Okhuysen, Miguel Escobar, Robert Hunter, Haynes W. Sheppard, Carl Hanson, and Sudhir Paul. **Characterization of gp120 hydrolysis by IgA antibodies from humans without HIV infection**. *AIDS research and human retroviruses*, 23(12):1541–1554, December 2007.

[243] Sudhir Paul, Yasuhiro Nishiyama, Stephanie Planque, and Hiroaki Taguchi. **Theory of proteolytic antibody occurrence**. *Immunology Letters*, 103(1):8–16, February 2006.

[244] G. Gololobov, M. Sun, and S. Paul. **Innate antibody catalysis**. *Molecular Immunology*, 36(18): 1215–1222, December 1999.

[245] Stephanie Planque, Hiroaki Taguchi, Gary Burr, Gita Bhatia, Sangeeta Karle, Yong-Xin Zhou, Yasuhiro Nishiyama, and Sudhir Paul. **Broadly distributed chemical reactivity of natural antibodies expressed in coordination with specific antigen binding activity**. *The Journal of Biological Chemistry*, 278(22):20436–20443, May 2003.

[246] Sébastien Lacroix-Desmazes, Jagadeesh Bayry, Srini V. Kaveri, David Hayon-Sonsino, Nithyananda Thorenoor, Julien Charpentier, Charles-Edouard Luyt, Jean-Paul Mira, Valakunja Nagaraja, Michel D. Kazatchkine, Jean-François Dhainaut, and Vincent O. Mallet. **High levels of catalytic antibodies correlate with favorable outcome in sepsis**. *Proceedings of the National Academy of Sciences of the United States of America*, 102(11):4109–4113, March 2005.

[247] Stephanie A. Planque, Yasuhiro Nishiyama, Sari Sonoda, Yan Lin, Hiroaki Taguchi, Mariko Hara, Steven Kolodziej, Yukie Mitsuda, Veronica Gonzalez, Hameetha B R Sait, Ken Ichiro Fukuchi, Richard J. Massey, Robert P. Friedland, Brian O'Nuallain, Einar M. Sigurdsson, and Sudhir Paul. **Specific amyloid β clearance by a catalytic antibody**. *Journal of Biological Chemistry*, 290 (16):10229–10241, 2015.

[248] George P. Smith. **Filamentous Fusion Phage: Novel Expression Vectors That Display Cloned Antigens on the Virion Surface**. *Science*, 228(4705):1315–1317, June 1985.

[249] Christopher G. Ullman, Laura Frigotto, and R. Neil Cooley. **In vitro methods for peptide display and their applications**. *Briefings in Functional Genomics*, 10(3):125–134, May 2011.

[250] Miriam Kaltenbach and Florian Hollfelder. **SNAP display: in vitro protein evolution in microdroplets**. *Methods in Molecular Biology (Clifton, N.J.)*, 805:101–111, 2012.

[251] Bernhard Valldorf, Steffen C. Hinz, Giulio Russo, Lukas Pekar, Laura Mohr, Janina Klemm, Achim Doerner, Simon Krah, Michael Hust, and Stefan Zielonka. **Antibody display technologies: selecting the cream of the crop**. *Biological Chemistry*, 403(5-6):455–477, April 2022.

[252] Sudhir Paul, Alfonso Tramontano, Gennady Gololobov, Yong-Xin Zhou, Hiroaki Taguchi, Sangeeta Karle, Yasuhiro Nishiyama, Stephanie Planque, and Saji George. **Phosphonate Ester Probes for Proteolytic Antibodies**. *Journal of Biological Chemistry*, 276(30):28314–28320, July 2001.

[253] Dan S. Tawfik and Andrew D. Griffiths. **Man-made cell-like compartments for molecular evolution**. *Nature Biotechnology*, 16(7):652–656, 1998.

[254] Helen M. Cohen, Dan S. Tawfik, and Andrew D. Griffiths. **Altering the sequence specificity of HaeIII methyltransferase by directed evolution using in vitro compartmentalization**. *Protein Engineering, Design and Selection*, 17(1):3–11, January 2004.

[255] Amir Aharoni, Gil Amitai, Kalia Bernath, Shlomo Magdassi, and Dan S. Tawfik. **High-throughput screening of enzyme libraries: thiolactonases evolved by fluorescence-activated sorting of single cells in emulsion compartments**. *Chemistry & Biology*, 12(12):1281–1289, December 2005.

[256] Nobuhide Doi, Shin Kumadaki, Yuko Oishi, Nobutaka Matsumura, and Hiroshi Yanagawa. **In vitro selection of restriction endonucleases by in vitro compartmentalization**. *Nucleic Acids Research*, 32(12):e95, 2004.

[257] Andrew D. Griffiths and Dan S. Tawfik. **Directed evolution of an extremely fast phosphotriesterase by in vitro compartmentalization**. *The EMBO journal*, 22(1):24–35, January 2003.

[258] Letizia Diamante, Pietro Gatti-Lafranconi, Yolanda Schaerli, and Florian Hollfelder. **In vitro affinity screening of protein and peptide binders by megavalent bead surface display**. *Protein engineering, design & selection: PEDS*, 26(10):713–724, October 2013.

[259] Rui Gan, Yumiko Yamanaka, Takaaki Kojima, and Hideo Nakano. **Microbeads display of proteins using emulsion PCR and cell-free protein synthesis**. *Biotechnology Progress*, 24 (5):1107–1114, 2008.

[260] Viktor Stein, India Sielaff, Kai Johnsson, and Florian Hollfelder. **A covalent chemical genotype-phenotype linkage for in vitro protein evolution**. *Chembiochem: A European Journal of Chemical Biology*, 8(18):2191–2194, December 2007.

[261] Gillian Houlihan, David Lowe, and Florian Hollfelder. **SNAP display - an in vitro method for the selection of protein binders**. *Current Pharmaceutical Design*, 19(30):5421–5428, 2013.

[262] Sylwia A. Mankowska, Pietro Gatti-Lafranconi, Matthieu Chodorge, Sudharsan Sridharan, Ralph R. Minter, and Florian Hollfelder. **A Shorter Route to Antibody Binders via Quantitative in vitro Bead-Display Screening and Consensus Analysis**. *Scientific Reports*, 6(1): 36391, November 2016.

[263] MATTHEW LEVY, KARL E. GRISWOLD, and ANDREW D. ELLINGTON. **Direct selection of trans-acting ligase ribozymes by in vitro compartmentalization**. *RNA*, 11(10):1555–1562, October 2005.

[264] Jeremy J. Agresti, Bernard T. Kelly, Andres Jäschke, and Andrew D. Griffiths. **Selection of ribozymes that catalyse multiple-turnover Diels-Alder cycloadditions by using in vitro compartmentalization**. *Proceedings of the National Academy of Sciences of the United States of America*, 102(45):16170–16175, November 2005.

[265] Siddhartha Paul, Alexander Stang, Klaus Lennartz, Matthias Tenbusch, and Klaus Überla. **Selection of a T7 promoter mutant with enhanced in vitro activity by a novel multi-copy bead display approach for in vitro evolution**. *Nucleic Acids Research*, 41(1):e29, January 2013.

[266] Helen Song, Joshua D. Tice, and Rustem F. Ismagilov. **A Microfluidic System for Controlling Reaction Networks in Time**. *Angewandte Chemie International Edition*, 42(7):768–772, 2003.

[267] D. R. Link, S. L. Anna, D. A. Weitz, and H. A. Stone. **Geometrically mediated breakup of drops in microfluidic devices**. *Physical Review Letters*, 92(5):054503, February 2004.

[268] Darren R. Link, Erwan Grasland-Mongrain, Agnes Duri, Flavie Sarrazin, Zhengdong Cheng, Galder Cristobal, Manuel Marquez, and David A. Weitz. **Electric Control of Droplets in Microfluidic Devices**. *Angewandte Chemie International Edition*, 45(16):2556–2560, 2006.

[269] Jeremy J. Agresti, Eugene Antipov, Adam R. Abate, Keunho Ahn, Amy C. Rowat, Jean-Christophe Baret, Manuel Marquez, Alexander M. Klibanov, Andrew D. Griffiths, and David A. Weitz. **Ultrahigh-throughput screening in drop-based microfluidics for directed evolution**. *Proceedings of the National Academy of Sciences*, 107(9):4004–4009, March 2010.

[270] Haishui Huang, Yin Yu, Yong Hu, Xiaoming He, O. Berk Usta, and Martin L. Yarmush. **Generation and manipulation of hydrogel microcapsules by droplet-based microfluidics for mammalian cell culture**. *Lab on a Chip*, 17(11):1913–1932, May 2017.

[271] Keunho Ahn, Charles Kerbage, Tom P. Hunt, R. M. Westervelt, Darren R. Link, and D. A. Weitz. **Dielectrophoretic manipulation of drops for high-speed microfluidic sorting devices**. *Applied Physics Letters*, 88(2):024104, January 2006.

[272] Josephin M. Holstein, Christian Gylstorff, and Florian Hollfelder. **Cell-free Directed Evolution of a Protease in Microdroplets at Ultrahigh Throughput**. *ACS Synthetic Biology*, 10(2): 252–257, February 2021.

[273] Jeonghun Nam, Hyunjung Lim, Choong Kim, Ji Yoon Kang, and Sehyun Shin. **Density-dependent separation of encapsulated cells in a microfluidic channel by using a standing surface acoustic wave**. *Biomicrofluidics*, 6(2):24120–2412010, June 2012.

[274] Tengyang Jing, Ramesh Ramji, Majid Ebrahimi Warkiani, Jongyoon Han, Chwee Teck Lim, and Chia-Hung Chen. **Jetting microfluidics with size-sorting capability for single-cell protease detection**. *Biosensors and Bioelectronics*, 66:19–23, April 2015.

[275] Filip Hasecke, Chamani Niyangoda, Gustavo Borjas, Jianjun Pan, Garrett Matthews, Martin Muschol, and Wolfgang Hoyer. **Protofibril–Fibril Interactions Inhibit Amyloid Fibril Assembly by Obstructing Secondary Nucleation**. *Angewandte Chemie International Edition*, 60(6):3016–3021, 2021.

[276] Robert M. Koffie, Melanie Meyer-Luehmann, Tadafumi Hashimoto, Kenneth W. Adams, Matthew L. Mielke, Monica Garcia-Alloza, Kristina D. Micheva, Stephen J. Smith, M. Leo Kim, Virginia M. Lee, Bradley T. Hyman, and Tara L. Spires-Jones. **Oligomeric amyloid beta associates with postsynaptic densities and correlates with excitatory synapse loss near senile plaques**. *Proceedings of the National Academy of Sciences of the United States of America*, 106(10):4012–4017, March 2009.

[277] Thomas J. Esparza, Hanzhi Zhao, John R. Cirrito, Nigel J. Cairns, Randall J. Bateman, David M. Holtzman, and David L. Brody. **Amyloid-β oligomerization in Alzheimer dementia versus high-pathology controls**. *Annals of Neurology*, 73(1):104–119, January 2013.

[278] Alessandra Bigi, Roberta Cascella, Fabrizio Chiti, and Cristina Cecchi. **Amyloid fibrils act as a reservoir of soluble oligomers, the main culprits in protein deposition diseases**. *BioEssays*, n/a(n/a):2200086.

[279] D. M. Walsh, A. Lomakin, G. B. Benedek, M. M. Condron, and D. B. Teplow. **Amyloid beta-protein fibrillogenesis. Detection of a protofibrillar intermediate**. *The Journal of Biological Chemistry*, 272(35):22364–22372, August 1997.

[280] Asad Jan, Dean M. Hartley, and Hilal A. Lashuel. **Preparation and characterization of toxic Aβ aggregates for structural and functional studies in Alzheimer's disease research**. *Nature Protocols*, 5(6):1186–1209, June 2010.

[281] Jiyong Lee, Elizabeth K Culyba, Evan T Powers, and Jeffery W Kelly. **Amyloid-$\backslashupbeta$ forms fibrils by nucleated conformational conversion of oligomers**. *Nature Chemical Biology*, pages 602–609, September 2011.

[282] Mimi Nick, Yibing Wu, Nathan W. Schmidt, Stanley B. Prusiner, Jan Stöhr, and William F. DeGrado. **A long-lived Aβ oligomer resistant to fibrillization**. *Biopolymers*, 109(8):e23096, 2018.

[283] Mattias Törnquist, Risto Cukalevski, Ulrich Weininger, Georg Meisl, Tuomas P. J. Knowles, Thom Leiding, Anders Malmendal, Mikael Akke, and Sara Linse. **Ultrastructural evidence for self-replication of Alzheimer-associated Aβ42 amyloid along the sides of fibrils**. *Proceedings of the National Academy of Sciences of the United States of America*, 117(21):11265–11273, May 2020.

[284] Lyndsey E Collins-Praino, Yitshak I Francis, Erica Y Griffith, Anne F Wiegman, Jonathan Urbach, Arlene Lawton, Lawrence S Honig, Etty Cortes, Jean Paul, G Vonsattel, Peter D Canoll, James E Goldman, and Adam M Brickman. **Soluble amyloid beta levels are elevated in the white matter of Alzheimer's patients, independent of cortical plaque severity**. *Acta Neuropathologica Communications*, 2, 2014.

[285] E. Hellström-Lindahl, M. Viitanen, and A. Marutle. **Comparison of Aβ levels in the brain of familial and sporadic Alzheimer's disease**. *Neurochemistry International*, 55(4):243–252, 2009.

[286] Alex E. Roher, Chera L. Esh, Tyler A. Kokjohn, Eduardo M. Castaño, Gregory D. Van Vickle, Walter M. Kalback, R. Lyle Patton, Dean C. Luehrs, Ian D. Daugs, Yu-Min Kuo, Mark R. Emmerling, Holly Soares, Joseph F. Quinn, Jeffrey Kaye, Donald J. Connor, Nina B. Silverberg, Charles H. Adler, James D. Seward, Thomas G. Beach, and Marwan N. Sabbagh. **Amyloid beta peptides in human plasma and tissues and their significance for Alzheimer's disease**. *Alzheimer's & Dementia*, 5(1):18–29, 2009.

[287] Dag Sehlin, Hillevi Englund, Barbro Simu, Mikael Karlsson, Martin Ingelsson, Fredrik Nikolajeff, Lars Lannfelt, and Frida Ekholm Pettersson. **Large Aggregates Are the Major Soluble Aβ Species in AD Brain Fractionated with Density Gradient Ultracentrifugation**. *PLOS ONE*, 7(2):e32014, February 2012.

[288] Marie P. Schützmann, Filip Hasecke, Sarah Bachmann, Mara Zielinski, Sebastian Hänsch, Gunnar F. Schröder, Hans Zempel, and Wolfgang Hoyer. **Endo-lysosomal Aβ concentration and pH trigger formation of Aβ oligomers that potently induce Tau missorting**. *Nature Communications*, 12(1):4634, December 2021.

[289] Xiaoyan Hu, Scott L. Crick, Guojun Bu, Carl Frieden, Rohit V. Pappu, and Jin-Moo Lee. **Amyloid seeds formed by cellular uptake, concentration, and aggregation of the amyloid-beta peptide**. *Proceedings of the National Academy of Sciences of the United States of America*, 106(48):20324–20329, December 2009.

[290] L. Chaiet and F. J. Wolf. **THE PROPERTIES OF STREPTAVIDIN, A BIOTIN-BINDING PROTEIN PRODUCED BY STREPTOMYCETES**. *Archives of Biochemistry and Biophysics*, 106:1–5, July 1964.

[291] Jason DeChancie and K.N. Houk. **The Origins of Femtomolar Protein–Ligand Binding: Hydrogen Bond Cooperativity and Desolvation Energetics in the Biotin–(Strept)Avidin Binding Site**. *Journal of the American Chemical Society*, 129(17):5419–5429, May 2007.

[292] T. Kojima. **PCR amplification from single DNA molecules on magnetic beads in emulsion: application for high-throughput screening of transcription factor targets**. *Nucleic Acids Research*, 33(17):e150–e150, September 2005.

[293] Marcel Margulies, Michael Egholm, William E. Altman, Said Attiya, Joel S. Bader, Lisa A. Bemben, Jan Berka, Michael S. Braverman, Yi-Ju Chen, Zhoutao Chen, Scott B. Dewell, Lei Du, Joseph M. Fierro, Xavier V. Gomes, Brian C. Godwin, Wen He, Scott Helgesen, Chun He Ho, Gerard P. Irzyk, Szilveszter C. Jando, Maria L. I. Alenquer, Thomas P. Jarvie, Kshama B. Jirage, Jong-Bum Kim, James R. Knight, Janna R. Lanza, John H. Leamon, Steven M. Lefkowitz, Ming Lei, Jing Li, Kenton L. Lohman, Hong Lu, Vinod B. Makhijani, Keith E. McDade, Michael P. McKenna, Eugene W. Myers, Elizabeth Nickerson, John R. Nobile, Ramona Plant, Bernard P. Puc, Michael T. Ronan, George T. Roth, Gary J. Sarkis, Jan Fredrik Simons, John W. Simpson, Maithreyan Srinivasan, Karrie R. Tartaro, Alexander Tomasz, Kari A. Vogt, Greg A. Volkmer, Shally H. Wang, Yong Wang, Michael P. Weiner, Pengguang Yu, Richard F. Begley, and Jonathan M. Rothberg. **Genome sequencing in microfabricated high-density picolitre reactors**. *Nature*, 437(7057):376–380, September 2005.

[294] Devin Dressman, Hai Yan, Giovanni Traverso, Kenneth W. Kinzler, and Bert Vogelstein. **Transforming single DNA molecules into fluorescent magnetic particles for detection and enumeration of genetic variations**. *Proceedings of the National Academy of Sciences*, 100 (15):8817–8822, July 2003.

[295] Frank Diehl, Meng Li, Yiping He, Kenneth W. Kinzler, Bert Vogelstein, and Devin Dressman. **BEAMing: single-molecule PCR on microparticles in water-in-oil emulsions**. *Nature Methods*, 3(7):551–559, July 2006.

[296] Irene Tiemann-Boege, Christina Curtis, Deepali N. Shinde, Daniel B. Goodman, Simon Tavaré, and Norman Arnheim. **Product Length, Dye Choice, and Detection Chemistry in the Bead-Emulsion Amplification of Millions of Single DNA Molecules in Parallel**. *Analytical Chemistry*, 81(14):5770–5776, July 2009.

[297] Ryan H. P. Siu, Yang Liu, Kaitlin H. Y. Chan, Clara Ridzewski, Liane Siu Slaughter, and Angela R. Wu. **Optimization of on-bead emulsion polymerase chain reaction based on single particle analysis**. *Talanta*, 221:121593, January 2021.

[298] Frank Diehl, Meng Li, Devin Dressman, Yiping He, Dong Shen, Steve Szabo, Luis A. Diaz, Steven N. Goodman, Kerstin A. David, Hartmut Juhl, Kenneth W. Kinzler, and Bert Vogelstein. **Detection and quantification of mutations in the plasma of patients with colorectal tumors**. *Proceedings of the National Academy of Sciences*, 102(45):16368–16373, November 2005.

[299] MRC Centre for Protein Engineering, **V Base**. URL https://www2.mrc-lmb.cam.ac.uk/vbase/alignments2.php. Accessed on 2022-11-17.

[300] Bertil Macao, Wolfgang Hoyer, Anders Sandberg, Ann-Christin Brorsson, Christopher M. Dobson, and Torleif Härd. **Recombinant amyloid beta-peptide production by coexpression with an affibody ligand**. *BMC biotechnology*, 8:82, 2008.

[301] Bei-Wen Ying, Hideki Taguchi, Hiroshi Ueda, and Takuya Ueda. **Chaperone-assisted folding of a single-chain antibody in a reconstituted translation system**. *Biochemical and Biophysical Research Communications*, 320(4):1359–1364, August 2004.

[302] XiuPing Jiang, Yuji Ookubo, Ikuo Fujii, Hideo Nakano, and Tsuneo Yamane. **Expression of Fab fragment of catalytic antibody 6D9 in an *Escherichia coli* in vitro coupled transcription/translation system**. *FEBS Letters*, 514(2-3):290–294, March 2002.

[303] Lyubov A. Ryabova, Dominique Desplancq, Alexander S. Spirin, and Andreas Plückthun. **Functional antibody production using cell-free translation: Effects of protein disulfide isomerase and chaperones**. *Nature Biotechnology*, 15(1):79–84, January 1997.

[304] Claire Goldsbury, Peter Frey, Vesna Olivieri, Ueli Aebi, and Shirley A. Müller. **Multiple Assembly Pathways Underlie Amyloid-β Fibril Polymorphisms**. *Journal of Molecular Biology*, 352(2): 282–298, September 2005.

[305] Martin Muschol and Wolfgang Hoyer. **Amyloid oligomers as on-pathway precursors or off-pathway competitors of fibrils**. *Frontiers in Molecular Biosciences*, 10, 2023.

[306] Ting Yang, Shaomin Li, Huixin Xu, Dominic M. Walsh, and Dennis J. Selkoe. **Large Soluble Oligomers of Amyloid β-Protein from Alzheimer Brain Are Far Less Neuroactive Than the Smaller Oligomers to Which They Dissociate**. *The Journal of Neuroscience*, 37(1): 152–163, January 2017.

[307] Thomas J. Esparza, Norelle C. Wildburger, Hao Jiang, Mihika Gangolli, Nigel J. Cairns, Randall J. Bateman, and David L. Brody. **Soluble Amyloid-beta Aggregates from Human Alzheimer's Disease Brains**. *Scientific Reports*, 6(1):38187, December 2016.

[308] Else F. Gerresheim, Arne Herring, Lothar Gremer, Andreas Müller-Schiffmann, Kathy Keyvani, and Carsten Korth. **The interaction of insoluble Amyloid-β with soluble Amyloid-β dimers decreases Amyloid-β plaque numbers**. *Neuropathology and Applied Neurobiology*, 47(5):603–610, August 2021.

[309] Takahiro Yamaguchi, Hisashi Yagi, Yuji Goto, Katsumi Matsuzaki, and Masaru Hoshino. **A Disulfide-Linked Amyloid-β Peptide Dimer Forms a Protofibril-like Oligomer through a Distinct Pathway from Amyloid Fibril Formation**. *Biochemistry*, 49(33):7100–7107, August 2010.

[310] Tanja Blume, Maximilian Deussing, Gloria Biechele, Finn Peters, Benedikt Zott, Claudio Schmidt, Nicolai Franzmeier, Karin Wind, Florian Eckenweber, Christian Sacher, Yuan Shi, Katharina Ochs, Gernot Kleinberger, Xianyuan Xiang, Carola Focke, Simon Lindner, Franz-Josef Gildehaus, Leonie Beyer, Barbara von Ungern-Sternberg, Peter Bartenstein, Karlheinz Baumann, Helmuth Adelsberger, Axel Rominger, Paul Cumming, Michael Willem, Mario M. Dorostkar, Jochen Herms, and Matthias Brendel. **Chronic PPARγ Stimulation Shifts Amyloidosis to Higher Fibrillarity but Improves Cognition**. *Frontiers in Aging Neuroscience*, 14, 2022.

[311] D. W. Dickson. **Neuropathological diagnosis of Alzheimer's disease: a perspective from longitudinal clinicopathological studies**. *Neurobiology of Aging*, 18(4 Suppl):S21–26, 1997.

[312] B. T Hyman and T Gomez-Isla. **The Natural History of Alzheimer Neurofibrillary Tangles and Amyloid Deposits**. *Neurobiology of Aging*, 18(4):386–387, July 1997.

[313] Wen-Ying Qiu, Qian Yang, Wanying Zhang, Naili Wang, Di Zhang, Yue Huang, and Chao Ma. **The Correlations between Postmortem Brain Pathologies and Cognitive Dysfunction in Aging and Alzheimer's Disease**. *Current Alzheimer Research*, 15(5):462–473, March 2018.

[314] Justin M. Long and David M. Holtzman. **Alzheimer Disease: An Update on Pathobiology and Treatment Strategies**. *Cell*, 179(2):312–339, October 2019.

[315] Stephen R. Robinson and Glenda M. Bishop. **Abeta as a bioflocculant: implications for the amyloid hypothesis of Alzheimer's disease**. *Neurobiology of Aging*, 23(6):1051–1072, 2002.

[316] Stephanie J. Soscia, James E. Kirby, Kevin J. Washicosky, Stephanie M. Tucker, Martin Ingelsson, Bradley Hyman, Mark A. Burton, Lee E. Goldstein, Scott Duong, Rudolph E. Tanzi, and Robert D. Moir. **The Alzheimer's disease-associated amyloid beta-protein is an antimicrobial peptide**. *PloS One*, 5(3):e9505, March 2010.

[317] Deepak Kumar Vijaya Kumar, Se Hoon Choi, Kevin J. Washicosky, William A. Eimer, Stephanie Tucker, Jessica Ghofrani, Aaron Lefkowitz, Gawain McColl, Lee E. Goldstein, Rudolph E. Tanzi, and Robert D. Moir. **Amyloid-β peptide protects against microbial infection in mouse and worm models of Alzheimer's disease**. *Science Translational Medicine*, 8(340):340ra72, May 2016.

[318] Philipp Spitzer, Mateja Condic, Martin Herrmann, Timo Jan Oberstein, Marina Scharin-Mehlmann, Daniel F. Gilbert, Oliver Friedrich, Teja Grömer, Johannes Kornhuber, Roland Lang, and Juan Manuel Maler. **Amyloidogenic amyloid-β-peptide variants induce microbial agglutination and exert antimicrobial activity**. *Scientific Reports*, 6:32228, September 2016.

[319] Mitchell R. White, Ruth Kandel, Shweta Tripathi, David Condon, Li Qi, Jeffrey Taubenberger, and Kevan L. Hartshorn. **Alzheimer's associated β-amyloid protein inhibits influenza A virus and modulates viral interactions with phagocytes**. *PloS One*, 9(7):e101364, 2014.

[320] Karine Bourgade, Hugo Garneau, Geneviève Giroux, Aurélie Y. Le Page, Christian Bocti, Gilles Dupuis, Eric H. Frost, and Tamàs Fülöp. **β-Amyloid peptides display protective activity against the human Alzheimer's disease-associated herpes simplex virus-1**. *Biogerontology*, 16(1):85–98, February 2015.

[321] William A. Eimer, Deepak Kumar Vijaya Kumar, Nanda Kumar Navalpur Shanmugam, Alex S. Rodriguez, Teryn Mitchell, Kevin J. Washicosky, Bence György, Xandra O. Breakefield, Rudolph E. Tanzi, and Robert D. Moir. **Alzheimer's Disease-Associated β-Amyloid Is Rapidly Seeded by Herpesviridae to Protect against Brain Infection**. *Neuron*, 99(1):56–63.e3, July 2018.

[322] Daniela Puzzo, Lucia Privitera, Elena Leznik, Mauro Fà, Agnieszka Staniszewski, Agostino Palmeri, and Ottavio Arancio. **Picomolar amyloid-beta positively modulates synaptic plasticity and memory in hippocampus**. *The Journal of Neuroscience: The Official Journal of the Society for Neuroscience*, 28(53):14537–14545, December 2008.

[323] Ana Garcia-Osta and Cristina M. Alberini. **Amyloid beta mediates memory formation**. *Learning & Memory (Cold Spring Harbor, N.Y.)*, 16(4):267–272, April 2009.

[324] John E. Morley, Susan A. Farr, William A. Banks, Steven N. Johnson, Kelvin A. Yamada, and Lin Xu. **A physiological role for amyloid-beta protein:enhancement of learning and memory**. *Journal of Alzheimer's disease: JAD*, 19(2):441–449, 2010.

[325] C. A. Raby, M. C. Morganti-Kossmann, T. Kossmann, P. F. Stahel, M. D. Watson, L. M. Evans, P. D. Mehta, K. Spiegel, Y. M. Kuo, A. E. Roher, and M. R. Emmerling. **Traumatic brain injury increases beta-amyloid peptide 1-42 in cerebrospinal fluid**. *Journal of Neurochemistry*, 71(6):2505–2509, December 1998.

[326] David L. Brody, Sandra Magnoni, Kate E. Schwetye, Michael L. Spinner, Thomas J. Esparza, Nino Stocchetti, Gregory J. Zipfel, and David M. Holtzman. **Amyloid-beta dynamics correlate with neurological status in the injured human brain**. *Science (New York, N.Y.)*, 321(5893):1221–1224, August 2008.

[327] David J. Loane, Ana Pocivavsek, Charbel E.-H. Moussa, Rachel Thompson, Yasuji Matsuoka, Alan I. Faden, G. William Rebeck, and Mark P. Burns. **Amyloid precursor protein secretases as therapeutic targets for traumatic brain injury**. *Nature Medicine*, 15(4):377–379, April 2009.

[328] Ahdeah Pajoohesh-Ganji, Mark P. Burns, Sonali Pal-Ghosh, Gauri Tadvalkar, Nicole G. Hokenbury, Mary Ann Stepp, and Alan I. Faden. **Inhibition of amyloid precursor protein secretases reduces recovery after spinal cord injury**. *Brain research*, 1560:73–82, April 2014.

[329] Craig S. Atwood, Glenda M. Bishop, George Perry, and Mark A. Smith. **Amyloid-beta: a vascular sealant that protects against hemorrhage?** *Journal of Neuroscience Research*, 70 (3):356, November 2002.

[330] Craig S. Atwood, Richard L. Bowen, Mark A. Smith, and George Perry. **Cerebrovascular requirement for sealant, anti-coagulant and remodeling molecules that allow for the maintenance of vascular integrity and blood supply**. *Brain Research. Brain Research Reviews*, 43(1):164–178, September 2003.

[331] Emma Ristori, Sandra Donnini, and Marina Ziche. **New Insights Into Blood-Brain Barrier Maintenance: The Homeostatic Role of β-Amyloid Precursor Protein in Cerebral Vasculature**. *Frontiers in Physiology*, 11:1056, August 2020.

[332] Samuel C. Bartley, Madison T. Proctor, Hongjie Xia, Evelyn Ho, Dong S. Kang, Kristen Schuster, Maíra A. Bicca, Henrique S. Seckler, Kirsten L. Viola, Steven M. Patrie, Neil L. Kelleher, Fernando G. De Mello, and William L. Klein. **An Essential Role for Alzheimer's-Linked Amyloid Beta Oligomers in Neurodevelopment: Transient Expression of Multiple Proteoforms during Retina Histogenesis**. *International Journal of Molecular Sciences*, 23(4):2208, January 2022.

[333] Daniela Puzzo, Lucia Privitera, Elena Leznik, Mauro Fà, Agnieszka Staniszewski, Agostino Palmeri, and Ottavio Arancio. **Picomolar Amyloid-β Positively Modulates Synaptic Plasticity and Memory in Hippocampus**. *Journal of Neuroscience*, 28(53):14537–14545, December 2008.

[334] Elin K. Esbjörner, Fiona Chan, Eric Rees, Miklos Erdelyi, Leila M. Luheshi, Carlos W. Bertoncini, Clemens F. Kaminski, Christopher M. Dobson, and Gabriele S. Kaminski Schierle. **Direct Observations of Amyloid β Self-Assembly in Live Cells Provide Insights into Differences in the Kinetics of Aβ(1–40) and Aβ(1–42) Aggregation**. *Chemistry & Biology*, 21(6):732–742, June 2014.

[335] Yu-Sheng Fang, Kuen-Jer Tsai, Yu-Jen Chang, Patricia Kao, Rima Woods, Pan-Hsien Kuo, Cheng-Chun Wu, Jhih-Ying Liao, Shih-Chieh Chou, Vinson Lin, Lee-Way Jin, Hanna S Yuan, Irene H Cheng, Pang-Hsien Tu, and Yun-Ru Chen. **Full-length TDP-43 forms toxic amyloid oligomers that are present in frontotemporal lobar dementia-TDP patients**. *Nature communications*, 5: 4824, September 2014.

[336] Roger B. Knowles, Claire Wyart, Sergey V. Buldyrev, Luis Cruz, Brigita Urbanc, Michael E. Hasselmo, H. Eugene Stanley, and Bradley T. Hyman. **Plaque-induced neurite abnormalities: Implications for disruption of neural networks in Alzheimer's disease**. *Proceedings of the National Academy of Sciences*, 96(9):5274–5279, April 1999.

[337] J. D. D'Amore, S. T. Kajdasz, M. E. McLellan, B. J. Bacskai, E. A. Stern, and B. T. Hyman. **In Vivo Multiphoton Imaging of a Transgenic Mouse Model of Alzheimer Disease Reveals Marked Thioflavine-S-Associated Alterations in Neurite Trajectories**. *Journal of Neuropathology & Experimental Neurology*, 62(2):137–145, February 2003.

[338] Kirsten L. Viola, James Sbarboro, Ruchi Sureka, Mrinmoy De, Maíra A. Bicca, Jane Wang, Shaleen Vasavada, Sreyesh Satpathy, Summer Wu, Hrushikesh Joshi, Pauline T. Velasco, Keith MacRenaris, E. Alex Waters, Chang Lu, Joseph Phan, Pascale Lacor, Pottumarthi Prasad, Vinayak P. Dravid, and William L. Klein. **Towards non-invasive diagnostic imaging of early-stage Alzheimer's disease**. *Nature Nanotechnology*, 10(1):91–98, January 2015.

[339] Peng Liu, Miranda N. Reed, Linda A. Kotilinek, Marianne K. O. Grant, Colleen L. Forster, Wei Qiang, Samantha L. Shapiro, John H. Reichl, Angie C. A. Chiang, Joanna L. Jankowsky, Carrie M. Wilmot, James P. Cleary, Kathleen R. Zahs, and Karen H. Ashe. **Quaternary Structure Defines a Large Class of Amyloid-β Oligomers Neutralized by Sequestration**. *Cell Reports*, 11 (11):1760–1771, June 2015.

[340] Dominik Röhr, Baayla D. C. Boon, Martin Schuler, Kristin Kremer, Jeroen J. M. Hoozemans, Femke H. Bouwman, Samir F. El-Mashtoly, Andreas Nabers, Frederik Großerueschkamp, Annemieke J. M. Rozemuller, and Klaus Gerwert. **Label-free vibrational imaging of different**

Aβ plaque types in Alzheimer's disease reveals sequential events in plaque development. *Acta Neuropathologica Communications*, 8(1):222, December 2020.

[341] Yasuhiro Nishiyama, Hiroaki Taguchi, Mariko Hara, Stephanie A. Planque, Yukie Mitsuda, and Sudhir Paul. **Metal-dependent amyloid β-degrading catalytic antibody construct**. *Journal of Biotechnology*, 180:17–22, June 2014.

[342] Alexander K. Price, Andrew B. MacConnell, and Brian M. Paegel. **Microfluidic Bead Suspension Hopper**. *Analytical Chemistry*, 86(10):5039–5044, May 2014.

[343] Jean-Christophe Baret, Oliver J. Miller, Valerie Taly, Michaël Ryckelynck, Abdeslam El-Harrak, Lucas Frenz, Christian Rick, Michael L. Samuels, J. Brian Hutchison, Jeremy J. Agresti, Darren R. Link, David A. Weitz, and Andrew D. Griffiths. **Fluorescence-activated droplet sorting (FADS): efficient microfluidic cell sorting based on enzymatic activity**. *Lab on a Chip*, 9(13):1850–1858, July 2009.

[344] Ali Fallah-Araghi, Jean-Christophe Baret, Michael Ryckelynck, and Andrew D. Griffiths. **A completely in vitro ultrahigh-throughput droplet-based microfluidic screening system for protein engineering and directed evolution**. *Lab on a Chip*, 12(5):882–891, February 2012.

Eidesstattliche Erklärung

Ich versichere an Eides statt, dass die Dissertation von mir selbständig und ohne unzulässige fremde Hilfe unter Beachtung der „Grundsätze zur Sicherung guter wissenschaftlicher Praxis an der Heinrich-Heine-Universität Düsseldorf” erstellt worden ist.

Düsseldorf, den _____

_____